UNIVERSIDADE DE LISBOA
INSTITUTO SUPERIOR TÉCNICO

Monotonic, cyclic and seismic behaviour of pultruded structures: from connections to full-scale frames

David José Medeira Martins

Supervisor: Doctor José Manuel Cabecinhas de Almeida Gonilha

Co-Supervisors: Doctor João Pedro Ramôa Ribeiro Correia

Doctor Nuno Miguel Rosa Pereira Silvestre

Thesis approved in public session to obtain the PhD Degree in Civil Engineering

Jury final classification: **Pass with Distinction and Honour**

2022

TÉCNICO LISBOA

UNIVERSIDADE DE LISBOA

INSTITUTO SUPERIOR TÉCNICO

Monotonic, cyclic and seismic behaviour of pultruded structures: from connections to full-scale frames

David José Medeira Martins

Supervisor: Doctor José Manuel Cabecinhas de Almeida Gonilha

Co-Supervisors: Doctor João Pedro Ramôa Ribeiro Correia

Doctor Nuno Miguel Rosa Pereira Silvestre

Thesis approved in public session to obtain the PhD Degree in Civil Engineering

Jury final classification: **Pass with Distinction and Honour**

Jury

Chairperson: Doctor Eduardo Nuno Brito Santos Júlio, Instituto Superior Técnico, Universidade de Lisboa

Members of the Committee:

Doctor Tao Yu, Faculty of Construction and Environment, The Hong Kong Polytechnic University, Hong Kong

Doctor Luís Manuel Calado de Oliveira Martins, Instituto Superior Técnico, Universidade de Lisboa

Doctor Luís Manuel Coelho Guerreiro, Instituto Superior Técnico, Universidade de Lisboa

Doctor Francesco Ascione, Università Degli Studi di Salermo, Italy

Doctor José Manuel Cabecinhas de Almeida Gonilha, Instituto Superior Técnico, Universidade de Lisboa

Funding Institutions

Fundação para a Ciência e a Tecnologia (SFRH/BD/141089/2018)

2022

ABSTRACT

Pultruded glass fibre reinforced polymer (GFRP) profiles are being increasingly used as structural members in civil engineering applications. These profiles have significantly higher strength-to-weight ratio than conventional construction materials, high corrosion resistance and electromagnetic transparency. Due to these properties, pultruded GFRP profiles are already state-of-the-art in some niches of the construction industry, as energy and water treatment facilities. However, these profiles are not widely used in non-industrial structural applications, mostly due to the lack of design standards providing material-adapted and comprehensive design guidelines and rules. The available standards are incomplete in critical topics concerning the design of pultruded structures, in particular regarding the connections between profiles and the seismic behaviour of these structures (two topics with undeveloped research). This thesis aims at providing relevant scientific contributions for the current state of knowledge of these two topics, by presenting experimental, analytical and numerical studies concerning the: (i) monotonic and cyclic behaviour of beam-to-column connections between pultruded profiles; (ii) monotonic and cyclic sway behaviour of 2-dimensional pultruded frames; and (iii) seismic behaviour of 3-dimensional pultruded frames.

Four beam-to-column connection systems were developed for pultruded profiles: (i) for tubular sections, one sleeve connection system, including two interior steel parts, and one cuff connection system, comprising an exterior stainless steel cuff part; (ii) for I-sections, one cleated connection system, including stainless steel cleat parts, and one cuff connection system, comprising an exterior stainless steel cuff part. The auxiliary metallic parts were intended to improve the connections' performance by taking advantage of the steel's ductility. Regarding the experimental tests, all four systems presented significant stiffness, strength, ductility and capacity to dissipate energy (albeit considerable pinching was registered in most specimens). The cuff connection system was the best solution to join pultruded tubular profiles, as it presented the best overall performance. In what concerns the connections for I-section profiles, the cleated connections outperformed the cuff connections, especially regarding the ductility and capacity to dissipate energy. It should also be noted that the experimental tests comprised different series for each connection system, in which several details were varied (*i.e.* the bolts disposition, geometry of the auxiliary parts), providing valuable insights on how such parameters influence the connections' behaviour. The analytical "component method" was used to predict the initial stiffness of the sleeve connections (for tubular profiles) and of the cleated connections (for I-section profiles) with reasonable accuracy. The strength of both these systems was also predicted with reasonable accuracy, by a combination of analytical (for the design verifications) and numerical (for obtaining the load distribution per component) procedures.

The 2-dimensional frames included the connection systems previously developed and the same tubular or I-section profiles. The type of connection used had significant influence on the frames' behaviour, as connections with higher stiffness led to higher frame's stiffness. In addition to unfilled frames, the influence of infill walls or a cables bracing system on the frames' response was also assessed. The experimental results showed that infill walls and cables bracing system have remarkable effect on the frames' structural behaviour, significantly increasing their stiffness and load carrying capacity, as well as their cyclic performance, namely regarding energy dissipation. However, all 2-dimensional frames presented poor hysteretic response, owing to the high flexibility of the GFRP columns or to the inefficiency of the bracings and walls under cyclic loading conditions. Finally, a numerical study was developed which included the simulation of the cyclic tests of unfilled and unbraced frames, by means of relatively simple finite element models, comprising frame elements and spring joints, simulating the behaviour of the connections, using a multilinear hysteresis model. The comparison between experimental and numerical results shows that these simple and design-oriented FE models can provide an effective (and conservative) tool for the simulation of pultruded GFRP frames under horizontal cyclic loads.

The seismic tests were performed in a two-storey, one-bay, 3-dimensional frame composed by pultruded GFRP I-section profiles and cleated connections, fixed to a shaking table. In these tests, the seismic displacement histories consisted of design earthquakes for mainland Portugal. Twenty displacements histories were applied to the 3-dimensional frame, differing on the displacements' magnitude. The displacement histories were applied consecutively, presenting increasing magnitude order. The 3-dimensional frame was able to withstand the highest design seismic action for mainland Portugal without losing its structural integrity, demonstrating the feasibility of using such structural systems in zones prone to considerable seismic activity.

Keywords: Seismic behaviour; design; ductility; hysteretic; non-linear analysis.

RESUMO

Os perfis pultrudidos de polímero reforçado com fibras de vidro (GFRP) são cada vez mais utilizados como elementos estruturais em aplicações de Engenharia Civil. Estes perfis possuem elevada resistência e leveza, resistência à corrosão e transparência eletromagnética, tendo já, por isso, uma implantação significativa nalguns nichos da indústria da construção, como por exemplo em aplicações estruturais em estações de energia e tratamento de águas. No entanto, estes perfis ainda não são correntemente utilizados em aplicações estruturais sem carácter industrial, principalmente devido à inexistência de normas de projeto que contenham metodologias de dimensionamento abrangentes e adequadas a estes materiais compósitos. As normas de projeto disponíveis atualmente são ainda bastante incompletas em pontos críticos do dimensionamento, nomeadamente no que se refere às ligações entre perfis e ao comportamento sísmico deste tipo de estruturas (dois tópicos de investigação ainda pouco desenvolvidos). A presente tese tem como objetivo fornecer contribuições científicas relevantes para o estado-da-arte atual referente às ligações entre perfis pultrudidos e ao comportamento lateral de pórticos constituídos por estes perfis, apresentando estudos experimentais, analíticos e numéricos referentes ao: (i) comportamento monotónico e cíclico de ligações viga-coluna entre perfis pultrudidos; (ii) comportamento lateral monotónico e cíclico de pórticos bidimensionais com perfis pultrudidos; e (iii) comportamento sísmico de pórticos tridimensionais com perfis pultrudidos.

Foram desenvolvidos quatro sistemas de ligação para perfis pultrudidos: (i) com secção tubulares, um sistema de ligação de encaixe, com duas peças interiores em aço, e um sistema de ligação de capacete, com uma peça exterior em aço inoxidável; e (ii) com secção em I, um sistema de ligação de cantoneira, em aço inoxidável, e um sistema de ligação de capacete, com uma peça exterior em aço inoxidável. Foram escolhidas peças auxiliares em aço (carbono ou inoxidável) com o objetivo de melhorar o comportamento das ligações, tirando partido da ductilidade deste material. No que refere aos ensaios experimentais, todos os sistemas de ligação apresentaram considerável rigidez, resistência, ductilidade e capacidade de dissipar energia. Para perfis tubulares, o sistema de ligação de capacete apresentou melhor desempenho do que o sistema de ligação de encaixe, sendo por isso a solução mais indicada. Para perfis com secção em I, o desempenho do sistema de ligação de cantoneira superou o do sistema de ligação de capacete, principalmente no que se refere à ductilidade e à capacidade de dissipar energia. É também de referir que os ensaios experimentais incluíram diferentes tipologias por sistema de ligação, nas quais se variou alguns pormenores construtivos (tais como a disposição dos parafusos ou a geometria das peças auxiliares), permitindo avaliar a influência que estes parâmetros têm no comportamento das ligações. A rigidez das ligações de encaixe (para perfis tubulares) e de cantoneira (para perfis com secção em I) foi estimada analiticamente através do "método das componentes", apresentando valores consideravelmente próximos dos experimentais. Por sua vez, a resistência destes dois sistemas de ligação foi estimada com razoável precisão, através de uma combinação de procedimentos analíticos (para as verificações de segurança) e numéricos (para obter a distribuição de forças pelos diferentes componentes).

Os pórticos bidimensionais foram compostos pelos sistemas de ligação desenvolvidos anteriormente (e pelos mesmos perfis tubulares e de secção em I). Verificou-se que o comportamento dos pórticos bidimensionais é bastante influenciado pelo tipo de ligação utilizado, aumentando a rigidez dos pórticos com a maior rigidez das suas ligações. Além de serem ensaiados pórticos simples, foram também estudados pórticos com paredes divisórias leves ou com um sistema de contraventamento com cabos. Os ensaios experimentais permitiram concluir que estes elementos adicionais têm bastante influência no comportamento monotónico dos pórticos, aumentando significativamente a sua rigidez e resistência, e no seu desempenho cíclico, nomeadamente no que refere à dissipação de energia. No entanto, todos os pórticos bidimensionais apresentaram fraco comportamento histerético, devido à elevada flexibilidade das colunas ou à ineficiência dos contraventamentos ou das paredes quando solicitados por ações cíclicas. Por fim, foi desenvolvido um estudo numérico que abrangeu a simulação do comportamento cíclico de pórticos sem contraventamentos ou paredes, através de modelos de elementos finitos de relativa simplicidade, que incluíram elementos de barra e molas de junção que simularam o comportamento das ligações (com recurso a um modelo histerético multilinear). Os resultados obtidos através do estudo numérico foram relativamente semelhantes aos resultados experimentais, demonstrando que estes modelos simples (e direcionados para o projeto de estruturas) podem ser utilizados para simular o comportamento de pórticos constituídos por perfis pultrudidos em GFRP solicitados por ações laterais cíclicas.

Os ensaios sísmicos foram realizados num pórtico tridimensional de dois pisos, composto por perfis pultrudidos em GFRP com secção em I e ligações de cantoneira, fixo a uma mesa sísmica. Nestes ensaios, os históricos de deslocamento consistiram em sismos regulamentares para Portugal continental. Foram aplicados 20 históricos de deslocamento, nos quais foi variada a magnitude dos deslocamentos. Os históricos de deslocamento foram aplicados consecutivamente, de forma incremental no que refere aos deslocamentos absolutos. O pórtico tridimensional manteve intacta a sua integridade estrutural para o sismo regulamentar com magnitude máxima em território português, demonstrando a viabilidade de utilizar estes sistemas estruturais em zonas de risco sísmico.

Palavras-chave: Comportamento sísmico; dimensionamento; ductilidade; histerético; análise não-linear.

AKNOWLEDGEMENTS

First and foremost, I would like to express my deepest gratitude to Doctor José Gonilha, my scientific supervisor, who was instrumental in the development of this thesis with his constant friendship, support, patience, knowledge and insight. It was a pleasure to work with Doctor José Gonilha.

I would also like to express my deepest gratitude to my thesis co-supervisors, Professor João Ramôa Correia and Professor Nuno Silvestre, who were always available and supportive and whose contributions were crucial for the success of this thesis. The deep knowledge, vast experience and work ethics of Professor João Ramôa Correia and Professor Nuno Silvestre are inspiring.

I am very grateful for the help of Professor Fernando Branco and Professor Luis Guerreiro for their contributions and insight on numerous stages of this thesis.

I would also want to thank my colleagues and fellow researchers from Core Group. Their help and friendship were essential to accomplish this difficult task and will always be remembered.

I also have to thank my friends inside and outside IST for their contributions and, mostly, for their support.

I am grateful to Mr. Fernando Alves, the laboratory technician and a friend whose skills made the experimental campaign of this thesis possible.

I am thankful for FCT, CERIS and IDMec for sponsoring my PhD. I would also like to thank Alto Perfis Pultrudidos Lda. for providing the materials used in this thesis.

I am very grateful for my Mother’s endless support and love.

Finally, I would like to express my deepest gratitude to my colleague and, more importantly, my friend Miguel Proença, that will forever be missed. We started together and we should be ending this together. I dedicate this thesis to you.

TABLE OF CONTENTS

PART II Beam-to-column connections for pultruded tubular profiles

PART IV 2-dimensional frames made of pultruded GFRP profiles

LIST OF FIGURES

LIST OF TABLES

PART I

Introduction

Chapter 1

Introduction

1.1. CONTEXT AND MOTIVATION

Pultruded glass fibre reinforced polymer (GFRP) profiles have significantly higher strength-to-weight ratio than conventional construction materials, chemical inertness in aggressive environments and electromagnetic transparency [1.1]. Owing to these key advantages, pultruded GFRP profiles are already extensively used in some niches of the construction market, for example in structural applications for the transportation, energy and water treatment industries (Figure 1.1).

However, pultruded GFRP profiles present intrinsic limitations, especially when compared to steel profiles (their main competitor), such as lower stiffness and lack of ductility [1.3]. Due to these limitations, the design of pultruded structures must follow material-adapted methodologies that are considerably different from the well-established procedures used by civil engineering practitioners for the design of conventional structures.

In this context, the wider adoption of pultruded GFRP profiles in non-industrial structural applications is being delayed by the lack of adequate design standards for pultruded structures. The design codes available today are not normative in most countries and present limited guidance in critical subjects [1.4-1.6], such as the connections between profiles and the seismic behaviour. In fact, the current state of knowledge about such subjects still does not allow for the definition of adequate design provisions.

Figure 1.1 - Pultruded structure for cooling tower [1.2].

The first frame connection systems developed for pultruded profiles resembled details of steel structures and comprised only composite parts [1.7]. These connection systems were proved to be inadequate for joining pultruded profiles, presenting premature brittle failure modes that considerably limited their strength. Subsequent research on the subject aimed at improving the connections' behaviour by implementing material-adapted details and/or by using proprietary composite or metallic parts [1.8-1.11]. However, the results obtained from most of these efforts were still not promising, as some connection systems were not practical for general applications and most did not present adequate mechanical performance, especially in what concerns their ductility. Additionally, it is also worth noting that most studies reported in the literature did not evaluate the hysteretic behaviour of pultruded connections, focusing only on their monotonic response.

Possibly due to their scale, very few research works focused on characterizing the structural behaviour of pultruded frames. Of those, only two experimental studies addressed their response to horizontal loads [1.12,1.13], which were of monotonic nature. Such limited number of studies is clearly insufficient to enable a proper understanding of these structural systems, especially in what regards their seismic behaviour.

The present PhD thesis aims at providing relevant scientific contributions for the state-of-the-art of these two undeveloped research fields, namely (i) pultruded beam-to-column connections and (ii) lateral behaviour of pultruded frames.

1.2. OBJECTIVES AND METHODOLOGY

The main objectives of this PhD thesis were the development and study of material-adapted beam-to-column connections for pultruded profiles and the characterization of pultruded frame structures, particularly in what refers to their response under lateral actions. To that end, this work was divided in three main axes, corresponding to: (i) beam-to-column connections for pultruded GFRP profiles; (ii) 2-dimensional frames made of pultruded GFRP profiles; and (iii) 3-dimensional frames made of pultruded GFRP profiles.

The study concerning beam-to-column connections for pultruded GFRP profiles aimed at:

- Developing material-adapted beam-to-column connection systems for pultruded GFRP profiles with improved ductility;
- Characterizing the monotonic and cyclic behaviour of such beam-to-column connections for pultruded profiles;
- Developing methodologies to predict the behaviour of beam-to-column connections for pultruded GFRP profiles.

The first step of the first axis was to conceive and design different connection systems for tubular and I-section profiles. These connection systems comprised metallic auxiliary parts, and their geometries were defined to allow taking advantage of the material's ductility. Then, a comprehensive experimental campaign was carried out, including: (i) material characterization coupon tests; (ii) quasi-static monotonic double-lap tests of GFRP connections; and (iii) quasi-static monotonic and cyclic full-scale beam-to-column connection tests comprising such connection systems. In the connection tests, several details of the specimens were varied, such as the bolts configuration and the geometry of the steel auxiliary parts, in order to study their influence on the overall response of the connections. The monotonic tests of beam-to-column connections aimed at evaluating the initial stiffness, ultimate strength, failure modes and ductility. Regarding the cyclic tests of beam-to-column connections, the main objective was to assess the hysteretic properties, particularly in what concerns the capability to dissipate energy. In addition to the experimental campaign, analytical and numerical models were developed aiming at predicting the behaviour of the beam-to-column connections. The analytical models were based in methodologies and formulae available in GFRP and steel standards, the former referring to very simple geometries and loading conditions. The numerical finite element models were developed using the commercial software *Abaqus*.

The study concerning 2-dimensional frames made of pultruded GFRP profiles aimed at:

- Characterizing the monotonic and cyclic sway behaviour of 2-dimensional frames comprising pultruded GFRP profiles and the beam-to-column connections developed in the previous axis;
- Assessing the influence of bracings and in-fill walls on the overall behaviour of 2-dimensional pultruded frames;
- Presenting methodologies for predicting the behaviour of 2-dimensional pultruded frames.

In this axis, quasi-static monotonic and cyclic lateral tests were performed on full-scale 2-dimensional pultruded frames, comprising tubular and I-section profiles and the beam-to-column connections developed and characterized in the previous stage. Several frame configurations were tested: (i) non-braced and unfilled (*i.e.* without walls) frames with different beam-to-column connections, to assess how different ways of joining the profiles affect the frames' behaviour; (ii) frames with a cable bracing system, to assess its ability to improve the frames' response; and (iii) frames with non-structural and structural in-fill walls, to evaluate their effect on the frames' behaviour. The monotonic lateral tests aimed at evaluating the frames' initial stiffness, ultimate strength, failure modes and ductility. For the cyclic lateral tests, the main objective was to assess the frames' hysteretic properties, with particular focus on the dissipated energy. Finite element models of 2-dimensional frames were developed using *SAP2000* commercial software, aiming at simulating their non-linear response.

Finally, the study concerning 3-dimensional frames made of pultruded GFRP profiles aimed at:

- Characterizing the modal parameters of 3-dimensional pultruded frames;
- Characterizing the seismic response of 3-dimensional pultruded frames.

In this axis, a full-scale two-storey 3-dimensional pultruded frame was subjected to the following experimental tests: (i) modal identification tests, to assess the frames' natural frequencies, and corresponding modal shapes and damping values; and (ii) seismic tests, to evaluate the frames' response to design seismic actions for mainland Portugal. The 3-dimensional two-storey frame specimen was composed by I-section profiles and one connection system developed and characterized in the first axis of this work. In the modal analysis, the frame was tested in different conditions: (i) without vertical loads or bracings; (ii) with vertical loads and without bracings; (iii) without vertical loads and with bracings, and (iv) with both vertical loads and bracings – this allowed assessing the influence of each of these factors on the dynamic behaviour of the frame. In the seismic tests, the frame with vertical loads and without bracings was subjected to 18 ground displacement histories, with increasing peak ground accelerations, allowing to evaluate how these seismic actions affected the structural response of the frame.

1.3. MAIN SCIENTIFIC CONTRIBUTIONS AND PUBLICATIONS

As mentioned, one of the main reasons delaying the widespread use of pultruded structures is the lack of adequate design guidelines – these are still incomplete in relevant topics (for which research is underdeveloped), such as the connections between profiles and the seismic behaviour of pultruded structures. The research work developed in this PhD thesis addresses those two interconnected topics, providing scientific contributions to the current state of knowledge, with both academic and practical relevance. The main contributions are summarized in the following paragraphs.

This thesis comprises a comprehensive study concerning beam-to-column connections that not only provided a wealth of experimental data, but also presented practical solutions to more efficiently join pultruded tubular and open section profiles. The connection systems developed herein presented improved mechanical response, especially in what regards their ductility and ability to dissipate energy, characteristics that are not usually associated to pultruded connections, due to the brittle behaviour of the GFRP material. From a scientific point of view, these results constitute proof that efficient pultruded connections are feasible and points to ways of achieving them, namely by using auxiliary metallic parts. From a practical point of view, this study presented connection systems and details that can already be used in pultruded frame structures. Additionally, this investigation included the development of analytical and numerical models that allow predicting the connections' behaviour with reasonable accuracy, and therefore can be regarded as complementary analysis and design tools for academics and practitioners. Six scientific publications (all in Q1 SCI-indexed journals) resulted from the aforementioned work concerning pultruded beam-to-column connections:

1. Martins D, Proença M, Correia JR, Gonilha J, Arruda M, Silvestre N. (2017). *Development of a novel beam-to-column connection system for pultruded GFRP tubular profiles*. Composite Structures, 171, 263-276.
2. Martins D, Proença M, Gonilha JA, Sá MF, Correia JR, Silvestre N. (2019). *Experimental and numerical analysis of GFRP frame structures. Part 1: Cyclic behaviour at the connection level*. Composite Structures, 220, 304-317.
3. Martins D, Gonilha J, Correia JR, Silvestre N. (2021). *Monotonic and cyclic behaviour of cuff beam-to-column connection system for tubular pultruded GFRP profiles*. Engineering Structures, 247, 113165.
4. Martins D, Gonilha J, Correia JR, Silvestre N. (2021). *Exterior beam-to-column bolted connections between GFRP I-shaped pultruded profiles using stainless steel cleats. Part 1: Experimental study*. Thin-Walled Structures, 163, 107719.
5. Martins D, Gonilha J, Correia JR, Silvestre N. (2021). *Exterior beam-to-column bolted connections between GFRP I-shaped pultruded profiles using stainless steel cleats, Part 2: Prediction of initial stiffness and strength*. Thin-Walled Structures, 164, 107762.

6. Martins D, Gonilha J, Correia JR, Silvestre N. (2021). *Monotonic and cyclic behaviour of a stainless steel cuff system for beam-to-column connections between pultruded I-section GFRP profiles*. Engineering Structures, 249, 113294.

The main contributions of the experimental research concerning the 2-dimensional frames are (i) the assessment of their behaviour under monotonic and cyclic lateral loading conditions, and (ii) the evaluation of how several relevant parameters influence that behaviour, such as the type of connections and the presence and type of infill walls. This experimental work provided relevant data for understanding the lateral response of pultruded frames, especially in what concerns their ability to dissipate energy, which directly correlates with the seismic performance of structures comprising them. The numerical models of 2-dimensional frames were able to predict their non-linear response with reasonable accuracy, which indicates that they can be used in the seismic design of pultruded structures or in future research works, for example in parametric studies aiming at defining behaviour factors for pultruded structures. Additionally, these numerical models were used to assess the hysteretic behaviour of the pultruded frames when including a GFRP bracing system with a steel plate damper. Two scientific publications (both in Q1 SCI-indexed journals) resulted from the work concerning 2-dimensional pultruded frames:

7. Martins D, Sá MF, Gonilha JA, Correia JR, Silvestre N, Ferreira JG. (2019). *Experimental and numerical analysis of GFRP frame structures. Part 2: Monotonic and cyclic sway behaviour of plane frames*. Composite Structures, 220, 194-208.
8. Martins D, Gonilha JA, Correia JR, Silvestre N, Guerreiro L, Branco F. (2022). *Monotonic and cyclic sway behaviour of 2-dimensional frames made of pultruded GFRP I-section profiles*. Composite Structures (submitted).

The final work included in this thesis, concerning 3-dimensional pultruded frames, allowed to increase the understanding of the dynamic and seismic response of these structural systems. The experimental campaign developed in this study is unique in what regards the scale of the specimen, a full-scale 2-storey frame including the profiles and the connections characterized in the previous studies, and the test types, as it included modal analyses and comprehensive seismic tests with increasing magnitude.

The modal analysis of the frame provided relevant data regarding the natural frequencies and modal shapes of this pultruded structure, as well as on how different members and components, such as floor loads and bracings, affect those parameters. Additionally, the results of such analysis can be used to calibrate numerical models of similar pultruded structural systems. The seismic tests proved that it is possible to build pultruded structures with satisfactory seismic response, provided that the profiles and, more specifically, their connections are well designed. As so, not only this last experimental work provides relevant scientific contributions, but it also serves as a proof of concept for the remaining studies conducted within this thesis.

1.4. DOCUMENT OUTLINE

This PhD thesis is organized in twelve chapters[1], grouped in six parts. The content of these chapters is briefly described in the following paragraphs and is summarized in Table 1.1.

- **Part I - Introduction**

  Chapter 1 describes the context of the thesis theme and motivation, presenting also an overview of the main objectives of this work, the methodology pursued and its main scientific contributions.

  Chapter 2 presents a brief overview concerning pultruded GFRP profiles, namely in what regards their constituent materials, manufacturing process, main characteristics, connections, design guidelines and structural applications.

- **Part II - Beam-to-column connections for tubular profiles**

  Chapter 3 presents the research work concerning the monotonic behaviour of a sleeve beam-to-column connection system for pultruded GFRP tubular profiles. The experimental campaign described in this chapter includes: (i) material characterization coupon tests; (ii) quasi-static

[1] It is worth referring that the content of several chapters corresponds to the above-mentioned papers, with only slight modifications.

monotonic double-lap tests; and (iii) quasi-static monotonic beam-to-column connection tests of four series with different bolt configurations. Analytical and numerical predictions of the beam-to-column connections' initial stiffness and strength are also presented in this chapter. This chapter corresponds to Paper 1 (*cf.* Section 1.3).

Chapter 4 addresses the quasi-static cyclic behaviour of the aforementioned sleeve beam-to-column connection series for pultruded GFRP tubular profiles. The first part of the chapter presents the experimental cyclic tests, in which several hysteretic parameters were evaluated, including the capacity to dissipate energy. The second part of this chapter presents the numerical simulation of the hysteretic response of one sleeve connection series. This chapter corresponds to Paper 2 (*cf.* Section 1.3).

Chapter 5 concerns the experimental study of a cuff connection system for pultruded GFRP tubular profiles. The monotonic tests are firstly presented, comprising four connection series with different cuff geometries, followed by the description of the cyclic tests on the best performing cuff connection series. The results of the best performing cuff connection series are compared to those of the best performing sleeve connection series (from the previous two chapters). This chapter corresponds to Paper 3 (*cf.* Section 1.3).

- **Part III - Beam-to-column connections for I-section profiles**

Chapter 6 presents an experimental campaign aiming at assessing the behaviour of a cleated beam-to-column connection system for pultruded GFRP I-section profiles, comprising: (i) material characterization coupon tests; (ii) quasi-static monotonic double-lap connection tests; and (iii) quasi-static monotonic and cyclic beam-to-column connection tests. A total of nine beam-to-column connection series were tested. This chapter corresponds to Paper 4 (*cf.* Section 1.3).

Chapter 7 presents analytical and numerical studies concerning four series of the aforementioned cleated beam-to-column connections. Firstly, this chapter presents initial stiffness predictions of analytical and numerical models, separately. The second part of this chapter presents the connections' strength predictions, obtained using a combination of analytical and numerical procedures. This chapter corresponds to Paper 5 (*cf.* Section 1.3).

Chapter 8 addresses the quasi-static behaviour of cuff beam-to-column connections for pultruded GFRP I-section profiles. This chapter presents monotonic tests of four connection series, differing in the cuff part geometry, and cyclic tests of one connection series, the best performing in the monotonic tests. The response of the best performing cuff series was compared to that of the best performing sleeve series (from the previous two chapters). This chapter corresponds to Paper 6 (*cf.* Section 1.3).

- **Part IV - 2-Dimensional pultruded frames**

  Chapter 9 presents an experimental and numerical study concerning the lateral response of 2-dimensional pultruded frames made of tubular profiles. The first part of this chapter focuses on the quasi-static monotonic and cyclic tests of frame specimens with and without infill structural walls (composed by sandwich panels). Subsequently, a finite element model of the unfilled frame is presented and the results obtained are discussed and compared with test data. This chapter corresponds to Paper 7 (*cf.* Section 1.3).

  Chapter 10 addresses the lateral behaviour of 2-dimensional pultruded frames made of I-section profiles. This chapter presents the monotonic and cyclic tests of different frame series and the numerical simulations of one frame series. This chapter corresponds to Paper 8 (*cf.* Section 1.3).

- **Part V - 3-Dimensional pultruded frames**

  Chapter 11 presents an experimental work focused on the dynamic and seismic behaviour of a full scale 2-storey 3-dimensional pultruded frame. Firstly, this chapter presents the modal identification tests of four different frame systems: (i) without floors nor bracings; (ii) without floors and with bracings; (iii) with floors and without bracings; and (iv) with floors and with bracings. Then, the seismic tests are presented, in which the frame with floors and without bracings was subjected to 18 ground displacement histories.

- **Part VI - Conclusions and future developments**

  Chapter 12 summarizes the main conclusions of the present work and identifies relevant future developments.

Table 1.1 - General outline of the thesis and resulting SCI journal papers.

Part	Chapter	Topic	Type of profile	Type of study	Paper
I	1. Introduction	-	-	-	-
	2. Pultruded GFRP profiles for civil engineering applications	-	-	-	-
II	3. Monotonic behaviour of a sleeve connection system for pultruded tubular profiles	Beam-to-column connections	Tubular	Experimental, analytical and numerical	1
	4. Cyclic behaviour of a sleeve connection system for pultruded tubular profiles			Experimental and numerical	2
	5. Monotonic and cyclic behaviour of a cuff connection system for pultruded tubular profiles			Experimental	3
III	6. Monotonic and cyclic behaviour of a cleated connection system for pultruded I-section profiles	Beam-to-column connections	I-section	Experimental	4
	7. Stiffness and strength predictions of cleated connection system for pultruded I-section profiles			Analytical and numerical	5
	8. Monotonic and cyclic behaviour of a cuff connection system for pultruded I-section profiles			Experimental	6
IV	9. Sway behaviour of 2-dimensional frames made of pultruded GFRP tubular profiles	2-dimensional frames	Tubular	Experimental and numerical	7
	10. Sway behaviour of 2-dimensional frames made of pultruded GFRP I-section profiles		I-section	Experimental and numerical	8
V	11. Seismic behaviour of 3-dimensional pultruded frames	3-dimensional frames	I-section	Experimental and numerical	-
VI	12. Conclusions and future developments	-	-	-	-

1.5. REFERENCES

[1.1] Bank LC. (2006). Composites for Construction: Structural Design with FRP Materials. *John Wiley & Sons*.

[1.2] Fiberline Composites web site: http://www.fiberline.com/, visited in January 2022.

[1.3] Correia JR (2008). GFRP pultruded profiles in civil engineering: hybrid solutions, bonded connections and fire behaviour. *PhD Thesis in Civil Engineering.* Instituto Superior Técnico, Lisboa.

[1.4] Italian National Research Council (2007). CNR-DT 205/2007 – Guide for the Design and Construction of Fiber-Reinforced Concrete Structures.

[1.5] ASCE (2010). Pre-Standard for Load & Resistance Factor Design (LRFD) of Pultruded Fiber Reinforced Polymer (FRP) Structures.

[1.6] CEN/TC250/WG4 (2014). Fibre Reinforced Polymer Structures: Scientific and Technical Report.

[1.7] Bank LC, Mosallam AS, Gonsior HE. (1990). Beam-to-column connections for pultruded FRP structures. In *Serviceability and Durability of Construction Materials* (pp. 804-813). ASCE.

[1.8] Mosallam AS, Abdelhamid MK, Conway JH. (1994). Performance of pultruded FRP connections under static and dynamic loads. *Journal of Reinforced Plastics and Composites*, 13(5), 386-407.

[1.9] Smith SJ, Parsons ID, Hjelmstad KD. (1999). Experimental comparisons of connections for GFRP pultruded frames. *Journal of Composites for Construction*, 3(1), 20-26.

[1.10] Singamsethi SK, LaFave JM, Hjelmstad KD. (2005). Fabrication and testing of cuff connections for GFRP box sections. *Journal of Composites for Construction*, 9(6), 536-544.

[1.11] Mottram JT, Zheng Y. (1996). State-of-the-art review on the design of beam-to-column connections for pultruded frames. *Composite structures*, 35(4), 387-401.

[1.12] Na G. (2008). Load-displacement behaviour of frame structures composed of FRP composite materials. *PhD thesis in Civil Engineering*, Georgia Institute of Technology.

[1.13] Cavaleri L, Di Paola M, Ferroto MF, Valenza A. (2019). Structural performances of pultruded GFRP emergency structures – Part 2: Full-scale experimental testing. *Composite Structures*, 214, 304-15.

Chapter 2

Pultruded GFRP profiles for civil engineering applications

2.1. PRELIMINARY CONSIDERATIONS

Composite materials are produced by combining, without dissolving or blending, two or more materials, resulting in a new material with different properties than the original constituents. Composite materials have been used in construction for thousands of years. In ancient Egypt, sundried bricks were the most used construction material, being often produced by combining mud from the Nile alluvium with chopped straw [2.1]. A more recent and widely used example of composite material is reinforced concrete, which results from the combination of concrete with a reinforcement (usually steel) that improves its tensile capabilities.

Fibre reinforce polymers (FRPs) are emerging composite materials that combine a polymetric matrix with fibre reinforcement. At first, FRPs were mainly adopted by the aerospace and defence industries [2.2], but more recently they started to be seen as an alternative to traditional materials in the building industry, for both rehabilitation and new construction, due to their high strength-to-weight ratio and improved resistance to corrosion and environmental degradation. These composites can be produced in different forms, one being pultruded profiles, which has the additional advantage of being fabricated in an almost automatic process, allowing to reduce labour costs and increase production speed [2.3,2.4]. However, the widespread use of pultruded profiles in structural applications is being hindered by the lack of proper regulation and design recommendations that take into account the limitations related to some of the material's intrinsic characteristics, such as its brittle behaviour, the poor fire behaviour and the lower stiffness when compared to traditional materials (*i.e.* steel).

This chapter presents the main characteristic of pultruded FRP profiles, namely in what regards the constituent materials (*cf.* Section 2.2), the pultrusion process (*cf.* Section 2.3) and their main features (*cf.* Section 2.4). Then, the subject of the connections between pultruded FRP profiles is introduced (*cf.* Section 2.5) and the final part of the chapter presents the main structural applications of these profiles (*cf.* Section 2.6).

2.2. CONSTITUENT MATERIALS OF PULTRUDED FRP PROFILES

The composite material of pultruded FRP profiles comprises fibres and a polymeric matrix. The fibres are responsible for providing most of the profiles' stiffness and strength along their direction. The matrix allows the transfer of internal stresses across the fibre reinforcement, while maintaining them protected from environmental degradation agents and ensuring their positioning in the profile.

The fibre reinforcement corresponds to 30-70% of the volume of pultruded profiles [2.5]. These fibres can be made from a variety of materials, such as carbon, aramid and glass. Among these types of fibres, the most used in civil engineering are glass fibres (resulting in glass fibre reinforced polymer, GFRP), as they present lower cost compared to the other types of high-performance fibres [2.6]. There are several grades of glass fibres, the most common being: (i) *E-glass*, which is a borosilicate glass with high electrical resistivity (also known as electrical glass); (ii) *A-glass*, which is an alkali glass that is used where electrical resistivity is not a prerequisite; (iii) *C-glass*, which is made with calcium borosilicates and presents high resistance to corrosion; and (iv) *S-glass*, which is made with magnesium aluminosilicates and is used where high strength, high stiffness and corrosive resistance are needed. The main properties of these glass fibres are presented in Table 2.1. In civil engineering applications, most pultruded profiles are produced with *E-glass* fibres. The fibres are used in the form of rovings and mats. Rovings are continuous filaments that are provided in coils and can be arranged in the unidirectional (*cf.* Figure 2.1a), spun (*cf.* Figure 2.1b) and mock (*cf.* Figure 2.1c) forms. Rovings provide most of the strength and stiffness of FRP profiles along their longitudinal axis. The mats are a textile product made of fibres, which can be randomly stranded or oriented (Figure 2.2). The fibre mats are mainly used to improve the profiles' mechanical properties on directions other than the axial one.

Table 2.1 - Typical properties of common grades of glass fibres [2.6].

Grade of glass fibre	Density (g/cm^3)	Tensile modulus (GPa)	Tensile strength (MPa)	Max. elongation (%)
E	2.57	72.5	3400	2.5
A	2.46	73	2760	2.5
C	2.46	74	2350	2.5
S	2.47	88	4600	3.0

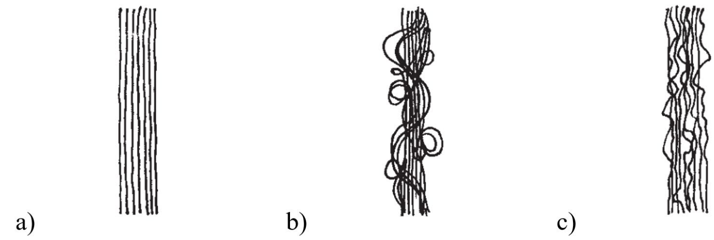

Figure 2.1 - Types of roving reinforcement [2.7]: a) unidirectional; b) spun; and c) mock.

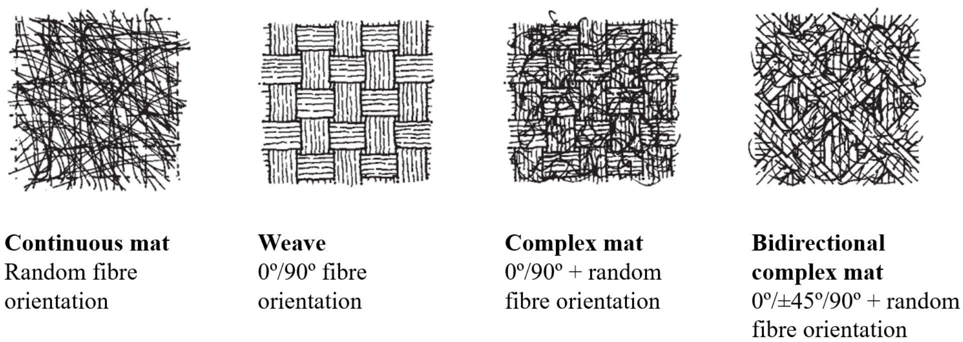

Figure 2.2 - Types of mat reinforcement [2.7].

Most pultruded profiles are produced using polyester or vinylester resins [2.6]. Unsaturated polyester resins are affordable while presenting good chemical and mechanical properties, being widely used in structural pultruded profiles. Additionally, polyester resins are easy to process, owing to their reduced viscosity, and are highly customizable, being easily filled and pigmented. On the other hand, vinylester resins, which are more expensive than polyester resins, are mostly used when higher corrosion resistance is necessary. The typical properties of these two resins are presented in Table 2.2.

Table 2.2 - Typical properties of polyester and vinylester resins [2.6].

Resin type	Density (g/cm^3)	Tensile modulus (GPa)	Tensile strength (MPa)	Max. elongation (%)
Polyester	1.2	4.0	65	2.5
Vinylester	1.12	3.5	82	6.0

In addition to the reinforcement fibres and the resin, other components are often used in the production of pultruded profiles [2.8]: (i) polymerisation agents, to initiate the polymerisation reaction; (ii) fillers, to reduce the final cost of the profile and/or to improve its properties (*i.e.* enhance the fire response by reducing the organic content of the matrix); and (iii) additives, to modify given properties of the final product (*i.e.* profile's coloration) and to improve its resistance to exterior agents (*i.e.* flame retardants or UV stabilizers).

2.3. PULTRUSION PROCESS

Pultrusion is an almost automated process of manufacturing FRP profiles with constant cross section [2.8]. In the first stage of the process, the fibres (roving and mats) are impregnated with the liquid matrix, either by bathing or by injection. After that, both the matrix and the fibres go through a heated mould, with interior temperatures ranging between 90-180 ºC. There, the matrix hardens, and the profile acquires its final shape, corresponding to the intended cross section. In this process, the cured profile is pulled by a pulling system, being cut to the desired length with a cut-off saw. This process, which is illustrated in Figure 2.3, allows to produce profiles at an average rate of 2 m/min [2.9] (production times can vary depending on the machine used or the profiles' cross section).

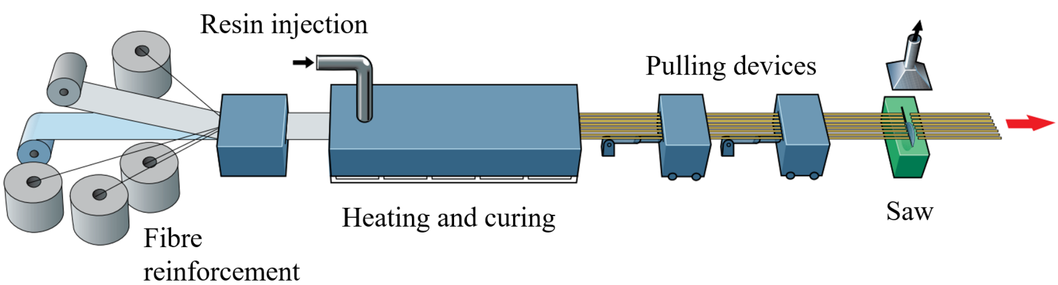

Figure 2.3 - Pultrusion process [2.7].

The first generation of pultruded shapes corresponds to profile elements with cross sections similar to those of profiles used in steel construction (illustrated in Figure 2.4). However, the FRP material has considerably less stiffness than steel and, therefore, pultruded profiles are more prone to suffer from instability phenomena. Although these limitations can prevent taking full advantage of the composite material's capabilities, these structural shapes remain prevalent in pultruded structural applications.

More recently, a second generation of pultruded shapes, with deck panel configuration, has been developed and commercialized by several manufacturers. These pultruded panels present multicellular cross sections (as illustrated in Figure 2.5) that are better adapted to the composite material properties. As this type of profiles can only be used in the form of slabs (or walls), comprising several adjacent panels joined by means of adhesive bonding and/or interlock, they are less found in pultruded structural applications. Therefore, they will be disregarded in the remaining sections of this chapter.

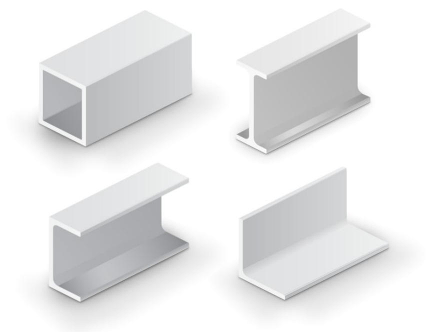

Figure 2.4 - First generation of pultruded profiles (adapted from Fiberline catalogue [2.10]).

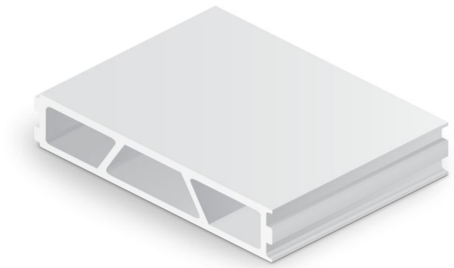

Figure 2.5 - Second generation of pultruded profiles (adapted from Fiberline catalogue [2.10]).

2.4. PROPERTIES OF PULTRUDED PROFILES

Pultruded profiles are highly orthotropic, presenting considerably more stiffness and strength in the longitudinal direction than in the transverse direction, due to the fact that most fibres are parallel to the profiles' axis. The properties of pultruded profiles depend highly on the types of fibres and matrix and on the fibre content and architecture. These properties are usually provided by manufacturers. However, there is lack of proper standardization regarding the properties of pultruded GFRP profiles, with well-defined distinct grades (as defined for steel profiles, or timber). For example, EN 13706 [2.13] only establishes two different grades of GFRP pultruded profiles, with the corresponding minimum requirements (Table 2.3). Therefore, similar profiles from different manufacturers often present considerable variation of their properties [2.10-2.12].

When compared to steel profiles, their main competitor, pultruded GFRP profiles offer several advantages [2.3,2.6], such as: (i) low self-weight; (ii) high strength-to-weight ratio; (iii) electromagnetic transparency; and (iv) better corrosion resistance and durability, which reduces maintenance costs. However, pultruded GFRP profiles have some limitations that need to be accounted for when used as structural members. Although these profiles present comparable axial strength, their stiffness is significantly lower than that of steel profiles. As a consequence, the design of GFRP structures is often governed by serviceability limits or by local/global buckling phenomena, which prevents taking full advantage of the material's strength. In addition, the orthotropic material of pultruded GFRP profiles can fail on a variety of modes, through fibre of inter-fibre fracture, which leads to complex and often more numerous design verifications when compared to equivalent steel profiles. Moreover, these failure modes are usually brittle, contrasting to established design philosophies of steel structures that aim at exploiting the material ductility.

Table 2.3 - Minimum properties required for each grade [2.13].

Property	Unit	Minimum properties	
		E17	E23
Longitudinal tensile modulus	GPa	17	23
Transverse tensile modulus	GPa	5	7
Longitudinal tensile strength	MPa	170	240
Transverse tensile strength	MPa	30	50
Longitudinal pin-bearing strength	MPa	90	150
Transverse pin-bearing strength	MPa	50	70
Longitudinal flexural strength	MPa	170	240
Transverse flexural strength	MPa	70	100
Longitudinal interlaminar shear strength	MPa	15	25

2.5. CONNECTIONS BETWEEN PULTRUDED PROFILES

The connections between pultruded profiles have significant influence in the behaviour of GFRP structures and special attention must be taken in their design. As shown ahead, these connections often present premature brittle failure modes, either in the profiles or in the auxiliary parts, limiting their strength and capacity to dissipate energy. In addition, the consideration of their semi-rigid behaviour is deemed as relevant to reduce the deflections of beams and of the overall structure.

The connections between pultruded profiles can be materialized by adhesive bonding, by bolting, or by a combination of both. Although bonded connections present considerable stiffness and allow for a more even stress distribution along the joined surfaces, adhesive failure is of brittle nature and these connections often present an almost linear behaviour up to failure [2.14-2.16]. Nonetheless, bonded beam-to-column connections have also been object of several studies, some of which aimed at developing connections with pseudo-ductile failure modes [2.17].

Bolted connections are more common in pultruded structures, mostly due to their easy and quick application. The geometry of the first bolted pultruded beam-to-column connection systems mimicked that of steel construction (Figure 2.6). Additionally, in the first studies, the authors made an effort to use only composite auxiliary parts (cleats and plates), often obtained by cutting pultruded profiles [2.18]. In these studies, the pultruded beam-to-column connections presented premature failure modes: (i) tensile tearing of the columns' web-flange junction (*cf.* Figure 2.7), due to the low transverse tensile and shear strengths of the GFRP material; and (ii) delamination of the composite auxiliary parts (*cf.* Figure 2.8), as the stresses are transmitted in their weak direction (perpendicular to the fibres). These first studies allowed to conclude that pultruded connections should include details to mitigate the limitations of the profiles' composite material (*i.e.* column reinforcements [2.19-2.21]) and that composite auxiliary connection parts used threrein are inappropriate for frame connections. Therefore, the following research concerning the pultruded connection technology focused on improving their behaviour by using either proprietary composite parts [2.19,2.21,2.22] or by using metallic parts [2.22-2.24]. However, most of these new studies failed at either developing practical solutions or at materializing connection systems with proper mechanical response, especially in what regards the ability to dissipate energy, essential for their application in seismic regions.

Bonded-bolted connections are also used to join pultruded profiles. The ultimate strength of these connections may be provided (i) by the adhesive, in which the bolts may be used to improve the bonded connection (by applying clamping pressure), or (ii) by the bolts, in which the adhesive is used to increase the joint stiffness.

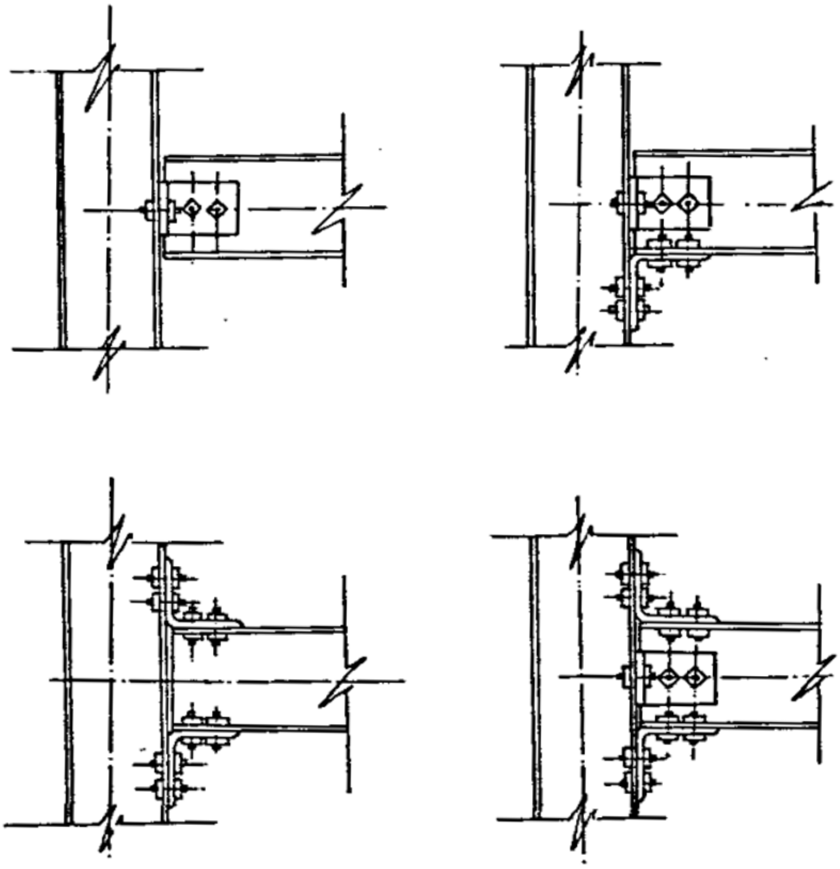

Figure 2.6 - Example of first pultruded connections [2.19].

Figure 2.7 - Tensile rupture of the column's web-flange junction [2.19].

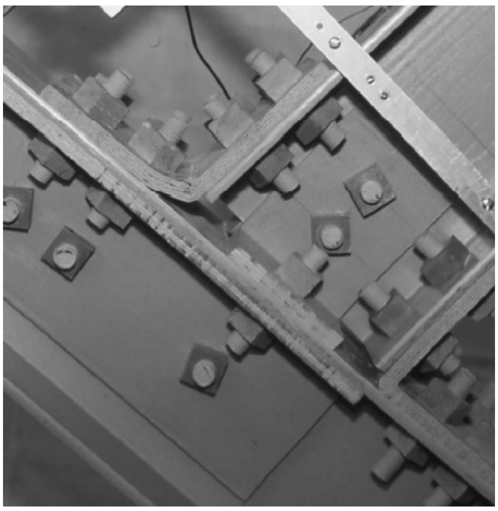

Figure 2.8 - Delamination of the composite cleat part [2.19].

2.6. DESIGN GUIDELINES FOR PULTRUDED STRUCTURES

The first guidelines available for the design of pultruded structures were provided in the EuroComp Design Code and Handbook [2.25] or by the manufacturers of pultruded profiles [2.7,2.26-2.28]. However, the recommendations available in these documents are not normative and are incomplete in crucial topics. For example, the EuroComp [2.25] states in its first pages that the requirements for seismic design are not covered in the document. Furthermore, it also presents limited recommendations concerning frame connections, that are insufficient to guarantee their efficient design. The Italian National Research Council published its own set of recommendations for the design of FRP structures in 2007 [2.29], which are normative only in Italy. In 2010, another document with guidelines for the design of pultruded FRP structures [2.30] was published, that was funded by the American Society of Civil Engineers, but without being an official standard from this association (serving only for general information, as stated in the document's disclaimer). In 2014, a scientific and technical report, comprising design guidelines for pultruded structures, was published by the Working Group 4 (WG4) of the Technical Committee 250 (TC250) of the European Committee for Standardisation (CEN) [2.31]. Although the Italian, American and CEN documents are more comprehensive than the former ones (the American document also presents a commentary section providing references from the literature), they are still lacking relevant recommendations, in particular, in what regards the design of connections and seismic provisions. Finally, it should be noted that a future Eurocode, covering structures made of pultruded profiles, is currently under development.

2.7. PULTRUDED PROFILES IN STRUCTURAL APPLICATIONS

Currently, pultruded profiles are mostly used in very specific applications, owing to their chemical resistance, electromagnetic transparency and lightness. In particular, they are often used as secondary structural members (*i.e.* in walkways, staircases and platforms, Figures 2.9 and 2.10) in aggressive environments, such as in water and wasteland plants, or where their non-conductivity is a major advantage, such as in railway tracks.

Figure 2.9 - Walkway composed by pultruded profiles [2.12].

Figure 2.10 - Platform with staircase composed by pultruded profiles [2.10].

Pultruded profiles are used as primary structural members in large buildings for the cooling tower industry, corresponding to the biggest building segment using these profiles [2.6], as they do not corrode in wet or though industrial conditions. Large quantities of profiles are used by this industry; for example, more than 100 ton of GFRP profiles were used in the construction of a cooling tower in Hamm Uentrop (built in 2005) [2.31].

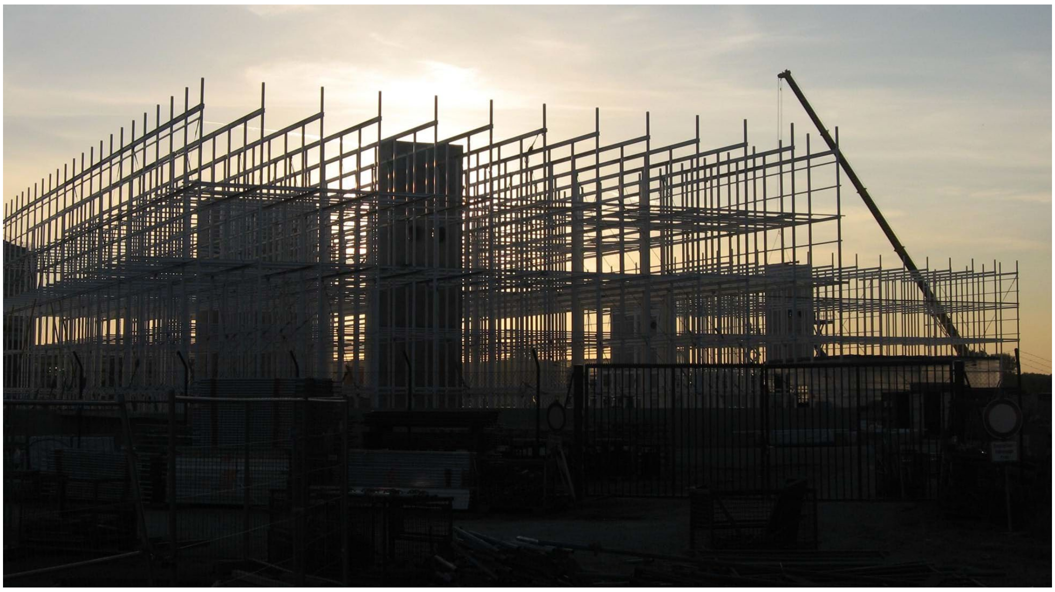

Figure 2.11 - Pultruded structure of cooling tower [2.10].

Regarding primary structures non-related to industrial purposes, pultruded profiles have been used predominantly in footbridges [2.9]. Two well-known examples of footbridges with structures entirely composed by pultruded profiles are the Pontresina two-span bridge (*cf.* Figure 2.12), in Switzerland,

and the Lleida arch bridge (*cf*. Figure 2.13), in Spain. One of the requirements for the profiles of both bridges was having low maintenance, associated to the corrosion resistance. As the Lleida bridge crossed an electrified railway, another requirement for the profiles was to have electromagnetic transparency. Due to their lightness, the installation time of both bridges was very reduced, with durations below 5 hours. It is worth noting that the Pontresina bridge is removed every year at the end of the winter, when there is risk of flooding due to the melting of snow.

Figure 2.12 - Pontresina bridge [2.32].

Figure 2.13 - Lleida bridge [2.33].

The use of pultruded profiles in the structure of new residential or commercial buildings is still very limited, which may be justified by the lack of effective ways of joining the profiles [2.6] and of proper design guidelines, and also the concerns about their fire behaviour. In 1999, a five-storey building (*cf*. Figure 2.14), entitled the *Eyecatcher*, was built at the Swiss Building Fair in Basel [2.34]. The main structure of this building consists of three trapezoidal frames materialized by pultruded GFRP profiles with adhesively bonded built-up sections (*cf*. Figure 2.15). As most connections were previously assembled at a workshop, the main structure was mounted on-site in only 3 days.

Figure 2.14 - *Eyecatcher* building [2.35].

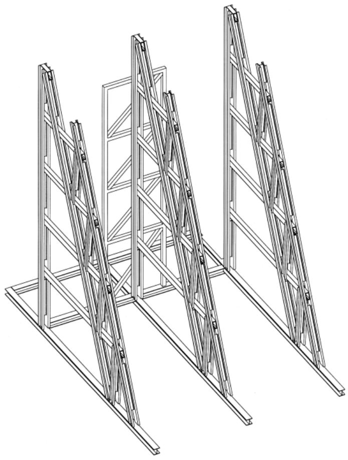

Figure 2.15 - Pultruded structural frames of *Eyecatcher* building [2.35].

Owing to their low self-weight, pultruded profiles are also used at temporary buildings/structures, such as the Ephemeral Cathedral of Créteil, in France, and the temporary roof for the Santa Maria Paganica church, in Italy. The Ephemeral Cathedral of Créteil (*cf*. Figure 2.16) was built in 2013 to substitute the permanent cathedral during its two-year renovation [2.36]. The structure of this temporary cathedral consisted of a gridshell comprising tubular pultruded GFRP profiles (*cf*. Figure 2.17). Between 2010 and 2011, a large temporary roof was built inside the partially collapsed Santa Maria Paganica church [2.38] (*cf*. Figure 2.18) to provide protection to its interior until renovation funds were gathered. The temporary roof consisted of four different structures, the tallest measuring almost 30 m. All roof structures were composed by pultruded profiles with standard ("off-the-shelve") cross-section (*cf*. Figure 2.19).

Figure 2.16 - Outside view of the Ephemeral Cathedral of Créteil [2.36].

Figure 2.17 - Inside view of the Ephemeral Cathedral of Créteil [2.36].

Figure 2.18 - Outside view of the temporary roof for the Santa Maria Paganica church [2.39].

Figure 2.19 - Inside view of the temporary roof for the Santa Maria Paganica church [2.40].

2.8. CONCLUDING REMARKS

This chapter briefly presented the main aspects of pultruded FRP profiles and their structural applications. These profiles are becoming increasingly used in structural applications, as they present several advantages compared to traditional materials (*i.e.* steel), such as their high strength-to-weight ratio, electromagnetic transparency and corrosion resistance. However, their lower stiffness (again, compared to steel) and brittle failure modes are limitations that need to be accounted for in the design of pultruded structures.

The connections between profiles have considerable influence in the costs and overall response of pultruded structures. The first types of connections between pultruded profiles copied details found in steel structures. However, the research concerning these pultruded connections highlighted that they are prone to brittle failure modes that are significantly different than those found in steel connections. The development of material adapted connection systems is considered essential to promote a wider use of pultruded structures.

The lack of proper design guidelines is also delaying the widespread use of pultruded profiles in structural applications. The current standards are still incomplete regarding crucial aspects of the design of pultruded structures; these aspects are usually related to research topics that are still underdeveloped, such as the connection technology and the structures' seismic response.

This thesis aimed precisely at contributing to the better understanding of the behaviour of pultruded beam-to-column connections, while developing material adapted connection systems, and structures in view of their possible use in primary structural applications, including in seismic areas. For that, the following chapters present a comprehensive experimental campaign, usually complemented by numerical and/or analytical studies, regarding (i) beam-to-column connections between pultruded GFRP profiles and the response of (ii) 2- and 3-dimentional frames comprising pultruded GFRP profiles and those connections.

2.9. REFERENCES

[2.1] Morgenstein ME, Redmount CA. (1998). Mudbrick typology, sources, and sedimentological composition: A case study from Tell el-Muqdam, Egyptian Delta. *Journal of the American Research Center in Egypt*, 35, 129-146.

[2.2] Bakis CE, Bank LC, Brown V, Cosenza E, Davalos JF, Lesko JJ, Machida A, Rizkalla SH, Triantafillou TC. (2002). Fiber-reinforced polymer composites for construction—State-of-the-art review. *Journal of Composites for Construction*, 6(2), 73-87.

[2.3] Correia JR (2008). *GFRP pultruded profiles in civil engineering: hybrid solutions, bonded connections and fire behaviour*. PhD Thesis in Civil Engineering. Instituto Superior Técnico, Lisboa.

[2.4] Buragohain MK. (2017). *Composite Structures: Design, Mechanics, Analysis, Manufacturing, and Testing*. CRC press.

[2.5] Groover MP. (2020). *Fundamentals of Modern Manufacturing: Materials, Processes, and Systems.* John Wiley & Sons.

[2.6] Bank LC. (2006). *Composites for Construction: Structural Design with FRP Materials*. John Wiley & Sons.

[2.7] Fiberline Composites. (2003). *Fiberline design manual*. Kolding, Denmark.

[2.8] Correia JR. (2015). Fibre-reinforced polymer (FRP) composites. In *Materials for Construction and Civil Engineering* (pp. 501-556). Springer, Cham.

[2.9] Gonilha, JG. (2014). *GFRP-concrete hybrid structural systems. Application to the development of a footbridge prototype*. PhD thesis in Civil Engineering. Instituto Superior Técnico, Lisboa.

[2.10] Fiberline Composites web site: http://www.fiberline.com/, visited in January 2022.

[2.11] Strongwell Corporation web site: http://www.strongwell.com/, visited in January 2022.

[2.12] ALTO Perfis Lda. web site: http://www.alto.pt/, visited in January 2022.

[2.13] CEN (2002) EN 13706: Reinforced plastics composites — Specifications for pultruded profiles. Part 1: Designation; Part 2: Methods of test and general requirements; Part 3: Specific requirements. European Committee for Standardisation, Brussels.

[2.14] Ascione F, Granata L, Carozzi G. (2021). Flexural and shear behaviour of adhesive connections for large scale GFRP frames: influence of the bonded area and hygro-thermal aging. *Composite Structures*, 115122.

[2.15] Ascione F, Lamberti M, Razaqpur AG, Spadea S. (2017). Strength and stiffness of adhesively bonded GFRP beam-column moment resisting connections. *Composite Structures*, 160, 1248-1257.

[2.16] Razaqpur AG, Ascione F, Lamberti M, Spadea S, Malagic M. (2019). GFRP hollow column to built-up beam adhesive connection: Mechanical behaviour under quasi-static, cyclic and fatigue loading. *Composite Structures*, 224, 111069.

[2.17] Ascione F, Lamberti M, Razaqpur AG, Spadea, S, Malagic M. (2018). Pseudo-ductile failure of adhesively joined GFRP beam-column connections: An experimental and numerical investigation. *Composite Structures*, 200, 864-873.

[2.18] Bank LC, Mosallam AS, Gonsior HE. (1990). Beam-to-column connections for pultruded FRP structures. In *Serviceability and Durability of Construction Materials* (pp. 804-813). ASCE.

[2.19] Bank LC, Mosallam AS, McCoy GT. (1994). Design and performance of connections for pultruded frame structures. *Journal of Reinforced Plastics and Composites,* 13(3), 199-212.

[2.20] Smith SJ, Parsons ID, Hjelmstad KD. (1998). An experimental study of the behavior of connections for pultruded GFRP I-beams and rectangular tubes. *Composite Structures*, 42, 281-90.

[2.21] Mosallam AS, Abdelhamid MK, Conway JH. (1994). Performance of pultruded FRP connections under static and dynamic loads. *Journal of Reinforced Plastics and Composites*, 13, 386–407.

[2.22] Smith SJ, Parsons ID, Hjelmstad KD. (1999). Experimental comparisons of connections for pultruded frames. *Journal of Composites for Construction*, 3, 20-6.

[2.23] Bass AJ, Mottram JT. (1996). Behaviour of connections in frames of fibre-reinforced-polymer section. *Structural Engineers*, 72(17), 280-284.

[2.24] Mottram JT, Zheng Y. (1996). State-of-the-art review on the design of beam-to-column connections for pultruded frames. *Composite Structures*, 15, 387–401.

[2.25] Clarke JL. (2003). Structural Design of Polymer Composites: Eurocomp Design Code and Background Document. CRC Press.

[2.26] Extren Design Manual (2003), Strongwell, Bristol, VA.

[2.27] The Pultex Pultrusion Global Design Manual (2004), Creative Pultrusions, Alum Bank, PA.

[2.28] Bedford Reinforced Plastics Design Guide (2005), Bedford Plastics, Bedford, PA.

[2.29] Italian National Research Council (2007). CNR-DT 205/2007 – Guide for the Design and Construction of Fiber-Reinforced Concrete Structures.

[2.30] ASCE (2010). Pre-Standard for Load & Resistance Factor Design (LRFD) of Pultruded Fiber Reinforced Polymer (FRP) Structures.

[2.31] CEN/TC250/WG4 (2014). Fibre Reinforced Polymer Structures: scientific and technical report.

[2.32] Composite Construction Laboratory (CCLAB) web site: https://www.epfl.ch/labs/cclab/, visited in January 2022.

[2.33] PEDELTA web site: https://www.pedelta.com/, visited in January 2022.

[2.34] Keller T. (2002). Fibre Reinforced Polymer Materials in Building Construction. In *IABSE Symposium Report* (Vol. 86, No. 20, pp. 73-78). International Association for Bridge and Structural Engineering.

[2.35] Keller T, Theodorou NA, Vassilopoulos AP, De Castro J. (2016). Effect of natural weathering on durability of pultruded glass fiber-reinforced bridge and building structures. *Journal of Composites for Construction*, 20(1), 04015025.

[2.36] Du Peloux L, Tayeb F, Caron JF, Baverel O. (2015). The Ephemeral Cathedral of Créteil: a 350m2 lightweight gridshell structure made of 2 kilometers of GFRP tubes. In *CIGOS 2015:"Innovations in Construction".*

[2.37] THINkSHELL web site: https://www.thinkshell.fr/, visited in January 2022.

[2.38] Russo S, Boscato G, Mottram JT. (2012). Design and free vibrations of a large temporary roof FRP structure for the Santa Maria Paganica Church in L'Aquila, Italy. In *6th Int. Conf. on FRP Composites in Civil Engineering* (CICE 2012).

[2.39] L'Aquila Blog web site: https://www.laquilablog.it/laquila-santa-maria-paganica-presentato-progetto-recupero-della-chiesa-capo-quarto/, visited in January 2022.

[2.40] Energia ambiente e innovazione web site: https://www.eai.enea.it/archivio/knowledge-diagnostics-and-preservation-of-cultural-heritage.html?view=article&id=887, visited in January 2022.

PART II

Beam-to-column connections for pultruded tubular profiles

Chapter 3

Monotonic behaviour of a sleeve connection system for tubular profiles

3.1. INTRODUCTION

Pultruded glass fibre reinforced polymer (GFRP) profiles are being increasingly used in civil engineering due to their lightness, strength and non-corrodibility [3.1]. The first-generation GFRP profiles mimicked the cross-section of steel profiles, and so did the technology used in their connections, which basically copied bolted steel connections arrangements [3.2]. However, such technology transfer did not take into account the considerable differences between the materials, in particular the orthotropy, brittle failure and creep susceptibility of the GFRP material.

Due to the above-mentioned differences, the first tests on steel-like cleat GFRP beam-to-column bolted connections highlighted unique failure modes, namely (i) tensile tearing and (ii) delamination of the GFRP angle profiles [3.3-3.5]. The former mode occurred on the web-flange junction of the column due to the low transverse tensile and shear strengths of the GFRP material. In order to avoid this failure mode, several authors proposed different solutions [3.4,3.6,3.7], in particular: (i) reinforcing the web-flange junction by means of two angle parts; and (ii) extending the bolts through both flanges in order to mobilize the whole section of the column instead of just the facing flange. Nevertheless, these solutions, although preventing the tensile tearing failure mode, allowed only for limited improvements of the connections' performance, with failure being triggered henceforth by the delamination of the GFRP angle profiles of the cleat connection. Furthermore, due to the common disposition of these elements, the loads and stresses are transmitted perpendicularly to the main reinforcing fibres (weak direction), making them inappropriate for frame connection systems.

In order to overcome the limitations of steel-like cleat connection systems, several authors have proposed connection systems comprising novel composite parts. Bank *et al*. [3.4] developed and tested a connection system materialized by build-up parts (*cf.* Figure 3.1a), comprising "T" flanges and a triangular plate gusset, obtaining higher stiffness and strength when compared to conventional systems. This concept was further developed by Mosallam *et al*. [3.8], who idealized an all-composite (E-glass/vinylester) new part (*cf.* Figure 3.1b) made by resin transfer moulding (RTM). The use of this new part allowed increasing the connection strength and stiffness when compared to the previous solution tested by Bank *et al*. [3.4].

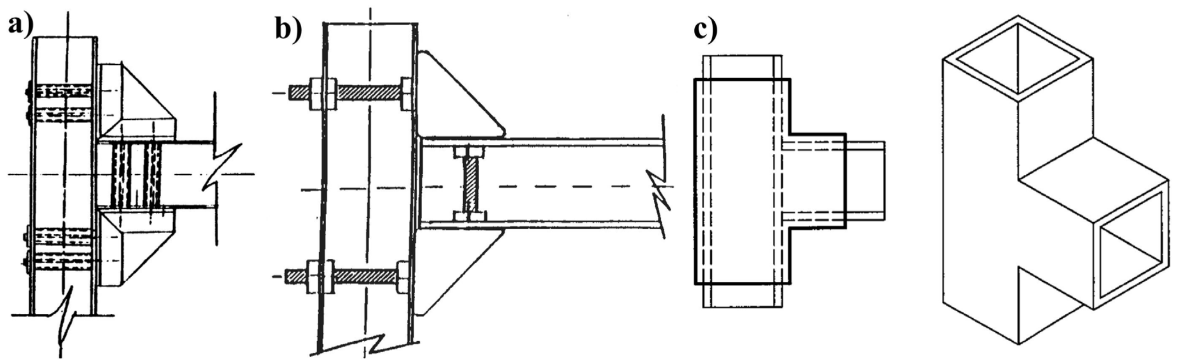

Figure 3.1 - a) Gusset plate connection [3.4]; b) Universal connector connection [3.12]; c) Cuff connection [3.9].

While the aforementioned studies concerned the connection between open-walled profiles, Smith *et al.* [3.9] idealized a connection system for tubular profiles that included a new composite connection part, called "cuff" (*cf.* Figure 3.1c), which accommodated the profiles. The authors tested specimens with cuff connections materialized by bolted angle-sections that presented improved stiffness and strength when compared to conventional solutions. In light of these results and owing to the simplified assembly process, this solution was further investigated and materialized by other authors. Singamsethi *et al.* [3.10] confirmed the improved mechanical response of the cuff connection system, obtaining higher stiffness (up to 10%) and strength (up to 50%) when compared to those of traditional connections, while

Carrion *et al*. [3.11] reported that the flexural strength of some cuff connections was similar to the full flexural capacity of the GFRP tubular beams. Although significantly improving the structural performance of GFRP connections, most of these composite parts are difficult to manufacture at an industrial level and, therefore, they have not been widely used in practice.

As an alternative, some authors tested connections comprising steel parts. Smith *et al*. [3.9] tested beam-to-column connections between I-shaped profiles (with seated and clip angles) and between box profiles (with seated angles and two plates joining the members' webs) using steel connection parts. They obtained higher stiffness than that of similar solutions with composite parts. However, steel connection parts are much stiffer than pultruded profiles, which may lead to undesirable and less ductile failure modes in the beams and columns. In the study of Mottram and Zheng [3.6], the use of steel angle clips led to the flexural rupture of the beam at the top flange. In these studies, steel ductility was not exploited.

The current design codes and guidelines [3.13-3.16] provide limited guidance regarding connection design, covering relatively simple geometries and load conditions (*i.e.* lap joints) and not comprehensively addressing out-of-plane solicitations inherent to beam-to-column connections. Furthermore, no guidance is provided on how to consider the semi-rigid behaviour of the connections, which could be beneficial to fulfil serviceability design requirements in flexural members (that often govern the overall design). Such lack of design guidance is also hindering the widespread use of GFRP structures.

This chapter presents an experimental study concerning the development of beam-to-column connections between pultruded GFRP profiles with square tubular cross-section. This study was conducted within the scope of the ClickHouse research project [3.17], which aims at developing a modular house for emergency scenarios or temporary shelter. This project (abridged in Section 3.2) comprised the development of a novel, straightforward to implement beam-to-column connection system, which comprises steel parts embedded at the openings of the GFRP tubular profiles. The experimental programme (*cf*. Section 3.3) included (i) small-scale coupon tests to determine the GFRP material mechanical properties, (ii) double-lap tests to assess the in-plane behaviour of bolted connections between GFRP and steel plates, and (iii) monotonic tests on full-scale beam-to-column connections with different geometrical configurations in order to evaluate their stiffness, strength and failure mechanisms. Alongside the experimental study, currently available design guidelines were used to predict the strength of the proposed connection system, for all configurations tested. The forces used in these predictions were derived not only from analytical formulae, which were also used to predict the stiffness of the different connections, but also from numerical models.

3.2. OVERVIEW OF THE CLICKHOUSE PROJECT

The main goal of the ClickHouse project was the development of a prefabricated housing system for disaster zones, emergency situations, construction sites and/or temporary shelters, using GFRP materials. When compared to more conventional solutions commercially available, in light of the most recent international recommendations for this type of housing [3.18], the use of GFRP houses can guarantee better performance at a competitive cost in terms of the following aspects: (i) lightness; (ii) ease of transportation; (iii) quickness and ease of assembly and disassembly; (iv) possibility/flexibility of reutilization; (v) fulfilment of structural safety and thermal performance requirements, and (vi) durability and low maintenance cost.

The structure of the house is composed of pultruded GFRP profiles. The façade, the floor and the roof are made of sandwich panels with GFRP skins and an insulating polyurethane core, comprising windows, doors and piping networks. The connections between the panels and the profiles are materialized by splicing. The house incorporates water, sewage and electricity networks, as well as sanitation facilities.

This emergency housing system may be assembled by combining individual modules, which share the adjacent beams and columns. The dimensions of the unit module are 3×3×3 m3 (measured at the axes of the frame elements). The basic house prototype consists of the arrangement of two modules (*cf.* Figure 3.2), comprising one living room with kitchenette, one bedroom for 4–5 persons and one small bathroom.

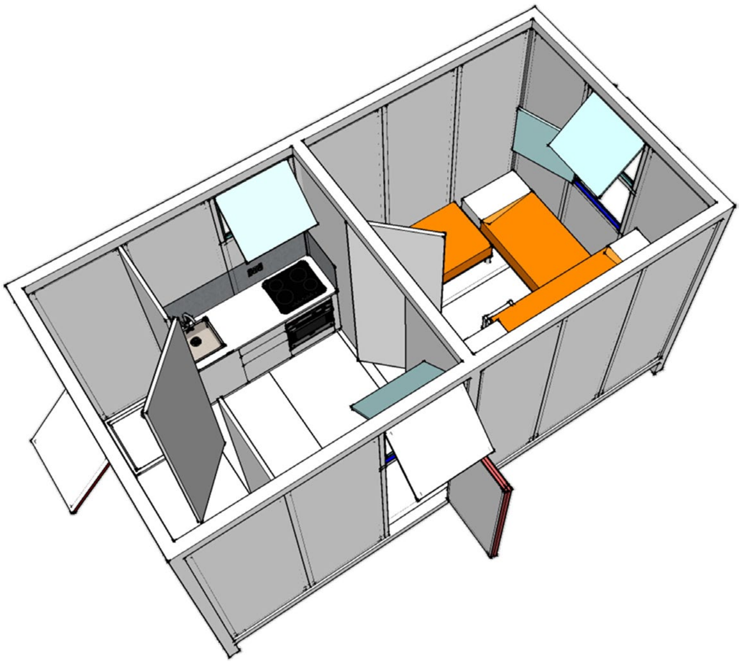

Figure 3.2 - 3D view of the first prototype.

The profiles used in the beams and columns of the ClickHouse module have a square hollow section (120×10 mm^2). As mentioned, the novel beam-to-column connection system comprises metal parts that are inserted/embedded in the cavity of the profiles. These parts are made of metallic tubular profiles. The column part has holes drilled in its four sides in order to fit the bolts (*cf*. Figure 3.3), while the beam part has a welded stainless steel back plate, which also has pre-drilled holes (*cf*. Figure 3.4). In order to avoid the need for positioning nuts inside the closed profiles, all the pre-drilled holes of both parts are threaded. This solution has the following advantages: (i) the production of the steel parts is straightforward and the connection is easy to assemble; (ii) these parts are not visible, not interfering with the aesthetics of the house, and (iii) the connection system does not obstruct the assembly of floor and wall panels.

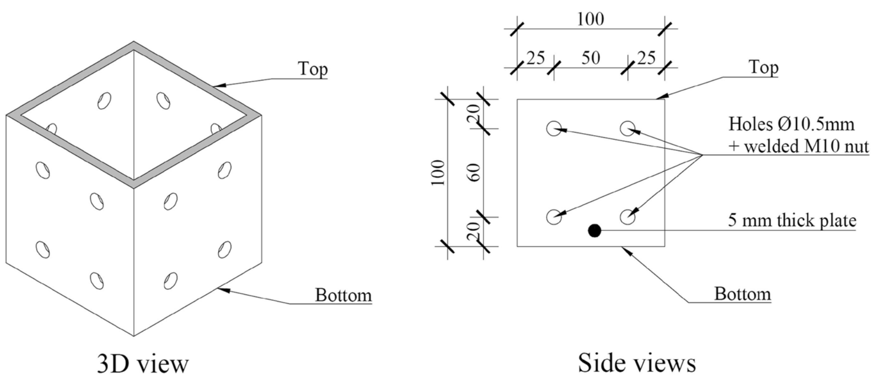

Figure 3.3 - Column connection part geometry.

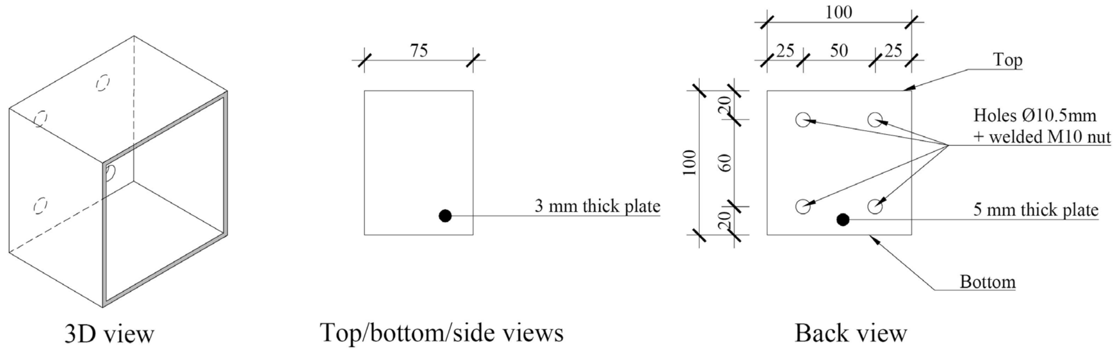

Figure 3.4 - Beam connection part geometry.

Since the connector parts are positioned inside the profiles, the connection assembly involves three stages: (i) the column part is first placed in position; (ii) the beam part is then bolted to the column part, and finally (iii) the beam is fixed to the beam connection part with M8 bolts. It is worth noting that the first two assembly stages may be performed before construction (in the shop), thus saving time on the job site. Figure 3.5 illustrates the assembly of the two steel parts.

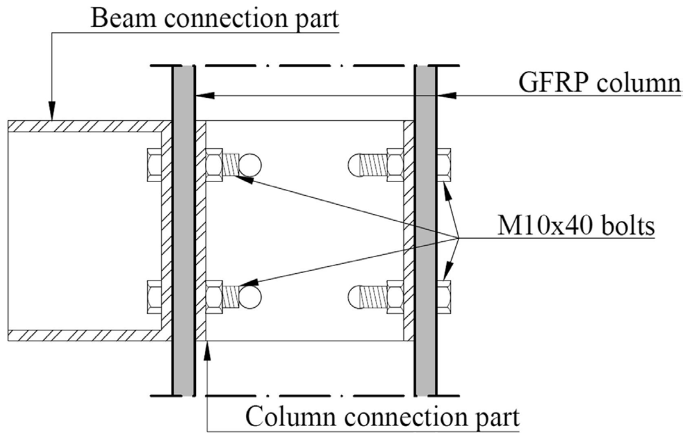

Figure 3.5 - Beam connection part geometry.

3.3. EXPERIMENTAL PROGRAMME

3.3.1. Material mechanical characterization tests

The following mechanical properties of the GFRP material used in the experiments were determined by means of small-scale coupon tests: (i) strength (σ_{cu}) and modulus of elasticity (E_c) in compression, in both longitudinal (L) and transverse (T) directions; (ii) longitudinal tensile strength ($\sigma_{tu,L}$), modulus of elasticity ($E_{t,L}$) and Poisson ratio (ν_{LT}); (iii) longitudinal flexural strength ($\sigma_{fu,L}$) and modulus of elasticity ($E_{f,L}$); (iv) interlaminar shear strength (τ_{is}); and (v) in-plane shear strength by means of Iosipescu shear tests (τ_{LT}).

The results of the performed tests and the standards followed are presented in Table 3.1. As expected, the material presented orthotropic behaviour, with higher stiffness and strength in the longitudinal direction of the profile. It is worth mentioning that the longitudinal tensile strength was somehow lower than the longitudinal compressive strength. This may be explained by the relatively high proportion of fibre reinforcement in the transverse direction of closed thin-walled section profiles (when compared with that of open thin-walled sections).

Table 3.1 - Mechanical properties of the GFRP material tested.

Test	Method	Property	Average ± Std. dev.	Unit
Compression	ASTM-D695 [3.19]	$\sigma_{cu,L}$	435.1 ± 52.6	[MPa]
		$E_{c,L}$	21.2 ± 3.3	[GPa]
		$\sigma_{cu,T}$	88.9 ± 16.3	[MPa]
		$E_{c,T}$	4.8 ± 0.9	[GPa]
Tension	EN ISO 527 [3.20]	$\sigma_{tu,L}$	326.2 ± 16.8	[MPa]
		$E_{t,L}$	32.7 ± 3.0	[GPa]
		ν_{LT}	0.32 ± 0.0	(-)
Flexure	EN ISO 14125 [3.21]	$\sigma_{fu,L}$	415.1 ± 61.3	[MPa]
		$E_{f,L}$	24.9 ± 5.8	[GPa]
Interlaminar shear	ASTM-D2344 [3.22]	τ_{is}	30.6 ± 2.6	[MPa]
In-plane shear	ASTM-D5379 [3.23]	τ_{LT}	41.4 ± 6.2	[MPa]

3.3.2. Double-lap tests

To evaluate the strength of the GFRP-to-steel bolted connections, 12 specimens divided in two series were tested in a double lap configuration, as illustrated in Figure 3.6. The specimens, comprising GFRP plates trimmed from the tubular profiles used in the full-scale connection tests, had 450 mm of length, 90 mm of width and nominal thickness of 10 mm. Each GFRP plate was bolted to two steel plates, using full-threaded M8 bolts, with enough clearance between the plates to avoid friction. The bolts were centred in the transverse direction of the plates and placed at a distance from the GFRP plate's bottom edge (*e*) of 37 mm for series 1, and 70 mm for series 2. Six specimens of each series were tested in a universal testing machine using displacement control at a cross-head rate of 1 mm/min. The axial relative displacement of two points spaced by 350 mm (between alignments A‑A' and B‑B' represented on Figure 3.6a), was measured by two displacement transducers, from *TML* with a stroke of 50 mm and precision of 0.01 mm, while the applied force was measured by the test machine's built-in load cell.

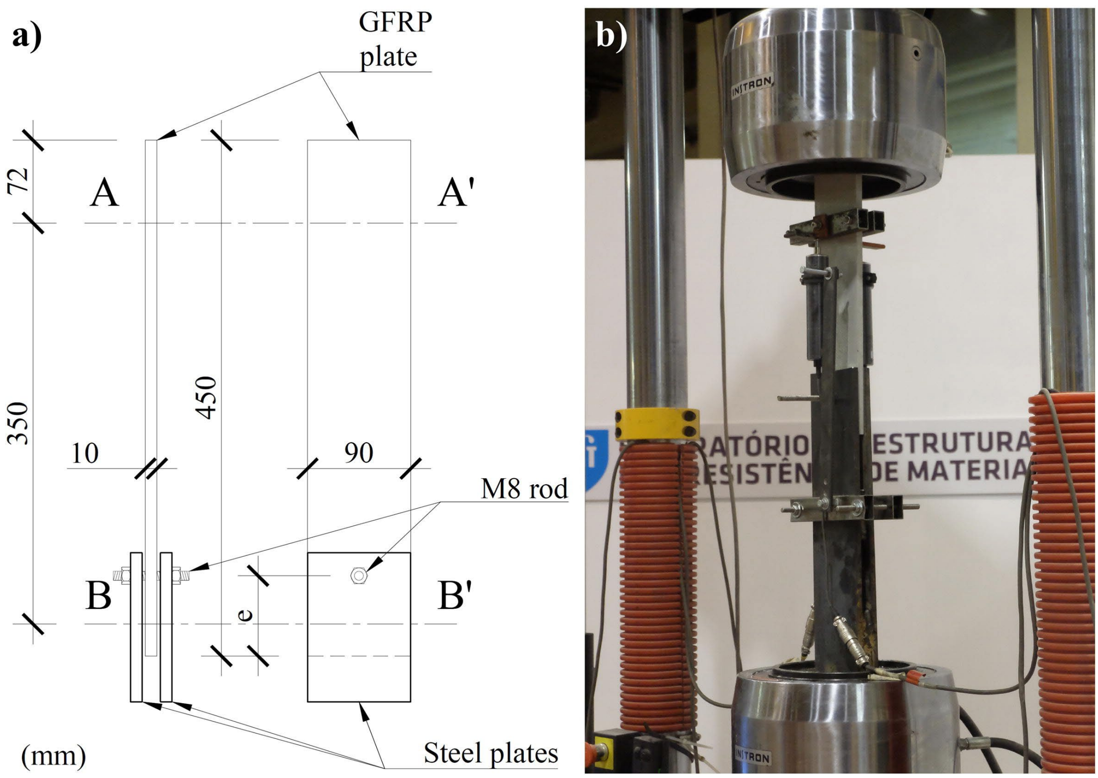

Figure 3.6 - Double-lap connection test: a) illustrative scheme; b) test setup.

The load *vs*. relative displacement curves obtained for series 1 and 2 are presented in Figure 3.7. In both series, the initial response was linear until the peak load was attained. In series 1, this was followed by a significant load drop and the peak load was never recovered. On the other hand, in series 2, the load drop was much smaller (in some cases it was followed by a small plateau) and subsequently the load considerably increased up to a second peak load. As expected, specimens from series 2, presenting higher edge distance than those of series 1 (e=70 mm *vs*. 37 mm), were able to attain higher failure loads and larger relative displacements before collapse. In terms of failure modes, specimens of series 1 failed due to a shear-out mechanism when the peak load was achieved, while the non-linear response of specimens of series 2 corresponded to a bearing failure phenomenon, before the second peak load was attained; after this stage, the collapse occurred due to a shear-out failure mechanism. Figure 3.8 presents a failed specimen of each series.

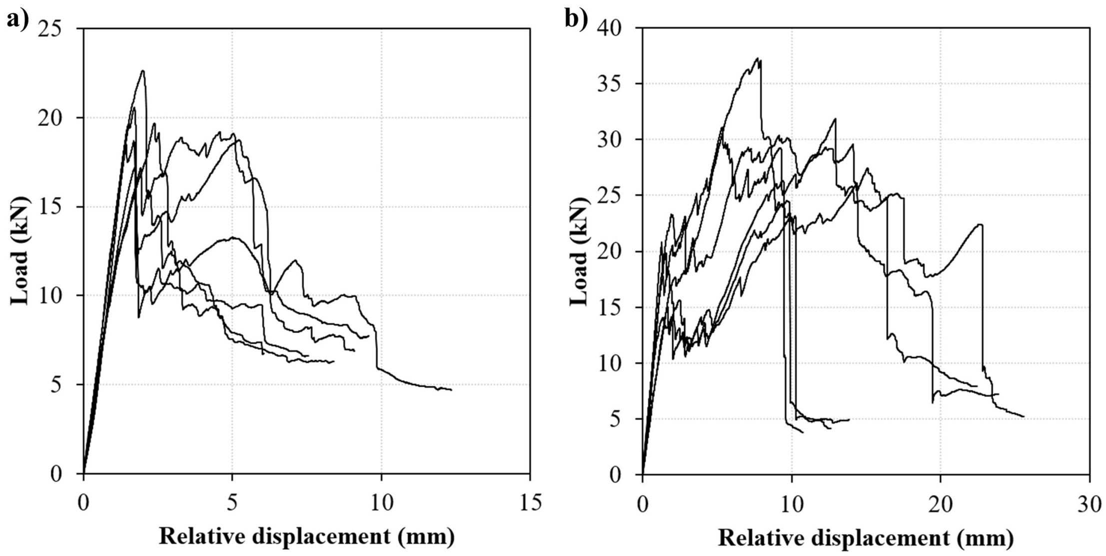

Figure 3.7 - Double-lap tests, load vs. relative displacement curves: a) series 1 (e = 37 mm); b) series 2 (e = 70 mm).

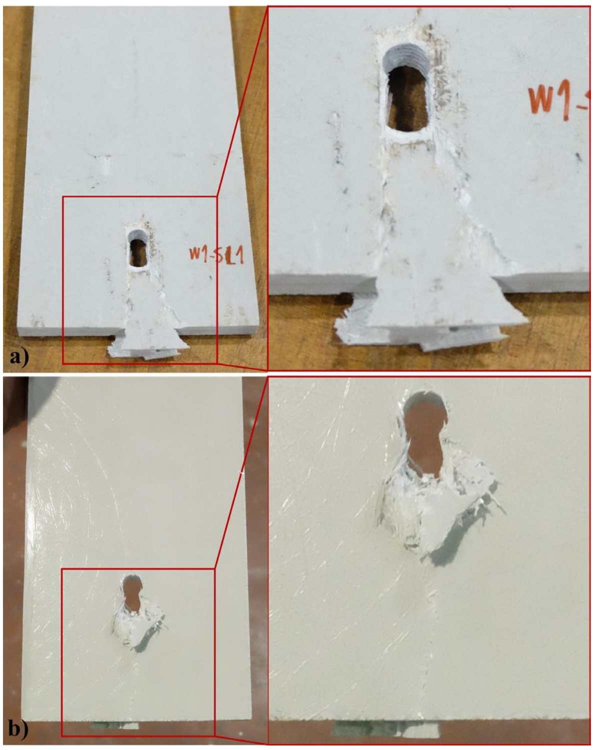

Figure 3.8 - Double-lap tests, typical failure modes: a) series 1 (e = 37 mm), due to shear-out; b) series 2 (e = 70 mm), due to bearing.

The maximum shear-out strength (τ_{so}) and the bearing strength ($\sigma_{br,L}$) of the material were estimated using Eq. (3.1), (3.2), respectively, in accordance with the recent prospect of a European Guidance for the Design of FRP Structures [3.16] (also included in the Italian CNR design guidelines [3.13]),

$$\tau_{so} = \frac{F_u}{(2e - d)t} \tag{3.1}$$

$$\sigma_{br,L} = \frac{F_u}{d \times t} \tag{3.2}$$

where F_u is the failure load, d is the bolt diameter (8 mm) and t is the plate thickness. Eq. (3.1) was applied to the results of series 1 (failure governed by shear-out), while Eq. (3.2) was applied to the results of series 2 (bearing failure).

Table 3.2 summarizes the test results for each experimental series, including the stiffness (K), the failure load (F_u) and the maximum stresses (τ_{so} or $\sigma_{br,L}$) estimated as explained above. As expected, the stiffnesses of both series were very similar. In opposition, increasing the edge distance provided a strength increase of 48%. The average shear strength estimated from Eq. (3.1) is similar to the interlaminar shear strength obtained from the coupon tests (30.6 MPa, *cf.* Section 3.3.1) and is 28.7% lower than the coupon in-plane shear (41.4 MPa, *cf.* Section 3.3.1), which seems to support the recommendations of the prospect of a European [3.16] and Italian design guidelines [3.13] regarding the use of such mechanical property for design purposes. Regarding the average bearing strength obtained, it is also of the same order of magnitude of the compressive strength (435.1 MPa, *cf.* Section 3.3.1), being 13.3% lower.

Table 3.2 - Summary of double-lap tests results.

Series	Series 1 (e = 37 mm)			Series 2 (e = 70 mm)		
Property	K (kN/mm)	F_u (kN)	τ_{so} (MPa)	K (kN/mm)	F_u (kN)	$\sigma_{br,L}$ (MPa)
Average	12.5	19.6	29.5	13.5	29.0	377.4
CoV	5.6%	8.4%	7.3%	12.5%	7.3%	18.3%

3.3.3. Beam-to-column tests

3.3.3.1. Description of test series

The novel connection system proposed herein (described in Section 3.2) was tested in four different configurations, namely: (i) with one bolt per web, series W1 (Figure 3.9a); (ii) with two bolts per flange, series F2 (Figure 3.9b); (iii) with four bolts per flange, series F4 (Figure 3.9c), and (iv) with two bolts per flange and a higher edge distance (e) than that used in series F2, series F2S (Figure 3.9d). Series W1 was idealized as a pinned connection with potentially low stiffness and moment distribution capacity. The remaining series were idealized as semi-rigid connections: series F2 and F4 aimed at evaluating the influence of the number of bolts used in each flange, while series F2S intended to assess the influence of the edge distance in the overall behaviour of the connection, namely in its failure mode and moment distribution capacity. Three specimens were tested per series.

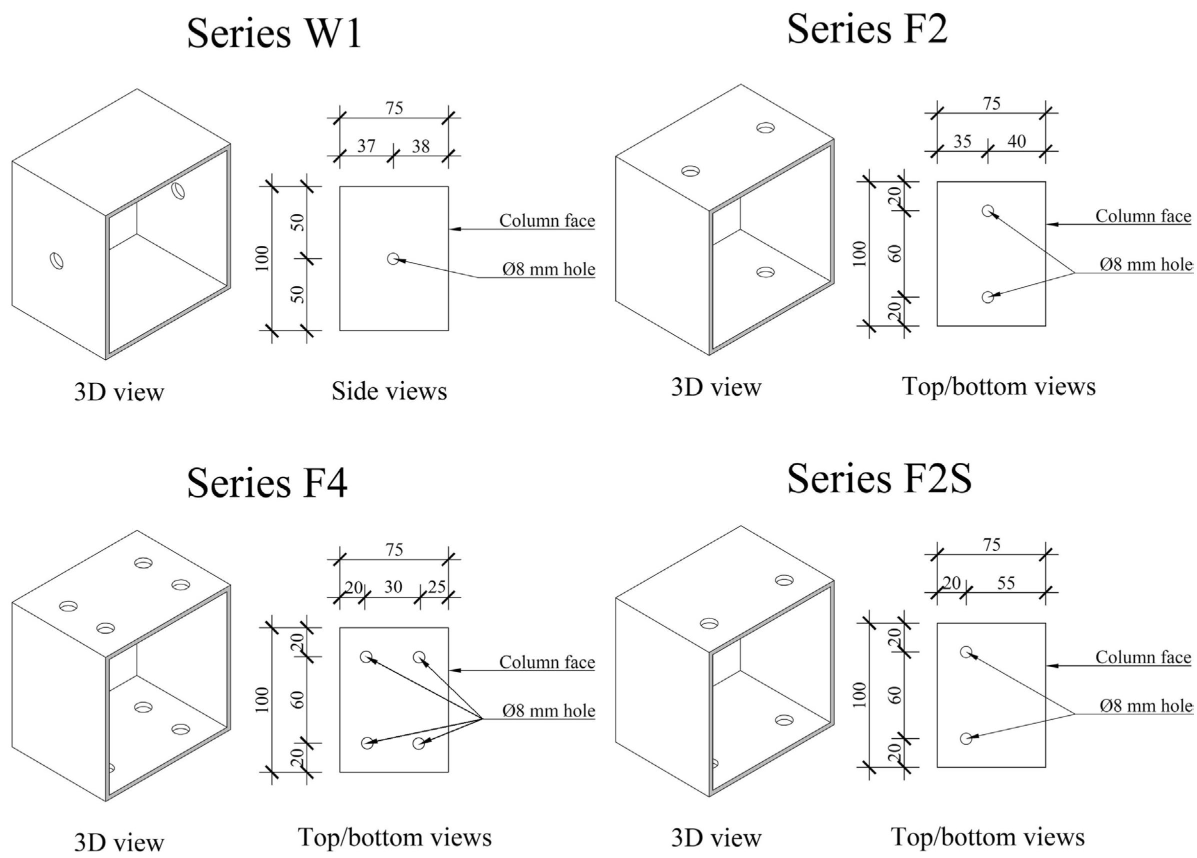

Figure 3.9 - Beam part: a) series W1; b) series F2; c) series F4; d) series F2S.

3.3.3.2. Test setup and procedure

The full-scale connection test specimens aimed at replicating an exterior frame connection where only one beam is joined to the column. These specimens comprised a 960 mm long beam and a 1080 mm long column, with the joint placed at mid-height of the column. Figure 3.10a depicts the test setup, while Figure 3.10b shows a specimen about to be tested.

The tests were performed in a closed steel loading frame anchored to the laboratory strong floor. The load was applied by an *Enerpac* hydraulic jack with capacity of 600 kN in compression and 250 kN in tension, and stroke of ±125 mm. The load was measured with a *TML* load cell with capacity of 300 kN. In order to guarantee the verticality of the applied load, two hinges were installed between the load cell and the specimens. Load was applied under displacement control at an average rate of 0.5 mm/s. The vertical load was applied to the beam at a distance of 600 mm from the front face of the column profile. In order to ensure that the load was always applied in the same section, a steel rod was inserted through 17 mm diameter holes drilled on both beam flanges, fixing the profile to the load application system. In addition, in order to avoid local crushing of the GFRP material, a steel spreading plate ($200\times50\times20$ mm^3) was placed in-between the two hinges and the specimens.

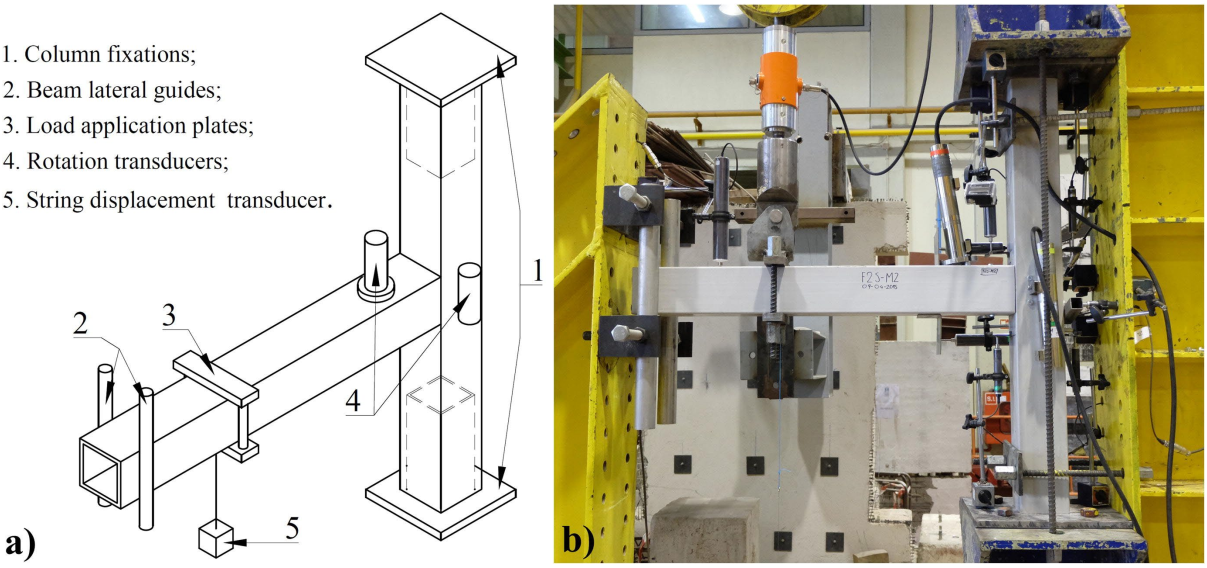

Figure 3.10 - Test setup: a) illustrative scheme; b) frontal view.

Both column ends of the specimens were fixed to the loading frame. The full-fixation of these sections, both in term of rotation and translation, was guaranteed by steel auxiliary parts (small length tubular profiles) which were inserted inside the GFRP column, as depicted in Figure 3.10a. Furthermore, out-of-plane displacements were restricted at the free end of the beam by means of two aluminium bars, as shown in Figure 3.10.

Displacements were measured at the load application point by a string pot displacement transducer, from *TML* with stroke of 500 mm. Two inclinometers, from *TML* with a range of ±10°, were used to measure (i) the rotation of the beam (transducer placed on the top flange of the beam, at a distance of 130 mm from the column face), and (ii) the rotation of the column (transducer placed at the intersection of the beam's and column's centre axes).

3.4. BEAM-TO-COLUMN TESTS RESULTS AND DISCUSSION

Table 3.3 presents the results obtained from the beam-to-column tests of the different series, namely the initial (linear) displacement and rotation stiffness (K_d and K_θ, respectively), the failure load (F_u), the corresponding displacement (d_{Fu}) and the ductility index (μ_d).

Table 3.3 - Summary of beam-to-column tests results.

Series	K_d (kN/m)	K_θ (kN·m/rad)	F_u (kN)	d_{Fu} (mm)	Failure mode	μ_d (–)
W1	142.5 ± 13.2	53.4 ± 8.6	4.1 ± 0.89	33.4 ± 6.80	Shear-out	0.45 ± 0.14
F2	212.7 ± 60.1	89.7 ± 18.8	6.3 ± 0.19	56.3 ± 24.24	Shear-out	0.68 ± 0.13
F4	273.4	115.7	6.8	60.4	Shear-out	0.89
F2 S	198.5 ± 20.4	70.7 ± 9.6	8.7 ± 0.75	114.4 ± 19.31	Bearing	0.81 ± 0.05

3.4.1. Load *vs*. displacement and moment *vs*. rotation behaviour

The load *vs*. displacement curves of the various specimens (labelled from M1 to M3) of all series tested are presented in Figure 3.11 and the corresponding bending moment *vs*. rotation curves[1] are presented in Figure 3.12.

The load *vs*. displacement (and moment vs. rotation) behaviour of specimens from series W1 was linear almost until failure; after the maximum load was attained, the load progressively decreased with residual loads at the end of the tests ranging from ∼1 to ∼2 kN. All specimens presented a similar stiffness, while the failure load (F_u) presented higher scatter.

The specimens of series F2 presented a linear behaviour until loads of ∼4 kN were attained, after which a gradual stiffness decrease occurred. All specimens failed for loads slightly higher than 6 kN, followed by an abrupt load reduction. The post-failure behaviour was not as progressive as that of series W1, with several sudden load drops occurring. At the end of the tests, the residual load of all specimens was lower than 3 kN.

[1] The relative rotation presented is the difference between the rotation of the beam and the rotation of the column; the bending moment was computed considering the distance between the centre of the applied load and the intersection between the centre axes of the beam and column (660 mm).

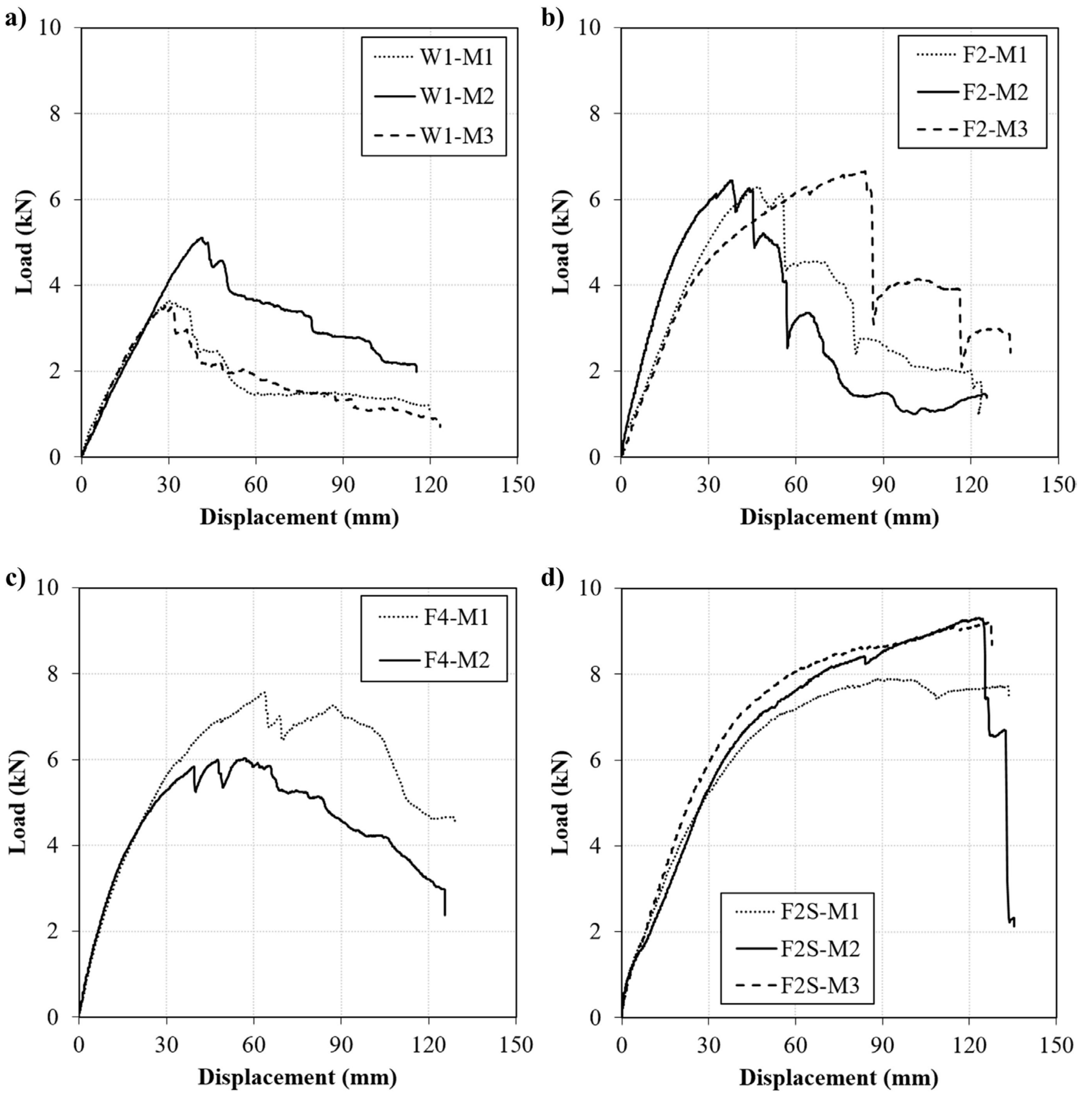

Figure 3.11 - Force *vs*. displacement curves of connections from series a) W1, b) F2, c) F4 and d) F2S.

Regarding series F4, the specimens presented non-linear behaviour from nearly the beginning of the tests. The load *vs*. displacement curves presented two load drops before failure followed by a gradual load recovery until the failure load was attained. After that point, the load decreased until the end of the test. A third specimen of series F4 was not considered in the analysis due to existence of a fabrication defect that affected the connection behaviour.

The specimens of series F2S also presented non-linear response, with progressive loss of stiffness for loads above ~5 kN until the final stages of the test, for which the maximum stroke of the hydraulic jack was reached. Consequently, only one specimen (F2S-M2) within this series failed, which corresponded to an abrupt load reduction.

The moment *vs*. rotation behaviour, depicted in Figure 3.12, exhibit very similar trends to the load *vs*. displacement curves, thus providing the same conclusions.

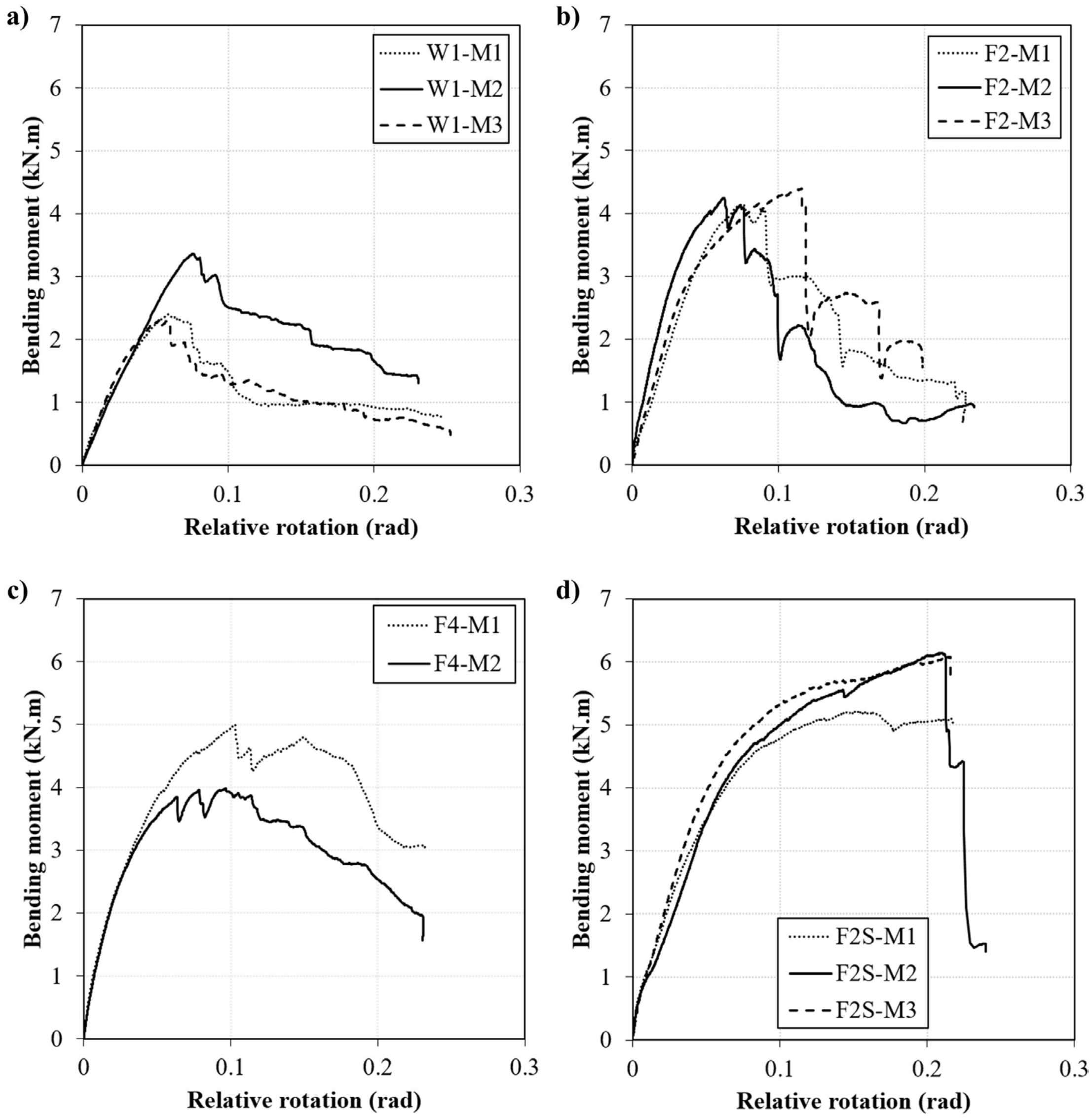

Figure 3.12 - Bending moment *vs*. relative rotation of connections from series a) W1, b) F2, c) F4 and d) F2S.

3.4.2. Failure behaviour

The damage progression of specimens of series W1 involved several mechanisms (*cf*. Figure 3.13a), namely: (i) crushing of the beam's bottom flange; (ii) tensile rupture of the beam's top web-flange junctions (the beam's connection part prevents the top flange from following freely the beam's rotation); (iii) shear-out of the bolts and (iv) shear failure of the beam's bottom web-flange junctions.

The previous failure mechanisms did not necessarily occur in the same order for all specimens; however, the failing sequence always started with the crushing of the beam's bottom flange while the ultimate load corresponded to the shear-out failure mechanism.

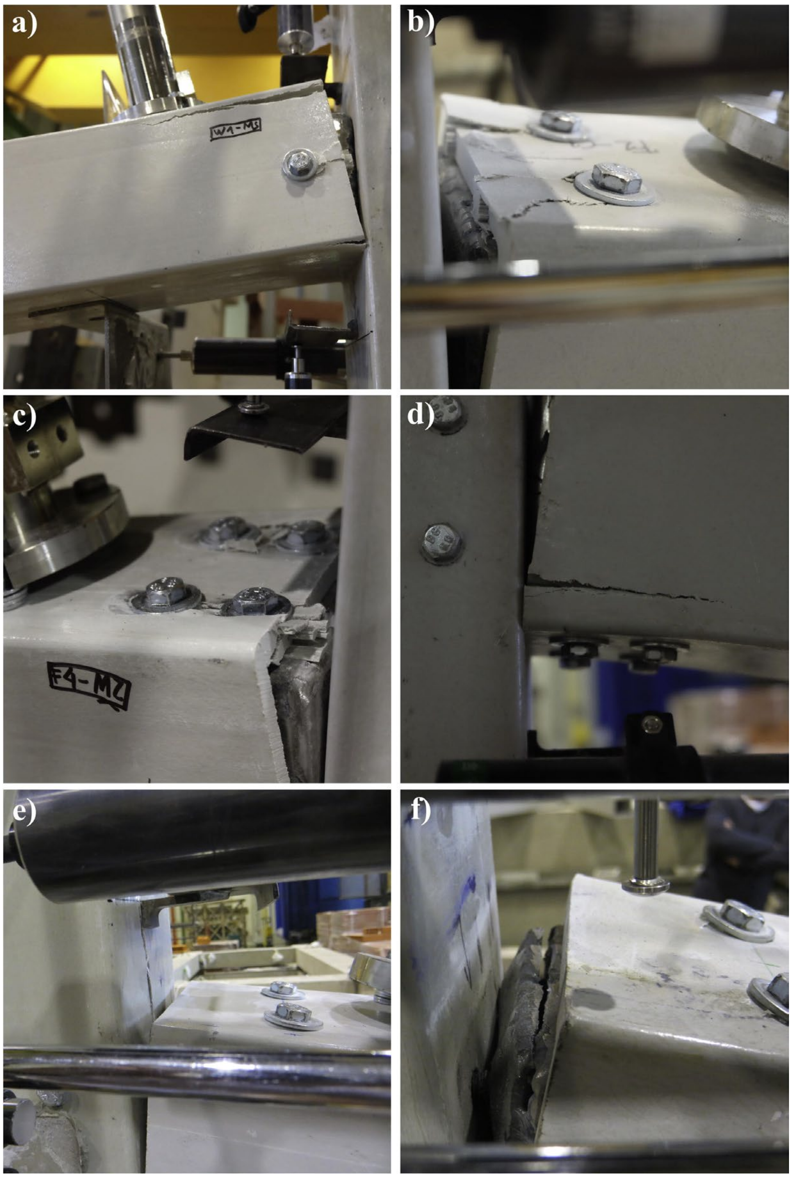

Figure 3.13 - Failure modes observed: a) series W1: beam's top web-flange junction failure, bolt shear-out and bottom flange crushing; b) series F2: bolt shear-out failure at beam's top flange; c) series F4: bolt shear-out failure at beam's top flange; d) series F4: shear failure of the beam's bottom web-flange junctions; e) series F2S: longitudinal cracking on the column; f) specimen F2S-M2: weld fillet failure.

The damage progression of series F2 was similar for all specimens, involving the (i) shear failure of the beam's bottom web-flange junctions followed by the (ii) shear-out of the top flange bolts (*cf.* Figure 3.13b). In specimen F2-M3, in addition, it was possible to identify the damage caused by the pull-out stresses introduced by the column's bolts on its facing plate, which ultimately led to axial cracks in the bolts alignments.

The typical damage progression in series F4 involved the (i) shear-out failure of bolts of the row with lower edge distance, followed by the (ii) shear-out failure of the bolts of the next row, both in the top flange of the beam (*cf.* Figure 3.13c). The ultimate failure mechanism was the (iii) shear failure of the beam's bottom web-flange junctions (*cf.* Figure 3.13d).

As mentioned earlier (*cf.* Section 3.4.1), only one specimen of series F2S was tested until failure (F2S-M2). For the remaining specimens, the maximum stroke of the hydraulic jack was reached before collapse. For the latter specimens, the damage progression involved several mechanisms, namely: (i) bearing of the beams top flange bolts; (ii) crushing of the beam's bottom flange; (iii) shear failure of the beam's bottom web-flange junctions and (iv) flexure of the column facing flange, which led to the development of longitudinal cracks in the alignment of the bolts (*cf.* Figure 3.13e). The damage due to the bearing of the bolts and to the column facing flange were hidden by the washers and by the beam's connecting part, respectively, thereafter it was not possible to determine the order in which the damage progression occurred. In opposition to the previous specimens, specimen F2S-M2 did not present signs of flexure of the column facing flange and the specimen collapse was caused by the rupture of the top weld fillet of the beam connection part (*cf.* Figure 3.13f).

3.4.3. Discussion

This section presents the analysis and discussion of results, namely regarding the influence of the bolts arrangement (number and disposition) on the mechanical performance of the connections and also on the serviceability behaviour of GFRP structures.

3.4.3.1. Influence of bolts arrangement on initial stiffness, failure modes and ductility

As mentioned earlier, the arrangement of the bolts had remarkable influence on the mechanical performance of the different connections. The most relevant aspect is concerned with the influence of the bolts edge distance on (i) the failure modes and associated sequence of damage events exhibited by each type of connection and (ii) the failure loads.

The connection typology F2S was the only one that did not present shear-out failure. In fact, in this series the extended edge distance (compared to that of the other connection typologies) increased the area of the shear resisting surfaces and, consequently, provided an increase of shear-out resistance. By preventing this failure mode, the damage was transferred to the column. Overall, series F2S presented the highest strength among the series tested, showing the importance of the shear-out phenomenon and the edge distance on the detailing of GFRP connections.

On the other hand, connection F4 had the lowest bolt edge distance, which led to an initial shear-out failure in two specimens, while in the majority of tests performed on the other connection typologies, different initial failure modes occurred, namely at the beam's web-flange junctions. Furthermore, the comparison between the failure loads of series F2 and F4 shows that increasing the number of bolt rows had limited effects on the strength. However, it should be mentioned that in the present study this increase was achieved at the expense of a larger edge distance, which led to a decrease on the shear-out failure strength of this series. In fact, the stress distribution between bolt rows, which is linear, as pointed out in several standards and earlier studies [3.13,3.16,3.24], did not fully compensate the strength decrease due to lower edge distance.

The test results also showed that using bolts on the beam's top flanges prevented the occurrence of the tensile rupture on the beam's top web-flange junctions. Indeed, as mentioned earlier, this failure mechanism was only observed in connection W1.

For some specimens, in particular those of the series which sustained higher loads, F4 and F2S, the bending of the column's facing flange led to its damage in the form of longitudinal cracking aligned with the columns bolts. This proved to be a (pseudo-)ductile mechanism, as it did not lead to an abrupt load reduction. It seems that the column steel connection part was responsible for maintaining the integrity of the connection at this point due to the steel material strength and plasticity properties.

Regarding the initial stiffness, as expected, connection W1 presented the lowest performance due to the fact that the bolts are positioned closer to the beam's rotation centre; note that owing to the lowest lever arm, this series also presented the lowest failure loads. As expected, connection F4 also exhibited the highest stiffness, as both bolt rows provided a higher deformation restraint to the beam's flanges when compared to that of series F2 and F2S, which presented intermediate stiffness figures.

Additionally, the ductility index (μ_d) was also evaluated for the different series, using one of the methods suggested by Jorissen and Fragiacomo [3.25] for timber nailed connections (which also comprise brittle and ductile materials, wood and steel, respectively). Thereafter, the ductility index estimated corresponds to the ratio between the displacement at failure (d_u) minus the displacement at "yield" (d_y) and the former, being given by

$$\mu_d = \frac{d_u - d_y}{d_u} \tag{3.3}$$

Given the non-ductile nature of the failure modes observed, it was considered that the "yield" displacement (d_y) corresponded to the end of the initial linear stage (end of proportionality between load and displacement) while the failure displacement (d_u) was that corresponding to 80% of the maximum force (F_u) in the descending branch of the load-displacement curves. Since specimens of connection F2S did not collapse and no considerable strength decrease was registered until the end of the tests, the failure displacement (d_u) was taken as the maximum displacement measured (limited by the hydraulic jack's stroke). It should be mentioned that, given the non-ductile material behaviour of the GFRP material, this index measures the pseudo-ductility of the connection, as an indicator of the residual strength associated with the damage progression of the components of the connection systems; in other words, unlike steel connections/structures, it is not a measure of their (material) plastic behaviour. The ductility indexes estimated for each series (*cf.* Table 3.3) showed that connections F2S and F4 are more (pseudo-)ductile than their counterparts, presenting ductility indexes that are almost twice those of connection W1. This behaviour confers those connection types an added degree of robustness, contrasting with the usual typical brittle failure modes of GFRP structures.

3.4.3.2. Influence of connection stiffness in GFRP structural design

As mentioned earlier, since the design of GFRP structures is often governed by serviceability limit states, namely by deformability requirements, the consideration of the semi-rigid behaviour of the connections (if possible) may be beneficial for the structural design. Some design standards provide limits for the connection classification according to the type of joints. For example, the Eurocode 3 [3.26] for steel structures specifies the following categories for an elastic analysis: (i) normally pinned joints, in which no moment is considered to be transmitted through the joint; (ii) rigid joints, in which the connections can be assumed to be fully fixed (no rotations); and (iii) semi-rigid joints, in which the stiffness of the connections needs to be taken into account in the analysis.

Figure 3.14 compares the limits established in that standard with the results obtained in the present experiments, showing that the stiffness of the connection systems studied herein may be classified as semi-rigid connections. Moreover, it can be seen that the stiffness of the different connections is much closer to that of the pinned limit; this is basically due to the fact that the connection between the beam connection part and the column is made by bolts placed inside the beam's tubular section and, consequently, with a reduced lever arm. Turvey and Cooper [3.27] catalogued connection typologies between I-section profiles. In their study, they defined connections with only cleats in the beam's web as having rotation stiffness between 30 and 80 kN.m/rad; these results are similar to those obtained for the connections tested in this experimental campaign. By using top and bottom flange cleats, the stiffness of the connections could be increased (in the mentioned study, up to 500–1100 kN.m/rad).

Finally, the influence of the connections' stiffness on the overall beam deflection was evaluated. For this purpose, the deflections of a beam with a span of 2.88 m (identical to those used in the ClickHouse project) was estimated for a uniformly distributed unitary load, using the Timoshenko Beam Theory [3.28] and accounting for the connection stiffness obtained in the tests for each series, as illustrated in Figure 3.15. This comparison shows significant deflection reductions, when compared to pinned connections, ranging from 15% (connection W1) to 26% (connection F4).

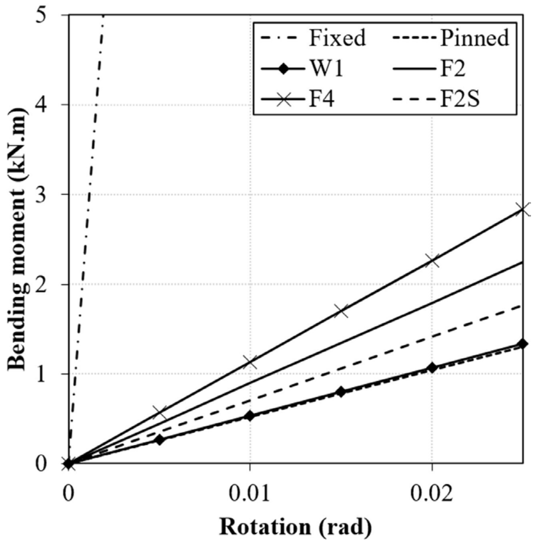

Figure 3.14 - Comparison between fixed and pinned connection stiffness limits and the experimental results.

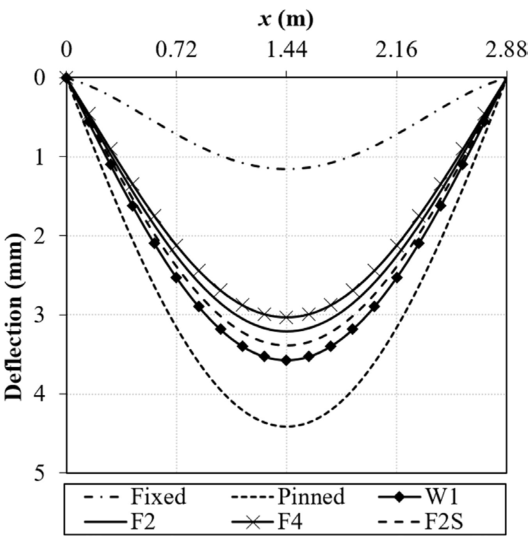

Figure 3.15 - Estimated beam deflections for different connection systems; with an applied load = 1 kN/m.

3.5. ESTIMATES OF STIFFNESS AND FAILURE LOAD

In this section, an analytical study is presented with the following objectives: (i) to estimate the rotational stiffness of connections series; and (ii) to predict their strength. Additionally, a numerical study is presented to estimate the connections' ultimate load in the light of the limitations of the analytical models used.

3.5.1. Stiffness

To estimate the stiffness of the connections, analytical studies were performed using the "component method", in which a joint is considered as a set of individual basic components. The component method model considered for each connection is illustrated in Figure 3.16a. The following components were considered in this analysis: (i) the beam's bolts and plate interface (K_b); and (ii) the column's facing flange and the facing plate of the column's steel connection part (K_p); and combined with Eq. (3.4):

$$\frac{1}{K_{\theta,an}} = \frac{1}{k_p(d_{p1}^2 + d_{p2}^2)} + \frac{1}{K_b d_b^2} \tag{3.4}$$

The stiffness of the beam's bolts and plate interface (K_b) was that derived from the double-lap tests, which proved to be independent from the edge spacing (*cf.* Section 3.3.2). On the other hand, the stiffness of the column's facing flange and the facing plate of the column's steel connection part (K_p) component was estimated considering the following assumptions: (i) the elasticity modulus considered for the GFRP plate is that determined for compression in the transverse direction (*cf.* Section 3.3.1), while for steel an elasticity modulus of 210 GPa was used; (ii) no interaction was considered between the steel and the GFRP plates; (iii) the stiffness was estimated per row of bolts, considering that they are independent and have an influence height of 50 mm (corresponding to half of the height of the column connection part), using a simply supported beam model (Figure 3.16b). The stiffnesses estimated for the beam and for the column components were K_b=13 kN/mm per bolt and K_p=10 kN/mm, respectively.

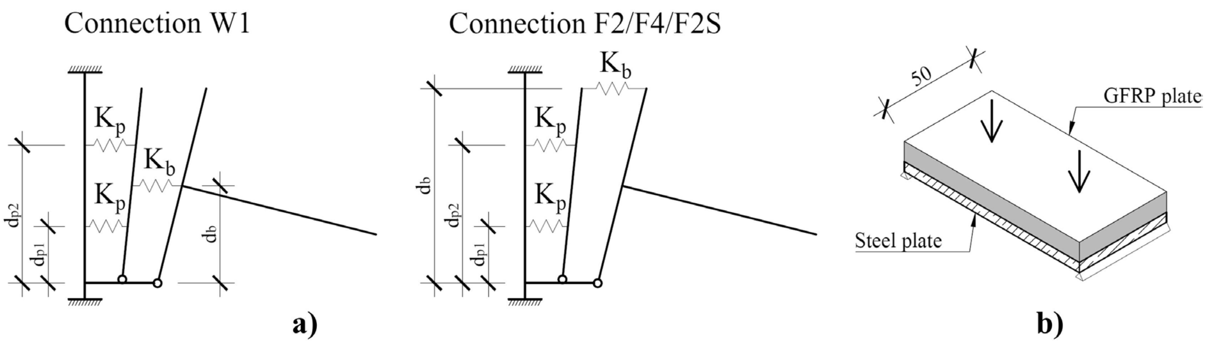

Figure 3.16 - Analytical models: a) component method; b) model for estimating the GFRP column face and steel plate bending stiffness.

Table 3.4 lists the stiffnesses of the different connection typologies estimated using the analytical models described above. The stiffnesses estimated for connection typologies W1, F2 and F4 were very similar to those obtained experimentally (relative differences below 10%); however, for connection F2S the agreement was worse (~30%). In this respect, it is worth mentioning that the estimated stiffness of the beam-to-column connections does not consider the edge spacing of the beam bolts, which is in accordance with the double-lap tests results (*cf.* Section 3.3.2), therefore the same estimates were obtained for series F2 and F2S. The difference between the rotational stiffness of series F2 and F2S registered in the tests is most likely related with the inherent experimental variability, including the effects of clearances between the specimens' components. The relative difference between the estimated rotational stiffness and that of the average of specimens of both series F2 and F2S together

(80.2 kN.m/rad) is only 23%; moreover, the overall relative difference considering all connection typologies is 10.4%, which is quite reasonable given the complexity of the connections studied and seems to validate the hypotheses assumed.

Table 3.4 - Analytically estimated stiffness, analytically and numerically estimated failure loads and relative difference to experimental data (Δ).

Series	Stiffness			Strength					
	K_θ (kN.m/rad)	$K_{\theta,an}$ (kN.m/rad)	Δ	F_u (kN)	$F_{u,an}$ (kN)	Δ	Failure mode	$F_{u,nu}$ (kN)	Δ
W1	53.4 (16.1%)	55	+2.9%	4.1 (21.7%)	4.4	7.3%	Shear-out	4.7	+13.8%
F2	89.7 (21.0%)	99	−9.4%	6.3 (3.0%)	9.1	44.4%	Shear-out	7.5	+19.2%
F4	115.7	114	−0.7%	6.8	8.6	26.5%	Shear-out	9.8	+39.3%
F2S	70.7 (13.6%)	99	+28.6 %	8.7 (8.6%)	12.6	46.0%	Bearing	9.7	+11.5%

3.5.2. Strength

3.5.2.1. Analytical estimates

For each connection type, the estimated strength of the beam's bolts and plate interface were those corresponding to the governing failure mode, either the shear-out failure or the bearing failure, which were determined with Eqs. (3.1), (3.2), respectively, with the interlaminar shear strength and bearing strengths determined experimentally (*cf*. Section 3.3.2).

The failure loads and modes estimated analytically and their comparison to the experimental results are presented in Table 3.4. The predicted failure mode (shear-out or bearing) was that associated with the lowest predicted failure load. The resistant bending moment for each connection was estimated by multiplying the governing failure load (shear-out/bearing) by the lever arm corresponding to the distance between the top flange/web bolts (connections F2, F2S and F4/connection W1) and the bottom flange of the beam; considering that the beam rotation axis was located in the interception of the beam's bottom edge with the column. On the other hand, the estimated ultimate load to be compared with the test results corresponds to the bending moment divided by the distance between the load application point and the concerned bolt row. Additionally, for connection F4, due to the brittle nature of the GFRP material, an elastic load distribution between bolt rows was considered, namely with 60% of the load on the row closest to the column face and the remaining 40% on the farthest row, as recommended in the prospect of a European Guidance for the Design of FRP Structures [3.16] (similar recommendations are given in [3.13]).

The failure modes estimated are in accordance with those observed: connection F2S was expected to present a bearing failure mode[2], while in the remaining systems the predicted governing failure mode was shear-out. Regarding the analytical prediction of the shear-out failure load of connection W1, good agreement with the experiments was obtained (relative difference of 7.3%); regarding series F2, F4 and F2S, the analytical predictions for strength were considerably higher than the test results (relative differences of respectively 44.4%, 26.5% and 46.0%). These significant relative differences (overall average of 31%) indicated that the failure mechanisms are far more complex than those considered in this straightforward analytical approach.

3.5.2.2. Numerical estimates

In order to obtain more accurate estimates of the forces in the bolts, linear elastic finite element models were developed in ABAQUS commercial package.

The geometry of the different connection components was similar to that described in Sections 3.2 and 3.3.3.1. The several components of the connections were modelled using solid elements: (i) the beam and column parts were modelled using 8-node hexagonal elements with full integration (C3D8); (ii) the bolts and column connection part were modelled using 10-node tetrahedral elements (C3D10); and (iii) the beam connection part was modelled with 20-node hexagonal elements with full integration (C3D20). The overall dimension of the finite elements was 3 mm (corresponding to approximately 170.000 elements, 290.000 nodes and 770.000 variables[3] in the models). The contact between the

---

[2] Even if the shear-out failure load is only slightly higher (13.2 kN) than the bearing failure load (12.6 kN).

[3] Degrees of freedom plus maximum number of Lagrange multiplier variables.

surfaces was modelled using $*HARDCONTACT$ formulation and no friction was considered. On the other hand, to simulate the threaded segments of the bolts attached to the connection parts, ties were used connecting the bolts to the steel connection parts. The GFRP mechanical properties considered in the models are those obtained in the material characterization tests (*cf.* Section 3.3.1), while for steel an elasticity modulus of 210 GPa and Poisson coefficient of 0.3 were assumed.

In terms of boundary conditions, a symmetry simplification along the longitudinal axis of the profiles was considered and the column ends were considered as fixed. A vertical displacement of 40 mm was applied in the beam edge. As an example, the model of connection F2 is presented in Figure 3.17.

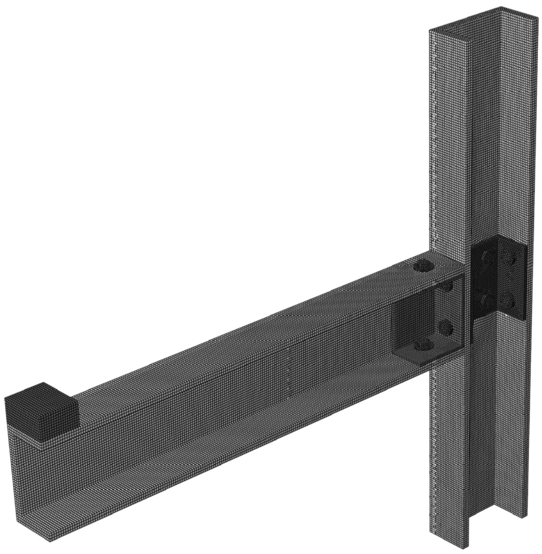

Figure 3.17 - Finite element model of connection F2.

The numerical models were then used to obtain not only the shear forces but also the axial (pull) loads on the beam's bolts, as a function of the applied load. One of the aspects that was not included in the analytical approach is the influence of the out-of-plane loads (prying forces) transmitted by the bolts, which may also explain why the strength predictions obtained are non-conservative. This aspect, together with the force interaction, was then considered in these numerical investigations. The failure load of each connection was then estimated using the linear interaction curve proposed in the prospect of a European Guidance for the Design of FRP Structures [3.16],

$$\frac{V_{Sb}}{R_{Vb}} + \frac{N_{Sb}}{R_{Nb}} \leq 1 \tag{3.5}$$

where V_{Sb} and N_{Sb} are the shear and tensile applied loads in the bolt, respectively, and R_{Vb} and R_{Nb} are the bolt strength for such types of mechanical loads (these depend on the geometrical configuration of the connection being analysed). Accordingly, for R_{Vb}, the shear-out failure load estimated in the previous section was used for connections W1, F2 and F4, while for connection F2S the bearing failure load was considered. Regarding R_{Nb}, the pull-out strength formula suggested in the prospect of a European Guidance for the Design of FRP Structures [3.16],

$$F_{u,pull} = \tau_{is} \pi d_w t \tag{3.6}$$

where, τ_{is} is the interlaminar shear strength, d_w is the bolt washer diameter and t is the thickness of the GFRP beam plates.

The strength estimates and the comparison with their experimental counterparts are presented in Table 3.4. It can be seen that the estimated failure loads have, in general, an overall good agreement with the experimental values. The worse agreement was obtained for typology F4, most likely due to the more complex failure mechanism of this configuration, which involves two rows of bolts, preventing it from being accurately simulated using a linear elastic model. The overall average relative difference between strength estimates and experimental failure loads was ~21%, which is a reasonable result especially taking into account the relative simplicity of the prediction method and the complexity of the phenomena involved. However, the predicted strength overestimated the experimental results, suggesting that the prospect design guidance [3.16] should be used with reserve in the design of GFRP beam-to-column connections.

3.6. CONCLUSIONS

This chapter presented a novel connection system for pultruded GFRP tubular profiles using internal steel parts and bolts, which was developed to be used in modular constructions for temporary shelter or emergency scenarios.

The results obtained in the experiments proved the feasibility of the proposed connection system and the geometrical variations tested allowed to understand the influence of different parameters on the overall behaviour of the connection system. In particular, the experimental results presented herein have shown that (i) the bolt edge distance is the key parameter for the connection strength, being determinant for the governing failure mode (shear-out for short edge distances and bearing for long edge distances), while (ii) the number of bolt rows per plate has a relevant influence on the stiffness of the connection, being less influential on the overall strength. On the other hand, the results have shown that (iii) both semi-rigid and almost pinned connections (series W1) can be achieved with this system. Additionally, it was shown that series W1 and F2 presented considerable residual strength after failure, while connection systems F2S and F4 actually presented a "yield" stage. This is a promising result regarding ductility and inelastic energy dissipation of GFRP structures under cyclic/seismic loading. Nevertheless, this indication must be verified under cyclic test conditions.

The analytical study presented has shown that the stiffness of the connection system can be estimated with reasonable accuracy using the "component method" for the different geometries tested. However, it fails to achieve reasonable estimates regarding the connections' strength. The use of simple analytical models (featuring the components method) to predict the connections' stiffness may be of great importance at design level, especially in early design stages, since it was shown that the connection stiffness may contribute to reduce the structural deformations that often govern the design of GFRP structures. In order to estimate the strength of the connections with more accuracy, numerical models were developed; they were able to predict the strength of the connections with reasonable precision, especially for series with a single bolt row, however overestimating the experimental results.

Just a final word to mention that based on the results reported herein it was finally decided to use connection system F2S in the ClickHouse project structure, due to its better performance regarding strength and ductility, while its stiffness was sufficient to guarantee that service deflections complied with the project limits.

3.7. REFERENCES

[3.1] Correia JR (2008). *GFRP pultruded profiles in civil engineering: hybrid solutions, bonded connections and fire behaviour*. PhD Thesis in Civil Engineering. Instituto Superior Técnico, Lisboa.

[3.2] Keller T. (1999). Towards structural forms for composite fibre materials. *Structural engineering international*, 9(4), 297-300.

[3.3] Bank LC, Mosallam AS, Gonsior HE. (1990). Beam-to-column connections for pultruded FRP structures. In *Serviceability and Durability of Construction Materials* (pp. 804-813). ASCE.

[3.4] Bank LC, Mosallam AS, McCoy GT. (1994). Design and performance of connections for pultruded frame structures. *Journal of reinforced plastics and composites*, 13(3), 199-212.

[3.5] Coelho AMG, Mottram JT. (2015). A review of the behaviour and analysis of bolted connections and joints in pultruded fibre reinforced polymers. *Materials & Design*, 74, 86-107.

[3.6] Mottram JT, Zheng Y. (1996). State-of-the-art review on the design of beam-to-column connections for pultruded frames. *Composite structures*, 35(4), 387-401.

[3.7] Smith SJ, Parsons ID, Hjelmstad KD. (1998). An experimental study of the behavior of connections for pultruded GFRP I-beams and rectangular tubes. *Composite structures*, 42(3), 281-290.

[3.8] Mosallam AS, Abdelhamid MK, Conway JH. (1994). Performance of pultruded FRP connections under static and dynamic loads. *Journal of Reinforced Plastics and Composites*, 13(5), 386-407.

[3.9] Smith SJ, Parsons ID, Hjelmstad KD. (1999). Experimental comparisons of connections for GFRP pultruded frames. *Journal of Composites for Construction*, 3(1), 20-26.

[3.10] Singamsethi SK, LaFave JM, Hjelmstad KD. (2005). Fabrication and testing of cuff connections for GFRP box sections. *Journal of Composites for Construction*, 9(6), 536-544.

[3.11] Carrion JE, LaFave JM, Hjelmstad KD. (2005). Experimental behavior of monolithic composite cuff connections for fiber reinforced plastic box sections. *Composite structures*, 67(3), 333-345.

[3.12] Mosallam AS, Bedewi NE. (1994). Design optimisation of FRP universal connectors. *Polymer and Polymer Composites*, 2(2), 115A.

[3.13] Italian National Research Council (2007). CNR-DT 205/2007 – Guide for the Design and Construction of Fiber-Reinforced Concrete Structures.

[3.14] ASCE (2010). Pre-Standard for Load & Resistance Factor Design (LRFD) of Pultruded Fiber Reinforced Polymer (FRP) Structures.

[3.15] Clarke JL. (2003). *Structural Design of Polymer Composites: Eurocomp Design Code and Background Document.* CRC Press.

[3.16] CEN/TC250/WG4 (2014). Fibre Reinforced Polymer Structures: scientific and technical report.

[3.17] Correia JR, Martins D, Gonilha JA, Nascimento JG, Arruda M, Castelo A, Branco F. (2015). Clickhouse project – an all-composite emergency housing system. In *International Conference on Advances in Composite Materials and Structures* (CACMS), Istanbul.

[3.18] The Sphere Project. (2011). *Humanitarian charter and minimum standards in humanitarian response*. Sphere Project. http://www.jstor.org/stable/j.ctt1hj54z7

[3.19] ASTM D 695-02 (2006) – Standard Test Method for Compressive Properties of Rigid Plastics. West Conshohocken.

[3.20] EN ISO 527-1 (1997) Plastics – Determination of Tensile Properties – Part 1: General Principles. Brussels.

[3.21] EN ISO 14125 (1998) – Fibre-reinforced plastic composites: Determination of Flexural Properties. Brussels.

[3.22] ASTM D 2344/D 2344M-00 (2006) – Standard Test Method for Short-Beam Strength of Polymer Matrix Composite Materials and Their Laminates. *West Conshohocken*.

[3.23] ASTM D 5379/D 5379M (2005) – Standard Test Method for Shear Properties of Composite Materials by the V-Notched Beam Method. West Conshohocken.

[3.24] Bank, L. C. (2006). *Composites for construction: structural design with FRP materials*. John Wiley & Sons.

[3.25] Jorissen A, Fragiacomo M. (2011). General notes on ductility in timber structures. *Engineering structures*, 33(11), 2987-2997.

[3.26] EN1993 (2004): Design of Steel Structures – Part 1–8: Design of Joints.

[3.27] Turvey GJ, Cooper C. (2004). Review of tests on bolted joints between pultruded GRP profiles. In *Proceedings of the Institution of Civil Engineers-Structures and Buildings*, 157(3), 211-233.

[3.28] Weaver Jr W, Timoshenko SP, Young DH. (1991). *Vibration problems in engineering*. John Wiley & Sons.

Chapter 4

Cyclic behaviour of a sleeve connection system for tubular profiles

4.1. INTRODUCTION

As mentioned in Section 3.1, while there have been several studies focussing on the behaviour of beam-to-column connections between FRP pultruded profiles, few have reported on their cyclic behaviour In fact, very few studies are available on the cyclic behaviour of GFRP beam-to-column connections. Bruneau *et al*. [4.1] studied the cyclic behaviour of beam-to-column connections between I-shaped GFRP pultruded beams and columns, materialized by auxiliary parts consisting of cuts of T- and L-shaped GFRP profiles. The profiles and auxiliary parts were joined by means of bolts and epoxy adhesive. The cyclic loading was defined during the tests, with loading reversals operated when noticeable failure occurred. The authors registered several brittle failures throughout the tests, involving delamination of the T-shaped parts, and limited ductility. The energy dissipation capacity of the connections was not assessed.

Mosallam [4.2] tested two beam-to-column connection specimens under cycling loading. Proprietary composite auxiliary parts (entitled as "Universal Connector") were used to join the profiles. One specimen consisted of a bolted-only connection using composite rods and nuts, while the other used the same elements and epoxy adhesive. The loading history aimed at simulating the cyclic loading due to an earthquake, but no details were provided regarding its definition. The author concluded that the failure of the connections was not only reasonably ductile, but also provided warnings before critical failure, which was ascribed to the composite rods. The moment vs. rotation curves show that both types of specimens presented substantial pinching and low dissipated energy.

Carrion *et al*. [4.3] assessed the behaviour of beam-to-column connections between GFRP tubular profiles using "cuff" auxiliary parts fabricated with E-glass fibres and epoxy resin. Two different cuffs with different thicknesses (6.35 mm and 9.55 mm) were tested. These auxiliary parts were bonded to the GFRP profiles with epoxy adhesive. The loading history comprised consecutive cycles with increasing displacement (no information was provided regarding their definition). Specimens using "cuff" parts with higher thickness presented approximately linear behaviour, losing their structural integrity immediately after critical damage (debonding of the "cuff" or crushing failure of the beam). On the other hand, in specimens with a thinner "cuff" connection part, damage was located on this auxiliary part, resulting in a more ductile behaviour. This type of specimens was able to maintain residual strength after peak-load was achieved, allowing the connection to dissipate some energy, although this parameter was not directly assessed in the paper.

Zhang *et al*. [4.4] tested three specimens of beam-to-column connections between GFRP tubular profiles with sleeve connection parts. The sleeve connection system was adhesively bonded to the beam, using an epoxy adhesive, and welded to a steel end-plate that was bolted to the column. In this latter connection, the authors varied the number of bolts and the thickness of the steel end-plate. The loading history was defined in accordance to ANSI/AISC 341-16 procedures for steel structures [4.5]. The failure modes included yielding of the steel end-plate, cohesive failure at the steel-GFRP interface and rupture of the web-flange junction of the beams. The connection with thicker end-plates presented higher stiffness, however this detail led to a lower strength and ultimate rotation. Moreover, the connections with thinner end-plates presented more ductility, owing to the yielding of the steel end-plate and, therefore, were able to dissipate more energy. Additionally, the authors developed finite element (FE) models of the connections using commercial software *ANSYS APDL*, in which the GFRP material failure initiation and steel yielding were assessed with respectively, the Tsai-Wu failure criterion and the Von Mises criterion; however, the damage progression of the GFRP material was not considered. The bending moment *vs*. rotation behaviour predicted by the FE models presented a good agreement with test data, although the failure initiation (which occurred on the bonded interface) was overestimated.

The In-plane shear behaviour up to failure of lap joint bolted connections between GFRP multi-directional laminates has been object of a small number of numerical investigations with marginal success (*e.g*., [4.6], [4.7]). Those investigations generally employed very complex models, (i) typically considering several layers to simulate each members' plate, and (ii) generally applying unidirectional failure criteria, such as the Hashin failure criteria [4.8], not accounting for through-thickness delamination. Regardless of their precision, owing to the inherent complexity and fine mesh discretization needs, this type of models has high computational costs, rendering their use cumbersome for the design of full-scale structures in particular and for engineering practice in general. Furthermore, to the author's best knowledge, no models have been proposed to simulate cyclic damage on GFRP bolted connections.

Another limitation of the technical literature on GFRP bolted connections reviewed above is concerned with the fact that it focused only at a single level of analysis. In fact, a comprehensive study comprising (i) the assessment of the monotonic and cyclic behaviour of a connection system and also (ii) the evaluation of the monotonic and cyclic behaviour of full-scale frame structures using that connection system has not yet been reported.

The work presented in this chapter was developed in the scope of the ClickHouse project (*cf*. Chapter 3), which aimed at the development of a modular housing system to be used in emergency situations and to assist disaster zones. The ClickHouse structural system is a tri-dimensional frame comprising pultruded tubular GFRP profiles connected with internal steel auxiliary parts. The infill walls are materialized by sandwich panels, with two GFRP face skins and polyurethane core. This chapter presents experimental and numerical investigations about the cyclic behaviour of the beam-to-column sleeve connection system used in the ClickHouse frames. In this study, different connection series were tested under cyclic loads, pursuing a previous investigation on their monotonic behaviour (*cf*. Chapter 3). The results obtained at the connection level were then used to select the connection series employed in the GFRP frames, which were subjected to monotonic and cyclic quasi-static frame sway tests, presented in Chapter 9. Additionally, in order to evaluate the feasibility of analysing the cyclic behaviour of pultruded GFRP frame structures with relatively simple numerical models, which can be particularly useful when seismic design is required, the cyclic behaviour of the selected connection series was numerically investigated, using one-dimensional frame elements and spring-type connections, where the Pivot hysteresis model [4.9] was considered. The parameters used to model the connection's hysteretic behaviour were then used to model the 2D frame behaviour, as detailed in Chapter 9.

4.2. EXPERIMENTAL PROGRAMME

4.2.1. Material mechanical characterization tests

The experimental tests were performed using pultruded tubular GFRP profiles (120×120×10 mm^2) made of E-glass fibres and an isophthalic polyester resin matrix, produced by *ALTO, Perfis Pultrudidos, Lda*. The mechanical properties of the GFRP material, summarized in Table 4.1, were determined through coupon tests, namely regarding: (i) compressive strengths and elastic moduli in both longitudinal ($\sigma_{cu,L}$ and $E_{c,L}$) and transverse ($\sigma_{cu,T}$ and $E_{c,T}$) directions; (ii) longitudinal tensile strength ($\sigma_{tu,L}$), modulus of elasticity ($E_{t,L}$) and Poisson ratio (ν_{LT}); (iii) longitudinal flexural strength ($\sigma_{fu,L}$); (iv) interlaminar shear strength (τ_{is}); (v) in-plane shear strength (τ_{LT}); and distortional modulus (G_{LT}). Note that, owing to the reduced dimensions of the profile, it was not possible to extract tensile coupons for the transverse direction. The steel auxiliary parts were made with S235 grade steel and the steel bolts used were 8.8 class.

4.2.2. Beam-to-column connection system

The beam-to-column connection system used in the present experimental programme comprises metallic auxiliary parts that are positioned inside the GFRP tubes, which are then used to connect the beams to the columns through bolting, as depicted in Figure 4.1. This connection system was previously tested regarding its monotonic behaviour (*cf.* Chapter 3).

Table 4.1 - Main mechanical properties of the GFRP pultruded profiles (average ± standard deviation).

Test	Property	Average ± Std. deviation	Standard
Compression	$\sigma_{cu,L}$	435.1 ± 52.6 MPa	ASTM D 695-02 [4.10]
	$E_{c,L}$	21.2 ± 3.3 GPa	
	$\sigma_{cu,T}$	88.9 ± 16.3 MPa	
	$E_{c,T}$	4.8 ± 0.9 GPa	
Tension	$\sigma_{tu,L}$	293.8 ± 16.8 MPa	EN ISO 527-1 [4.11]
	$E_{t,L}$	32.7 ± 3.0 GPa	
	ν_{LT}	0.32 ± 0.0	
Flexure	$\sigma_{fu,L}$	415.1 ± 61.3 MPa	EN ISO 14125 [4.12]
Interlaminar shear	τ_{is}	30.6 ± 2.6 MPa	ASTM D 2344 [4.13]
In-plane shear	τ_{LT}	41.4 ± 6.2 MPa	ASTM D 5379 [4.14]
	τ_{TL}	58.7 ± 7.2 MPa	
10° off-axis tension	G_{LT}	3.2 ± 0.7 MPa	Hodgkinson [4.15]

Four different connection series were studied in order to select the one with better mechanical performance, in terms of initial stiffness, strength and corresponding failure mode(s), and pseudo-ductility. The connection series, presented in Figure 4.2, differed only in the position and number of bolts (M8, class 8.8) joining the beam profile to the beam auxiliary connection part.

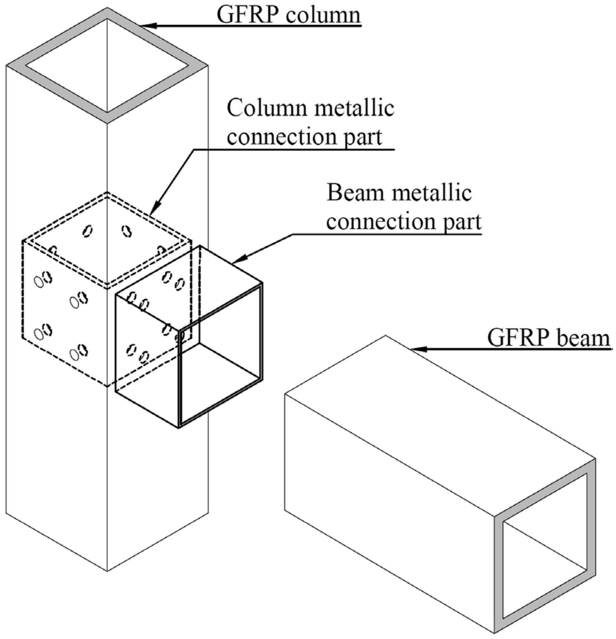

Figure 4.1 - Overall view of the proposed beam-to-column connection system.

The results of the monotonic tests on this connection system (described in detail in Chapter 3) showed that the addition of bolt rows (series F4) has a significant impact on the stiffness and ductility of the connection system, but does not increase the strength significantly. On the other hand, a larger bolt edge distance (series F2S) leads to significant strength and ductility increases, but does not improve the stiffness of the connection system.

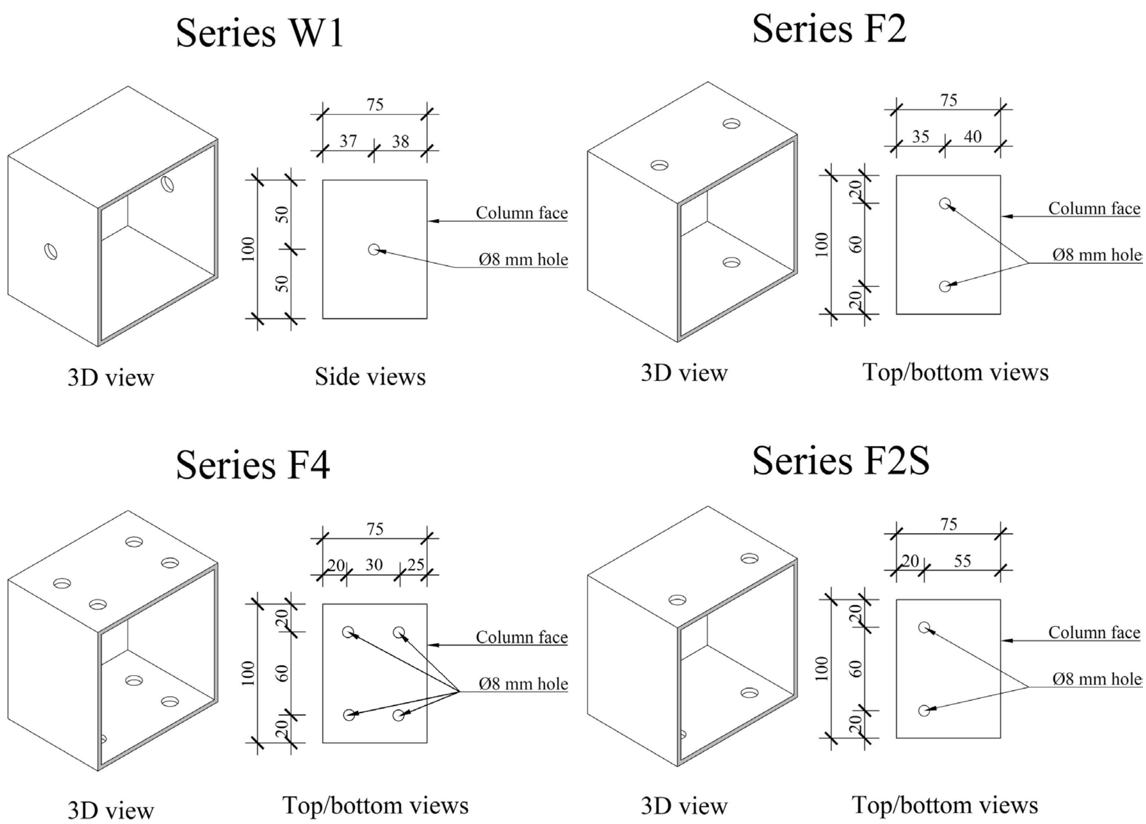

Figure 4.2 - Details of each series of the beam-to-column connection system.

4.2.3. Test setup and load protocol

The beam-to-column connection tests were performed on specimens comprising a 960 mm long beam and a 1080 mm long column, with the joints placed at mid-height of the column; the tests were conducted in a closed steel loading frame anchored to the laboratory strong floor, as depicted in Figure 4.3. The load was applied to the beam at a distance of 600 mm from the nearest face of the column flange (*cf*. Figure 4.3, point A) by an *Enerpac* hydraulic jack, with load capacities of 600 kN in compression and 250 kN in tension, and maximum stroke of ±125 mm. Two hinges were installed in-between the hydraulic jack and the specimens to guarantee the perpendicularity of the applied load. The load was measured by a *TML* load cell with capacity of 300 kN (*cf*. Figure 4.3, point B). Both column ends were fixed (rotations and displacements prevented) to the steel frame and the out-of-plane displacements of the beam were prevented with two aluminium cylindrical bars (*cf*. Figure 4.3, points C and D, respectively). The displacement of the beam at the load application point was measured with a *TML* string pot displacement transducer, while the rotations of the column (centre) and the beam (at 130 mm from the column face) were measured with two inclinometers, also from *TML*. The tests were performed by applying a vertical displacement to the beam, at a rate of 1.0 ± 0.5 mm/min, until failure or the stroke of the jack was reached, while the data was gathered with a datalogger (model *QuantumX MX840* from *HBM*) and stored in a PC at a rate of 5 Hz. The cyclic tests were conducted for all four series of the connection system (*cf*. Section 4.2.2), similarly to the monotonic tests (*cf*. Chapter 3). Three specimens were tested per series and the following nomenclature was adopted: W1-C2 corresponds to the specimen #2 of series W1.

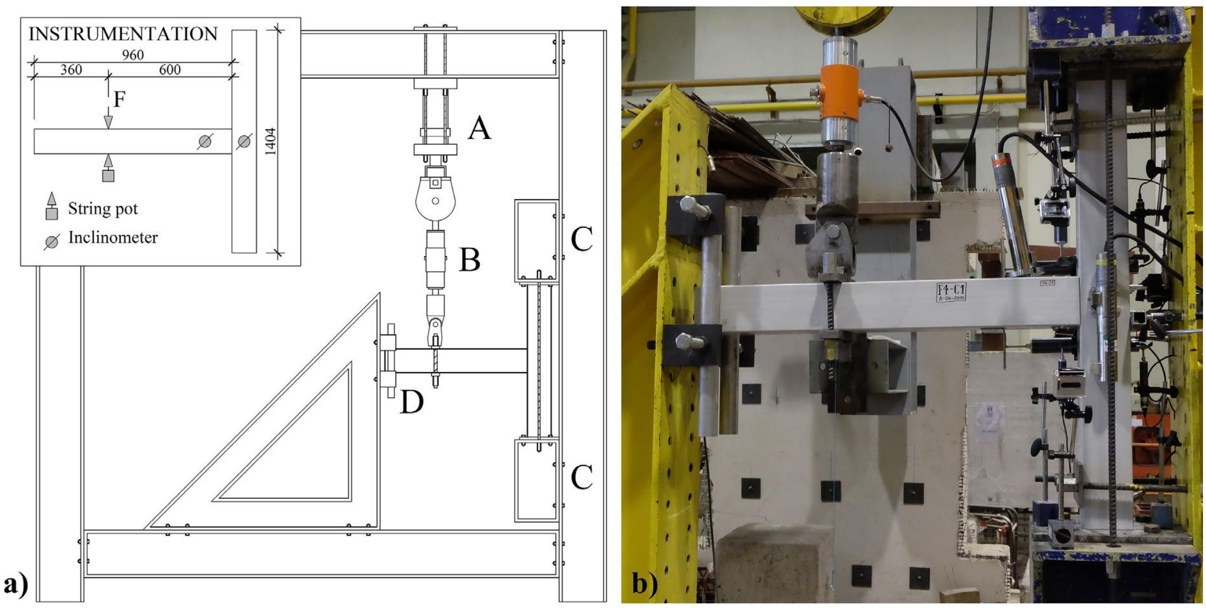

Figure 4.3 - Beam-to-column connection cyclic tests set-up.

In the absence of specific loading protocols for GFRP structures, the cyclic tests on beam-to-column connections were performed in accordance with ECCS' Recommended testing procedure for assessing the behaviour of structural steel elements under cyclic loads [4.16]. The complete test procedure recommended by ECCS [4.16] was adopted, and the displacement history was defined with the parameters obtained in the monotonic tests performed earlier (Chapter 3). Thereafter, the definition of the displacements of each test cycle is based on the displacement corresponding to the yield load (δ_y and F_y, respectively). Since, unlike steel materials, GFRP generally presents linear-elastic behaviour until failure, the "yield" displacements were defined by the limit of the elastic range (end of proportionality between load and displacement), attained in the corresponding monotonic tests. This choice (allowed by the ECCS recommendations [4.16]) was made taking into consideration the brittle behaviour of the GFRP, which resulted in abrupt load reductions after occurrence of significant damage in the connection. Table 4.2 presents the values of "yield" displacement (δ_y) and corresponding load (F_y), bending moment (M_y) and rotation (θ_y) of all series, which were derived from the monotonic tests (*cf.* Chapter 3).

Table 4.2 - "Yield" parameters of each connection typology (average ± standard deviation), from Chapter 3.

Series	F_y (kN)	δ_y (mm)	M_y (kN.m)	θ_y (rad)
W1	3.2 ± 1.1	23.2 ± 9.0	2.1 ± 0.7	0.042 ± 0.017
F2	3.6 ± 0.5	17.6 ± 5.5	2.3 ± 0.3	0.027 ± 0.009
F4	2.9 ± 0.7	11.3 ± 3.5	1.9 ± 0.5	0.017 ± 0.006
F2S	4.7 ± 0.6	24.0 ± 5.0	3.1 ± 0.4	0.040 ± 0.009
Average	–	19.0	–	0.03
Std. Dev.	–	6.3	–	0.01 ± 53

Thereafter, in order to define the loading protocol, it was decided to consider the same "yield" displacement for all series (δ_y=19 mm, the average of all series, *cf.* Table 4.2), as it allowed an easier and more consistent comparison between the different connection series. The resulting displacement history adopted for the beam-to-column connection cyclic tests includes the following cycles (*cf.* Figure 4.4): (i) within the elastic range, one cycle at ¼, ½, ¾ and 1 times the "yield" displacement; and (ii) after "yield", two cycles up to 2*n* of the "yield" displacement, where *n* is an integer, up to failure or until the maximum stroke of the hydraulic jack used (±125 mm) was reached. The ECCS protocol [4.16] recommends three repetitions of the displacements above the yield point. However, since previous studies (*e.g.*, [4.17]) have shown that the third cycle with the same displacement is often redundant, only one repetition was performed.

4.3. EXPERIMENTAL RESULTS AND DISCUSSION

4.3.1. Results

This section presents the experimental results of the beam-to-column connection cyclic tests, regarding (i) the overall moment *vs*. rotation behaviour, (ii) the cyclic performance, and (iii) the failure modes.

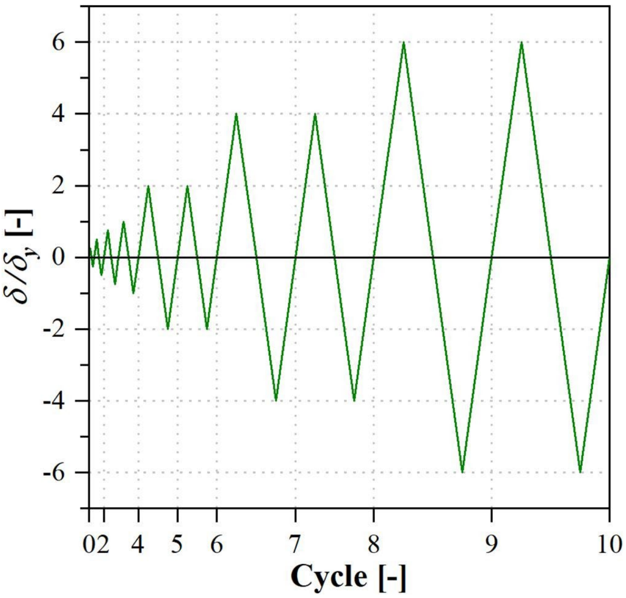

Figure 4.4 - Displacement history of the beam-to-column connection cyclic tests.

4.3.1.1. Overall moment vs. Rotation behaviour

Figure 4.5 presents the bending moment *vs*. rotation curves measured in the cyclic tests for a representative specimen of each series. The results obtained prompt the following main comments: (i) for all configurations, the hysteretic curves presented reasonable symmetry in the early stages of the tests; (ii) in general, series F2S presented higher loads at the end of each cycle compared to the remaining connection series; (iii) for the different specimens from each series, after the development of substantial damage, the connections' behaviour differed significantly depending on the loading direction (this being more evident in connections from series W1); (iv) pinching effect was observed for all configurations, as none of the hysteretic curves presented stiffness in quadrants II and IV (*cf*. Figure 4.5).

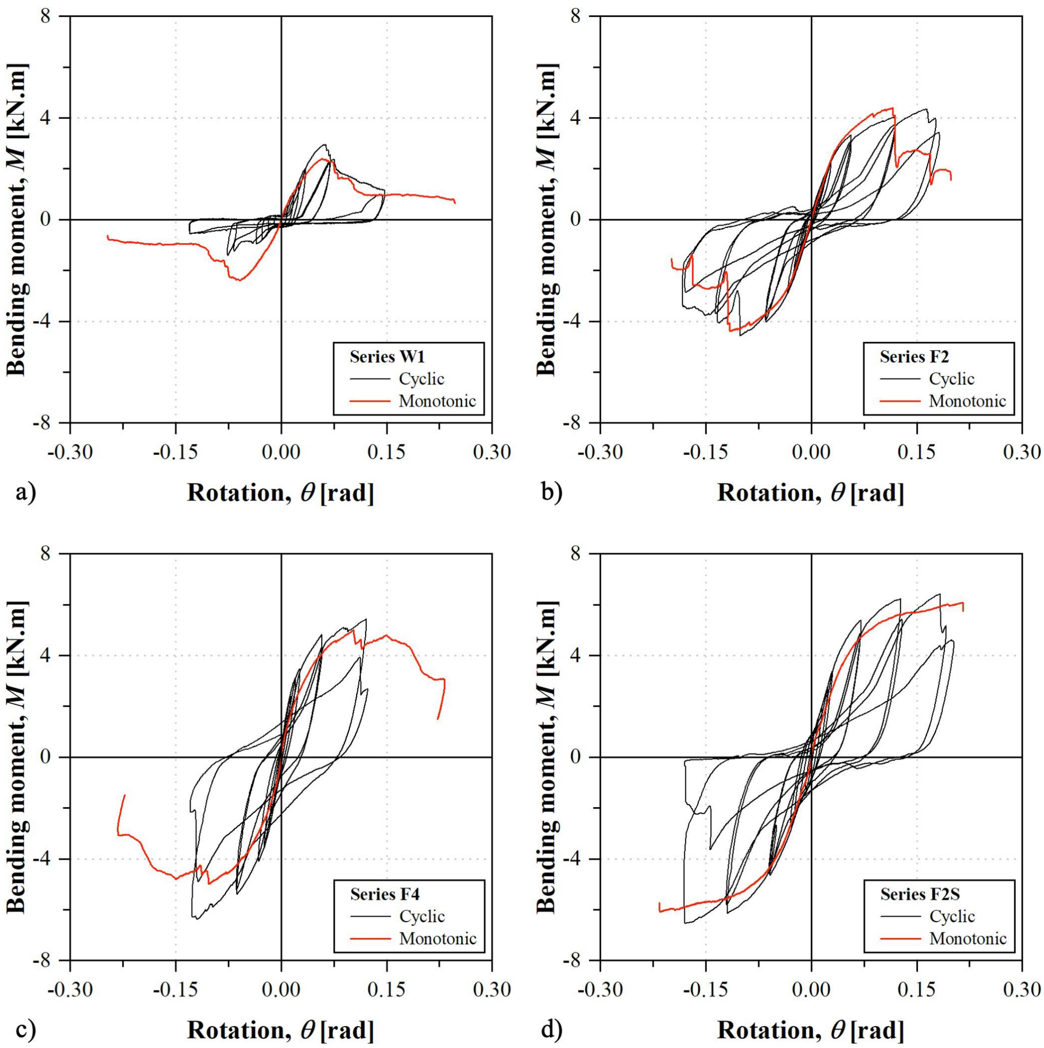

Figure 4.5 – Representative cyclic moment *vs.* rotation behaviour of each beam-to-column connection series: a) series W1; b) series F2; c) series F4; d) series F2S.

4.3.1.2. Cyclic performance

The cyclic performance of each series was evaluated regarding their stiffness, strength and dissipated energy, according to the formulations proposed in the ECCS [4.16].

The stiffness ratio was defined, at each cycle, and for each loading direction, by the quotient between (i) the slope of the bending moment *vs*. rotation curves (*cf.* Figure 4.5) when the bending moment signal inverts, and (ii) the initial stiffness, as measured in the monotonic tests (*cf.* Chapter 3). Figure 4.6 presents the stiffness ratio evolution per cycle for all specimens from the 4th cycle ("yield" cycle), together with the numerical results for series F2S, to be presented and discussed in Section 4. It can be seen that the stiffness of all connections decreased gradually due to the damage progression, which increased the pinching effect, responsible for the reduction of the tangent of the plots at the horizontal axis intersection. Series F2S presented the highest residual stiffness after 8 cycles, with average stiffness ratio of 0.18, while series W1 registered the highest (relative) loss of stiffness, presenting almost no residual stiffness, with an average stiffness ratio of 0.03 at the 8th cycle. Series F4 and F2 presented intermediate average stiffness ratios after 8 cycles of 0.09 and 0.07, respectively. Additionally, the stiffness differences in the positive and negative rotations are often easy to identify in the moment-rotation curves, more visibly for series W1, showing that part of the damage that occurs when positive rotations are imposed is not recoverable; this observation is consistent with the occurrence of brittle failure modes.

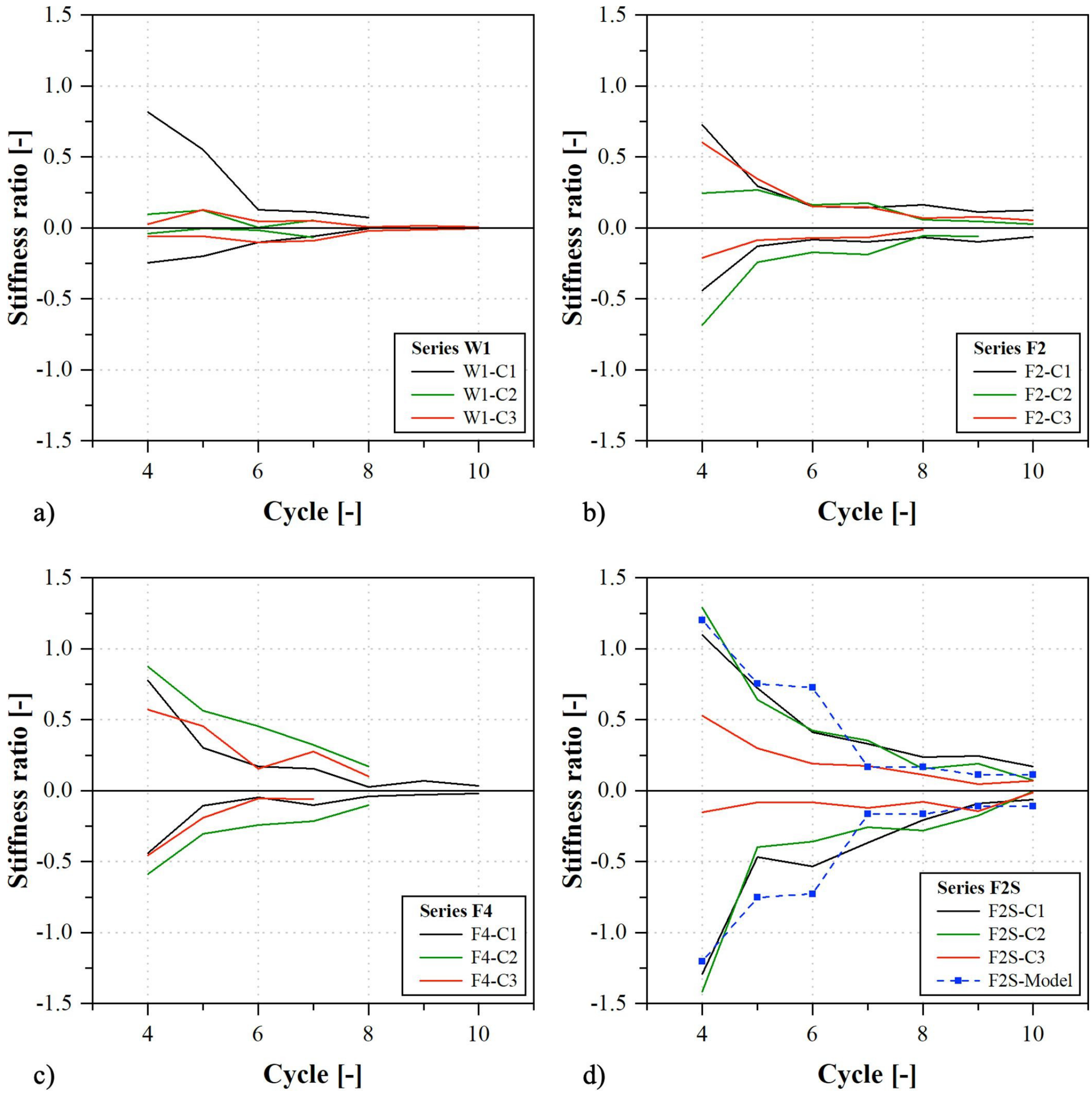

Figure 4.6 - Stiffness ratio evolution of each beam-to-column connection series: a) series W1; b) series F2; c) series F4; d) series F2S.

The strength progression was evaluated considering the bending moment at the two points of maximum and minimum displacement at each cycle, as suggested by ECCS [4.16]. Figure 4.7 presents, for each configuration, the evolution of the maximum bending moment with the cycles, starting on the 4th cycle ("yield" cycle), with the identification of the value of the "yield" bending moment (M_y) attained in the monotonic tests (*cf.* Table 4.2 – black dot line), together with the numerical results for series F2S, to be discussed in Section 4.

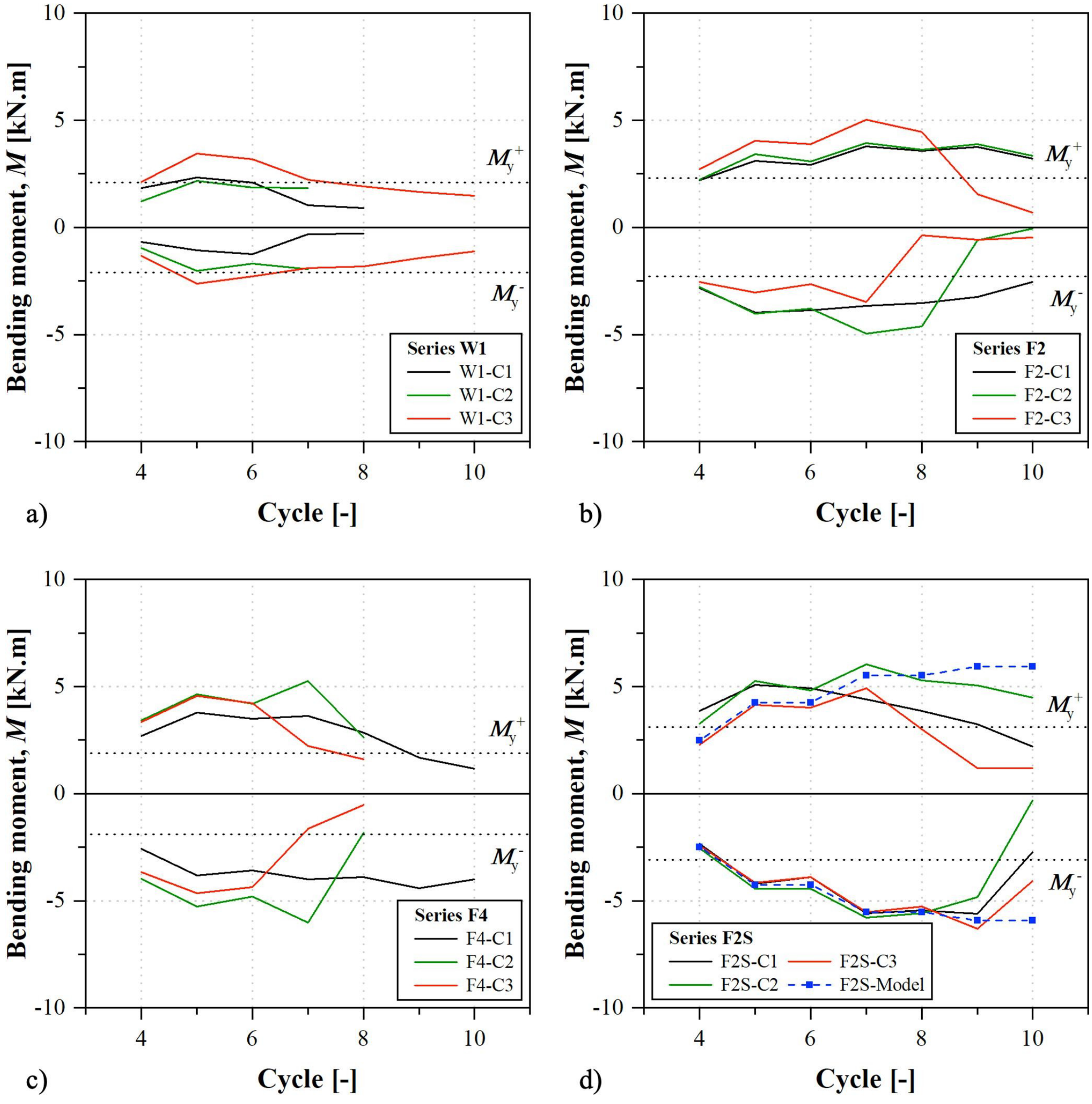

Figure 4.7 - Strength evolution of each beam-to-column connection series: a) series W1; b) series F2; c) series F4; d) series F2S.

Since the cycles were all defined taking into account an average δ_y (*cf.* Section 4.2.3), the bending moment at the 4th cycle often differed from the bending moment corresponding to the "yield" of each connection. For instance, specimens of series F2 registered bending moments at the end of 4th cycle closer to M_y than those of the remaining series, as the "yield" displacement of the referred connection series is closer to the average δ_y considered in the cycles compared to that of the remaining series. On the other hand, for all series except W1, the strength of the subsequent cycles surpassed M_y; this is possibly due to the (more) brittle failure mode observed in this series, for both monotonic (*cf.* Chapter 3) and cyclic tests (*cf.* Section 4.3.1.3), which occurred at the end of the linear range of the moment *vs.* rotation curve, being followed by steep load reductions. Therefore, the strength of this connection series was practically limited to its "yielding" point. Conversely, for series F2 and F2S the maximum bending moment registered was often higher than 1.5 times M_y, and specimens of series F4 could reach bending moments almost 3 times higher than M_y, reflecting the lower brittleness of these series. Similar differences were observed in the monotonic tests (*cf.* Chapter 3). From the analysis of the strength curves (*cf.* Figure 4.7), it can be seen that series F2S maintained a high percentage of its strength along the cycles for both positive and negative displacements, while most specimens from series W1 and F4 had already lost their structural integrity by the 8th cycle.

In order to evaluate the energy dissipation capacity of each connection series, one estimated the dissipated energy ratio, which compares the energy dissipated by the connection with the energy dissipated by a connection with perfect elasto-plastic behavior (and the same "yield" bending moment). The energy dissipation ratio (η) was estimated in accordance to ECCS [4.16] as follows,

$$\eta_i = \frac{W_i}{\Delta M_y(\Delta\theta_i + \Delta\theta_y)} \tag{4.1}$$

where W_i is the energy dissipated in cycle i (measured by the area delimited by the loop of the moment *vs.* rotation curves, *cf.* Figure 4.5), ΔM_y is the difference between the positive and negative "yield" bending moments, $\Delta\theta_i$ is the range of the imposed rotations in cycle i, and $\Delta\theta_y$ is the range of the "yield" rotations. The evolution of the estimated energy dissipation ratio (η) is presented in Figure 4.8 for the different series, starting in the first cycle after "yield" (5th cycle); for series F2S experimental data is plotted together with numerical results, to be discussed in Section 4.4. For all series, it can be seen that for the same imposed displacement, the second cycle presents lower dissipated energy than the first one. This is due to the fact that damage occurred/progressed in the first cycle, resulting in a lower stiffness (and, in some cases, load) in the second cycle. Series F2 and F2S presented similar η ratios, while series F4 presented the highest ratios – owing to the fact that the M_y of this connection was considerably lower than the maximum bending moment it could sustain. Series W1 presented the lowest dissipated energy ratios and also the sharpest decrease of this parameter. Finally, it is worth referring that for all series the connection system presents a lower energy dissipation capacity than a perfectly elasto-plastic connection; this stems from the several brittle failure modes that occur throughout the cyclic tests (*cf.* Section 4.3.1.3).

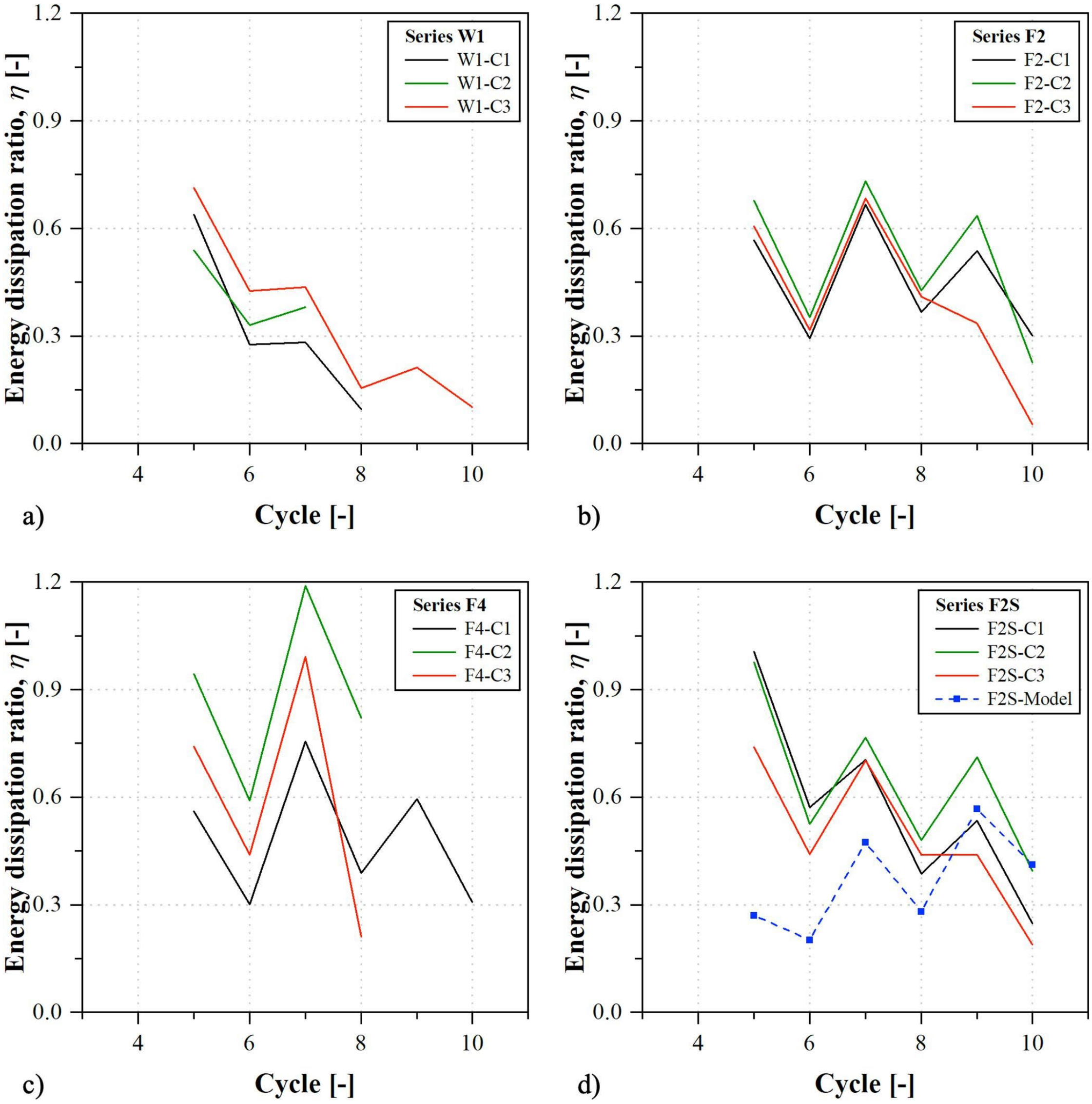

Figure 4.8 - Energy dissipation ratio of each beam-to-column connection series: a) series W1; b) series F2; c) series F4; d) series F2S.

The cyclic performance of the different series was also assessed by means of the accumulated dissipated energy. Figure 4.9 shows the evolution of the average accumulated dissipated energy per cycle for all series (for series F2S, the numerical predictions are also plotted, to be discussed in Section 4.4). In this regard, series F2S clearly outperformed the remaining series – the final average accumulated energy of series F2S was 48%, 39% and 174% higher than those of series F2, F4 and W1, respectively, reflecting its higher capacity to endure inelastic deformations.

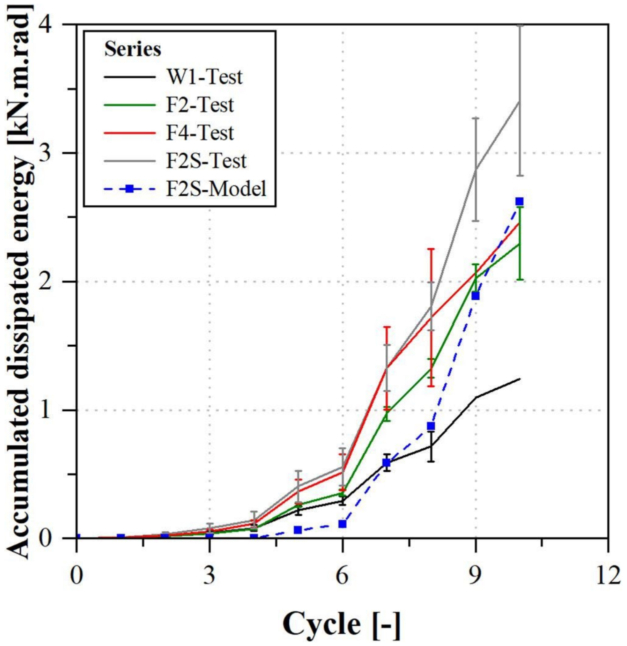

Figure 4.9 - Accumulated dissipated energy of each beam-to-column connection series.

4.3.1.3. Failure modes

As expected, most of the failure modes and damage observed in the beam-to-column connection cyclic tests were similar to those reported in the monotonic tests (*cf.* Chapter 3), namely: (i) specimens of series W1 failed first by tensile rupture of the web-flange junctions of the GFRP beam (Figure 4.10a), followed by shear-out of the bolts (Figure 4.10a) that led to significant strength loss of the connections; (ii) the same failure modes were observed on specimens of series F2 and F4, although with lower strength reductions, followed by failure of the weld fillet of the beam steel part (Figure 4.10b) or by failure of the M10 bolts connecting the two auxiliary steel parts (Figure 4.10c); (iii) specimens of series F2S presented bearing of the GFRP material near the bolts (Figure 4.10d), fracture in the beam web-flange junction, shear-out failure of the beam's bolts and, in one of the specimens, shear failure of the beam's bolts (Figure 4.10e) – this series was able to maintain higher residual strength than the others (*cf.* Figure 4.5) and the shear-out failure only occurred on the final 2/3 cycles. It should be noted that, all specimens from series F2S presented brittle failure modes during the cyclic tests contrary to what was registered in the monotonic tests (Chapter 3). Additionally, for all specimens with beam flange bolts, the cracking of the GFRP column along the bolts' alignment was observed (Figure 4.10f).

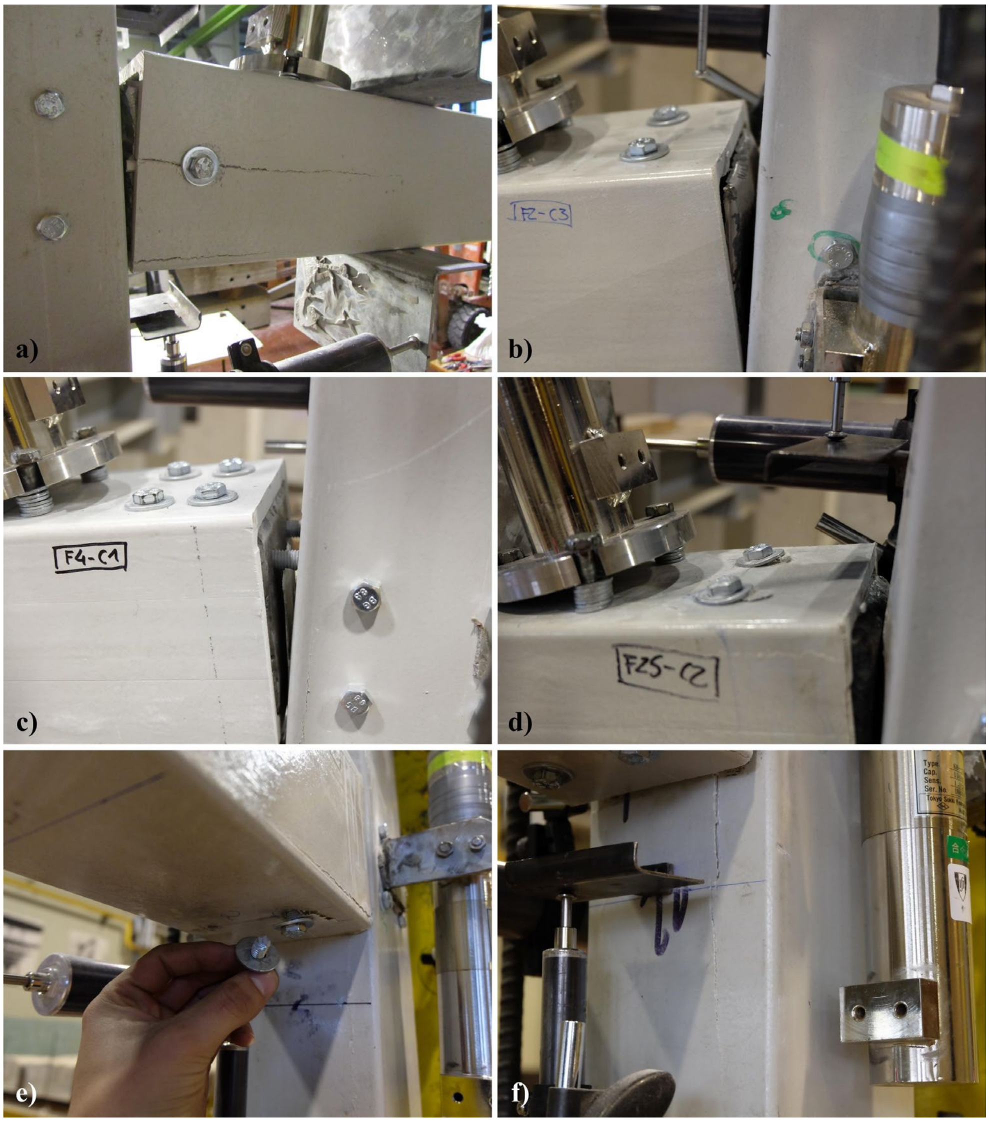

Figure 4.10 - Failure modes: a) web-flange junction and shear-out failure, specimen W-C1; b) weld failure, specimen F2-C3; c) bolt tensile failure, specimen F4-C1; d) bearing, specimen F2S-C2; e) bolt shear failure, specimen F2S-C2; and f) cracking on the column, specimen F2S-C1.

Moreover, yielding at the beam steel connection part was also observed in all the specimens tested. The accumulation and propagation of damage in these failure modes led to an increase of the distance between the beams' edge and the columns' face as the tests progressed.

4.3.2. Discussion

From the analysis of the experimental results presented above, it is clear that series W1 presented the worst overall performance, proving to be more susceptible to brittle failure modes. In this series, the bolts are positioned in the centre of beams' webs which is the point of the cross-section with null normal stress but the highest shear stress. The maximum longitudinal shear flow at the mid height of the webs led to the failure mode shown in Figure 4.10a. In fact, having fewer bolts, this series is also less able to redistribute stresses when the initial damage occurs. It should be mentioned that series W1 also presented the poorest performance in the monotonic tests, providing the lowest strength and stiffness (*cf.* Chapter 3). These results, in addition to the low residual strength, resulted in a lower energy dissipation capacity when compared to the other series.

On the other hand, the connection series with bolts in the beam's flanges displayed an improved performance. The results obtained show that these series are able to sustain higher loads, and have higher stiffness and residual strength compared to series W1.

The results of the monotonic tests (*cf.* Chapter 3) had already showed that in series F4, the addition of another bolt row did not translate into a significant increase of the connection strength when compared with that of series F2, but had a noticeable (positive) effect in the stiffness. However, the increased stiffness led to the occurrence of significant damage for lower imposed deformations. Overall, no significant increase in the accumulated dissipated energy of series F4 was observed when compared to that of series F2 (+7%).

Similarly to what was observed in the monotonic tests (*cf.* Chapter 3), the higher edge distance used in series F2S delayed the occurrence of shear-out, relocating the initial damage to other elements, like the column and the steel connection parts. This resulted in higher ductility indexes and an increased accumulated dissipated energy compared to series F2. Overall, series F2S presented the best performance both in the monotonic (*cf.* Chapter 3) and cyclic tests.

4.4. NUMERICAL ANALYSIS

4.4.1. Model description

In order to evaluate the feasibility of analyzing the cyclic behaviour of pultruded GFRP frame structures with relatively simple numerical models, which can be particularly useful when seismic design is required, the author have developed a finite element (FE) model based on one-dimensional frame elements and spring-type connections, using SAP2000 commercial package [4.18]. The model aimed at simulating the experimental behaviour of connection series F2S which was selected for the frame tests presented Chapter 9.

Figure 4.11 shows an overview of the FE model, comprising one dimensional frame elements and a 2-link joint element. The column element was modelled with its real length (1080 mm), while the beam was modelled from the contact point with the column to the load application point, with a total length of 600 mm.

In these models, the GFRP was modelled as an orthotropic material with linear-elastic behaviour. This is a reasonable assumption since the failure modes observed in the experimental tests were, essentially, concentrated in the joints and were accounted for in their properties, as discussed below. The average values of the GFRP material properties obtained in the coupon tests (*cf*. Table 4.1) were used as input, namely the elastic modulus in tension in the longitudinal direction ($E_{t,L}$, considered for the main (11) direction) and the elastic modulus in compression in the transverse direction ($E_{c,T}$, taken for the transverse (22) and through-thickness (33) directions), since for the transverse direction the tensile elastic modulus could not be determined (*cf*. Section 4.2.1). The longitudinal-to-transverse Poisson coefficient in tension (υ_{LT}) was used for the main-to-transverse direction (12) and the in-plane distortional modulus (G_{LT}) was used for that same direction. In the absence of further experimental data, the author considered those same values for the Poisson coefficient and distortional moduli for directions 13 and 23.

The (beam-to-column) connections between the GFRP elements were modelled as non-linear 2-joint links (MultiLinear Plastic). All directions were considered fixed with the exception of the rotations around the out-of-plane axis (R3), for which the monotonic moment *vs*. rotation curves of the experimental tests were used as input (*cf*. Chapter 3). The hysteretic behaviour of the joints was defined with the Pivot hysteresis model [4.9], described below, based on those monotonic moment *vs*. rotation curves.

Both column ends were fixed and a vertical deflection was applied to the beam at a distance of 660 mm from the column's midline, according to the experimental displacement history (*cf*. Figure 4.4), namely the deformation cycles at the tip of the cantilever beam. A geometrically linear direct integration time-history analysis was performed. In this in-plane analysis, no mass was attributed to the models in order to avoid dynamic effects.

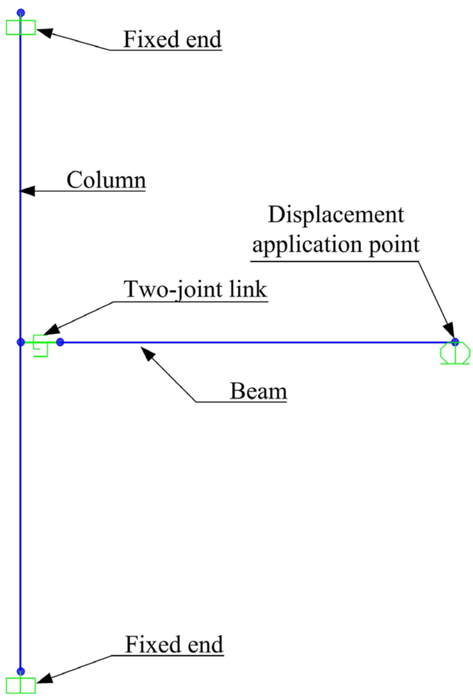

Figure 4.11 - FE model, including the identification of all elements, boundary conditions and displacement application point.

The Pivot hysteresis model [4.9], developed for reinforced concrete members, allows for a relatively simple definition of different hysteretic behaviours, accounting for unsymmetrical responses and pinching effect. This model requires a monotonic bending moment *vs*. rotation (or load *vs*. displacement) curve as input, as illustrated by the blue curve in Figure 4.12. The monotonic curve is used to define the initial stiffness and the outer boundaries of the hysteretic curve. It is necessary to define four quadrants (Q_1–Q_4), since different rules apply for the loading and unloading paths of the hysteretic curves in each quadrant. These quadrants, illustrated in Figure 4.12, are defined by the horizontal axis and the elastic loading lines. Thereafter, it is necessary to define four main pivot points, P_1 to P_4, based on the yielding moment/force and the initial stiffness, as described ahead, which control the softening, *i.e.* the unloading paths in quadrants Q_1–Q_4, respectively. Additionally, two pinching Pivot points are required, PP_2 and PP_4, also a function of the yielding moment/force and the initial stiffness, as described ahead, which determine the degree of pinching after load reversal. It should be mentioned that as strength degradation progresses, according to the monotonic strength envelope, these pinching points move towards the origin. The loading and unloading rules in each quadrant are summarized in the Appendix A.

Regarding the quantification of the pivot points, the magnitude of P_1 and P_2 on the load/moment axis is defined by multiplying a factor (α_1) by minus the positive yield force or moment ($-F_{y1}$ or $-M_{y1}$). P_1 and P_2 are then marked over the positive and negative elastic load lines, respectively, as illustrated in Figure 4.12a. On the other hand, the magnitude of pivot points P_3 and P_4 is defined by multiplying a factor (α_2) by the absolute value of the negative yield force or moment (F_{y2} or M_{y2}); the points are then marked on the negative and positive elastic lines, respectively (*cf.* Figure 4.12a). It should be mentioned that, given this definition, the unloading paths in quadrants Q_1 and Q_3 tend to be parallel to the positive and negative elastic lines, respectively, as parameters α increase.

Pinching pivot points PP_2 and PP_4 are located in the positive and negative elastic load lines, respectively. Their initial magnitude, in the load/moment axis, is defined by multiplying a factor (β_2 and β_1, respectively) by the negative and positive yield force or moment (F_{y2} or M_{y2} and F_{y1} or M_{y1}, respectively), as shown in Figure 4.12a. These multiplying factors are limited between 0 and 1. As mentioned earlier, the pinching pivot points move towards the origin after strength degradation has occurred, with their magnitude being corrected by adjusting the multiplying factors according to Eq. (4.2),

$$\beta_i^* = \begin{cases} \beta_i, & d \leq d_{F_{max}} \\ \dfrac{F}{F_{max}}\beta_i, & d > d_{F_{max}} \end{cases} \tag{4.1}$$

where, β_i^* is the adjusted positive or negative (i = 1 or 2, respectively) pinching pivot multiplying factor, d and F represent the maximum corresponding (positive or negative) displacement/rotation and load/moment, respectively, of the cycle, F_{max} is the maximum load/moment of the monotonic strength envelope and $d_{F_{max}}$ is its corresponding displacement/rotation. Note that, for the sake of clarity, these new pinching pivot points are marked as PP_2', PP_4' and PP_4' in Figures 4.12c and 4.12d, where the upper ticks mark the number of the reduction, *i.e.*, in this case, first or second.

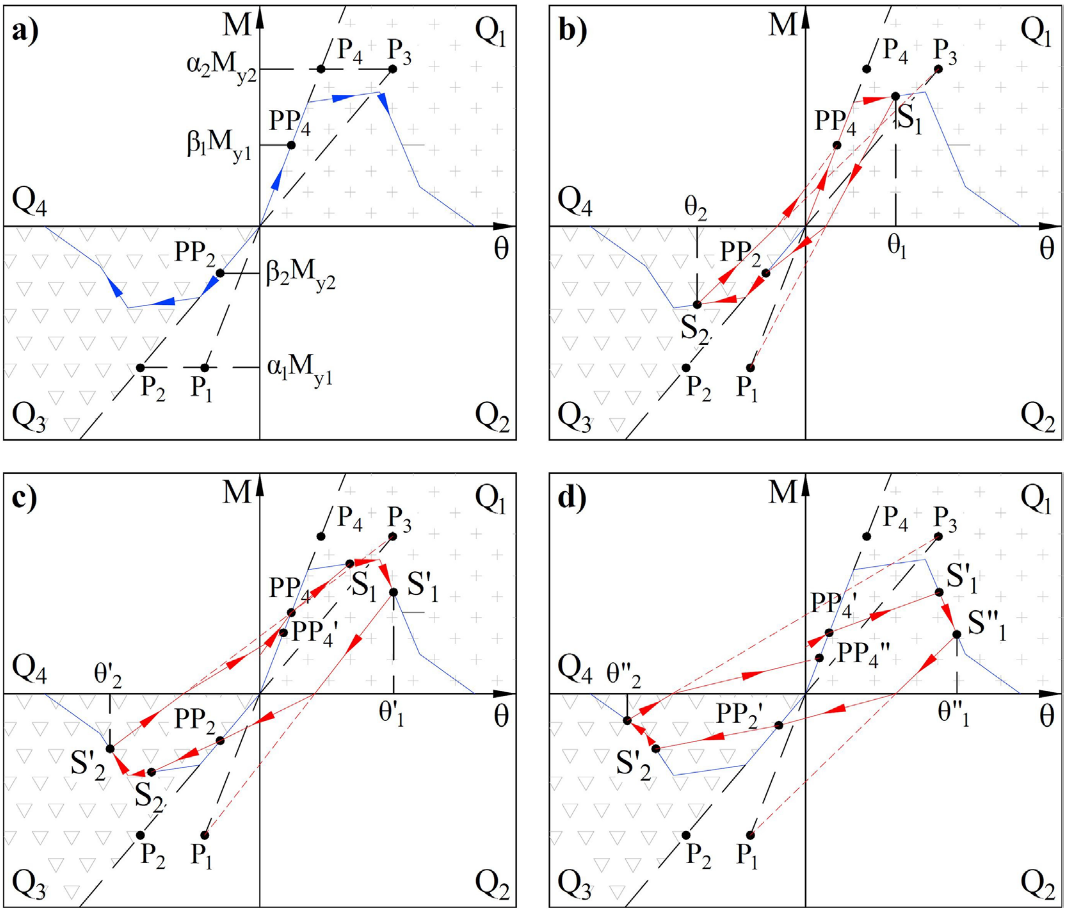

Figure 4.12 - Pivot hysteresis model, including monotonic base curve (blue), hysteretic path (red) and quadrant definition: a) monotonic (input) curve (adapted from [4.9]); b) first cycle; c) second cycle; and d) third cycle.

The main objective of the beam-to-column test models was to calibrate the parameters of the Pivot hysteresis model [4.9], in particular parameters α_1, α_2, β_1 and β_2, which will then be used in the models of the frame tests, presented in Chapter 9. Therefore, as mentioned earlier, this study focused only on the connection series F2S (*cf.* Figure 4.2), which was the only one used in the frame tests (*cf.* Chapter 9). As mentioned, the model developed (*cf.* Figure 4.11) comprised two frames representing the column and the beam. Since the connection presents symmetric conditions, *i.e.* the length of the column is the same above and below the connection, the moment *vs*. rotation curves obtained from the monotonic experimental tests (*cf*. Chapter 3) were used as input for both positive and negative rotations, as depicted in Figure 4.13. The parameters that define the Pivot hysteresis model were calibrated based on the comparison between numerical and experimental cyclic moment *vs*. rotation curves, in particular those of specimen F2S-C2, deemed as representative of this series. In this regard, it should be mentioned that owing to the high scatter obtained in the experimental tests, both from specimen to specimen and from cycle to cycle within the same specimen, the clear quantification of parameters β_i was not always straightforward. It should be mentioned that, within the first 6 cycles, these parameters range from 0.01 to 0.34. On the other hand, for the particular experimental specimen used to compare the hysteretic loops (F2S-C2), the positive and negative parameters (β_1 and β_2) average 0.24 ± 0.07 and 0.28 ± 0.06, respectively, considering cycles 3 to 6, i.e. disregarding the two initial cycles where some adjustments of the experimental setup are expected, while guaranteeing that the evaluation is made within a deformation range where no strength degradation occurs. On the other hand, the α_i parameters seemed to present a threshold at 100, from which the unloading path was practically parallel to the initial stiffness.

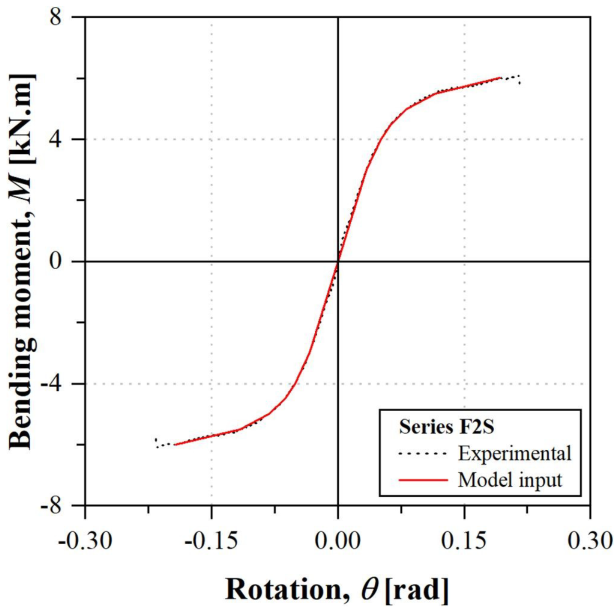

Figure 4.13 - Monotonic moment *vs*. rotation curves of series F2S, used has input in the FE models.

Based on the calibration procedure described above, and taking into account that no asymmetry is obvious from the analysis of the experimental hysteretic curves, the Pivot hysteresis model parameters were defined as symmetric. Moreover, parameters α_1 and α_2 were defined as 100 in order to obtain unloading paths (quadrants Q_1 and Q_3) as parallel to the elastic load lines as possible. On the other hand, parameters β_1 and β_2 were defined as 0.25, within the average range observed experimentally (0.24–0.28), as mentioned earlier.

4.4.2. Numerical results

Figure 4.14 compares the numerical and experimental moment *vs*. rotation hysteresis curves. It can be seen that the numerical results show an overall good agreement with their experimental counterparts in terms of moment *vs*. rotation behaviour, with the main differences resulting from the experimental scatter and/or from limitations of the Pivot hysteresis model, namely through the imposition of a maximum slope of the unloading path equal to the initial stiffness in the Q_1 and Q_3 quadrants (*cf*. Section 4.4.1). In particular, the comparison of the curves shows that the model underestimates the stiffness (−26%) of the initial cycles; as mentioned earlier, this is mainly due to the fact that the model follows the experimental monotonic curve (*cf*. Figure 4.14), which presented lower stiffness than its cyclic counterpart (−32%). The maximum bending moment estimated by the model was also slightly underestimated (−8.4%), since the monotonic curve (considered by the model) also presents lower strength that its cyclic counterpart.

In terms of stiffness ratio, Figure 4.6d shows that the results obtained from the FE model followed the main trends observed experimentally, namely presenting a progressive reduction up to the 7th cycle, after which it maintained a stable residual stiffness ratio, with a relative difference of 8% in comparison with the experimental results at the 8th cycle.

In terms of strength progression, Figure 4.7d shows that the FE model was also well able to reproduce the results obtained in the tests up to the final two cycles, namely the increase of the bending moment in the 1st cycle of increasing displacement followed by a stabilization in the subsequent cycles of that same displacement. In the last two cycles, the numerical results diverge considerably from the experimental ones and this increased relative difference is attributed to the extended GFRP damage (not considered in the model) that occurs for these higher displacements. Moreover, it should be noted that the experimental monotonic moment *vs*. rotation curve used as input for the model was derived from a specimen that did not collapse (in the monotonic tests, only one of three specimens of series F2S collapsed before the maximum stroke of the hydraulic jack was reached; *cf.* Chapter 3); therefore, the experimental curve does not include bending moment reductions.

Regarding the dissipated energy, Figure 4.9d (dissipated energy ratio) and Figure 4.10d (accumulated dissipated energy) show that numerical results present similar shapes to experimental data, although underestimating the energy absorbed in the tests. This can be explained by two main factors: on one hand, unlike the experimental specimens, which have gaps and settlements, the FE model does not dissipate any energy up to "yield" (4^{th} cycle, *cf.* Figure 4.10d); on the other hand, and more importantly, the stiffness of the monotonic moment *vs*. rotation curve used as input presents lower stiffness than that observed in the cyclic tests (−32%, as mentioned earlier). Therefore, for the same imposed rotation the FE model presents lower bending moments, resulting in a lower area of the bending moment *vs*. rotation plot (energy). Conversely, on the last two cycles, particularly on the last one, the FE model presents higher absorbed energy when compared to the experimental specimens, because, as mentioned earlier, the input monotonic moment *vs*. rotation curve does not have any strength losses, which were observed in the cyclic tests. Nevertheless, after 10 cycles the relative difference between numerical and experimental values of average accumulated dissipated energy was only −23%.

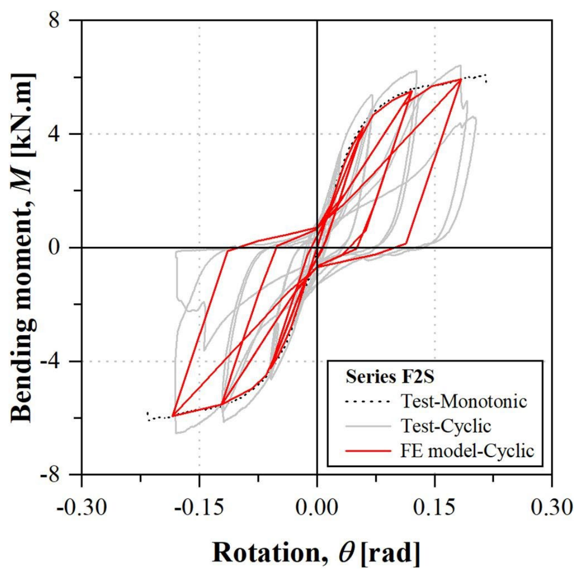

Figure 4.14 - Cyclic moment *vs*. rotation curves of series F2S: experimental and numerical results.

Overall, the results obtained point out the feasibility of using the Pivot hysteresis model to provide reasonably reliable (and conservative) predictions of the behaviour of this type of GFRP beam-to-column connections.

4.5. CONCLUSIONS

This chapter presented an experimental and numerical study about the cyclic behaviour of a GFRP beam-to-column sleeve connection system. Four different series of the same connection system were now tested under cyclic loads. In order to identify the best bolt distribution, the number and position of the bolts used to connect the GFRP beam to the internal steel auxiliary part were varied.

The connection with bolts on the beams' webs (series W1) presented the worst overall cyclic performance, with the lowest strength and energy dissipation capacity. On the other hand, the addition of more than one row of bolts in the beams' flanges (series F4 *vs*. series F2) did not improve the cyclic performance, with both series presenting similar strength and accumulated dissipated energy. Conversely, increasing the beams' flanges bolts edge distance (series F2S) shifted the failure mode from shear-out, which is brittle, to bearing, thereafter resulting in a significant improvement of the performance of the connection system under cyclic loads. In fact, when compared to series F2, the strength increased 18% and the accumulated dissipated energy after 10 cycles increased 48%. Overall, series F2S, which had presented the best performance in the monotonic tests performed earlier (*cf.* Chapter 3), presented the best performance under cyclic loading. Therefore, series F2S was selected as the connection system to be used in the full-scale frame sway tests presented in Chapter 9.

Alongside the experiments, a numerical investigation of the behaviour of series F2S was also performed. The main objective was to assess the feasibility of modelling the complex cyclic behaviour of this GFRP beam-to-column connection system with relatively simple and design-oriented FE models comprising frame elements and spring joints, namely using the Pivot hysteresis model [4.9] to simulate the hysteretic behaviour of the joints. The results obtained show that such models are able to simulate the experimental behaviour with reasonable accuracy, providing conservative predictions of their response. The parameters of the Pivot hysteresis model calibrated for the beam-to-column connections under cyclic loading are used in Chapter 9 to model the frame sway tests.

4.6. REFERENCES

[4.1] Bruneau M, Walker D. (1994). Cyclic testing of pultruded fiber-reinforced plastic beam-column rigid connection. *Journal of Structural Engineering*, 120(9), 2637-2652.

[4.2] Mosallam AS. (1997). Design considerations for pultruded composite beam-to-column connections subjected to cyclic and sustained loading conditions. *Marketing Technical Regulatory Sessions of The Composites Institutes International Composites Expo*, 14-B.

[4.3] Carrion JE, LaFave JM, Hjelmstad KD. (2005). Experimental behavior of monolithic composite cuff connections for fiber reinforced plastic box sections. *Composite structures*, 67(3), 333-345.

[4.4] Zhang Z, Bai Y, He X, Jin L, Zhu L. (2018). Cyclic performance of bonded sleeve beam-column connections for FRP tubular sections. *Composites Part B: Engineering*, 142, 171-182.

[4.5] AISC 341 (2016) – Seismic Provisions for Structural Steel Buildings. American Institute of Steel Construction, Chicago.

[4.6] Coelho AMG, Mottram JT. (2015). A review of the behaviour and analysis of bolted connections and joints in pultruded fibre reinforced polymers. *Materials & Design*, 74, 86-107.

[4.7] Warren KC, Lopez-Anido RA, Vel SS, Bayraktar HH. (2016). Progressive failure analysis of three-dimensional woven carbon composites in single-bolt, double-shear bearing. *Composites Part B: Engineering*, 84, 266-276.

[4.8] Hashin Z. (1980). Failure Criteria for Unidirectional Fiber Composites. *Journal of Applied Mechanics*, 47(2), 329–334

[4.9] Dowell OK, Seible F, Wilson EL. (1998). Pivot hysteresis model for reinforced concrete members. *ACI structural journal*, 95, 607-617.

[4.10] ASTM D 695-02 (2006) – Standard Test Method for Compressive Properties of Rigid Plastics. West Conshohocken.

[4.11] EN ISO 527-1 (1997) Plastics – Determination of Tensile Properties – Part 1: General Principles. Brussels.

[4.12] EN ISO 14125 (1998) – Fibre-reinforced plastic composites: Determination of Flexural Properties. Brussels.

[4.13] ASTM D 2344/D 2344M-00 (2006) – Standard Test Method for Short-Beam Strength of Polymer Matrix Composite Materials and Their Laminates. West Conshohocken.

[4.14] ASTM D 5379/D 5379M (2005) – Standard Test Method for Shear Properties of Composite Materials by the V-Notched Beam Method. West Conshohocken.

[4.15] Hodgkinson JM. (2000). *Mechanical testing of advanced fibre composites*. Woodhead Publishing, Elsevier Science.

[4.16] ECCS/TC1. (1986). Recommended testing procedure for assessing the behaviour of structural steel elements under cyclic loads.

[4.17] Ferreira JG. (2008). *Characterization of the Behaviour of Semi-Rigid Metallic Connections* (in Portuguese). MSc Thesis in Civil Engineering. Instituto Superior Técnico, Universidade de Lisboa, Lisboa.

[4.18] CSI (2016). SAP 2000 - Version 18, Integrated Software for Structural Analysis and Design, Analysis Reference Manual. *Computer & Structures Inc*., Berkeley.

Chapter 5

Monotonic and cyclic behaviour of a cuff connection system for tubular profiles

5.1. INTRODUCTION

A promising connection system for pultruded profiles reported in the literature, first idealized by Smith *et al*. [5.1], comprises the use of a composite auxiliary part, often named as "cuff", that encloses the beam and column members (generally made of tubular profiles). The first prototypes of this connection comprised bolted composite parts manufactured by cuts on angle profiles. The results of this study showed improvements on the connection stiffness and strength in comparison to other conventional solutions. Singamsethi *et al*. [5.2] developed a manufacturing process to produce cuff connection parts made of E-glass fabric sheets and epoxy resin matrix, using vacuum assisted resin transfer moulding. Cyclic tests were performed on two specimens with cuff parts adhesively bonded to two tubular profiles. The authors referred that the stiffness and strength of the cuff connections were higher (+10% and +50%, respectively) than those of equivalent bolted and adhesive cleated connections. However, these connections exhibited very limited non-linear behaviour, reflecting their lack of ductility. Reduced damage was observed in the cuff connection parts, suggesting that they could bear higher loads. Carrion *et al*. [5.3] also studied the behaviour of beam-to-column connections using similar cuff parts to those used in [5.2] - they performed two monotonic tests and three cyclic tests on beam-to-column connections between GFRP tubular profiles using cuffs with different wall thickness. As expected, in the monotonic tests, the connection with the thinner (3.2 mm) cuff presented lower stiffness (-20%) and strength (-47%) than the connection using cuff part with medium thickness (6.35 mm), and exhibited extensive damage in the GFRP cuff part. Both connection systems presented an almost linear behaviour until the peak load was attained, which was followed by an abrupt load reduction (less significant in the connection with the thinner cuff part). Nevertheless, both specimens presented some residual strength until the end of the tests. The authors noted that the flexural strength of the cuff connection system using a cuff part with medium thickness was comparable to the flexural strength of the GFRP tubular profiles. Carrion *et al*. [5.3] also performed cyclic tests on two cuff connections: (i) the series with thicker cuffs presented linear behaviour up to ultimate failure; and (ii) the series with thinner cuffs presented almost linear behaviour until the maximum load was reached, followed by a stage with substantial pinching and reduced strength. Therefore, the cuff connection systems tested by Carrion *et al*. [5.3] showed reduced energy dissipation capacity.

This chapter presents an experimental study about the monotonic and cyclic short-term behaviour of beam-to-column connections between pultruded tubular GFRP profiles using novel stainless steel cuff connection parts. The connection system proposed herein aims (i) at exploiting the stainless steel ductility using a connection shape that has shown an improved mechanical behaviour when compared to “typical” solutions, and simultaneously, (ii) at maintaining high corrosion resistance, comparable to that of all-GFRP structures. The experimental campaign included full-scale tests on four different connection series, which differed in the cuffs’ plate thickness and geometry, comprising: (i) monotonic tests, to characterize the stiffness, strength, ductility and failure modes of each series; and (ii) cyclic tests, based on the recommendations of the ECCS protocol [5.4], to assess the hysteretic behaviour of the connection series that presented the best overall mechanical response under monotonic loading.

5.2. EXPERIMENTAL PROGRAMME

5.2.1. Materials

The specimens used in the full-scale tests comprised: (i) pultruded GFRP profiles; (ii) stainless steel cuff connection parts; and (iii) stainless steel rods, washers and nuts. The GFRP profiles (produced by *ALTO, Perfis Pultrudidos, Lda.*) were made of E-glass fibres (alternating layers of rovings and mats) and an isophthalic polyester resin matrix, presenting a square hollow section (external dimensions of 120 mm and 10 mm of thickness). The cuff plates (thickness of 1.0 mm and 1.5 mm) and the rods were made of stainless steel, grades AISI 304 and A2-70, respectively.

The main mechanical properties of the GFRP profiles in the longitudinal and transverse directions (corresponding to '*L*' and '*T*' subscripts), summarized in Table 5.1: (i) compressive strength in both longitudinal ($\sigma_{cu,L}$) and transverse ($\sigma_{cu,T}$) directions, and corresponding elastic moduli ($E_{cu,L}$ and $E_{cu,T}$); (ii) longitudinal tensile strength ($\sigma_{tu,L}$), elastic modulus ($E_{t,L}$) and Poisson ratio (ν_{LT}); (iii) interlaminar shear strength (τ_{is}); and (iv) in-plane shear strength by means of Iosipescu tests (τ_{LT} and τ_{TL}) and shear modulus by means of 10º off-axis tensile tests (G_{LT}). Eight specimens per test type and fibre direction were tested to determine the aforementioned properties.

The 0.2% tensile proof stress ($f_{0.2\%}$), ultimate tensile strength (f_u) and elasticity modulus (E_s) of the AISI 304 stainless steel sheets used in the cuff connection parts, presented in Table 5.2, were determined from coupon tensile tests on three specimens per plate thickness. The nominal 0.2% tensile proof stress ($f_{0.2\%}$) and ultimate stress (f_u) of the stainless steel rods in tension (grade A2-70) were 450 MPa and 700 MPa, respectively, according to ISO 3506-1, as provided by the manufacturer.

Table 5.1 - Mechanical properties of the GFRP material.

Test	Property	Average ± Std. deviation	Standard/Method
Compression	$\sigma_{cu,L}$	435 ± 53 MPa	ASTM D 695-02 [5.5]
	$\sigma_{cu,T}$	88.9 ± 16 MPa	
Tension	$\sigma_{tu,L}$	294 ± 17 MPa	EN ISO 527-1 [5.6]
	$E_{t,L}$	32.7 ± 3.0 GPa	
	ν_{LT}	0.32 ± 0.0	
Interlaminar shear	τ_{is}	30.6 ± 2.6 MPa	ASTM D 2344 [5.7]
In-plane shear	τ_{LT}	41.4 ± 6.2 MPa	ASTM D 5379 [5.8]
	τ_{TL}	58.7 ± 7.2 MPa	
10º off-axis tension	G_{LT}	3.2 ± 0.7 GPa	Chamis and Sinclair [5.9]

Table 5.2 - Mechanical properties of the stainless steel material.

Property	Plate	Average ± std. Dev.	Standard
$f_{0.2\%}$	1.0 mm	288.8 ± 5.1 MPa	EN 10002-1 [5.10]
	1.5 mm	440.5 ± 37.4 MPa	
f_u	1.0 mm	707.1 ± 0.6 MPa	
	1.5 mm	679.7 ± 5.4 MPa	
E_s	1.0 mm	198.9 ± 3.5 GPa	
	1.5 mm	157.0 ± 18.0 GPa	

5.2.2. Beam-to-column tests

5.2.2.1. Description of the test series

Four series of full-scale beam-to-column connection specimens between tubular profiles were considered in the present study – their geometry is illustrated in Figure 5.1. The specimens comprised one beam (with 800 mm of length) joined, at mid-height, to one column (900 mm long). Two main geometrical parameters of the cuff connection were considered: the cuff length (240 mm and 360 mm) and the cuff plate thickness (1.0 and 1.5 mm). Regardless of the geometry, the cuff parts were manufactured by welding five stainless steel plates, two of them cold bent (Figure 5.2).

Two M12 rods and four M8 rods were used to join the beam and the column, respectively, to the cuff connection part. The threads of the rods were in contact with the GFRP material, washers were used in all rod ends, no clearance was considered between the rods and the holes and a torque of 10 N.m was applied with a torque wrench. The labelling of the connections is "BC-SC-L-t", where BC refers to beam-to-column, SC refers to square cuff, L is the cuff length (240 mm and 360 mm) and t is cuff plate thickness (1.0 and 1.5 mm).

All connection series were tested under monotonic loading; three replicate specimens were tested per series. Subsequently, the connection series that presented the best overall mechanical performance, namely series BC-SC-360×1.5 (based on results presented in Section 5.3 and discussed in Section 5.5), was subjected to cyclic tests (Section 5.4); here, also three replicate specimens were tested.

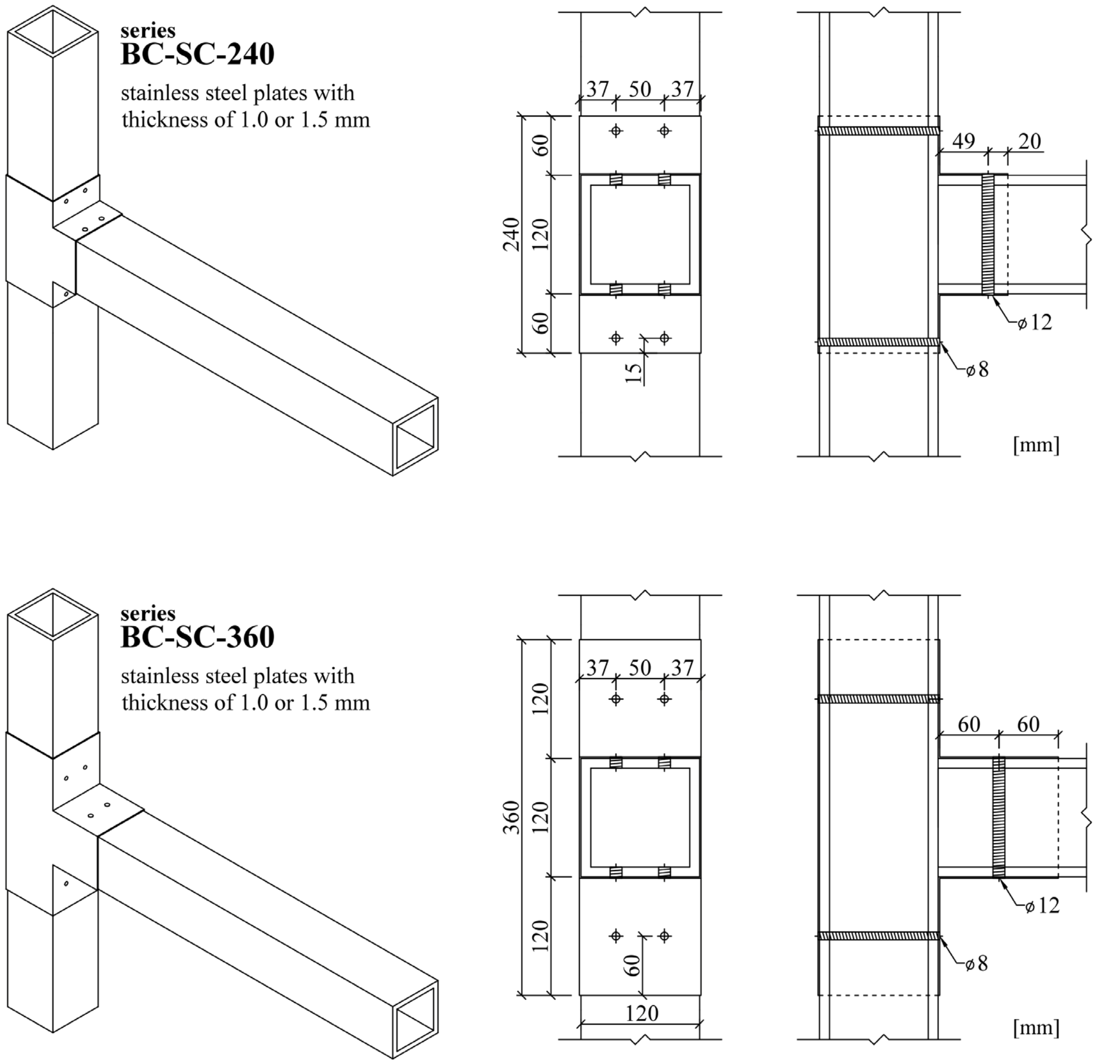

Figure 5.1 - Beam-to-column connection tests: test series.

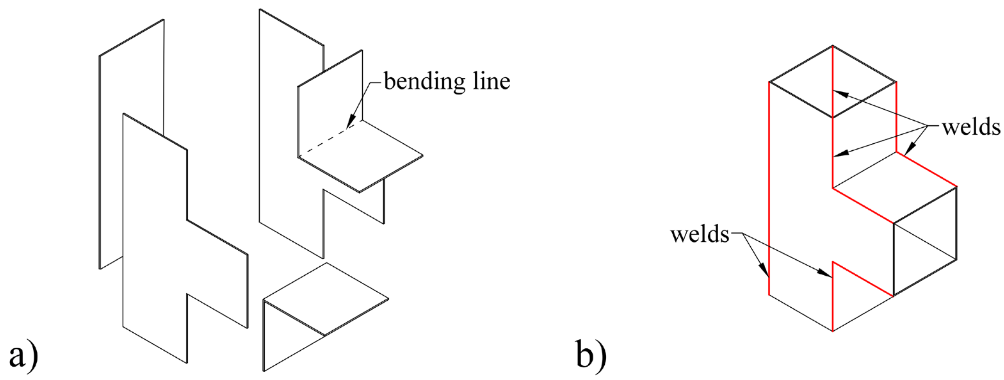

Figure 5.2 - Beam-to-column connection tests: cuff connection part – a) stainless steel plates; b) weld location.

5.2.2.2. Test setup

The full-scale beam-to-column tests were conducted in a closed loading frame consisting of steel profiles anchored to the laboratory's strong floor. The test setup and instrumentation are depicted in Figure 5.3. The loading system, positioned at 670 mm of the specimens' column axis, included: (i) a *Dartec* hydraulic jack (Figure 5.3a, label A), with capacity of 250 kN in compression and in tension, and maximum stroke of ±200 mm; (ii) two hinges that guaranteed the perpendicularity of the applied load (Figure 5.3a, B); and (iii) a *TML* load cell with capacity of 300 kN (Figure 5.3a, C). The end sections of the column were fixed by steel tubes (Figure 5.3a, D), which were introduced in the cavity of the GFRP column. Additionally, to prevent the tearing failure of the web-flange junction at the columns' ends, their front face was fixed by two rigid steel plates, connected to the steel loading frame with threaded rods (Figure 5.3a, E).

The vertical displacement of the hydraulic jack was measured by its built-in displacement transducer, while two *TML* inclinometers were used to measure the rotations of the beam and the column. However, owing to the considerable buckling of the cuff parts observed during the tests (*cf.* Section 5.3.2), at some point the rotation measurements of the column were no longer accurate and, thus, were disregarded in the analyses presented herein. Moreover, previous experimental tests (*cf.* Chapters 3 and 4) allowed concluding that the rotation of the column would be negligible. Thereafter, in this chapter, the rotation of the columns was considered to be null. Finally, the data was collected by a *HBM* datalogger, at a rate of 5 Hz, and stored in a PC.

5.3. MONOTONIC TESTS

The monotonic tests were performed under displacement control, at a rate of 0.25 mm/min and were stopped either when the maximum stroke of the hydraulic jack was attained or when the specimens collapsed. This section presents the results of the full-scale beam-to-column monotonic tests, namely (i) the load/moment *vs*. displacement/rotation response (Section 5.3.1) and (ii) the failure modes (Section 5.3.2). Table 5.3 summarizes the monotonic test results, in terms of maximum load (F_{max}), displacement corresponding to the maximum load (d_{Fmax}), maximum bending moment (M_{max}), initial rotational stiffness (K_θ) and ultimate failure mode. It should be noted that the stroke of the beam inclinometer (10º) ended before the end of most monotonic tests. Therefore, the results described in the following subsections will be presented in terms of load (kN) and displacement (mm).

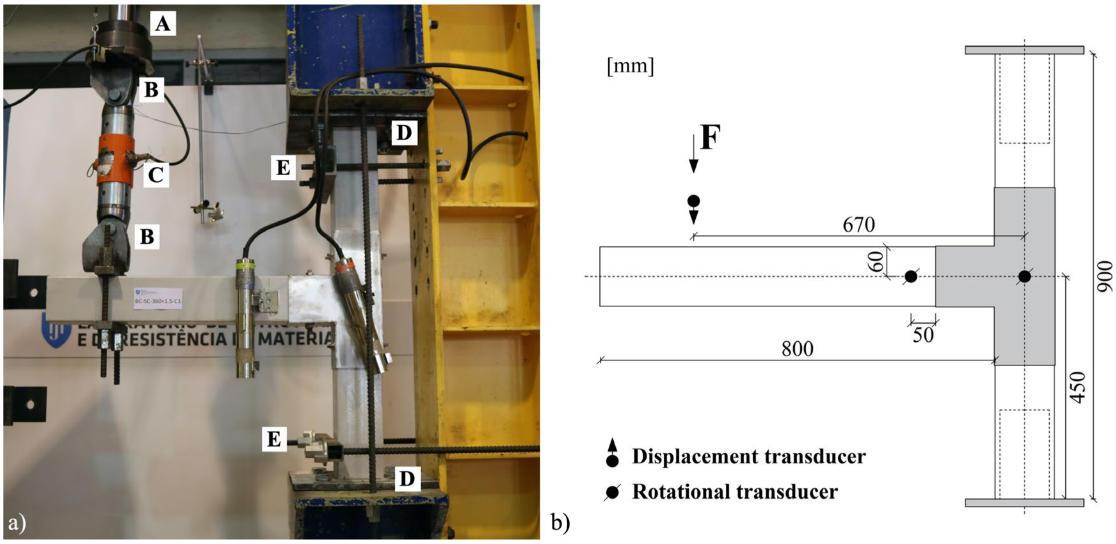

Figure 5.3 - Beam-to-column connection tests: test setup and instrumentation.

Table 5.3 - Beam-to-column monotonic tests: summary of experimental results.

Series	F_u (kN)	d_{Fu} (mm)	M_u (kN.m)	K_θ (kN.m/rad)	Ultimate failure mode	μ_d (-)
BC-SC-240×1.0	7.64 ± 0.97	198.2 ± 59.2	5.12 ± 0.65	48.2 ± 8.8	Cuff tearing near the beam rods	0.88 ± 0.01
BC-SC-240×1.5	9.46 ± 1.47	152.8 ± 62.0	6.34 ± 0.98	95.2 ± 6.5	Cuff tearing or GFRP shear-out near the beam rods	0.86 ± 0.03
BC-SC-360×1.0	8.59 ± 0.59	219.9 ± 74.3	5.76 ± 0.39	67.6 ± 19.8	-	0.90 ± 0.04
BC-SC-360×1.5	11.9 ± 0.61	142.6 ± 30.6	7.96 ± 0.41	106.6 ± 13.0	GFRP shear-out near the beam rods or corner weld failure in the cuff part	0.84 ± 0.02

5.3.1. Load *vs*. displacement and moment *vs*. rotation behaviour

Figure 5.4 presents the load *vs*. displacement (vertical, loading point) curves of all specimens tested (these results were used to define the end of proportionality displacement for the cyclic tests, *cf*. Section 5.4.1). Figure 5.5 presents the moment *vs*. rotation curves of all specimens of all connection series, which allowed determining their rotational stiffnesses and ultimate moments. The specimens of each series are identified from M1 to M3.

It should be noted that, for some specimens (with 1 mm thick cuff parts), the test ended at an ascending load stage or at a point considerably near a load peak (always for very significant vertical displacements), because the maximum stroke of the hydraulic jack was attained (identified in Figure 5.4). Therefore, the maximum load and moment attained in the monotonic tests of all series using tubular profiles with 1 mm thick cuff parts (M_{max}, Table 5.3) should be taken as a lower bound of the connections' actual capacity.

All specimens of series BC-SC-240×1.0 (Figure 5.4a) presented similar behaviour up to approximately 100 mm of displacement, in particular: (i) an initial linear response up to ~3.0 kN (~25 mm, coincident with the first noticeable damage, *cf*. Section 5.3.2); followed by (ii) another linear stage with lower stiffness (-74%). Specimen BC-SC-240×1.0-M1 maintained this lower stiffness stage until the maximum stroke of the hydraulic jack was reached, while specimens M2 and M3 of this series failed before that stroke was reached (*cf*. Section 5.3.2).

Specimens of series BC-SC-240x1.5 (Figure 5.4b) presented quasi-linear behaviour until a load of approximately 4.5 kN was reached (~30 mm of displacement, when the first noticeable damage was registered, *cf*. Section 5.3.2). After that point, all specimens presented a gradual stiffness loss, with minute load drops that were soon recovered. Specimens M2 and M3 reached the maximum load at this stage. Finally, for specimen M1 a third stage was registered in which an increase of stiffness (and load) was observed. The peak load for that specimen occurred for a considerably higher displacement (~225 mm) compared to the remaining specimens. All specimens of this series presented different load-displacement overall responses due to the different damage modes observed in the tests (*cf*. Section 5.3.2).

Specimens from series BC-SC-360×1.0 (Figure 5.4c) first presented a bilinear response, with higher initial stiffness (up to ~4.0 kN, when the first damage was observed in the steel cuff, *cf*. Section 5.3.2), which then decreased. At the end of the second linear branch, the curves presented a gradual transition to a peak load, which was followed by a gradual load drop. The test of specimen M3 was stopped earlier than its counterparts because the maximum stroke of the hydraulic jack was reached. On the other two specimens of this series, a load recovery was registered, exceeding the load attained in the first peak, with both specimens maintaining their integrity until the end of the test; such load recovery is explained in Section 5.3.2.

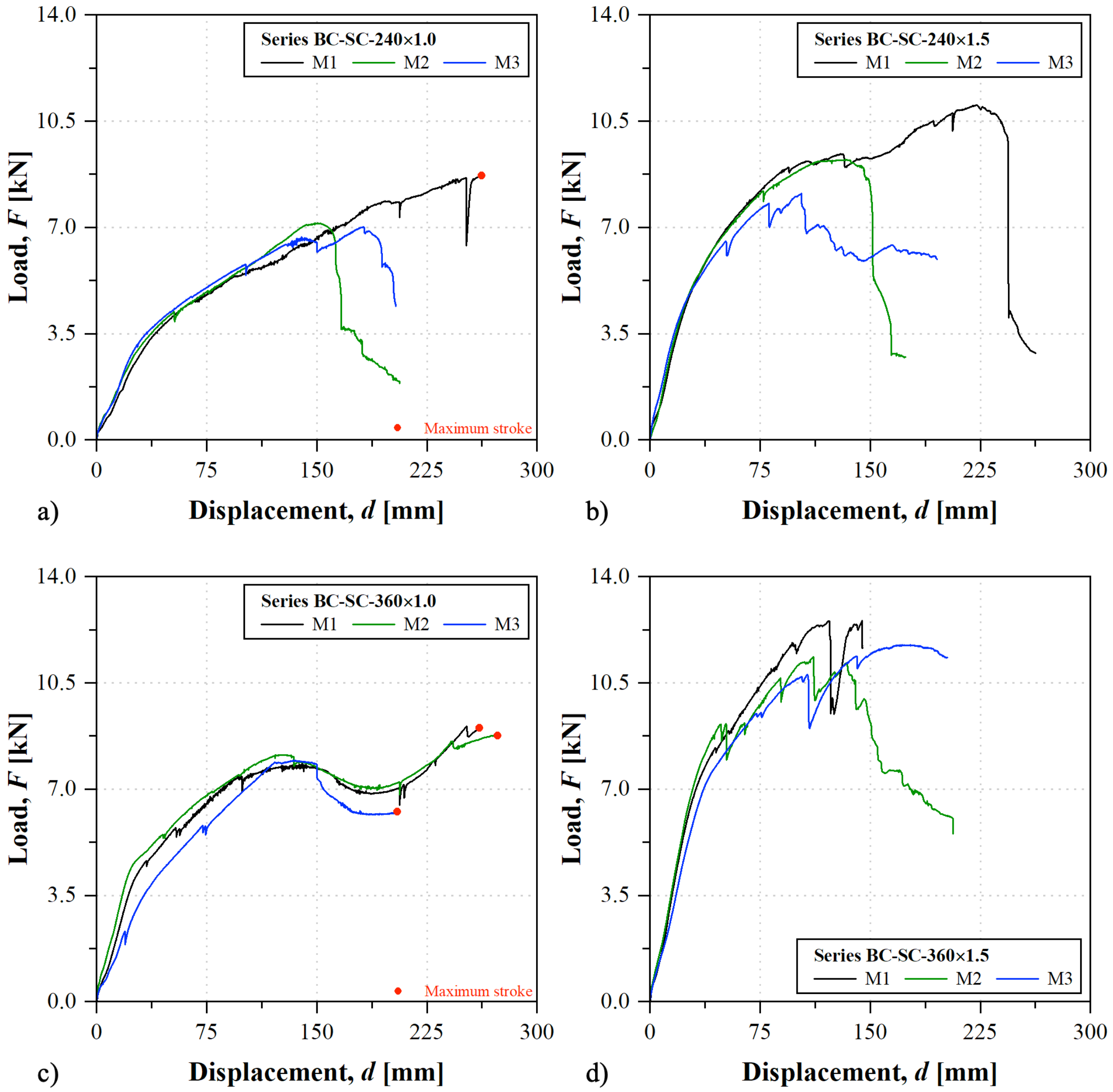

Figure 5.4 - Monotonic tests of beam-to-column connections: load *vs.* displacement curves of a) series BC-SC-240×1.0; b) series BC-SC-240×1.5; c) series BC-SC-360×1.0; d) series BC-SC-360×1.5.

Finally, the specimens of series BC-SC-360×1.5 (Figure 5.4d) presented an initial linear-elastic response up to a load of ~7 kN, shortly before first damage was observed in the specimens (*cf.* Section 5.3.2). Subsequently, all specimens presented a gradual stiffness reduction with minute load drops and recoveries until the maximum load was achieved; at this stage, the different specimens exhibited dissimilar responses owing to their different damage modes, as described in Section 5.3.2.

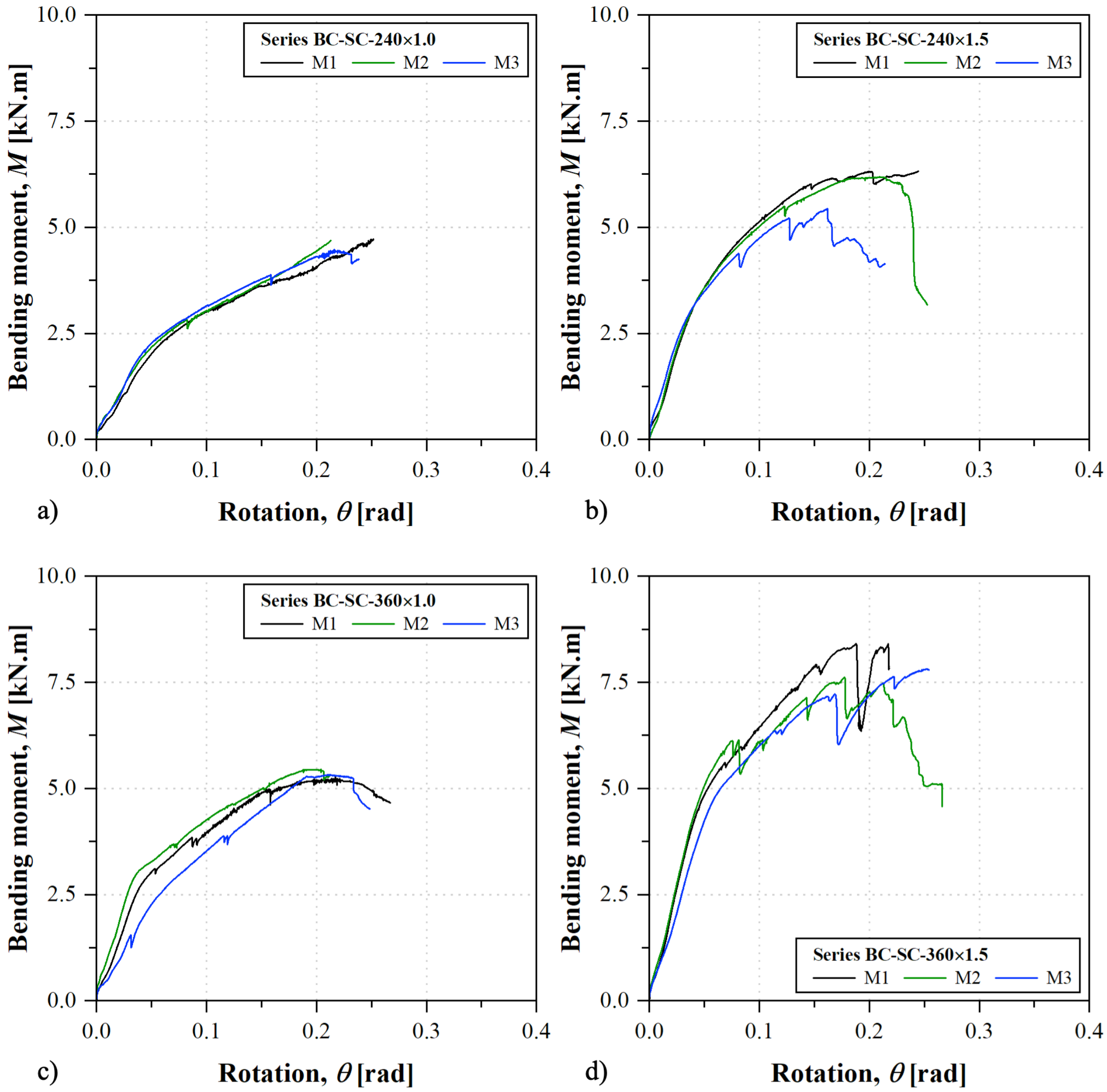

Figure 5.5 - Monotonic tests of beam-to-column connections: bending moment *vs.* rotation curves of a) series BC-SC-240×1.0; b) series BC-SC-240×1.5; c) series BC-SC-360×1.0; d) series BC-SC-360×1.5.

The initial stiffness of the test series with 1.5 mm thick cuffs was considerably higher than of their thinner (1.0 mm) counterparts, in particular when comparing series BC-SC-240×1.0 to BC-SC-240×1.5 (+97%) and series BC-SC-360×1.0 to BC-SC-360×1.5 (+58%), respectively. On the other hand, the initial stiffness was increased with the length of the cuff part (while keeping the same thickness): +40% from BC-SC-240×1.0 to BC-SC-360×1.0 and +12% from BC-SC-240×1.5 to BC-SC-360×1.5. Similar conclusions can be drawn regarding the ultimate loads, with thicker cuff plates providing higher ultimate (or maximum) loads: +24% from BC-SC-240×1.0 to BC-SC-240×1.5 and +38% from

BC-SC-360×1.0 to BC-SC-360×1.5. Longer cuffs also provided higher ultimate (or maximum) loads: +12% from BC-SC-240×1.0 to BC-SC-360×1.0 and +26% from BC-SC-240×1.5 to BC-SC-360×1.5. For the range of geometries tested, these figures show that the cuff plate thickness has higher influence on the monotonic response of the joints than the cuff length.

5.3.2. Failure behaviour

This section describes the damage progression and failure modes observed in the beam-to-column monotonic tests. It should be noted that, due to the geometry of these connections, the (potential) damage in the GFRP components was often hidden by the cuff connection parts; therefore, it was not possible to identify the exact instants (during the tests) corresponding to the occurrence of different failure mechanisms (e.g. cracks); the full extent of the damage that developed in the GFRP parts was only observed after the tests, when the specimens were disassembled.

For specimens of series BC-SC-240×1.0, noises were audible as soon as displacements reached ~20 mm. The first noticeable damage observed was the buckling of the cuffs' lateral plates (Figure 5.6a), for displacements around ~25 mm, followed by bearing of the cuff stainless steel material in contact with the beam's rods (Figure 5.6b), for displacements around ~55 mm. For specimen M1 of this series, damage was also observed in the welds at one top corner, for a displacement of ~80 mm and, soon after, a crack developed in the nearby stainless steel plates (Figure 5.6c); when the displacement reached ~190 mm, similar damage occurred in the opposite corner, with no additional damage being observed until the end of the test. In case of specimen M2, for a displacement of ~120 mm, the welds cracked in the bottom corners in the cuffs' edge in contact with the beam (Figure 5.6d). This was followed by the complete tearing (due to bearing) of the stainless steel plate in contact with the beam's rods (Figure 5.6e) at a displacement of ~150 mm. Finally, Specimen M3 presented damage at the welds' corners (similar to what occurred in specimen M1) for a displacement of ~130 mm, and the ultimate failure occurred at ~200 mm due to the tearing of the cuff plate in contact with the beam's rods (as in specimen M2).

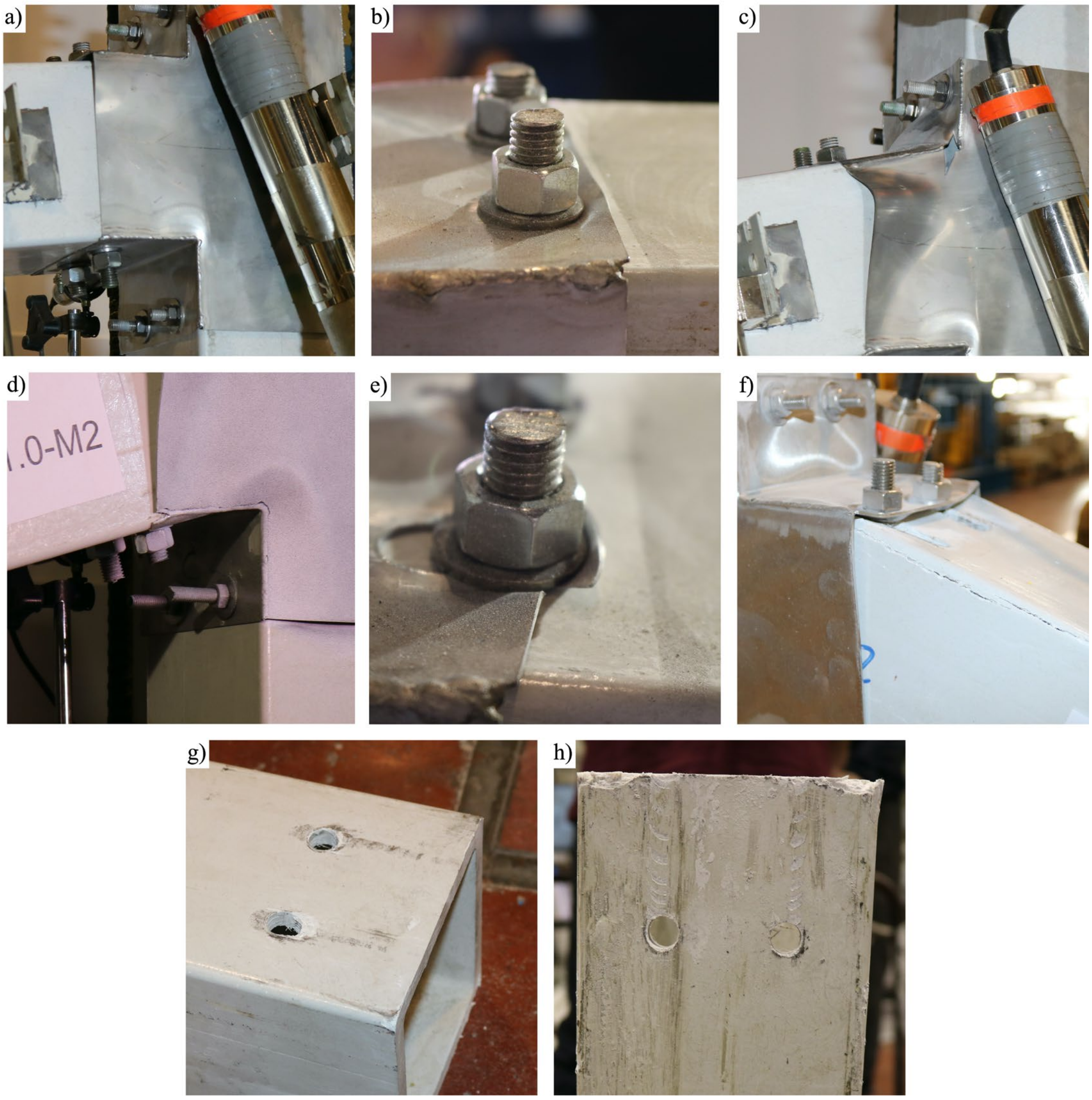

Figure 5.6 - Monotonic tests of beam-to-column connections: failure modes - a) buckling of the cuff part (series BC-SC-240×1.0); b) bearing of the cuff beam top holes (series BC-SC-240×1.0); c) cuff welds failure at the top corners and stainless steel cracks (series BC-SC-240×1.0); d) cuff weld failure at the beam bottom (series BC-SC-240×1.0); e) tear of the stainless steel material near the beam rods (series BC-SC-240×1.0); f) shear-out failure in the beam's top holes, web-flange tearing failure and flange flexural failure at the beam's top (series BC-SC-240×1.5); g) GFRP bearing failure at beam's top holes cleats (series BC-SC-360×1.5); h) GFRP bearing failure at beam's bottom edge (series BC-SC-360×1.5).

Regarding the specimens of series BC-SC-240×1.5, noises were audible soon after the beginning of the tests and buckling and bearing of the stainless steel plates was noticeable at ~30 mm. Specimen M1 failed first at the welds, in the top corners, near the intersection of the beam and column profiles, at ~130 mm, with a crack at the lateral plate developing from this location (similar to Figure 5.6c). This was followed by failure of the cuffs' bottom edge welds in contact with the beam (similar to Figure 5.6d) and tearing of the cuffs' plate in contact with the beam's rods (similar to Figure 5.6e), for a ~245 mm displacement. Specimen M2 presented tearing of the cuff top plate near the beam's rods (similar to Figure 5.6e), for a displacement of ~160 mm. Specimen M3 presented bearing of the cuff's stainless steel material near the beam's rods at ~65 mm (similar to Figure 5.6b), failure of the bottom welds of the cuff part (similar to Figure 5.6d) at ~80 mm, and shear-out failure in the beam's top holes[1] (Figure 5.6f).

For series BC-SC-360×1.0, all specimens presented failure at the welds in the top corner of the intersection between the column and the beam (similar to Figure 5.6c), when the buckling of the cuff plates was already substantial, at a displacement of ~25 mm. Beyond this point, cracks progressively developed from these corners, increasing until the end of the tests, being quite noticeable at displacements of ~65 mm (M1), ~75 mm (M2) and ~100 mm (M3). It is worth mentioning that, from displacement of ~185 mm, the welds connecting the lateral and top plates of the cuffs were completely opened and, from that point, the top plate worked as a truss tying the beam's rods to the column's rods, which resulted in a stiffness increase in the final stage of the tests (*cf*. Section 5.3.1 and Figure 5.4c). No ultimate failure mode was registered in the specimens of this series, as they maintained their structural integrity until the stroke of the hydraulic jack was reached.

Finally, for series BC-SC-360×1.5, the first visible damages registered were located in the stainless steel cuff for displacements of ~50 mm. In particular, the top part near the beam's rods presented bearing plastic deformations (similar to Figure 5.6b) and buckling was triggered in the lateral plates (similar to Figure 5.6a). Noises were audible in the GFRP material of all specimens starting from ~70 mm of displacement. After disassembly, the beam of specimen M1 presented visible bearing damage in the top holes (Figure 5.6g) and compressive damage at the bottom edge in contact with the column's face (Figure 5.6h). In specimen M2, the welds in the cuff part in contact with the bottom of the beam began to open for displacements of ~110 mm (similar to Figure 5.6d). Additionally, tearing of the beam's top web-flange junctions and shear-out at the beam's top holes (similar to Figure 5.6f) were also identified upon disassembly of the specimen. Regarding specimen M3, failure occurred in the welds corner in the

[1] The instant when this damage occurred could not be precisely identified; nevertheless, GFRP cracking was audible from displacements of ~110 mm.

intersection between the column and the beam, at ~110 mm, which cracked progressively the stainless steel plates until the end of the test (similar to Figure 5.6c).

5.4. CYCLIC TESTS

This section presents the results of the full-scale beam-to-column cyclic tests, namely (i) the adopted loading protocol (Section 5.4.1), (ii) the overall cyclic behaviour (Section 5.4.2) and (iii) the analysis of the hysteretic parameters (Section 5.4.3).

5.4.1. Load protocol

The cyclic tests (only for series BC-SC-360×1.5) were performed under displacement control, at a rate of 0.50 mm/min. The displacement history was defined based on the recommendations of the ECCS protocol [5.4], as follows: (i) four initial cycles corresponding to maximum absolute displacements of ¼, ½, ¾ and 1 times the displacement at the end of proportionality (EP) were first performed; (ii) next, groups of three cycles with maximum absolute displacements of *2n* the EP displacement were carried out, with *n* being an integer that increases after each three cycles. The adoption of the EP displacement (displacement at the end of the first linear stage of the monotonic load *vs*. displacement curve) follows a procedure recommended by the ECCS protocol [5.4] and was also adopted in Chapter 4. Accordingly, the estimated EP displacement of series BC-SC-360×1.5 was 25 mm and the displacement history for the cyclic tests is presented in Figure 5.7. The adoption of a protocol developed for steel structures [5.4] is justified by the fact that the behaviour of the cuff connection systems in the monotonic tests (*cf*. Section 5.3) was governed by the extensive plastic deformations observed in the stainless steel cuffs. The cyclic tests ended when the maximum stroke of the hydraulic jack was reached or when extensive damage (compromising the specimens' integrity) was observed.

The ECCS protocol [5.4] recommends the evaluation of several parameters at each cycle to assess the structural cyclic performance of the connections: (i) the stiffness ratio (ξ), which represents the ratio between the slope of the moment *vs*. rotation hysteretic curves when crossing the rotations' axis (α_i^+ or α_i^-, as depicted in Figure 5.8) and the initial monotonic stiffness (K_θ, Table 5.3); (ii) the strength, which was evaluated by considering the moment when the maximum and minimum displacement of each cycle was attained (M_i^+ or M_i^-, depicted in Figure 5.8); and (iii) the dissipated energy ratio (η) per cycle, given by:

$$\eta_i = \frac{W_i}{\Delta M_{\mathrm{EP}}(\Delta\theta_i - \Delta\theta_{\mathrm{y}})} \tag{5.1}$$

where W_i is the energy dissipated in cycle i (area delimited by the hysteric cyclic curve, W_i, depicted in Figure 5.8), ΔM_{EP} is the difference between the positive and negative EP bending moments, $\Delta\theta_i$ is the difference between the positive and negative imposed rotations in cycle i, and $\Delta\theta_{\mathrm{y}}$ is the difference between the positive and negative EP rotations.

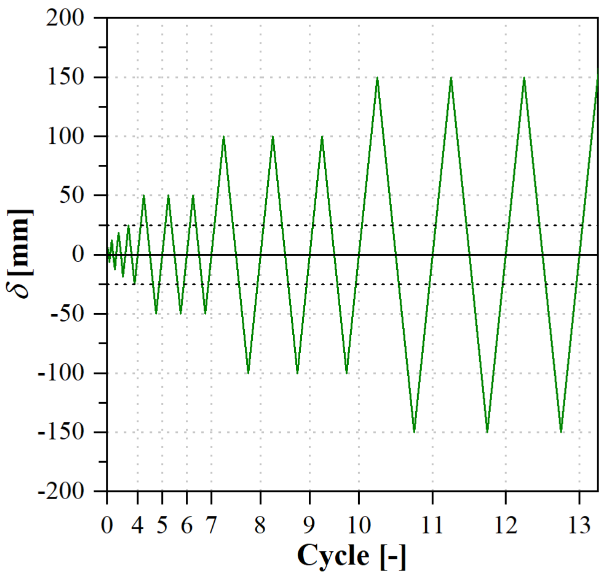

Figure 5.7 - Cyclic tests on beam-to-column connection BC-SC-360×1.5: load history.

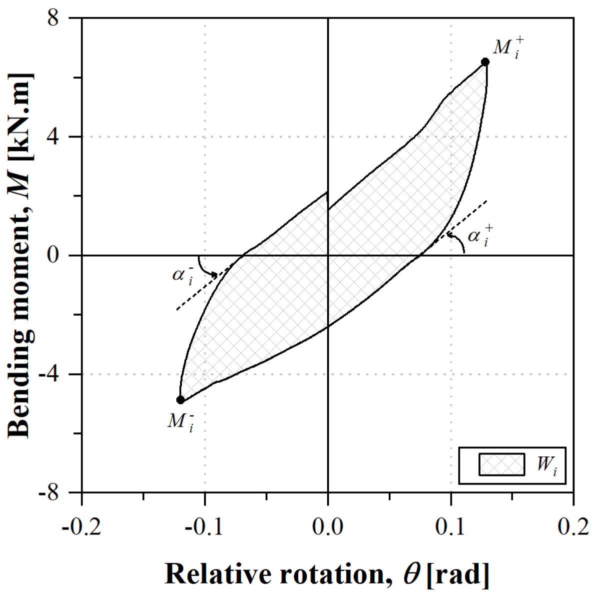

Figure 5.8 - Cyclic tests on beam-to-column connection BC-SC-360×1.5: ECCS [5.27] parameters.

5.4.2. General behaviour

Figure 5.9 presents the bending moment *vs*. rotation curve from the cyclic tests of series BC-SC-360×1.5, together with the corresponding monotonic curve (in red). The analysis of these curves prompts the following comments: (i) the hysteretic response reflects considerable pinching effect, with relatively low loads in quadrants II and IV; (ii) the behaviour is (almost) symmetric, with slightly higher loads in quadrant I, which corresponds to the upper movement of the hydraulic jack, compared to those of quadrant III; and (iii) the monotonic bending moment *vs*. rotation curve encloses closely its hysteretic counterpart. In each cycle group (with the same maximum absolute displacement), the moment *vs*. rotation curve presented the following progression: (i) the first cycle of the group registered an initial narrow path with lower stiffness, after which the stiffness increased until the maximum absolute rotation was reached (Figure 5.9, cycle 5); while (ii) in the next two cycles the initial narrow path was longer and the maximum absolute moments slightly lower than in the first cycle of the group (Figure 5.9, cycles 6 and 7). This behaviour is due to the occurrence of unrecoverable damage (GFRP damage, weld opening or stainless steel cracking) in the first cycle of a given cycle group.

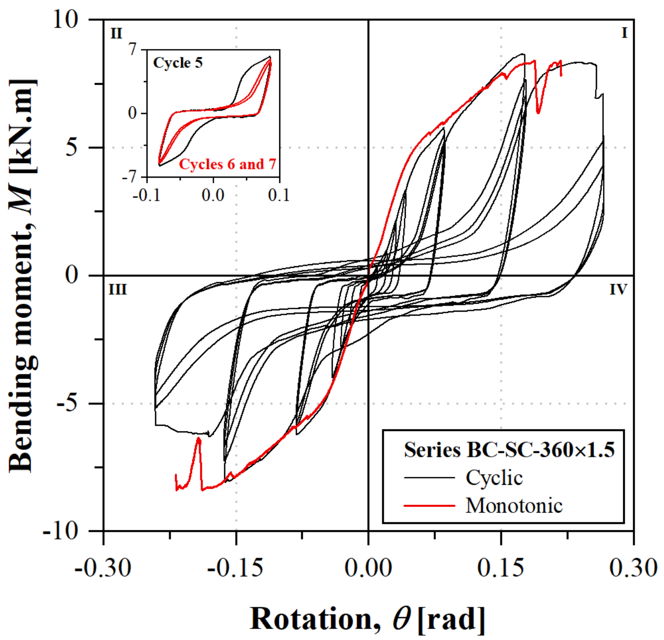

Figure 5.9 - Cyclic tests on beam-to-column connection BC-SC-360×1.5: representative moment *vs.* rotation curve (representative monotonic curve also included).

Regarding damage and failure modes, as expected noises were audible from cycles with maximum absolute displacements of ~25 mm (EP displacement). For specimen C1, audible cracks associated to the GFRP material were almost constant in the first cycle of maximum absolute displacements of 100 mm (absolute rotations of ~0.18 rad), possibly related to bearing or shear-out failure on the beam holes, while the welds of the cuff part opened at every corner between the beam and the column (similar to Figure 5.6c) at cycles with displacements ranging from -150 mm to +150 mm (absolute rotations of ~0.27 rad). For specimens C2 and C3, the tearing of the web-flange junctions (similar to Figure 5.6f) of the beam were visible at cycles with maximum absolute displacements of 50 mm (absolute rotations of ~0.09 rad), while bearing or shear-out failure at the beams' holes and failure of the welds at the corners of the cuff connection part (similar to Figure 5.6c) occurred on the next group of cycles, with maximum absolute displacements of 100 mm.

5.4.3. Hysteretic parameters

Figure 5.10 presents the progression of the stiffness ratio (ξ) with increasing cycles for series BC-SC-360×1.5; an additional curve corresponding to a sleeve connection - series F2S tested in Chapter 4 - was added to be compared in Section 5.5.2. For both ascending and descending branches, ξ for series BC-SC-360×1.5 presented an overall decreasing trend with reasonable symmetry, with the stiffness ratio decreasing within each group of three cycles with the same absolute maximum displacement. Moreover, regarding the first cycle of each cycle group, the following figures were registered: (i) in cycle 5, the stiffness ratios were +0.79 and -0.69 for the ascending and descending branches, respectively; (ii) in cycle 8, the values of this parameter were + 0.54 (ascending) and -0.59 (descending); and (iii) in cycle 11, they were +0.27 and -0.20.

Figure 5.11 presents the bending moment progression with increasing cycles of series BC-SC-360×1.5 (a representative curve of a sleeve connection - series F2S in Chapter 4 – is also included). The symmetry of the moment *vs*. rotation curves, described earlier, is reflected on the bending moment per increasing cycles. All specimens presented a very similar trend: as expected, the bending moment at the

4th cycle, corresponding to the cycle with maximum absolute displacement equal to the EP displacement (cycle 4), was almost equal to the monotonic EP moment; for a given group of three cycles with the same absolute maximum displacement, the 2nd and 3rd cycles presented slight moment reductions in comparison to the first cycle of the same group.

Figure 5.12 presents the evolution of the dissipated energy ratio (η) of series BC-SC-360×1.5(a representative curve of a sleeve connection - series F2S in Chapter 4 – is also included), where it can be seen that all specimens presented similar behaviour. The higher values of η were obtained for the first cycles of a given group of cycles, with equal absolute maximum displacement, in line with what was described for the stiffness ratio and the bending moment evolution. Furthermore, for each maximum rotation cycle group, as the stiffness and strength decreased in the 2nd and 3rd cycles (due to the occurrence of unrecoverable damage in the first cycle), the dissipated energy ratio, which is directly affected by the aforementioned parameters (*cf.* Eq. (5.1)), also decreased. Moreover, the maximum energy dissipated ratio was registered in cycle 8, in which the maximum moment was obtained.

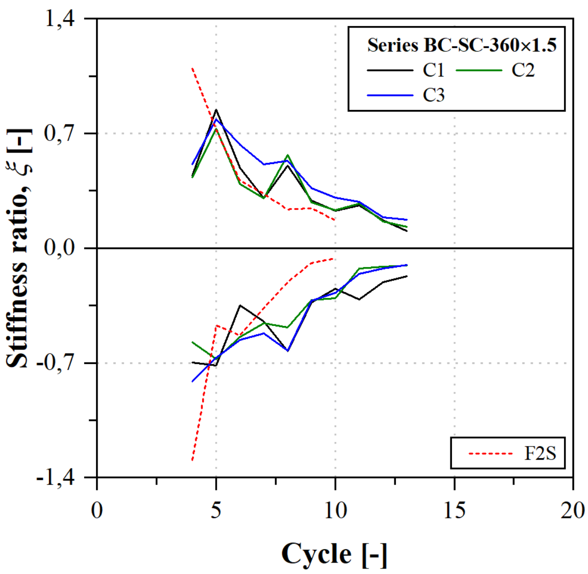

Figure 5.10 - Cyclic tests of beam-to-column connection BC-SC-360×1.5: stiffness ratio (ξ) evolution (representative specimen of a sleeve connection - series F2S [Chapter 4] - also included).

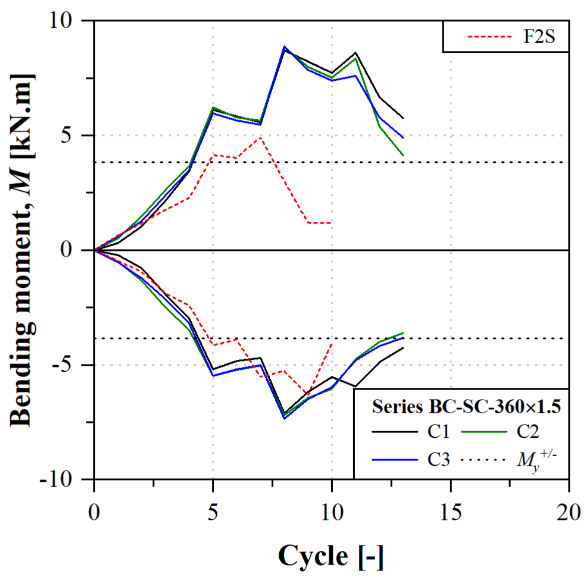

Figure 5.11 - Cyclic tests of beam-to-column connection BC-SC-360×1.5: strength evolution of (representative specimen of a sleeve connection - series F2S [Chapter 4] - also included).

In addition to the ECCS [5.4] parameters discussed above, the evolution of the accumulated dissipated energy was also assessed and is depicted in Figure 5.13. This parameter, which was very consistent for the different specimens, presented a steep increase starting from the 4th cycle. In fact, up to this cycle, the displacements/rotations were below their EP value and, therefore, the specimens presented an almost linear elastic behaviour. It should be noted that higher increases of accumulated dissipated energy were registered between cycles 4 to 5, 7 to 8, and 10 to 11, corresponding to the transition of one cycle group to another cycle with higher maximum/minimum rotations.

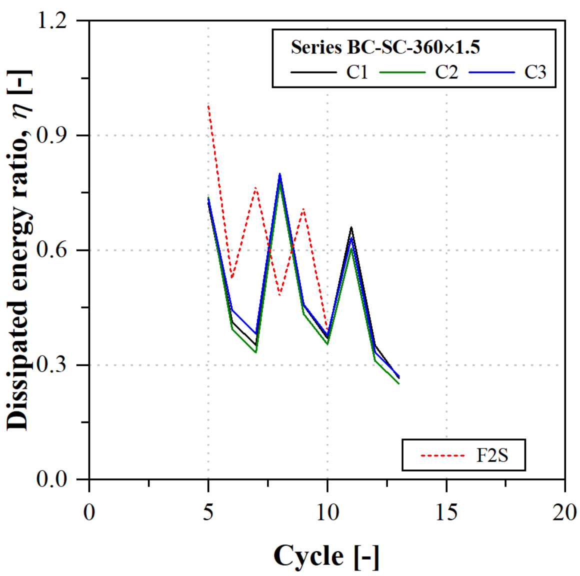

Figure 5.12 - Cyclic tests of beam-to-column connection BC-SC-360×1.5: dissipated energy ratio (η) evolution (representative specimen of a sleeve connection - series F2s from Chapter 4 - also included).

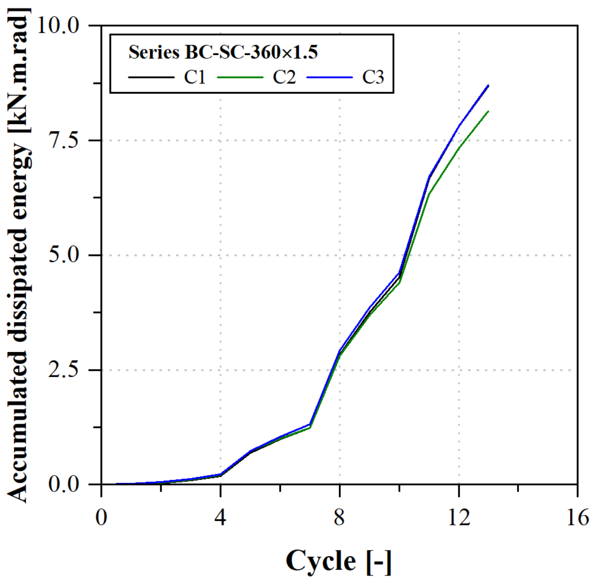

Figure 5.13 - Cyclic tests of beam-to-column connection BC-SC-360×1.5: accumulated dissipated energy.

5.5. DISCUSSION

5.5.1 Influence of plate thickness and cuff length

As presented in Section 5.3.1, the plate thickness and cuff length influenced the monotonic behaviour of the connection system: both thicker plates and longer cuffs increased the initial stiffness and strength, with the thickness presenting a higher influence on the connections' response (*cf.* Section 5.3.1). The increase of rotational stiffness afforded by thicker and longer cuffs is logical (up to +97% and +40%), as such connection parts are inherently stiffer and confine longer portions of the connected GFRP members, respectively.

If a beam spam of 3.0 meters is considered, three of the connection series studied, namely BC-SC-240×1.5, BC-SC-360×1.0 and BC-SC-360×1.5 may be classified as "semi-rigid" according to Eurocode 3 – Part 1-8 [5.11] for steel connections (the "semi-rigid" stiffness interval is of 48.8 to 2438.0 kN.m/rad), allowing the consideration of the connections stiffness on the structural analysis, thus reducing the design deflections of flexural members, when compared to the consideration of pinned connections; this is particularly relevant, since the design of GFRP structures is often governed by deflection limits. In fact, considering the cuff connections' stiffnesses in the beam design allows for substantial service load increases when compared to a simply supported beam. The maximum deflection allowed for a beam with a span of 3.0 meters is 0.012 meters, corresponding to *l*/250; represented in Figure 5.14a for a beam[2] loaded with a uniform distributed load and with pinned, rigid and cuffed joints. Despite the fact that the deflections of the beams with cuff connections are juxtaposed to the simply supported beam, the corresponding bending moments are different (Figure 5.14b) and are associated with significant increases of the distributed load compared to the that of the beam with pinned joints: +22% for series BC-SC-270×1.0; +40% for series BC-SC-270×1.5; +29% for series BC-SC-360×1.0; and +44% for series BC-SC-360×1.5.

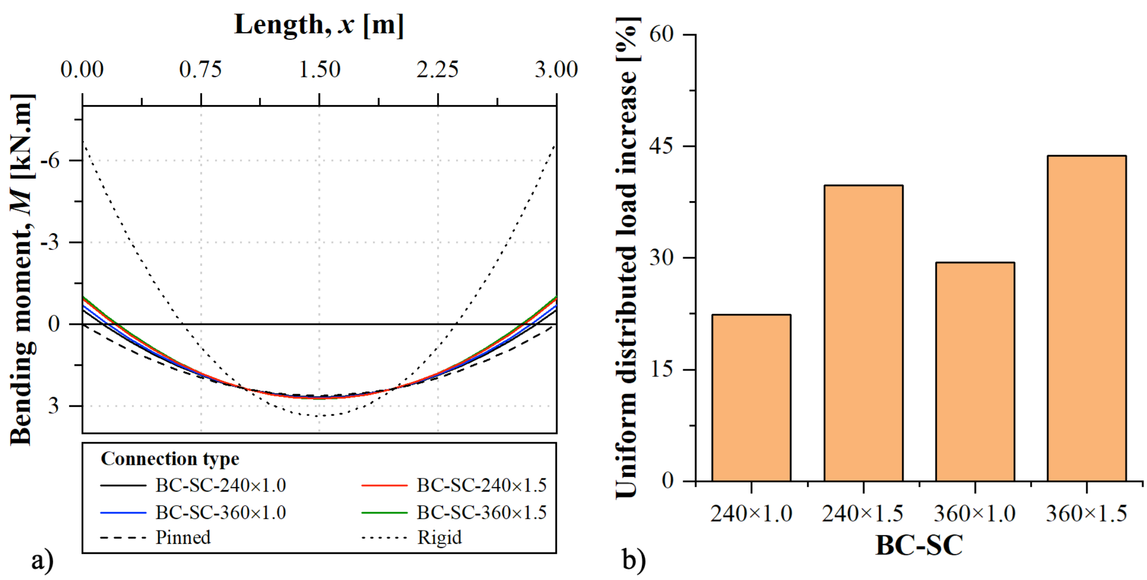

Figure 5.14 - Estimated beam a) deflections and b) moments for different connection types.

[2] Using the Timoshenko Beam Theory [5.12].

The fact that increasing the cuffs plate thickness also increased the connections' strength (up to +38%, *cf.* Section 5.3.1) is likely related to the influence of this geometrical parameter on the failure modes, with thicker cuffs leading to more damage in the GFRP profiles as a consequence of their higher stiffness and strength. This is particular evident when comparing series BC-SC-360×1.5 and BC-SC-360×1.0, as two specimens of the former series presented shear-out failure in the beam's top bolts (this failure mode was also observed in one specimen of series BC-SC-240×1.5). Additionally, increasing the length of the cuffs also resulted in an overall increase of the connections' strength (up to +26%, *cf.* Section 5.3.1). This may be explained by two main reasons: (i) longer stainless steel elements allow for a smother stress distribution, reducing stress peaks in the (brittle) GFRP material; and (ii) longer cuffs have higher bolt edge distance, thus delaying stainless steel shear-out failure. It is also worth mentioning that the welds proved to be a weak point on the stainless steel cuff parts, as all series presented damage in these elements.

In order to quantify the ductility of the connection series studied, a ductility index (μ_{d}) was calculated for each specimen using the formulae proposed by Jorissen and Fragiacomo [5.13], developed for timber structures and already used in previous studies on GFRP beam-to-column connections (*cf.* Chapter 3),

$$\mu_{\mathrm{d}} = \frac{d_{\mathrm{u}} - d_{\mathrm{EP}}}{d_{\mathrm{u}}} \tag{5.2}$$

where, d_{EP} corresponds to the EP displacement and d_{u} is the ultimate displacement, corresponding to 80% of the maximum load on the decreasing stage of the load *vs*. displacement curves. The ductility indexes (μ_{d}) of all series are presented in Table 5.3, being very similar for all series. It should be noted that all specimens of series BC-SC-360×1.0 and one specimen of series BC-SC-240×1.0 did not reach a peak load, therefore the ductility index estimated for these series corresponds to a lower bound of the actual values.

In summary, series BC-SC-360×1.5 presented the best monotonic performance, with higher initial stiffness and strength, while still presenting ductility on par with the remaining series.

5.5.2 Comparison with sleeve connection system

The connection system analysed in the present work can also be compared to those of previous studies using the same GFRP profiles (*cf*. Chapters 3 and 4). In these studies, the profiles were joined using a sleeve connection system with two auxiliary steel parts (grade S235), one inserted in the beam and the other inserted in the column profile (Figure 5.15a). The column connection part was materialized by SHS 100×5 profile segments with 100 mm of length. In order to join this part to the column and to the beam connection part, each face presented four Ø10.5 mm holes with M10 welded nuts that allowed the fastening of the M10 bolts. The beam connection part of series F2S (Figure 5.15b), the one with best overall behaviour in Chapters 3 and 4 comprised a 75 mm segment of the same SHS 100×5 profile and an end-plate welded to the internal surfaces of that segment. Four Ø10.5 mm holes were drilled in the end-plate, matching those of the column part, and two Ø8 mm threaded holes were drilled in the upper and bottom plates of the segment, at a distance of 55 mm from the column face, to accommodate the four M8 bolts used to join this part to the beam.

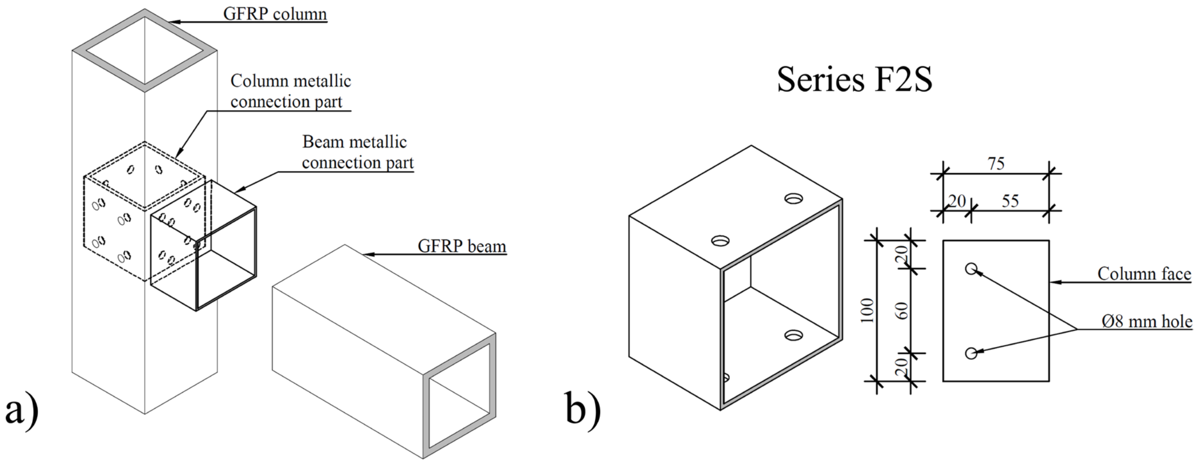

Figure 5.15 - Sleeve connection system (*cf*. Chapters 3 and 4): a) overall view of the sleeve beam-to-column connection system; b) beam auxiliary part of series.

Figure 5.16 depicts representative monotonic moment *vs*. rotation curves of the sleeve series BC-SC-360×1.5 and that of the sleeve connection series F2S. The cuff series BC-SC-360×1.5 registered higher initial stiffness (+51%) and ultimate bending moment (+37%) than sleeve series F2S, while presenting a similar average ductility index (+4%). The cyclic performance of series BC-SC-360×1.5 was also compared to that of series F2S. Figure 5.17 presents representative cyclic moment *vs*. rotation curve of series F2S, which presented overall lower moments than those of the cuff series (Figure 5.9).

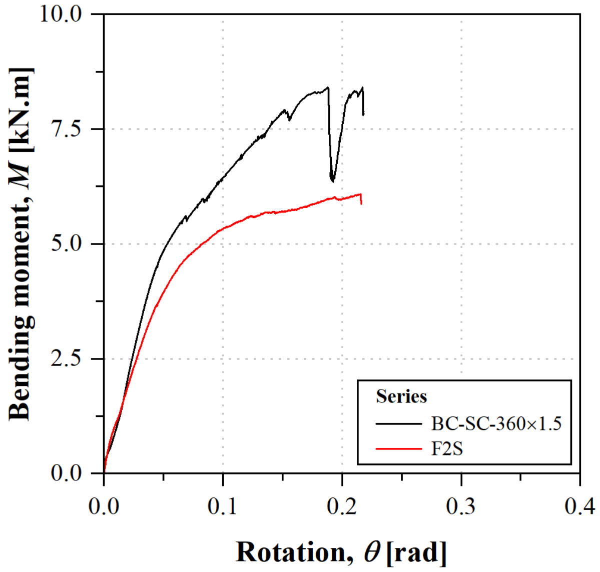

Figure 5.16 - Representative monotonic moment *vs.* rotation curves for series F2S (*cf.* Chapters 3 and 4); representative curve of series BC-SC-360×1.5 also included.

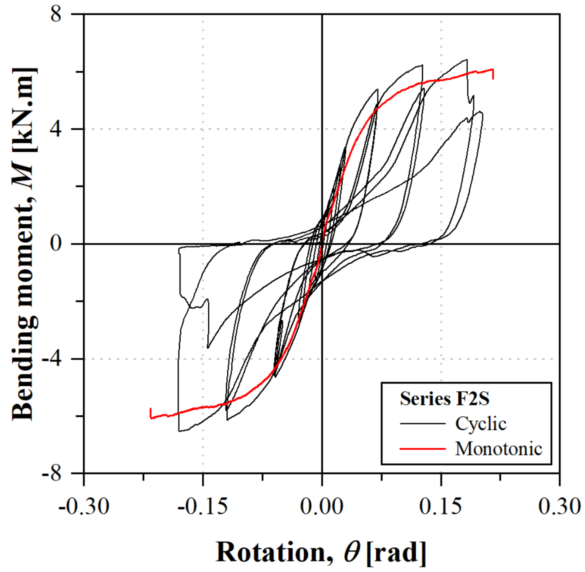

Figure 5.17 - Representative cyclic moment *vs.* rotation curves for series F2S (*cf.* Chapters 3 and 4); representative monotonic curve also included.

The cuff and sleeve connections were also compared regarding the ECCS [5.4] parameters, as shown in Figures 5.10 to 5.12. It should be noted that for series F2S only two repetitions of cycles with the same maximum absolute rotations were performed after the EP cycle (4th cycle). Therefore, cycles 5-6, 7-8 and 9-10 of series F2S should be compared to cycles 5-6, 8-9 and 11-12 of series BC-SC-360×1.5, respectively. Taking that into consideration, the stiffness and dissipated energy ratios plots of both connections presented very similar trends. On the other hand, the analysis of Figure 5.11 confirms that the cuff connection attained higher bending moments in the cyclic tests than the sleeve connection. The cyclic loading histories of the cuff and sleeve series differed regarding the maximum absolute displacements attained at each cycle, which prevents a direct comparison of the accumulated dissipated energy on the cyclic tests. Therefore, a comparison was made considering 4 cycles with comparable maximum absolute rotations (relative differences ranging from 11% to 23%); this comparison, illustrated in Figure 5.18, shows that cuff series BC-SC-360×1.5 is able to dissipate a higher amount of energy than sleeve series F2S - +21% when comparing cycle 8 of series BC-SC-360×1.5 to cycle 9 of series F2S. Since both series presented considerable pinching, this difference is related to the fact that the cuff series is able to achieve higher bending moments, owing to its aforementioned higher strength and stiffness.

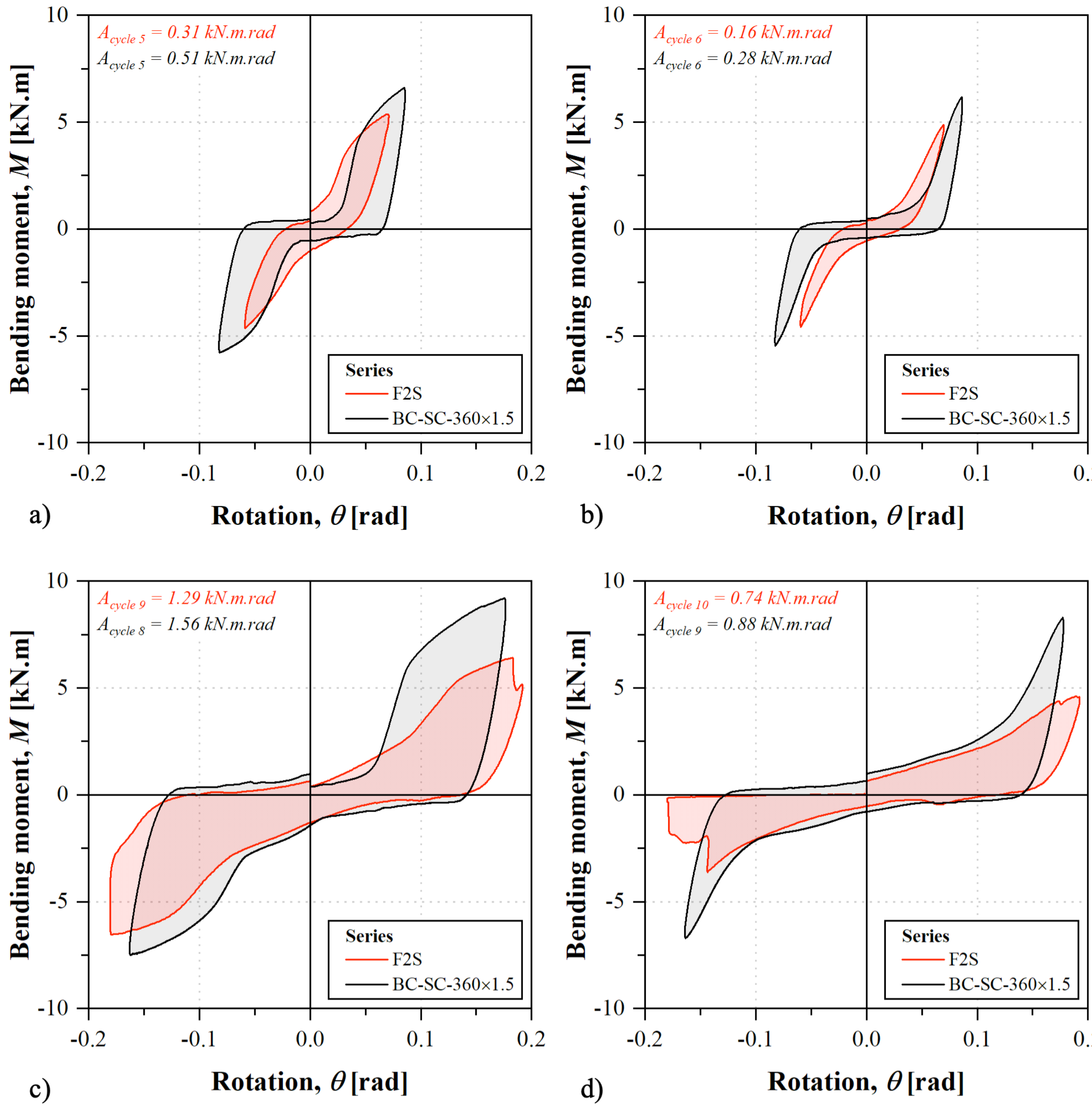

Figure 5.18 - Comparison of moment *vs.* rotation curves of cyclic tests of series F2S (*cf.* Chapters 3 and 4) and series BC-SC-360×1.5: a) cycle 5 of both series; b) cycle 6 of both series; c) cycle 9 of series F2S and cycle 8 of series BC-SC-360×1.5; d) cycle 10 of series F2S and cycle 9 of series BC-SC-360×1.5.

Overall, these results show that the stainless steel cuff connection system proposed herein provides enhanced mechanical performance, for both monotonic and cyclic actions, when compared to the sleeve connection system developed earlier (*cf.* Chapters 3 and 4). Additionally, the stainless steel cuff connection system analysed herein also presents improved durability over similar mild steel ones, being also faster and simpler to apply on site compared to the sleeve connection system, which requires arm-length access to the internal part of the column in order to fasten the bolts. On the other hand, from an aesthetical point of view, the sleeve connections have the advantage of being hidden inside the profiles.

5.6. CONCLUSIONS

This chapter presented an experimental study about the monotonic and cyclic short-term behaviour of beam-to-column connections between tubular pultruded GFRP profiles, involving the use of a novel stainless steel cuff part. The motivation of this study was two-fold: (i) the need to develop tailored and material-adapted connection systems for GFRP frames, and (ii) the promising results obtained in previous studies using composite cuff parts. Therefore, in the present study, the author aimed at further developing the cuff connection concept, by making use of the stainless steel properties, namely its ductility and durability. Monotonic tests were performed in four connection series, that differed in the plate thickness and length of the cuffs, and cyclic tests were performed in one connection series, the best performing one in the monotonic tests.

The mechanical performance of the cuff connections was highly influenced by the geometry and plate thickness of the stainless steel cuff part. The series with thicker cuff parts presented much higher initial stiffness and strength; the same applies to series with longer cuff parts, but the influence of this geometrical parameter was lower than the plate thickness. All connection series presented considerable ductility, taking advantage of the stainless steel material ductility. Additionally, more extensive GFRP damage was observed in series with thicker cuffs, as the profiles were subjected to higher stress concentrations, a consequence of using a stiffer connection part. Nonetheless, for the range of geometries tested, the connection series that presented the best overall performance in the monotonic tests was the one with the higher plate thickness and cuff length. Regarding the cyclic tests, the hysteretic response of the chosen cuff series presented significant pinching; however, a significant amount of energy dissipation was also registered in these tests.

The monotonic and cyclic performance of the connection series with the higher plate thickness and longer cuff part was also compared to a sleeve connection system previously investigated by the author (*cf.* Chapters 3 and 4). Regarding the monotonic behaviour, the cuff connection outperformed the sleeve connection in terms of initial stiffness and strength, while exhibiting similar ductility; moreover, it provided better cyclic performance, namely in terms of energy dissipation capacity.

Overall, the connection system with stainless steel cuff parts proposed in this study presented remarkable mechanical performance when used to join tubular GFRP profiles. Future optimization studies, using finite element models, should be performed regarding the cuffs' length and thickness, including other cross-section geometries, such as open section GFRP profiles.

5.7. REFERENCES

[5.1] Smith SJ, Parsons ID, Hjelmstad KD. (1999). Experimental comparisons of connections for GFRP pultruded frames. *Journal of Composites for Construction*, 3(1), 20-26.

[5.2] Singamsethi SK, LaFave JM, Hjelmstad KD. (2005). Fabrication and testing of cuff connections for GFRP box sections. *Journal of Composites for Construction*, 9(6), 536-544.

[5.3] Carrion JE, LaFave JM, Hjelmstad KD. (2005). Experimental behavior of monolithic composite cuff connections for fiber reinforced plastic box sections. *Composite Structures*, 67(3), 333-345.

[5.4] ECCS/TC1. (1986). Recommended testing procedure for assessing the behaviour of structural steel elements under cyclic loads.

[5.5] ASTM D 695-02 (2006) – Standard Test Method for Compressive Properties of Rigid Plastics. West Conshohocken

[5.6] EN ISO 527-1 (1997) Plastics – Determination of Tensile Properties – Part 1: General Principles. Brussels.

[5.7] ASTM D 2344/D 2344M-00 (2006) – Standard Test Method for Short-Beam Strength of Polymer Matrix Composite Materials and Their Laminates. West Conshohocken.

[5.8] ASTM D 5379/D 5379M (2005) – Standard Test Method for Shear Properties of Composite Materials by the V-Notched Beam Method. West Conshohocken.

[5.9] Chamis CC, Sinclair JH. (1977). Ten-deg off-axis test for shear properties in fiber composites. *Experimental Mechanics*, 17(9), 339-346.

[5.10] ISO/TC 164/SC 1 (2019). ISO 6892-1:2019. Metallic Materials - Tensile Testing - Part 1: Method of Testing at Room Temperature. British Standards Institution.

[5.11] CEN/TC 250 (2005). Eurocode 3 (EN1993): Design of Steel Structures – Part 1–8: Design of Joints.

[5.12] Weaver Jr W, Timoshenko SP, Young DH. (1991). *Vibration problems in engineering*. John Wiley & Sons.

[5.13] Jorissen A, Fragiacomo M. (2011). General notes on ductility in timber structures. *Engineering Structures*, 33(11), 2987-2997.

PART III

Beam-to-column connections for pultruded I-section profiles

Chapter 6

Monotonic and cyclic behaviour of a cleated connection system for I-section profiles

6.1. INTRODUCTION

This chapter presents an experimental study concerning the monotonic and cyclic behaviour of GFRP beam-to-column connections using stainless steel cleat parts. The main objective was to develop a beam-to-column connection system for GFRP structures, using readily available parts compatible with the corrosion resistance of GFRP and exploiting the metal's ductility. The experimental programme comprised four types of tests: (i) material characterization tests of the GFRP profiles and stainless steel plates used in the cleats; (ii) double-lap tests to evaluate the interface response between the GFRP and stainless steel bolts used in the beam-to-column connections; (iii) monotonic tests on full-scale beam-to-column connections with different cleat thicknesses, to assess their strength, stiffness and failure modes; and (iv) cyclic tests on full-scale beam-to-column connections to assess their hysteretic response, including their capacity to dissipate energy.

6.2. EXPERIMENTAL PROGRAMME

The following materials were used in the experiments: (i) pultruded GFRP I-section profiles ($150\times75\times8$ mm^2) made of E-glass fibres and an isophthalic polyester resin matrix (produced by *ALTO, Perfis Pultrudidos, Lda.*), comprising the same fibre architecture in the web and flanges; (ii) stainless steel cleats and plates, cold-formed from flat sheets, grade AISI 304, with thicknesses of 3, 6 and 8 mm; and (iii) stainless steel rods and bolts.

In addition, pultruded GFRP plates with rectangular section (40×8 mm^2) were used in the double-lap tests (*cf.* Section 6.2.2), with the same fibre architecture and matrix as the I-section profiles used in the beam-to-column tests (*cf.* Section 6.2.3).

6.2.1. Material characterization tests

The main mechanical properties of the GFRP profiles and plates (Table 6.1) were obtained from small-scale material characterization tests: (i) compressive strength in both longitudinal ($\sigma_{cu,L}$) and transverse ($\sigma_{cu,T}$) directions, and corresponding elastic moduli ($E_{c,L}$ and $E_{c,T}$); (ii) longitudinal tensile strength ($\sigma_{tu,L}$), modulus of elasticity ($E_{t,L}$) and Poisson ratio (ν_{LT}); (iii) longitudinal interlaminar shear strength ($\tau_{is,L}$); and (iv) in-plane shear strength (τ_{LT} and τ_{TL}) and corresponding shear moduli (G_{LT} and G_{TL}). Additionally, calcination tests (up to 800ºC) were performed, following the recommendations of ISO 1172 [6.1], on the section laminates, allowing to determine mass fibre ratios of 60% and 55% for the web and flange plates, respectively. Despite being produced using the same matrix and fibre architecture, some differences were observed in the properties of both pultruded shapes (I-section and flat plates), which may be related to the production and curing of the GFRP material.

Table 6.2 summarizes the main mechanical properties of the AISI 304 stainless steel (for the 3 mm and 8 mm thick plates), obtained from testing coupons extracted from the flat sheets used to cold-form the cleat auxiliary parts, namely the ultimate stress (f_u) and Young's modulus (E_s). Additionally, the bolts and rods used were M8 stainless steel grade A2-70, with yield stress (f_y) and ultimate stress (f_u) of 450 MPa and 700 MPa, respectively.

Additional details about the mechanical and physical characterization tests are provided in the Appendix B.

Table 6.1 - Mechanical properties of the GFRP material.

<table>
<tr><th>Test</th><th>Method</th><th>Specimen size</th><th>Property</th><th>Element</th><th>Average ± std. Dev.</th><th>Unit</th></tr>
<tr><td rowspan="9">Tension</td><td rowspan="9">EN ISO 527 [6.2]</td><td rowspan="9">15×8×300 mm³</td><td rowspan="3">$\sigma_{tu,L}$</td><td>I150-W</td><td>388.0 ± 25.0</td><td rowspan="3">[MPa]</td></tr>
<tr><td>I150-F</td><td>353.4 ± 32.7</td></tr>
<tr><td>Plate-40</td><td>334.5 ± 4.3</td></tr>
<tr><td rowspan="3">$E_{t,L}$</td><td>I150-W</td><td>43.4 ± 1.0</td><td rowspan="3">[GPa]</td></tr>
<tr><td>I150-F</td><td>39.6 ± 1.2</td></tr>
<tr><td>Plate-40</td><td>27.6 ± 0.4</td></tr>
<tr><td rowspan="3">υ_{LT}</td><td>I150-W</td><td>0.23 ± .02</td><td rowspan="3">[-]</td></tr>
<tr><td>I150-F</td><td>0.29 ± .02</td></tr>
<tr><td>Plate-40</td><td>0.27 ± 0.04</td></tr>
<tr><td rowspan="12">Compression</td><td rowspan="6">ASTM-D6641 [6.3]</td><td rowspan="4">12×8×156 mm³</td><td rowspan="2">$\sigma_{cu,L}$</td><td>I150-W</td><td>461.9 ± 31.0</td><td rowspan="2">[MPa]</td></tr>
<tr><td>I150-F</td><td>353.5 ± 32.7</td></tr>
<tr><td rowspan="2">$E_{c,L}$</td><td>I150-W</td><td>44.9 ± 1.7</td><td rowspan="2">[GPa]</td></tr>
<tr><td>I150-F</td><td>39.6 ± 1.2</td></tr>
<tr><td rowspan="2">12×8×123 mm³</td><td>$\sigma_{cu,T}$</td><td>I150-W</td><td>64.2 ± 2.12</td><td>[MPa]</td></tr>
<tr><td>$E_{c,T}$</td><td>I150-W</td><td>8.1 ± 0.6</td><td>[GPa]</td></tr>
<tr><td rowspan="6">ASTM-D695 [6.4]</td><td rowspan="6">20×8×35 mm³</td><td>$\sigma_{cu,L}$</td><td>Plate-40</td><td>316.0 ± 30.1</td><td>[MPa]</td></tr>
<tr><td>$E_{c,L}$</td><td>Plate-40</td><td>21.3 ± 1.2</td><td>[GPa]</td></tr>
<tr><td rowspan="2">$\sigma_{cu,T}$</td><td>I150-F</td><td>41.0 ± 3.6</td><td rowspan="2">[MPa]</td></tr>
<tr><td>Plate-40</td><td>51.9 ± 1.7</td></tr>
<tr><td rowspan="2">$E_{c,T}$</td><td>I150-F</td><td>2.8 ± 0.2</td><td rowspan="2">[GPa]</td></tr>
<tr><td>Plate-40</td><td>2.9 ± 0.3</td></tr>
<tr><td rowspan="3">Interlaminar shear</td><td rowspan="3">ASTM-D2344 [6.5]</td><td rowspan="3">18×8×48 mm³</td><td rowspan="3">$\tau_{is,L}$</td><td>I150-W</td><td>27.0 ± 1.3</td><td rowspan="3">[MPa]</td></tr>
<tr><td>I150-F</td><td>31.2 ± 1.0</td></tr>
<tr><td>Plate-40</td><td>33.8 ± 0.9</td></tr>
<tr><td rowspan="10">In-plane shear</td><td rowspan="10">ASTM-D5379 [6.6]</td><td rowspan="10">20×8×76 mm³
(Notched specimens)</td><td rowspan="3">τ_{LT}</td><td>I150-W</td><td>46.8 ± 3.1</td><td rowspan="3">[MPa]</td></tr>
<tr><td>I150-F</td><td>47.9 ± 2.6</td></tr>
<tr><td>Plate-40</td><td>52.4 ± 4.3</td></tr>
<tr><td rowspan="3">G_{LT}</td><td>I150-W</td><td>3.0 ± 0.3</td><td rowspan="3">[GPa]</td></tr>
<tr><td>I150-F</td><td>3.7 ± 0.3</td></tr>
<tr><td>Plate-40</td><td>3.0 ± 0.2</td></tr>
<tr><td rowspan="2">τ_{TL}</td><td>I150-W</td><td>31.2 ± 2.3</td><td rowspan="2">[MPa]</td></tr>
<tr><td>I150-F</td><td>27.3 ± 5.0</td></tr>
<tr><td rowspan="2">G_{TL}</td><td>I150-W</td><td>3.3 ± 0.5</td><td rowspan="2">[GPa]</td></tr>
<tr><td>I150-F</td><td>2.5 ± 0.2</td></tr>
</table>

Note: I150-F refers to the profile flange, I150-W refers to the profile web and Plate-40 refers to the 40 mm wide plate.

Table 6.2 - Mechanical properties of the GFRP material.

Test	Method	Property	Element	Average ± std. Dev.	Unit
Tension	EN 10002-1 [6.7]	$f_{0.2\%}$	3 mm plate	287 ± 9.9	[MPa]
			8 mm plate	300 ± 5.4	
		f_u	3 mm plate	651 ± 30.4	[MPa]
			8 mm plate	691 ± 14.4	
		E_s	3 mm plate	194 ± 9.4	[GPa]
			8 mm plate		

6.2.2. Double-lap tests

The interaction between the stainless steel bolts and GFRP plates was assessed through monotonic double-lap tests, allowing to determine the edge and pitch distances that maximized the strength of the GFRP plates under bearing loads. Figure 6.1 presents the configurations of five double-lap test series, namely with one bolt and edge distances of (i) 15 mm (DL-15); (ii) 25 mm (DL-25); (iii) 35 mm (DL-35); (iv) 70 mm (DL-70); and (v) with two bolts and edge distance and inner spacing of 35 mm (DL-2B). All specimens had a plate thickness of 8 mm and 40 mm of width. In this regard, it should be mentioned that available design codes [6.8-6.10] specify a minimum edge distance of 32 mm. Four specimens of each series were tested, comprising a total of 20 specimens.

The GFRP plates were bolted to two steel plates, according to the scheme presented in Figure 6.2. The bolts were not threaded in the specimens' plate-bolt interface (DIN931 M8×65), and the hole diameter matched that of the bolts (8 mm). A clearance of 2 mm was guaranteed between the auxiliary steel plates and the GFRP plates to assure that no friction existed throughout the tests. The tests were performed in a universal testing machine (*INSTRON*, model 1343) under displacement control at a rate of 2 mm/min. This rate was chosen to minimize strain-rate effects and the end of the linear stage was achieved in under 1 minute for all test specimens. In addition to the applied load, which was measured by the test machine's built-in load cell, the relative displacement between sections A-A' and B-B' (*cf.* Figure 6.2a) was measured by two displacement transducers (*TML*, model CDP-50).

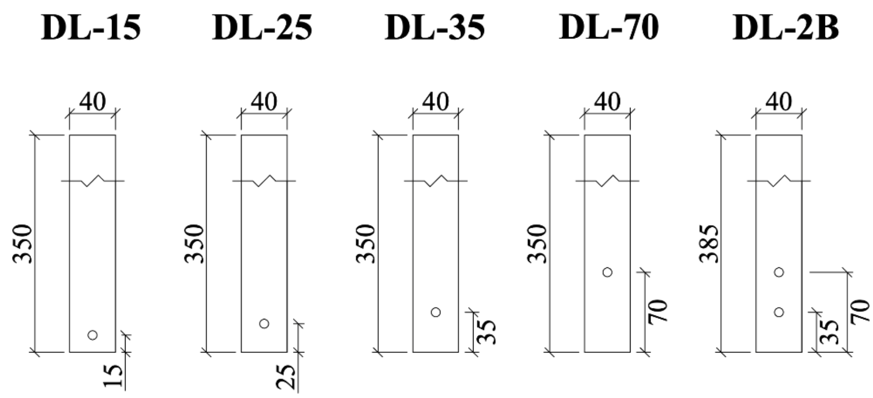

Figure 6.1 - Double-lap tests: test series.

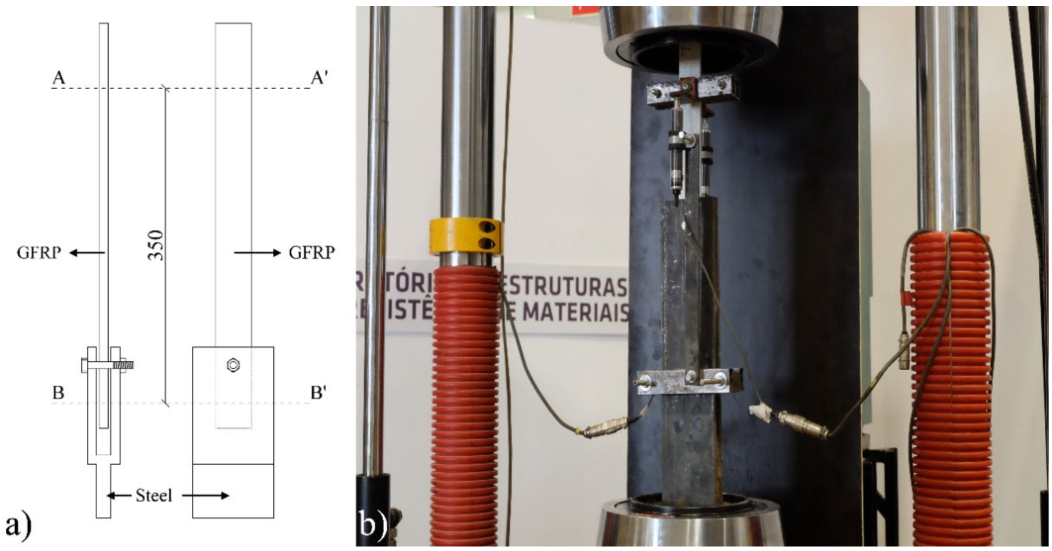

Figure 6.2 - Double-lap tests: a) illustrative scheme; b) test setup.

6.2.3. Beam-to-column connection tests

6.2.3.1. Description of test series

The test specimens consisted of exterior beam-to-column connections, representative of a façade column. The specimens comprised one GFRP column with 900 mm of length connected at mid-height to an 800 mm long GFRP beam by means of cold-formed stainless-steel cleats. The beam-to-column tests comprised nine different connection series, four of which including column reinforcements, as shown in Figure 6.3. In order to assess the influence of the bolt position and number, as well as the influence of the cleats' thickness and their location, the following configurations were considered: (i) series BC-3-F, with two 3 mm thick stainless steel cleats positioned on the beams' flanges, and one row of bolts (bolt edge distance in GFRP beam of 35 mm); (ii) series BC-3-W, with two 3 mm thick stainless steel cleats positioned on the beams' web, and one row of bolts (bolt edge distance in GFRP beam of 20 mm); (iii) series BC-8-F, with two 8 mm thick stainless steel cleats positioned on the beam's web, and one row of bolts (bolt edge distance in GFRP beam of 35 mm); (iv) series BC-6-F2, with two 6 mm thick stainless steel cleats positioned on the beam's web, and two rows of bolts (bolt edge distance in GFRP beam of 50 mm and 35 mm of pitch distance); (v) and series BC-8-F2, with two 6 mm thick stainless steel cleats positioned on the beam's web, and two rows of bolts (bolt edge distance in GFRP beam of 50 mm and 35 mm of pitch distance). The thickness of the stainless steel cleats was expected to have considerable influence on the connections response, especially regarding: (i) stiffness, with higher thicknesses likely to provide lower beam deflections; and (ii) ductility, with lower thicknesses likely to enable higher plastic deformations. Thereafter, the three thicknesses selected (3, 6 and 8 mm) aimed at testing a (reasonable) lower and higher bound of cleat thicknesses, as well as an intermediate solution, which should provide a compromise between acceptable initial stiffness and ductility.

Regarding the column's reinforcement, four additional series were tested, in which the column reinforcements presented in Figure 6.3 were added to the previously described flange cleated connections: (i) series BC-3-F-R; (ii) series BC-8-F-R; (iii) series BC-8-F2-R; and (iv) series BC-6-F2-R. The reinforcements consisted of replacing the bolts connecting the cleats to the column by stainless steel threaded rods (DIN975 M8, A2-70). These rods were extended from the cleat facing flange to the exterior flange of the column, where they were joined to stainless steel plates with the same thickness of the cleats used in each series. This type of reinforcement, already used with success in previous investigations [6.11,6.12,6.13,6.14], aimed at mobilizing the whole section of the column and avoid the premature rupture of its web-flange junction (*cf.* Section 6.4.2).

Similarly to the double-lap tests, the bolts used (DIN 931 M8×40) were not threaded in the contact with the GFRP material and the holes, in both GFRP and stainless steel elements; holes were drilled with a Ø8 mm drill, i.e. no clearance was provided. Washers (DIN 9021 M8×24) were used in-between the bolts, the GFRP material and the 3 mm stainless steel plates. A torque of 10 N.m, the minimum torque used in several previous works (*e.g.* [6.15]), was applied to all bolts using a torque wrench.

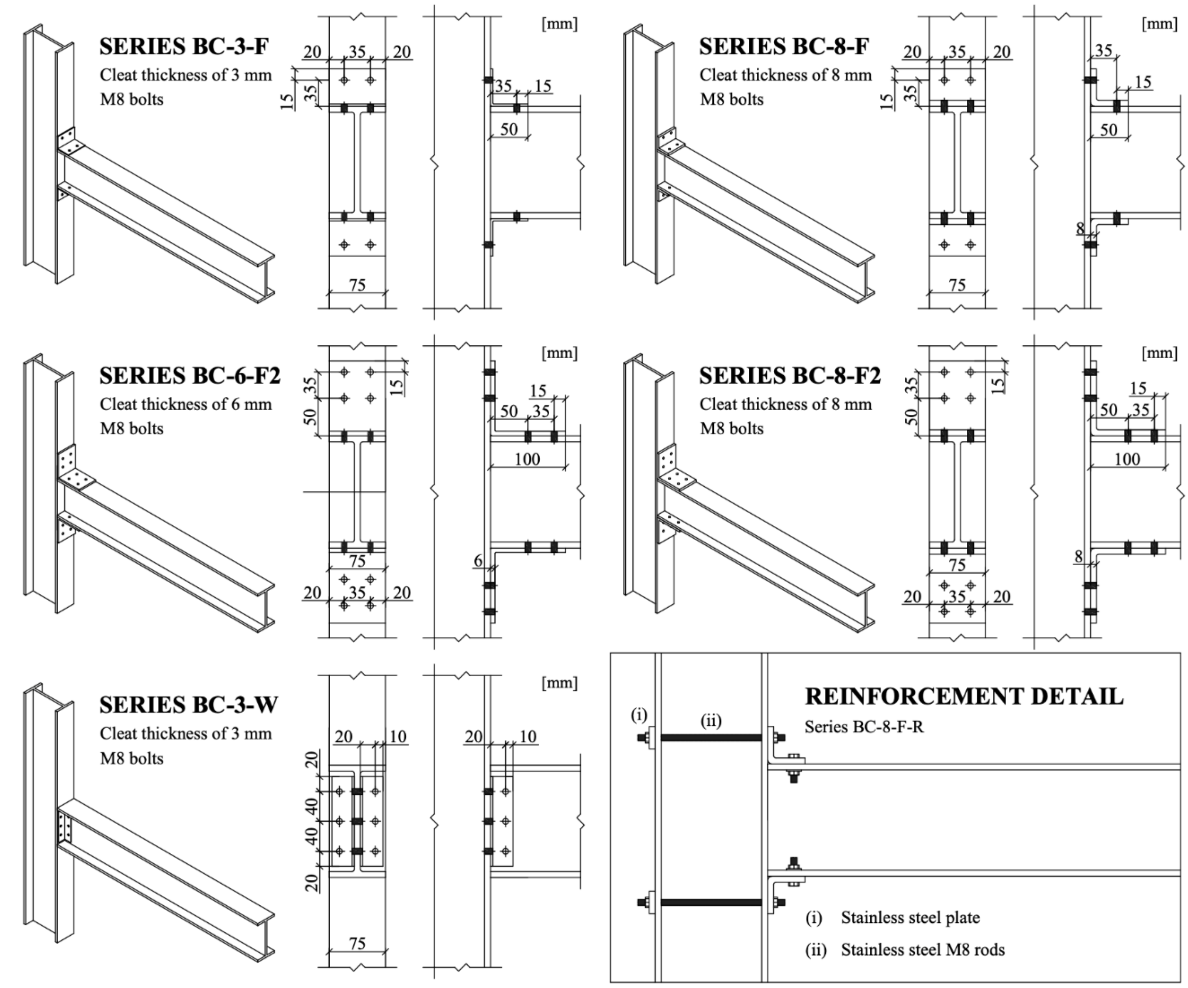

Figure 6.3 - Beam-to-column tests: non-reinforced test series and reinforcement detail.

Monotonic tests were performed for all nine connection series described above. The best performing ones, with and without reinforcement, were then selected for the cyclic tests, namely series (i) BC-3-F, (ii) BC-3-F-R, (iii) BC-6-F2, and (iv) BC-6-F2-R. Three specimens were tested for each series and type of loading, resulting in a total of 12 and 6 monotonic and cyclic tests, respectively.

6.2.3.2. Test setup and procedure

The test setup is presented in Figure 6.4a. The beam-to-column tests were performed in a steel closed loading frame anchored to the laboratory's strong floor. The load application system consisted of (i) a hydraulic jack (from *DARTEC*) with load capacity of 250 kN and maximum stroke of 400 mm (*cf.* Figure 6.4a, point A), and (ii) two mechanical hinges guaranteeing the perpendicularity of the applied load to the beam (*cf.* Figure 6.4a, point B). The applied load was measured by a load cell (from

TML) with capacity of 300 kN (*cf.* Figure 6.4a, point C). The rotations and displacements of the columns' ends were prevented by means of two machined steel blocks with 30 mm indentations shaped to match the profiles' I-section (*cf.* Figure 6.4a, points D), while the out-of-plane displacements of the beam were prevented by means of two aluminium bars positioned near the beams' free end (*cf.* Figure 6.4a, point E)[1].

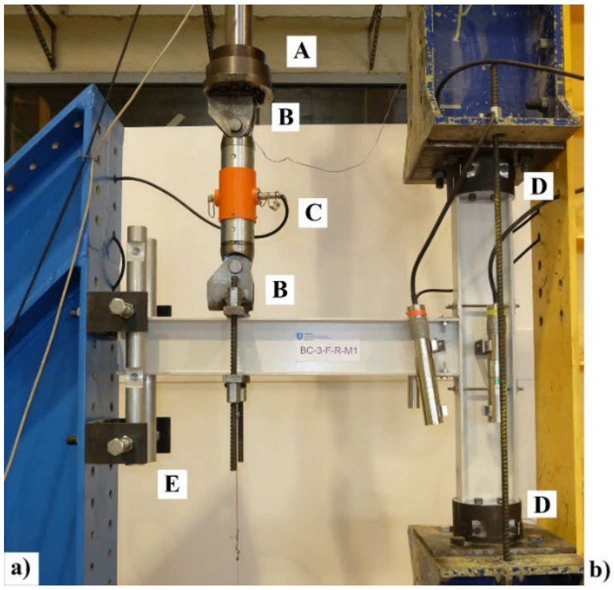

Figure 6.4 - Beam-to-column tests: a) test setup; b) instrumentation.

The positioning of the instrumentation used in the beam-to-column tests is presented in Figure 6.4b. The vertical displacement imposed to the beam was measured by the displacement transducer built-in the hydraulic jack and the rotations of the specimens were assessed by means of a pair of inclinometers (from *TML*), one located in the beam and the other in the column (the relative rotation of the connection was obtained from the difference between their measurements). The data was gathered by a data logger (from *HBM*) and stored in a PC at a rate of 5 Hz.

The monotonic tests were conducted under displacement control, at a rate of 0.25 mm/min, until the maximum stroke of the hydraulic jack was reached (± 200 mm) or until the structural integrity of the

[1] This test setup, fully restraining the columns' ends, allows to retrieve the behaviour of the connection itself (with little influence on the columns flexibility), while allowing damage modes in the column to occur. However, this setup may influence the post-failure behaviour of specimens which present failure in the column, in particular, web-junction tensile failure. In the present study this occurred only in the post-failure behaviour of non-reinforced specimens, as discussed on Section 6.4.1.

connection was compromised. The displacement histories of the cyclic tests were defined according to the ECCS protocol [6.16][2].

According to the complete test procedure described in the ECCS protocol [6.16], the maximum displacement in each load cycle is a multiple of the displacement at the end of proportionality (δ_{EOP}) attained in the monotonic tests: (i) before the displacement at the end of proportionality is reached, one cycle at ¼, ½, ¾ and 1 times the displacement at the end of proportionality is performed; (ii) after the displacement at the end of proportionality is reached, three cycles up to 2*n* of the displacement at the end of proportionality are performed, where *n* is an increasing integer, until the maximum stroke of the hydraulic jack is reached or until substantial failure of the connection is registered. Figure 6.5 presents the evolution of imposed displacements with the number of cycles used in the cyclic tests, which were also performed under displacement control at a rate of 0.5 min/mm. Both monotonic and cyclic displacement rates were chosen in order to allow the observation of damage evolution during the tests, within a feasible time period, while minimizing strain-rate effects.

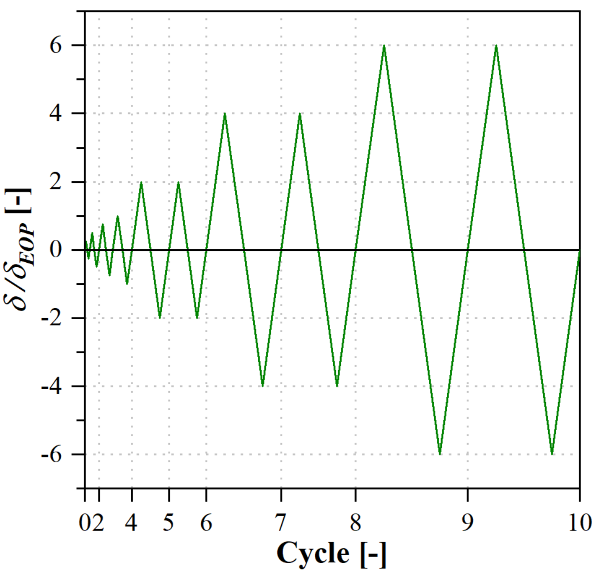

Figure 6.5 - Beam-to-column tests: cyclic tests load history.

[2] It should be mentioned that this protocol was originally developed for steel structures. To the author's best knowledge, the only paper reporting GFRP beam-to-column cyclic tests that provided details and rationale for a load protocol (Zhang *et al*. [6.17]) also used a test protocol that had been developed for steel structures. Moreover, owing to the adoption of stainless steel cleats (instead of FRP cleats), which were designed to present significant plastic deformations prior to extensive GFRP damage, the behaviour of the connection specimens tested agrees well with the typical behaviour of steel connections addressed by the ECCS protocol.

6.3. BEHAVIOUR OF DOUBLE-LAP CONNECTIONS

Figures 6.6 and 6.7 present the load *vs*. relative displacement curves for all series[3], and Table 6.3 summarizes the main results, namely the initial stiffness (K), the failure load (F_u), the failure modes and the estimates of shear-out (τ_{so}) and bearing ($\sigma_{br.L}$) strengths. Figure 6.8 shows the typical failure modes of each series.

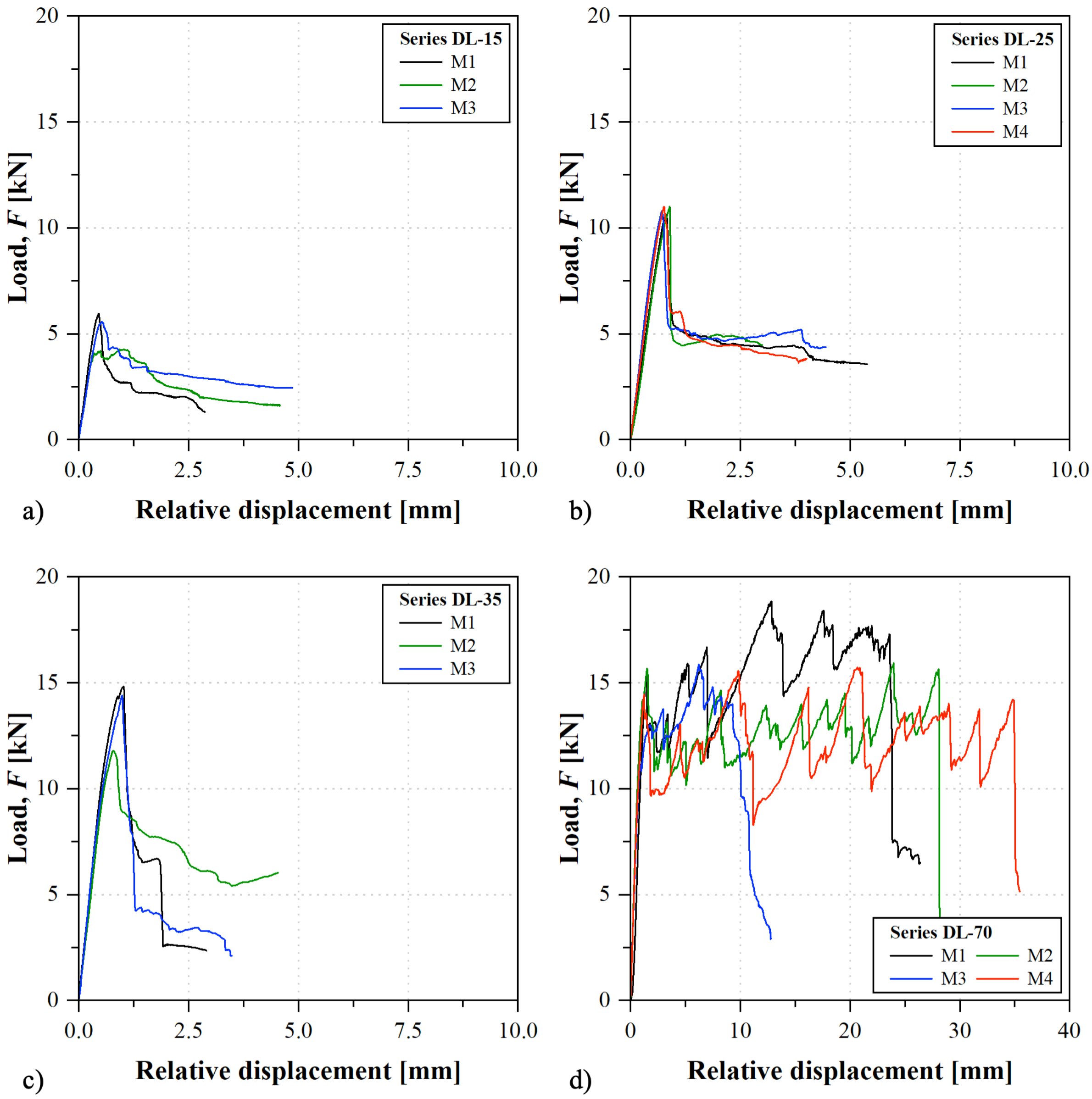

Figure 6.6 - Double-lap tests: relative displacement *vs*. load of one bolt series - a) series DL-15; b) series DL-25; c) series DL-35; and d) series DL-70.

[3] Two specimens (one of series DL-15 and one of series DL-35) were not included, as the results were considered not valid.

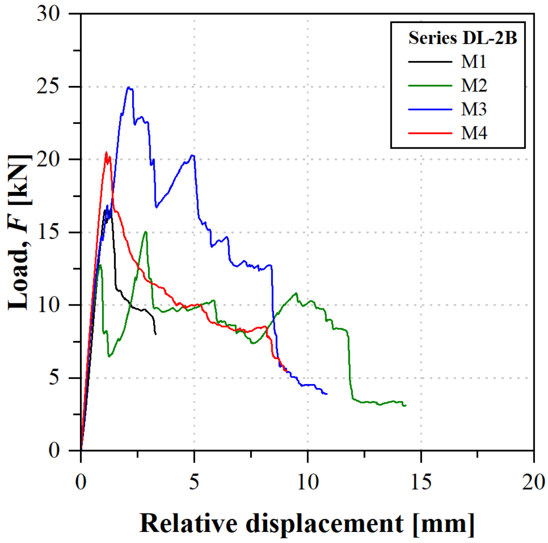

Figure 6.7 - Double-lap tests: relative displacement *vs*. load of two bolt series - series DL-2B.

Table 6.3 - Double-lap tests: summary of experimental results.

Series	K (kN/mm)	F_u (kN)	Failure mode	τ_{so} (MPa)	$\sigma_{br.L}$ (MPa)
DL-15	14.34 ± 1.52	5.25 ± 0.89	Shear-out	31.26 ± 6.65	-
DL-25	17.39 ± 2.39	10.85 ± 0.18	Shear-out	32.67 ± 0.84	-
DL-35	20.08 ± 1.42	13.67 ± 1.64	Shear-out	28.53 ± 3.44	-
DL-70	18.95 ± 0.23	16.58 ± 1.50	Bearing and shear-out	-	260.22 ± 23.48
DL-2B	19.85 ± 1.19	19.28 ± 4.43	Bearing and shear-out	-	-

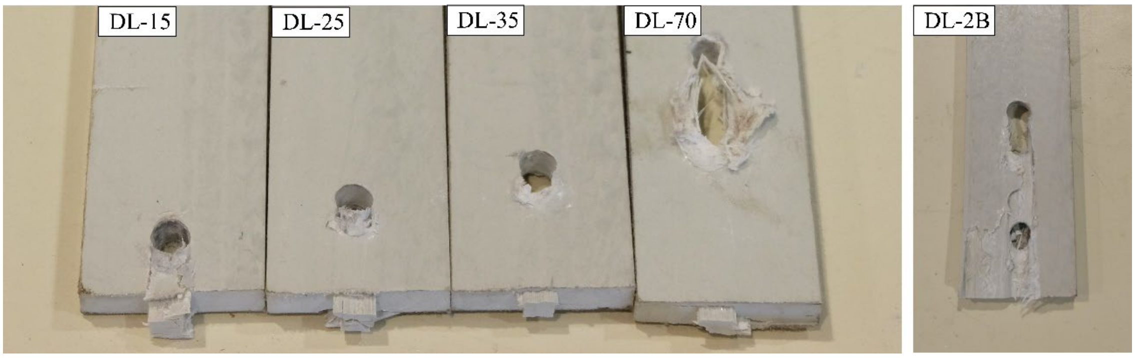

Figure 6.8 - Double-lap tests: details of a representative specimen of each series after test.

The various series of double-lap specimens with one bolt presented very consistent results. In all series, the behaviour was quasi-linear with similar stiffness (*cf.* Table 6.3) up to a peak load, associated to the first damage, which increased with the edge distance. In series DL-15, DL-25 and DL-35, the peak load was followed by a substantial load drop, caused by shear-out failure (*cf.* Figure 6.6). For series DL-70, the linear stage was followed by a markedly non-linear stage, with successive load reductions and increases around an almost horizontal plateau, until an ultimate load drop occurred. This different behaviour was due to the larger edge distance, which promoted the occurrence of a pseudo-ductile bearing failure mode. Nevertheless, the final failure of DL-70 specimens was still due to shear-out, but it occurred for much larger relative displacements (~2 to 8 times than those of the other series), when the damage on the GFRP plate was extensive and the (effective) edge distance was consequently reduced (*cf.* Figure 6.6). It should be noted that the end of the linear stage in series DL-70 occurred for similar loads to those of series DL-35, suggesting that the transition of the failure mode from shear-out to bearing occurs at an edge distance close to 35 mm. Thereafter, in order to promote more ductile failure modes, the geometrical recommendations of current design codes [6.8-6.10] may have to be reviewed, as they recommend a lower edge distance of 32 mm, as discussed earlier (*cf.* Section 6.2.2).

The GFRP double-lap tests with one bolt allowed to estimate the shear-out and bearing strengths in the longitudinal direction (τ_{so} and $\sigma_{br,L}$, respectively), in accordance with the Italian Guidelines [6.8] and CEN's Design Prospect [6.10]:

$$\tau_{so} = \frac{F_u}{(2e - d)t} \tag{6.1}$$

$$\sigma_{br,L} = \frac{F_u}{d \times t} \tag{6.2}$$

where F_u is the failure load, e is the edge distance, d is the bolt diameter, and t is the plate thickness. The shear-out strength was estimated for specimens of series DL-15, DL-25 and DL-35, while the bearing strength was estimated for specimens of series DL-70; both results are presented in Table 6.3. The shear-out strength estimated from Eq. (6.1) was consistent for the different series, being similar to the in-plane shear strength (τ_{LT}) obtained from the material characterization tests (*cf.* Table 6.1). In fact, the aforementioned standards suggest the use of this mechanical property to estimate the shear-out strength [6.8,6.10]. On the other hand, the estimated bearing strength is slightly lower than the longitudinal compressive strength ($\sigma_{cu,L}$) determined for the 40 mm plates (cf. Section 6.2.1). This result is consistent with previous studies for different FRP materials [6.18] and it raises concerns regarding the use of the compressive strength to determine the bearing load in the design of bolted connections, a procedure recommended by some authors [6.19,6.20].

Regarding series DL-2B (with two bolts), although all specimens showed an initial linear behaviour with similar stiffness, they presented significant scatter in terms of maximum load and post-peak behaviour (*cf*. Figure 6.7). All specimens of this series exhibited signs of shear-out and bearing failure; however, it was not possible to identify which failure mode occurred first. In comparison with the one-bolt series with shear-out failure, the load drop in series DL-2B was not so sudden, with most specimens being able to retain significant residual strength up to large relative displacements (>5 mm). On the other hand, compared to series DL-70, such residual strength was much lower and sustained for lower relative displacements; yet, the maximum strength in series DL-2B was 21% higher than that of series DL-70.

6.4. MONOTONIC BEHAVIOUR OF BEAM-TO-COLUMN CONNECTIONS

This section presents the experimental results of the monotonic tests of the beam-to-column connections, beginning with the discussion of the load/moment *vs*. displacement/relative rotation behaviour of all series, followed by a description of the failure modes. Table 6.4 summarizes the results obtained in the monotonic tests, namely the maximum load (F_u), the corresponding displacement (d_{Fu}) and bending moment (M_u), the initial rotation stiffness (K_θ), the failure modes and the ductility indexes (μ_d).

Table 6.4 - Beam-to-column monotonic tests: summary of experimental results.

Series	F_u (kN)	d_{Fu} (mm)	M_u (kN)	K_θ (kN.m/rad)	Ultimate failure mode	μ_d (-)
BC-3-F	1.48 ± 0.38	22.9 ± 11.4	0.97 ± 0.25	109.5 ± 34.6	Tensile rupture of the column's web-flange junction	-
BC-3-W	0.79	10.1	0.52	67.0		
BC-8-F	2.21 ± 0.46	11.7 ± 1.2	1.45 ± 0.30	170.0 ± 21.5		
BC-8-F2	2.28 ± 0.84	10.1 ± 0.4	1.49 ± 0.55	210.2 ± 53.1		
BC-6-F2	1.91 ± 0.20	27.9 ± 7.2	1.25 ± 0.13	212.6 ± 40.3		
BC-3-F-R	7.10 ± 0.56	111.9 ± 9.3	4.65 ± 0.37	139.4 ± 23.4	Shear-out of the beam's bolts	0.968 ± 0.004
BC-8-F-R	5.68 ± 0.38	36.4 ± 4.6	3.72 ± 0.25	234.7 ± 92.4	Transverse compression of column's web; shear-out of the beam's bolts	0.860 ± 0.065
BC-6-F2-R	10.87 ± 0.36	131.4 ± 43.2	7.12 ± 0.24	218.7 ± 28.3	Transverse compression of column's web	0.917 ± 0.013
BC-8-F2-R	8.64 ± 1.16	35.0 ± 12.9	5.66 ± 0.76	370.0 ± 34.0	Shear-out and tearing of the beam's top flange	0.839 ± 0.033

Note: Only two specimens were considered for series BC-3-W, therefore no standard deviation is presented.

6.4.1. Load *vs*. displacement and moment *vs*. relative rotation behaviour

Figures 6.9 and 6.10 present representative load *vs*. displacement and bending moment *vs*. relative rotation curves, respectively, of the non-reinforced series. The connection series with beam web-cleats (BC-3-W) presented considerably lower stiffness and strength than the remaining ones. On the other hand, the average stiffness and strength of the flange-cleated non-reinforced series was similar (with relative differences within the experimental scatter), indicating that using either thicker cleats or adding bolt rows without column reinforcements is not effective in improving the connections performance. It is worth referring that the results obtained in the monotonic tests presented significant scatter for most non-reinforced series (with CoVs up to 37%, *cf*. Table 6.4).

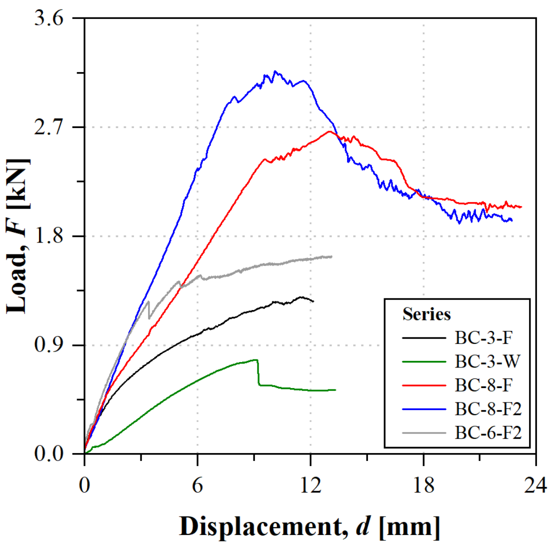

Figure 6.9 - Monotonic tests on non-reinforced beam-to-column series: representative load *vs*. displacement curves.

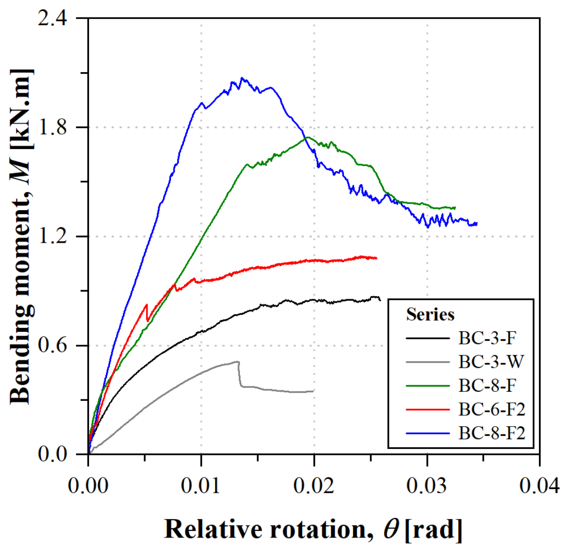

Figure 6.10 - Monotonic tests on non-reinforced beam-to-column series: representative bending moment *vs*. relative rotation curves.

Figures 6.11 and 6.12 present the load *vs*. displacement curves and representative moment *vs*. relative rotation curves of the reinforced specimens, respectively. The behaviour within each series was very similar, as attested by Figure 6.11. Regarding the stiffness, series BC-3-F-R and BC-8-F2-R presented the worst and best performance, respectively. Additionally, series with thinner cleats (BC-3-F-R and BC-6-F2-R) presented more markedly non-linear behaviour and higher ultimate displacement (d_{Fu}). Finally, the increase of the cleat thickness, for the same number of bolt rows, did not result in a strength increase, with series BC-3-F-R and BC-6-F2-R outperforming series BC-8-F-R and BC-8-F2-R, respectively.

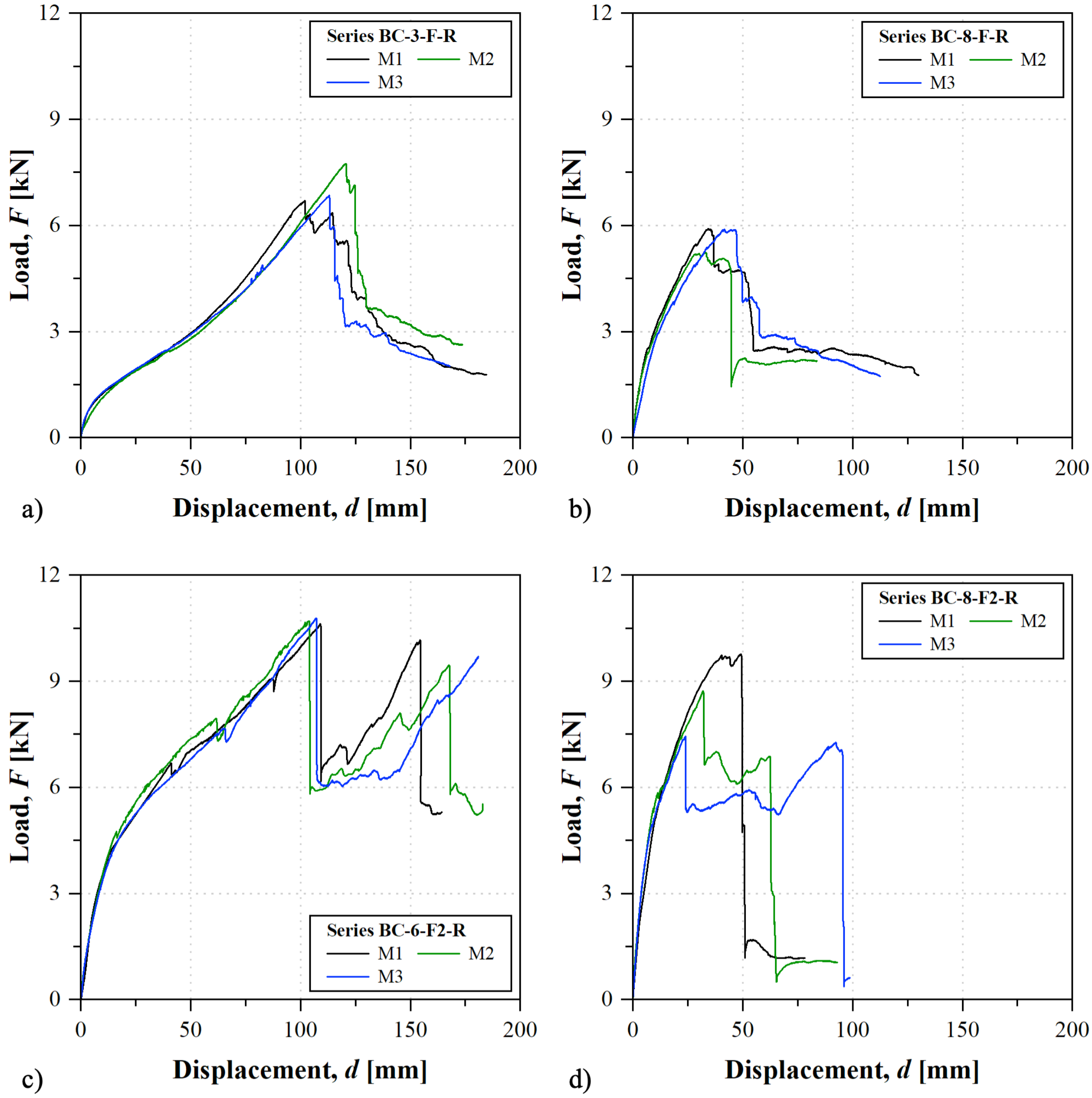

Figure 6.11 - Monotonic tests on reinforced beam-to-column series: load *vs.* displacement curves of a) series BC-3-F-R; b) series BC-8-F-R; c) series BC-6-F2-R; d) series BC-8-F2-R.

The specimens from series BC-3-F-R presented a gradual loss of initial stiffness up to a load of ~1.5 kN. Then, they presented linear behaviour up to ~3.0 kN and, after that point, the stiffness increased slightly until the peak load was reached. After this point, the load presented an abrupt reduction, followed by a more gradual decrease.

Regarding series BC-8-F-R, all specimens initially presented a quasi-linear behaviour up to a load of ~1.5 kN, after which a gradual stiffness reduction was observed. Finally, specimens failed for a load of 5.7 kN.

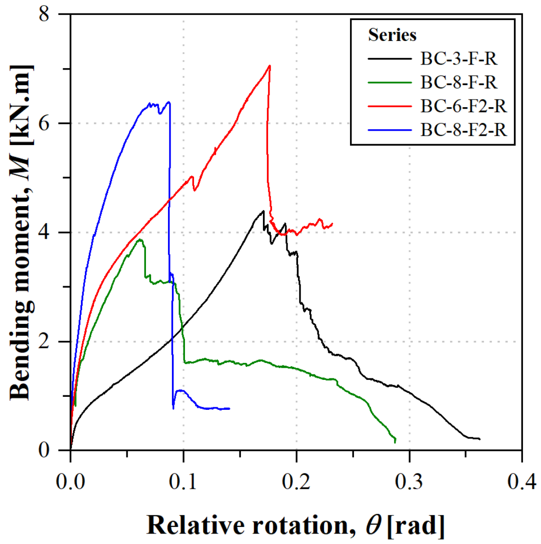

Figure 6.12 - Monotonic tests on reinforced beam-to-column series: representative bending moment *vs.* relative rotation curves.

In what concerns series BC-6-F2-R, the load *vs*. displacement behaviour presented the following stages: (i) an initial elastic stage until ~3 kN; (ii) a stage with progressive stiffness reduction up to a load of ~6 kN; (iii) a stage with constant stiffness until failure occurred, for a load of ~11 kN; and (iv) a final stage of load recovery. Two specimens of this series presented a final load drop for displacements close to the hydraulic jack's maximum stroke, while the third one did not fail and the test was stopped when the maximum stroke was reached.

Series BC-8-F2-R initially presented a quasi-linear stage followed by a non-linear path with progressive stiffness reduction and finally a sudden load drop. Two specimens were able to recover some load after that stage, one of which also withstood large displacement until finally failing at ~95 mm.

Overall, the connection systems tested presented an approximately bi-linear behaviour, with an initial stiffer behaviour followed by a more flexible response. A similar behaviour was also reported in previous studies of flange-cleated steel beam-to-column connections [6.21,6.22]. Thereafter, the intersection of the initial and final stiffness (extrapolated) lines, illustrated in Figure 6.13, was taken as the connections' point where the proportionality ends, a procedure that is in line with the ECCS protocol [6.16]. Table 6.5 presents the displacements (δ_{EOP}) and loads (F_{EOP}) at the end of proportionality of the series subjected to cyclic tests.

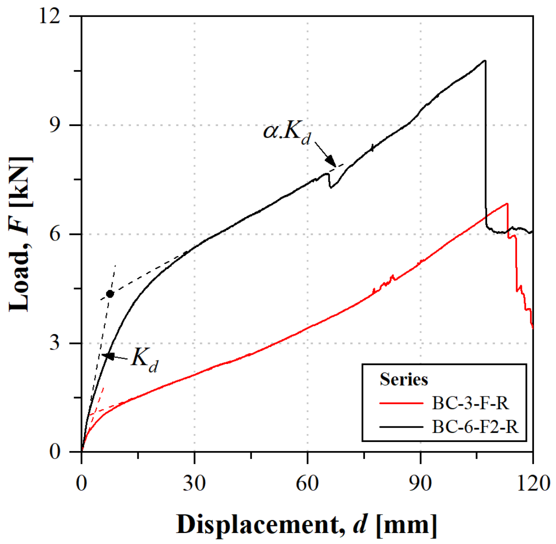

Figure 6.13 - Example of the definition of the point at the end of proportionality of the monotonic tests.

Table 6.5 - Beam-to-column monotonic tests: displacements and loads at the end of proportionality.

Series	F_{EOP} (kN)	d_{EOP} (mm)
BC-3-F	0.79 ± 0.13	2.24 ± 1.75
BC-6-F2	1.26 ± 0.03	2.61 ± 0.55
BC-3-F-R	1.04 ± 0.04	3.09 ± 0.62
BC-6-F2-R	4.49 ± 1.47	8.93 ± 0.14

6.4.2. Failure modes

The ultimate failure of all non-reinforced connection specimens occurred due to the tensile rupture of the web-flange junction of the columns, as shown in Figure 6.14a, for relatively low loads, as mentioned in Section 6.4.1. That was the only damage observed for all series with exception of those with 3 mm thick cleats, in which plasticity of the stainless steel cleats under bending was also observed (*cf.* Figure 6.14b).

The specimens of series BC-3-F-R presented the following damage modes: (i) plasticity of the stainless steel cleats under bending, visible from the early stages of the tests (*cf.* Figure 6.15a); (ii) tensile rupture of the top and bottom web-flange junctions of the beam (*cf.* Figure 6.15a) - the instant of occurrence and sequence of these damages differed for the three specimens; and, finally, (iii) shear-out of the bolts of the beams' top flange, for loads around ~7 kN and a displacement of ~125 mm (*cf.* Figure 6.15b).

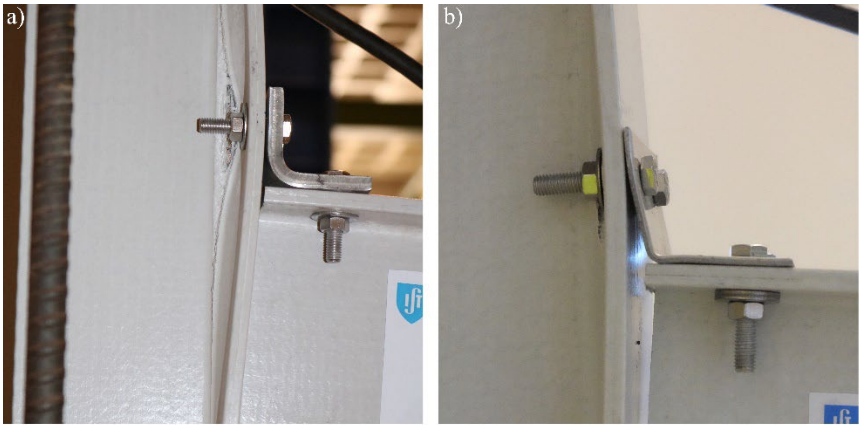

Figure 6.14 - Monotonic tests of beam-to-column non-reinforced connections: failure modes - a) tensile rupture of the web-flange junction of the column (all series); b) plasticity of the stainless steel cleats under bending (series BC-3-F and BC-3-W).

In the specimens of series BC-8-F-R, the first damage was observed for loads of ~3.0 kN consisting of the rupture of the top web-flange junction of the beams (*cf.* Figure 6.15c). After that point, the rotation of the top cleat as a rigid body was visible (*cf.* Figure 6.15c). Ultimately, the specimens failed due to a combination of different damages occurring almost at the same time: (i) compression failure of the columns' web (*cf.* Figure 6.15d); (ii) shear-out of the bolts at the top beam's flange (in some cases, also involving the tearing of the flanges, *cf.* Figure 6.15e); and (iii) rupture of the bottom web-flange junction of the beam.

As for series BC-6-F2-R, the initial damage modes involved (i) plasticity of the stainless steel cleats under bending, starting at ~4.0 kN, and (ii) rupture of the beams' top web-flange junction at ~6.0 kN. Specimen BC-6-F2-R-M2 also presented tensile failure of the beam's top web-flange junction for ~8 kN (similarly to Figure 6.15c). After that, all specimens presented compression failure of the columns' web, caused by the local stresses introduced by the top reinforcement, for loads of ~11.0 kN (*cf.* Figure 6.15f). After this point, although the crushing of the columns' web progressed (corresponding to minute load drops), specimens presented a load increase owing to the redistribution of stresses to connection elements that remained intact. For specimens BC-6-F2-R-M1 and BC-6-F2-R-M2, this was followed by compression failure of the column's web near the bottom cleat, when the displacement was ~150-160 mm.

Figure 6.15 - Monotonic tests of beam-to-column reinforced connections: failure modes - a) plasticity of the stainless steel cleats under bending and tensile rupture of the beam's bottom web-flange junction (series BC-3-F-R); b) shear-out failure at beams' top flange (series BC-3-F-R); c) tensile rupture of the beam's top web-flange junction and rotation of the top cleat (series BC-8-F-R); d) slight compression failure of the columns' web (series BC-8-F-R); e) shear-out and tearing failure combination on the beams' top flange (series BC-8-F2-R); f) compression failure of the column web panel (series BC-6-F2-R); g) plasticity of the stainless steel cleats under bending (series BC-8-F2-R); h) shear-out and tearing failure combination on the beams' top flange (series BC-8-F2-R).

Finally, the damage progression in series BC-8-F2-R was as follows: (i) rupture of the web-flange junction of the beams' top flange, at 3.0-4.0 kN; (ii) plasticity of the stainless steel cleats under bending (*cf.* Figure 6.15g), noticeable at around 6.0 kN; and final failure due to (iii) a combination of shear-out and tearing on the beams' top flange (*cf.* Figure 6.15h).

6.5. CYCLIC BEHAVIOUR OF BEAM-TO-COLUMN CONNECTIONS

This section presents the experimental results of the cyclic tests of beam-to-column connection series BC-3-F, BC-6-F2, BC-3-F-R and BC-6-F2-R. The results were analysed in terms of (i) moment *vs*. relative rotation response, (ii) hysteretic behaviour and (iii) failure modes.

6.5.1. Moment *vs*. relative rotation behaviour

Figure 6.16 presents representative bending moment *vs.* relative rotation curves for each series, together with a corresponding monotonic curve. For all series, the cyclic test curves showed considerable symmetry and fitted well within the curves obtained in the monotonic tests. A pinching effect was observed in all series (characterized by the reduction of the curves' slope when crossing the horizontal axis), which was much more pronounced for the non-reinforced series. In general, when compared to the other series, series BC-6-F2-R presented higher overall stiffness, bending moment at the end of each cycle and wider hysteretic loops.

The cyclic curves for the non-reinforced series (*cf.* Figures 6.16a and 6.16b) presented the maximum bending moment for relatively low relative rotations at an early stage of the tests. After that point, both the stiffness and the bending moment decreased progressively during the different cycles until the end of the tests. Regarding series BC-3-F-R, the moment *vs*. relative rotation curve of each cycle presented intermediate stages with lower stiffness, which increased when reaching the point of maximum relative rotations of that cycle – at this point, the moment registered a similar magnitude to those obtained in the monotonic curves for the same level of relative rotation (*cf.* Figure 6.16c). Finally, the behaviour of reinforced series BC-6-F2-R can be divided in two stages (*cf.* Figure 6.16d): (i) until the maximum moment was achieved, the hysteretic curves presented a wider shape with less pinching; and (ii) beyond the maximum moment, the pinching increased, the stiffness decreased and the hysteretic curves' shape became more similar to those of series BC-3-F-R.

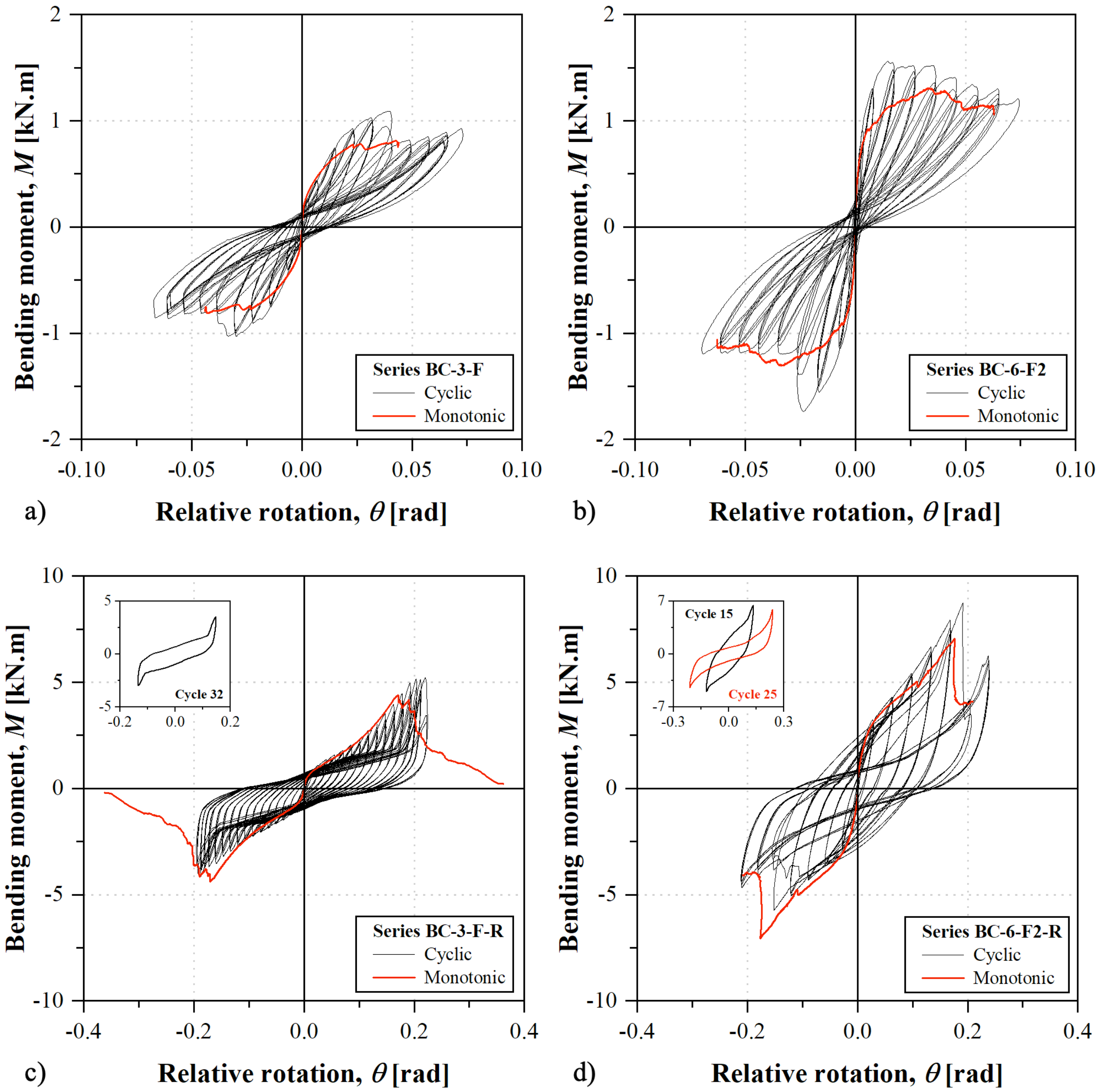

Figure 6.16 - Cyclic tests of beam-to-column connections: representative bending moment *vs.* relative rotation curves of a) series BC-3-F; b) series BC-6-F2; c) series BC-3-F-R; d) series BC-6-F2-R.

6.5.2. Failure modes

The failure modes observed in the cyclic tests of the non-reinforced connection series were the same as those observed in the monotonic tests, *i.e.* both series failed due to the tensile rupture of the columns' web-flange junction, while series BC-3-F also presented plasticity of the stainless steel flange cleats under bending.

The damage modes observed in the specimens of series BC-3-F-R included: (i) plasticity of the stainless steel flange cleats under bending, visible from the cycle with ±15.6 mm of maximum displacement; (ii) rupture of the web-flange junctions of the beam, starting at different cycles for the various specimens and increasing as the tests progressed; (iii) compression failure of the column's web (for specimen BC-3-F-R-C1, for the cycle with maximum displacement of ±93.6 mm) (*cf.* Figure 6.17a); (iv) shear-out at the beam's top flange, for cycles with maximum absolute displacement above 109.2 mm, which, in some specimens (BC-3-F-R-C2), occurred together with extensive delamination of the beam's flange (*cf.* Figure 6.17b); and (v) yielding and rupture of the stainless-steel rods of the column near the end of the tests (*cf.* Figure 6.17c).

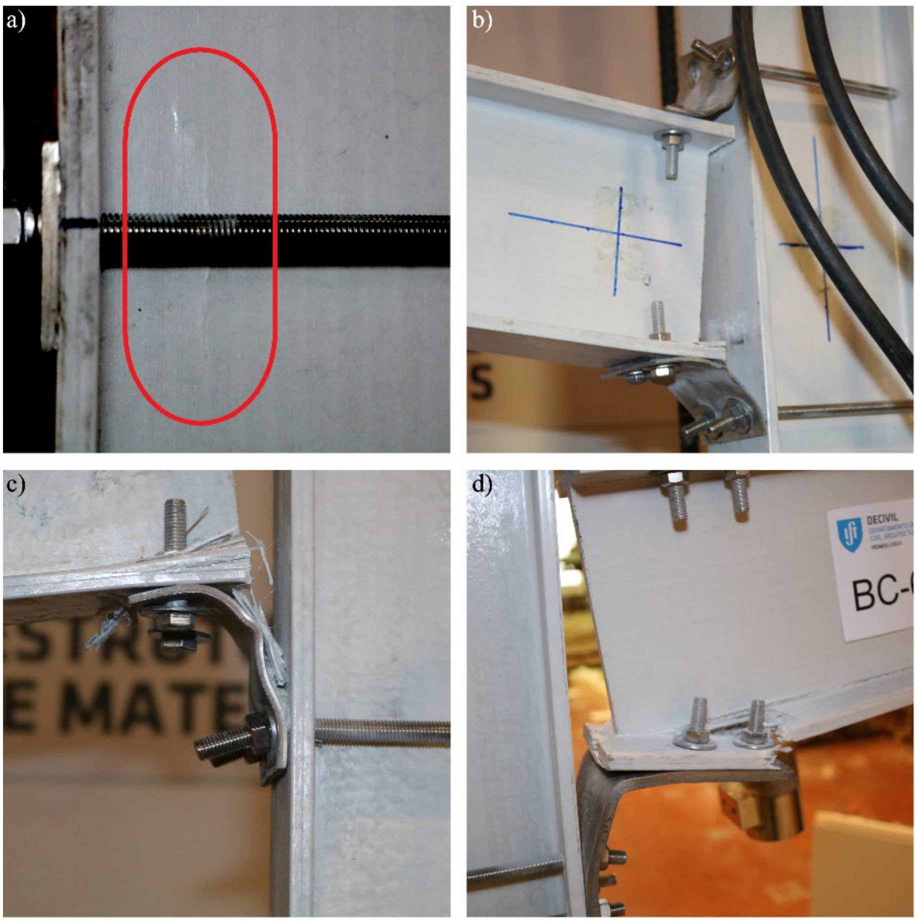

Figure 6.17 - Cyclic tests of beam-to-column connections: failure modes - a) compression failure of the column's web panel (series BC-3-F-R); b) shear-out and tearing failure combination on the beams' flange (series BC-3-F-R); c) yielding and rupture of the stainless-steel rods (series BC-3-F-R); d) compression failure of the column's web panel (series BC-6-F2-R).

Regarding the specimens of series BC-6-F2-R, the first damage observed was the plasticity of the stainless steel flange cleats under bending and the rupture of the web-flange junctions of the beam during the cycles with maximum displacement of ±18 mm. In one specimen (BC-6-F2-C1), these damages were followed by the tearing of the bottom beam’s flange at the 3rd cycle of maximum displacement of ±90 mm. In the other two specimens, the initial damages were followed by the compression failure of the column’s web at the levels of the top and bottom cleats, also for the cycles with maximum displacement above ±90 mm, and the final failure was due to shear-out and tearing of one of the beam's flanges (*cf.* Figure 6.17d).

It is worth noting that in all non-reinforced and reinforced series, as the tests progressed, the gap between the beams and columns increased, as shown in Figure 6.18, due to the occurrence and progression of the aforementioned failure modes, particularly the significant plastic deformations of the stainless steel cleats.

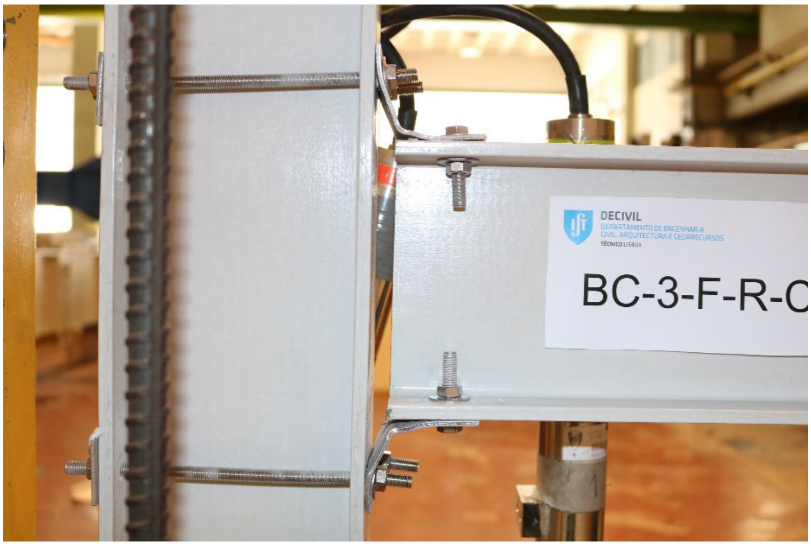

Figure 6.18 - Gap between beam’s edge and column during a cyclic test.

6.5.3. Hysteretic variation of stiffness, strength and dissipated energy

In order to further assess the cyclic performance of the different connection series, the progression of stiffness, strength and dissipated energy were evaluated according to the formulations proposed in the ECCS protocol [6.16].

According to ECCS [6.16], the stiffness ratio (ξ) at each cycle corresponds to the ratio between the slope of the moment *vs*. relative rotation curve when it crosses the horizontal axis (α_i^+ or α_i^-, depicted in Figure 6.19) and the initial stiffness measured in the monotonic tests (K_θ, *cf*. Table 6.4). Figure 6.20 presents the progression of the stiffness ratio for all series. In both non-reinforced and reinforced series, this parameter presented reasonable symmetry between the ascending and descending branches, presenting a similar trend for all series. The stiffness ratio decreased rapidly in the first 10 cycles, to ~0.3 and ~0.2 for the non-reinforced and reinforced series, respectively. This steep reduction is explained by the transition from an initial linear response (up to the 4th cycle – corresponding to the end of proportionality) to the non-linear stages that followed, during which the pinching effect was observed (with different magnitudes among the various series). Nevertheless, it should be noted that for the reinforced series the maximum relative rotations in the 10th cycle were much higher for series BC-6-F2-R than for series BC-3-F-R (± 36.0 mm *vs*. ± 15.2 mm, respectively). After that point, all series presented a gradual reduction of this parameter until reaching an almost null value at the end of the tests.

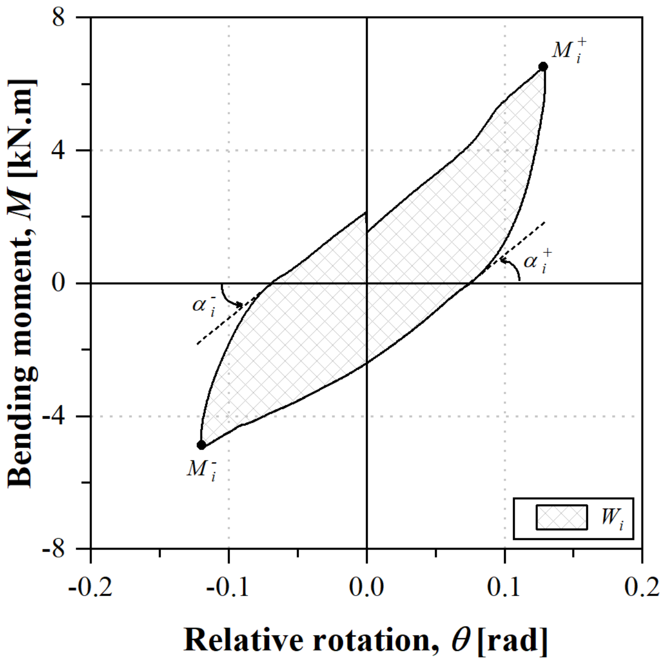

Figure 6.19 - ECCS [6.16] parameters.

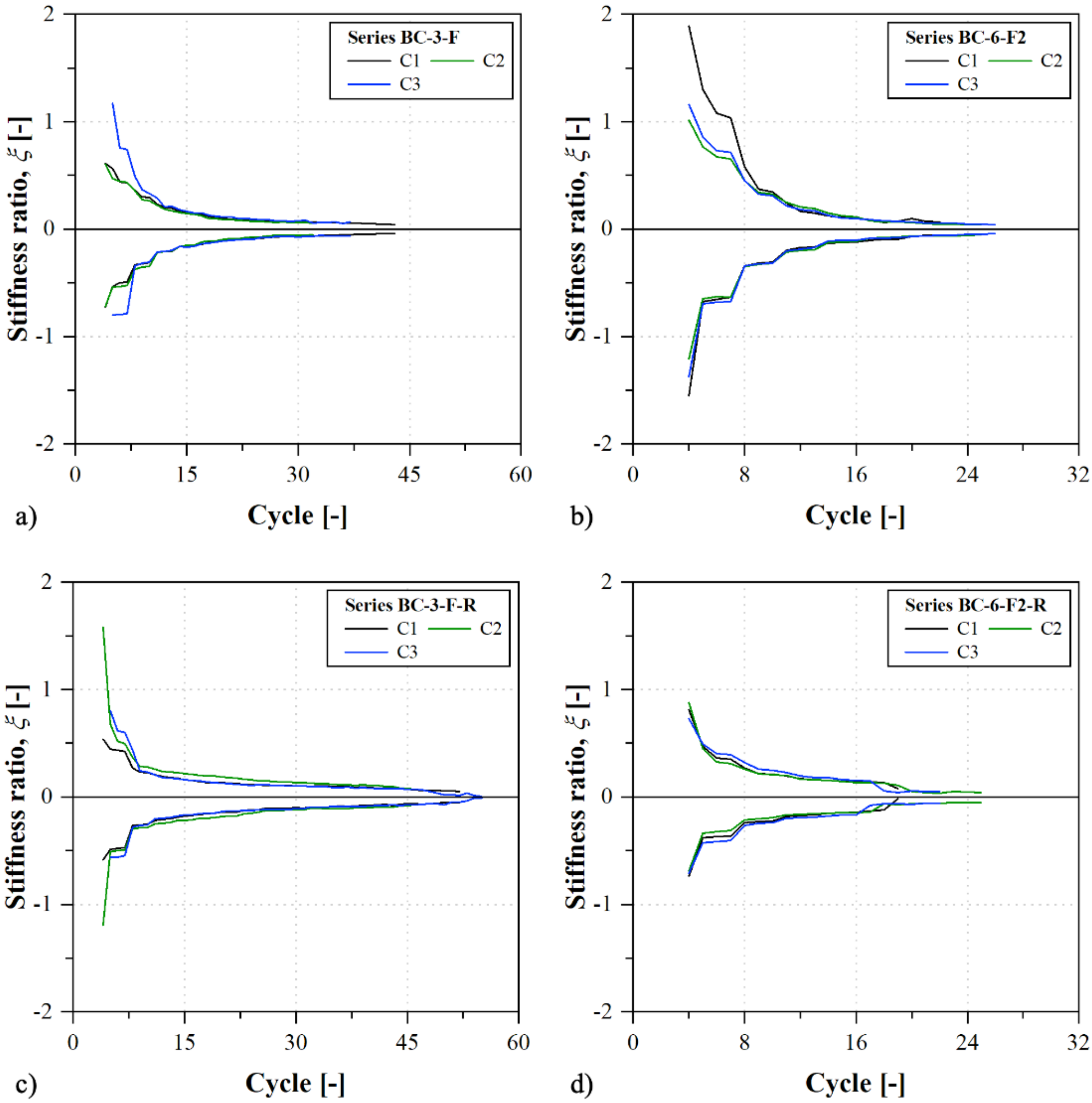

Figure 6.20 - Cyclic tests of beam-to-column connections: stiffness ratio (ξ) evolution of a) series BC-3-F; b) series BC-6-F2; c) series BC-3-F-R; d) series BC-6-F2-R.

The strength evolution throughout the tests was assessed by the moment at the points of maximum and minimum displacement of each cycle (M_i^+ or M_i^-, depicted in Figure 6.19), as recommended in [6.16]. The progression of the strength for each series is presented in Figure 6.21, where the value of the monotonic moment at the end of proportionality (M_{EOP}) of each series is also identified. In agreement with the bending moment *vs*. relative rotation curves, this parameter presented reasonable symmetry for all series and low scatter within each series. Additionally, for a given relative rotation magnitude, the moment at the end of the 2nd and 3rd cycles of the same maximum/minimum relative rotation decreased when compared to the moment at the 1st cycle. This effect occurred in all tests and was more evident as the relative rotation magnitude of the cycles increased (this is related to the unrecoverable damage that occurred at the 1st cycle of each different displacement). The non-reinforced series presented a stable increase of strength until reaching the maximum moment, which was similar to the ultimate moment measured in the monotonic tests at the 15th and 10th cycles for series BC-3-F and BC-6-F2, respectively. From that point until the end of the cyclic tests, the maximum bending moment kept the same value for series BC-3-F, while presenting a slight reduction for series BC-6-F2. Regarding the reinforced series, the strength progression curves present an overall steady increase until the maximum and minimum moment for series BC-3-F-R or until the first peak moment for series BC-6-F2-R. These peak moments corresponded to 442% and 133% of the monotonic moments at the end of proportionality, respectively. In series BC-3-F-R, the maximum and minimum moment occurred for cycles with displacements of ±101.4 mm, which is very similar to the response observed in the monotonic tests (~102 mm). As for series BC-6-F2-R, two of the specimens (BC-6-F2-R-C2 and BC-6-F2-R-C3) were able to recover the strength after the load drop that occurred near the 20th cycle, corresponding to ±108 mm, a behavior also observed in the monotonic tests, *cf.* Section 6.4.1.

The dissipated energy ratio (η) was also estimated according to the ECCS protocol [6.16] to assess the progression of the energy dissipation during the cyclic tests. This ratio equates the energy dissipated by the connections at a given cycle with the energy dissipated by a perfectly elastic-plastic connection, according to the following equation:

$$\eta_i = \frac{W_i}{\Delta M_{EOP}(\Delta\theta_i - \Delta\theta_{EOP})} \tag{6.3}$$

where W_i is the energy dissipated in cycle i (given by the area delimited by the hysteretic cyclic curve, W_i depicted in Figure 19), ΔM_{EOP} is the difference between the positive and negative bending moments at the end of proportionality, $\Delta\theta_i$ is the difference between the positive and negative imposed relative rotations in cycle i, and $\Delta\theta_{EOP}$ is the difference between the positive and negative relative rotations at the end of proportionality. Figure 6.22 presents the evolution of the energy dissipation ratio (η). It can be noted that for each group of three cycles with the same imposed displacement, the first cycle presented higher dissipated energy ratio than the other two; this (expected) result is due to the fact that damage occurs or progresses more in the first cycle and, consequently, the stiffness and/or strength decreases further in the remaining cycles of the same group.

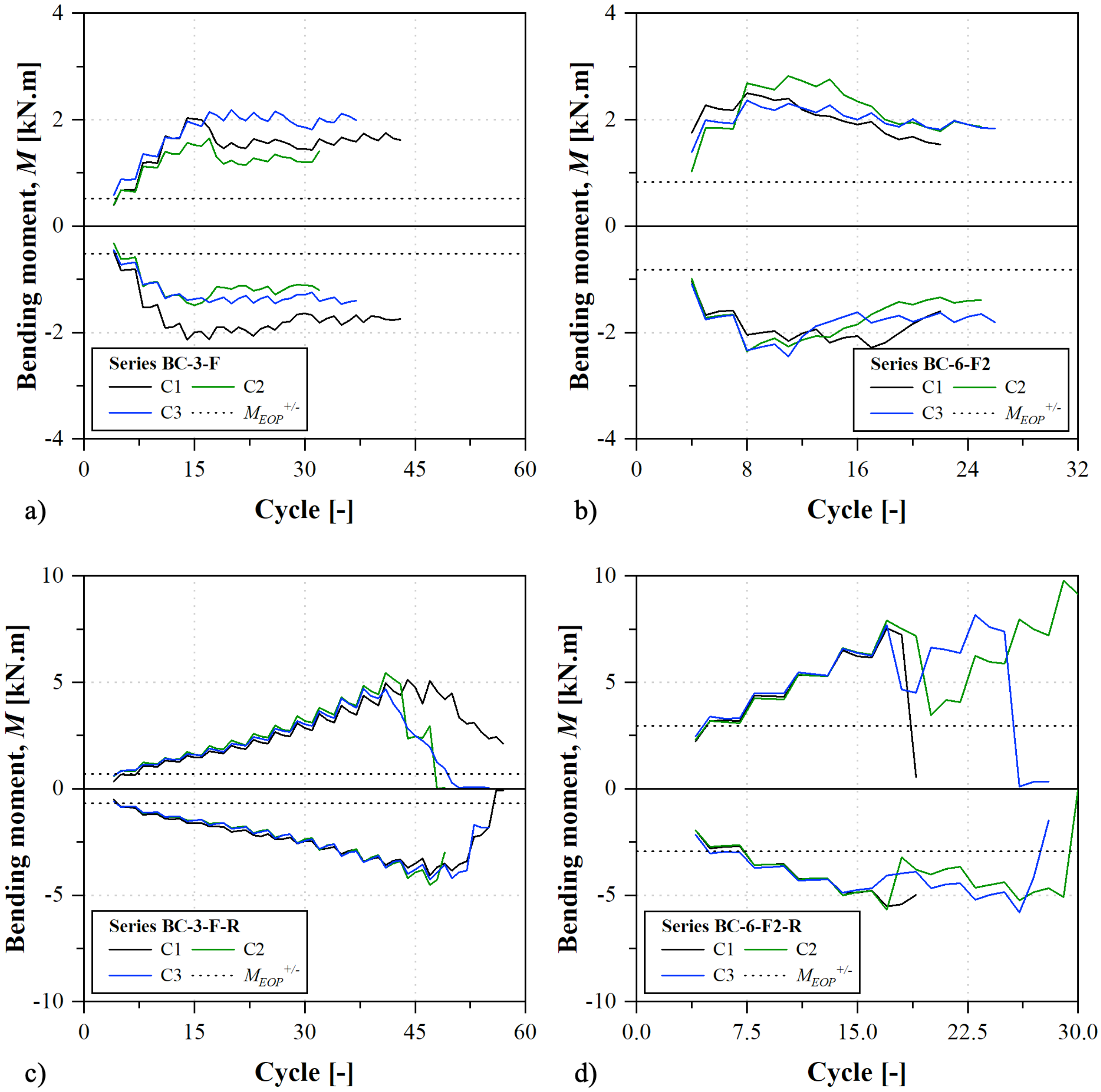

Figure 6.21 - Cyclic tests of beam-to-column connections: strength evolution of a) series BC-3-F; b) series BC-6-F2; c) series BC-3-F-R; d) series BC-6-F2-R.

The dissipated energy ratios of the non-reinforced series presented an overall decrease since the 5th cycle: (i) series BC-3-F presented a less marked decrease of η, with an initial average ratio of 0.46 and a final ratio ranging from 0.2 and 0.3; while (ii) the dissipated energy ratio of series BC-6-F2 decreased from an average of 0.75 (5th cycle) to 0.14 at the end of the tests. Moreover, the overall low values of the dissipated energy ratio registered for series BC-3-F and BC-6-F are a clear indication of the significant pinching featured by the connections' hysteretic behaviour.

Regarding the reinforced series, both series BC-3-F-R and BC-6-F2-R presented an initial stage of overall increase of the dissipated energy ratio until reaching, respectively, a maximum value of ~1.2 at the 41st cycle (displacement of 101.4 mm) and ~0.8 at the 17th cycle (displacement of 36.0 mm). Subsequently, both series presented a steep decrease until the end of the test. It is worth noting that series BC-3-F-R presented the highest dissipated energy ratios, including values above 1, which is explained by the fact that the elastic-plastic connection considered for the estimation of this parameter comprised a relatively low moment at the end of the proportionality in comparison with the maximum (ultimate) moments attained by the connection at mid-range of the cyclic tests.

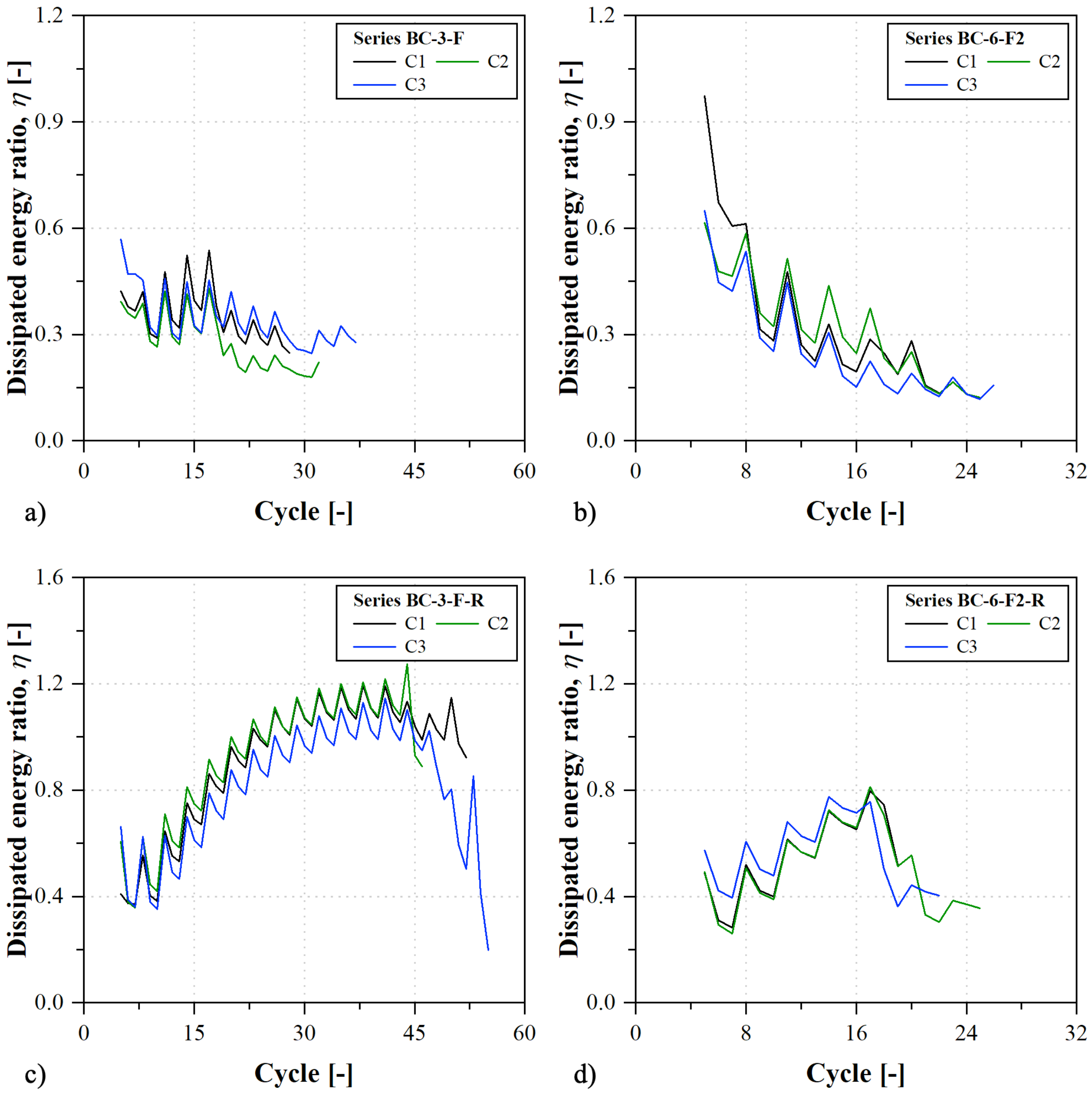

Figure 6.22 - Cyclic tests of beam-to-column connections: dissipated energy ratio (η) evolution of a) series BC-3-F; b) series BC-6-F2; c) series BC-3-F-R; d) series BC-6-F2-R.

Finally, the energy dissipation capacity of the different connection series was also evaluated through the estimation of the accumulated dissipated energy, presented in Figure 6.23. As expected, the series without reinforcements presented the lowest capacity to dissipate energy (one order of magnitude lower). As for the reinforced connections, both series appear to dissipate similar amounts of energy. However, in order to achieve the same accumulated dissipated energy, the series BC-3-F-R required approximately twice the cycles needed by series BC-6-F2-R. As an example, for a vertical displacement of ~70 mm, the series BC-3-F-R dissipated ~0.4 kN.m.rad of energy at the 30th cycle, while the series BC-6-F2-R dissipated ~1.0 kN.m.rad at the 20th cycle. These results illustrate the higher capacity to dissipate energy of series BC-6-F-R.

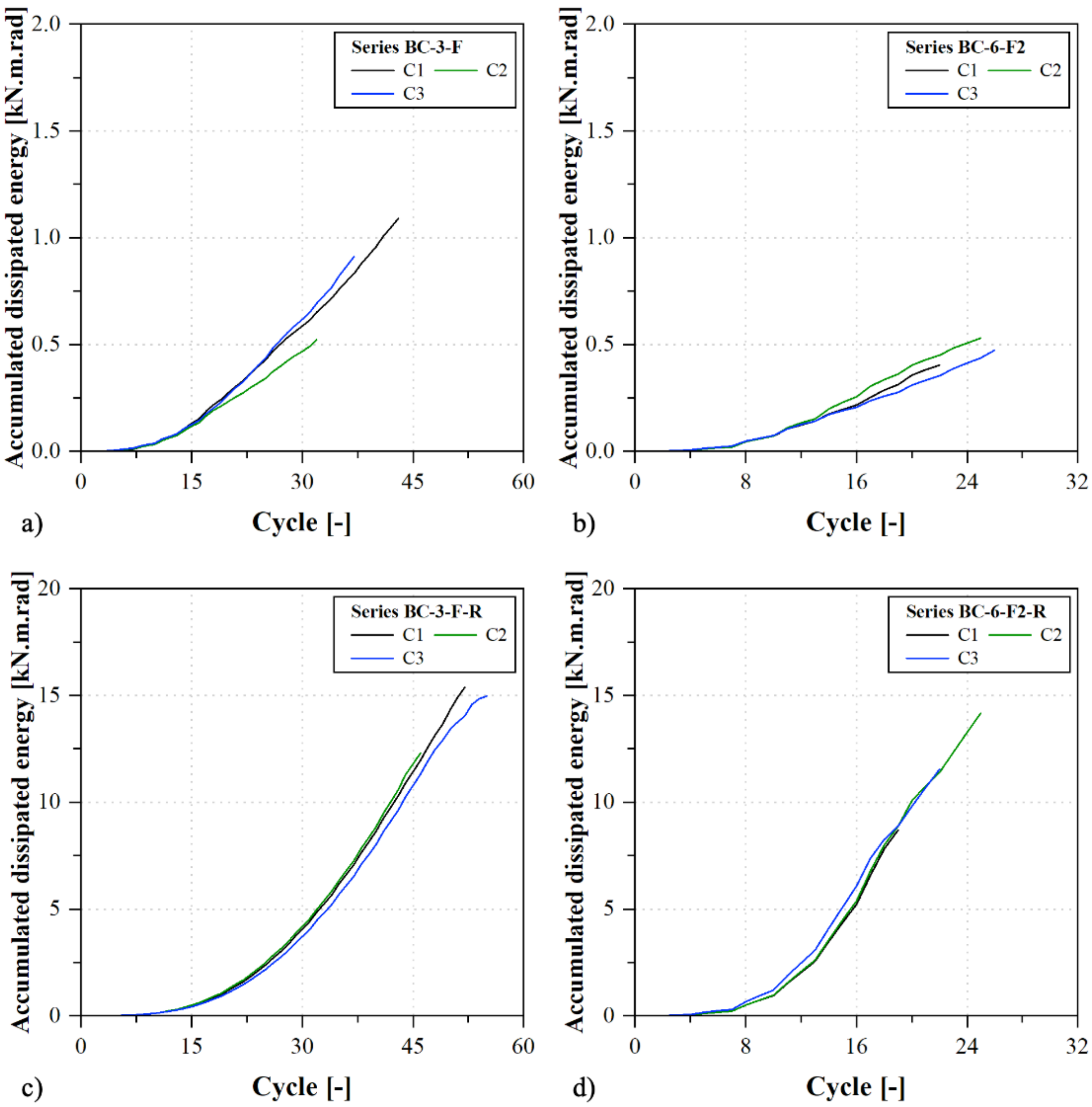

Figure 6.23 - Cyclic tests of beam-to-column connections: accumulated dissipated energy of a) series BC-3-F; b) series BC-6-F2; c) series BC-3-F-R; d) series BC-6-F2-R.

6.6. DISCUSSION

The results obtained in both monotonic and cyclic tests show that the cleats disposition and thickness, the number of bolt rows and the adoption of column reinforcements all have great influence on the connections' behaviour.

The non-reinforced connections presented premature failure on the columns' web-flange junction, owing to the limited transverse tensile strength of the GFRP material, especially in that matrix-rich zone without fibre continuity – a known limitation of the pultrusion manufacturing process [6.23]; this prevented the mobilization of ductility, namely by the plasticity of the stainless steel cleats under bending. The connections with flange cleats presented higher stiffness than that with web cleats. Concerning the cyclic tests, all non-reinforced connections presented reduced capacity to dissipate energy due to their linear-elastic behaviour up to failure. After that point, damage on the GFRP column was so extensive that substantial pinching was registered. Overall, and regardless of the cleats disposition, thickness and number of bolts, these results show that column reinforcements are needed to improve the connection system performance.

On the other hand, by using a simple and relatively inexpensive reinforcement system (similar to those presented by other authors [6.11,6.12,6.13,6.14]), early web-flange junction failure was prevented, allowing the connections to maintain their structural integrity for higher applied displacements/relative rotations. The initial stiffness of the reinforced connections was influenced by the thickness of the cleat plates, with higher thicknesses leading to higher stiffness (*i.e.* series BC-3-F-R *vs.* series BC-8-F-R and series BC-6-F2-R *vs.* series BC-8-F2-R). It was not possible to clearly assess the influence of the bolt number and location (*i.e.* series BC-8-F-R *vs.* series BC-8-F2-R) due to considerable scatter in the results.

For structural analysis purposes, according to Eurocode 3 – Part 1-8 [6.23], all connections tested herein are classified as semi-rigid (stiffness in-between 51 kN.m/rad and 2529 kN.m/rad), allowing to consider their stiffness and thus reducing the predicted deflections of flexural members with respect to a pinned connection – this can be particularly useful, as their design is often governed by deformability limits.

Regarding the strength of the reinforced connections, series BC-8-F-R, with 8 mm thick cleats, presented the poorest performance. This may be explained by the fact that the cleats used in this series are significantly stiffer than the GFRP profiles and, therefore, are not able to accommodate the deformations of the GFRP beam, leading to high stress concentrations in the contact areas and causing localized failure (*cf*. Section 6.4.2). Conversely, the cleats used in series BC-3-F-R presented extensive bending during the tests, which allowed for a smoother distribution of stresses in the GFRP elements and, consequently, provided higher ultimate strength (+25% compared to series BC-8-F-R). Series BC-8-F2-R, on the other hand, registered a 52% strength increase when compared to series BC-8-F-R. This difference shows that, albeit having the same cleat thickness, cleats of series BC-8-F2-R enabled a smoother stress distribution in the GFRP material, which can be attributed to two factors: (i) the two bolt rows lead to lower stress concentrations, and (ii) the longer distance between the corner of the cleat and the first bolt row (50 mm *vs*. 35 mm, *cf*. Figure 6.3) reduces the bending stiffness of the cleats of series BC-8-F2-R (plasticity under bending of these elements was clearly noticeable during the tests, *cf*. Section 6.4.2). Finally, series BC-6-F2-R had a thinner and slender cleat than that used in series BC-8-F2-R, and therefore such elements exhibited more elastic-plastic bending and avoided the flange tearing failure of the beam (*cf*. Section 6.4.2). Consequently, series BC-6-F2-R presented the best performance in terms of strength, which was 26% higher than that of series BC-8-F2-R.

Regarding ductility, it was clearly influenced by the thickness of the flange cleats. Series BC-3-F-R presented non-linear behaviour almost since the beginning of the monotonic tests, failing for displacements higher than 100 mm. Series BC-6-F2-R also presented significant non-linear behaviour, after an initial linear phase, also failing for displacements higher than 100 mm. On the other hand, series BC-8-F-R and series BC-8-F2-R presented less markedly non-linear behaviour until the peak loads were achieved, and the associated displacements were lower than 50 mm. The ductility of the reinforced connections was also assessed through a ductility index (μ_d), proposed by Jorissen and Fragiacomo

[6.25] for timber connections[4] and previously used in this thesis to assess the pseudo-ductility of GFRP beam-to-column connections (Chapters 3 and 5). This index was estimated with Eq. (6.4):

$$\mu_d = \frac{d_u - d_{EOP}}{d_u} \tag{6.4}$$

where, d_{EOP} is the displacement at the end of proportionality and d_u is the failure displacement (corresponding to 80% of the maximum force on the descending path of the load *vs*. displacement curves). As mentioned, the non-reinforced series failed by tensile rupture of the column web-flange junction. After this premature failure, any residual strength of the connection system was attributed to the fixed flanges of the column (*cf*. Figure 6.4). Since the post-failure behaviour of the non-reinforced series was highly influenced by the test setup, these series were not considered in the ductility index assessment. The ductility indexes obtained are presented in Table 6.4. These results confirm that series BC-3-F-R and BC-6-F2-R presented higher ductility than the series with 8 mm thick cleats, namely series BC-8-F-R and BC-8-F2-R.

The cyclic tests showed that series BC-6-F2-R presented better performance than series BC-3-F-R regarding the ability to dissipate energy, exhibiting higher stiffness, strength, larger hysteretic loops (*cf*. Section 6.4.1) and less pinching

In summary, series BC-6-F2-R presented the best overall performance, owing to its higher strength, considerable ductility and higher ability to dissipate energy.

6.7. CONCLUSIONS

This chapter presented an experimental study regarding the mechanical behaviour of beam-to-column connections between I-section pultruded GFRP profiles using stainless steel cleats. Five non-reinforced connection series and four reinforced connection series were tested under monotonic loading, while four series (two non-reinforced and two reinforced) were tested under cyclic loading. The connection

[4] It should be noted that despite the fact that GFRPs and wood are very distinct materials, both present brittle failure modes and orthotropic behaviour.

series differed on the bolts/rods number, cleats positioning and cleats thickness. The following main conclusions can be drawn:

- All non-reinforced series failed prematurely due to web-flange junction failure; therefore, the number of bolts, thickness and length of the cleats had minor influence on the strength of flange cleated connections.
- For reinforced connections, the initial stiffness increased with the increase of the cleat thickness and number of bolt rows.
- On the other hand, higher cleat thicknesses (8 mm) led to lower strength and ductility, with earlier damage on the GFRP and lower plastic deformations on the stainless steel.
- The series with intermediate cleat thickness (6 mm) presented the best overall performance, with the highest strength and second highest stiffness and ductility.
- Regarding the cyclic behaviour, series with intermediate cleat thickness (6 mm) presented better performance than those with thinner cleats (3 mm), with larger hysteretic loops and less pinching, owing to the higher stiffness and strength of the connection parts.

Overall, the results obtained show the feasibility of exploiting the ductility of stainless steel, especially for series with less thick cleats, and the connection systems developed were able to withstand large relative rotations before failing, displaying marked non-linear behaviour.

For different GFRP sections, the optimal thickness and length of the stainless steel cleats, and the number of bolts necessary to enhance the performance compared to conventional connections may differ from this particular case. The design of such connections should ensure that significant plastic deformations develop in the stainless steel components prior to GFRP ultimate failure, in order to overcome the mechanical mismatch between these two materials.

6.8. REFERENCES

[6.1] ISO 1172 (1996) Textile-glass-reinforced plastics. Prepregs, moulding compounds and laminates. Determination of the textile-glass and mineral-filler content. Calcination methods.

[6.2] EN ISO 527-1 (1997) Plastics – Determination of Tensile Properties – Part 1: General Principles. Brussels.

[6.3] ASTM D 6641/D 6641M-16e1 (2016) Standard Test Method for Compressive Properties of Polymer Matrix Composite Materials Using a Combined Loading Compression (CLC) Test Fixture. West Conshohocken.

[6.4] ASTM D 695-02 (2006) – Standard Test Method for Compressive Properties of Rigid Plastics. West Conshohocken.

[6.5] ASTM D 2344/D 2344M-00 (2006) – Standard Test Method for Short-Beam Strength of Polymer Matrix Composite Materials and Their Laminates. West Conshohocken.

[6.6] ASTM D 5379/D 5379M (2005) – Standard Test Method for Shear Properties of Composite Materials by the V-Notched Beam Method. West Conshohocken.

[6.7] ISO/TC 164/SC 1 (2019). ISO 6892-1:2019. Metallic Materials - Tensile Testing - Part 1: Method of Testing at Room Temperature. British Standards Institution.

[6.8] Italian National Research Council (2007). CNR-DT 205/2007 – Guide for the Design and Construction of Fiber-Reinforced Concrete Structures.

[6.9] ASCE (2010). Pre-Standard for Load & Resistance Factor Design (LRFD) of Pultruded Fiber Reinforced Polymer (FRP) Structures.

[6.10] CEN/TC250/WG4 (2014). Fibre Reinforced Polymer Structures: scientific and technical report.

[6.11] Bank LC, Mosallam AS, McCoy GT. (1994). Design and performance of connections for pultruded frame structures. *Journal of Reinforced Plastics and Composites*, 13(3), 199–212.

[6.12] Smith SJ, Parsons ID, Hjelmstad KD. (1998). An experimental study of the behavior of connections for pultruded GFRP I-beams and rectangular tubes. *Composite Structures*, 42, 281-90.

[6.13] Mosallam AS, Abdelhamid MK, Conway JH. (1994). Performance of pultruded FRP connections under static and dynamic loads. *Journal of Reinforced Plastics and Composites*, 13, 386–407.

[6.14] Mosallam A. (2011). *Design guide for FRP composite connections*. American Society of Civil Engineers.

[6.15] Manalo A, Mutsuyoshi H. (2012). Behavior of fiber-reinforced composite beams with mechanical joints. *Journal of Composite Materials*, 46(4), 483-496.

[6.16] ECCS/TC1. (1986). Recommended testing procedure for assessing the behaviour of structural steel elements under cyclic loads.

[6.17] Zhang Z, Bai Y, He X, Jin L, Zhu L. (2018). Cyclic performance of bonded sleeve beam-column connections for FRP tubular sections. *Composites Part B: Engineering*, 142, 171-82.

[6.18] Matharu, Navroop S, Mottram JT. (2017). Plain and threaded bearing strengths for the design of bolted connections with pultruded FRP material. *Engineering Structures*, 152, 878-887.

[6.19] Bank LC. (2006). *Composites for construction: Structural design with FRP materials*. John Wiley & Sons.

[6.20] Chamis CC. (1990). Simplified procedures for designing composite bolted joints. *Journal of reinforced plastics and composites*, 9(6), 614-626.

[6.21] Davison JB, Kirby PA, Nethercot DA. (1987). Rotational stiffness characteristics of steel beam-to-column connections. *Journal of Constructional Steel Research*, 8, 17-54.

[6.22] Skejic D, Dujmovic D, Beg D. (2014). Behaviour of stiffened flange cleat joints. *Journal of Constructional Steel Research*, 103, 61-76.

[6.23] Liu T, Yang JQ, Feng P, Harries KA. (2020). Determining rotational stiffness of flange-web junction of pultruded GFRP I-sections. *Composite Structures*, 236, 111843.

[6.24] EN1993 (2005). Design of Steel Structures – Part 1–8: Design of Joints.

[6.25] Jorissen A, Fragiacomo M. (2011). General notes on ductility in timber structures. *Engineering structures*, 33(11), 2987-2997.

Chapter 7

Stiffness and strength predictions of cleated connection system for I-section profiles

7.1. INTRODUCTION

Despite the fact that pultruded glass fibre reinforced polymer (GFRP) profiles are being increasingly used in civil engineering applications, their widespread acceptance in the construction industry is still hindered by the lack of comprehensive FRP design standards. In particular, existing standards for pultruded FRP structures [7.1-7.3] provide very limited guidance about the design of bolted frame connections. Most recommendations concern only the strength of connections under in-plane loads, providing design formulae for failure modes identified in previous works [7.4-7.8] (*e.g.,* shear-out failure, bearing failure or net-section failure). Regarding out-of-plane loads, such standards only provide formulae to estimate the laminates strength under bolt pull-out failure. Therefore, existing standards still do not provide guidance on how to predict the strength of composite beam-to-column connections, as they do not cover many of the failure mechanisms identified in the literature (*e.g.* tensile failure of the column web-flange junction). Moreover, these standards also fail to provide guidelines to predict the connections' stiffness, which is particular relevant for the design of GFRP flexural elements, such as beams, which is often governed by deformability limits.

The review of previous research and existing design standards highlight the need for further research about GFRP beam-to-column bolted connections, namely: (i) the development of easy-to-build/readily available connection systems with potential to provide ductile failure modes; and (ii) the proposal of more comprehensive design guidelines for beam-to-column connections, including geometrical recommendations and procedures to predict their stiffness and strength. In this regard, it should be mentioned that Mosallam [7.9] presents analytical guidelines for the design of GFRP beams and frame structures with semi-rigid connections; however, experimental moment-rotation curves of the connections are required as input. To date, no analytical procedure has been proposed to determine the initial stiffness of the connections nor to predict their failure loads and modes based on results from finite element (FE) analysis. Thereafter, to avoid design by testing (which is too onerous for many industries, including construction), in addition to experimentally assess the response of GFRP beam-to-column connections, it is also necessary to develop and calibrate reliable analytical and numerical tools that are able to predict their behaviour.

Part of the research efforts to predict the behaviour of bolted connections between GFRP profiles reported in the literature, have been conducted through the use of FE models. While most numerical studies focused on the response of single- and double-lap connections [7.10-7.15], some studies also concerned the behaviour of beam-to-column connections. Smith *et al.* [7.16] modelled seven types of bolted beam-to-column connections between tubular and I-section profiles previously tested by the authors. The different connections included typologies with cleats and plates, with gussets and cuff connection parts. The FE analyses were conducted using ABAQUS, with shell elements. The fasteners were not modelled and the different reference surfaces were connected using rigid links. No damage was considered in the GFRP material. The results obtained showed excellent agreement in terms of initial stiffness, with relative differences to the experimental data of less than 10%. No strength predictions were provided.

Harte and Cann [7.17] developed FE models of bolted beam-to-column connections between GFRP profiles using GFRP cleats. The beam, column and cleat connection parts were modelled with two-dimensional plane stress elements. The contact between the beam, column and connection parts was modelled with interface elements that operated by attaching springs between the nodes on the surface boundary. The stiffness of these springs was only mobilized when the surfaces interpenetrated. Two different ways of modelling the bolts were considered: (i) using two-dimensional link elements; and (ii) using plane stress elements to model the bolts (modelling the bolt shanks). The initial stiffness of the connections was accurately predicted by the FE models: models using link elements to simulate the bolts presented relative differences to test data between 6% and 21%, while in FE models with plane stress elements those differences were reduced to 3%. Again, this study did not provide strength predictions.

Zhang *et al*. [7.18] modelled a bolted connection between tubular GFRP beams to steel columns using steel flange cleats. Every element was modelled using solid elements. The contact/slip behaviour between shanks and holes, washers and plates/angles, plates and angles and column was modelled via surface-to-surface contact elements with predetermined friction coefficients. The pretension force of the bolts was taken into account in the model. The damage onset was identified using the Tsai-Wu failure criteria [7.19]. The failure modes obtained in the tests correlated well with the numerical results: the end plate yielding was observed and failure onset was identified in the GFRP material near the bolts. Overall, satisfactory agreement was found between the moment *vs*. rotation curves of the experimental and numerical studies, with the initial stiffness of the FE models differing by 9% w.r.t. that of the tests. However, no prediction of the actual connection strength was provided, as the GFRP material was modelled without the consideration of any damage progression model.

Feroldi and Russo [7.20] presented experimental and numerical investigations of the structural behaviour of all-GFRP beam-to-column plate-bolted joints. Three-dimensional elements were used to model every component of the connection. Different contact pairs were defined between some of the components of the connection. These contact pairs considered frictional sliding with a friction coefficient of 0.2. Pretension was applied in the bolts to simulate the thread torque. The damage onset was identified using the maximum stress criterion and the damage evolution corresponded to reductions of the tensile and compressive stiffness to 10% of their initial value after damage was identified. It should be mentioned that the 90% stiffness reduction implemented by the authors upon failure was calibrated based on the experimental results of the connection tests being modelled. For one of the simulated connections, the numerical model was able to predict reasonably well the maximum moment of the joint, but not its initial stiffness (the exact numerical stiffness and strength values were not reported). The authors argued that this difference stems from the fact that this connection specimen was already used in preliminary tests and the material in the vicinity of the bolt holes was damaged somehow. As for the other connection studied, a good agreement was reported between the numerical moment-rotation response and the experimental data for both the initial stiffness and the ultimate moment of the connection. Additionally, the damage propagation of the models corresponded to that of the experimental tests. As mentioned, the damage behaviour of GFRP was calibrated from the results of the beam-to-column connections, thus justifying such consistency between numerical and experimental results.

Only one of the previous numerical investigations (Feroldi and Russo [7.20]) presented predictions of the connections' strength (which was based on the direct calibration of the model parameters to the experimental results being simulated), which is a crucial parameter for the connections' design. In order to predict the strength of GFRP structures, two main FE approaches are presented in the literature: (i) considering the strength at first (initial) failure; and (ii) considering the final failure by using progressive damage models. The first step of both procedures entails a stress analysis. Then, failure criteria are applied to identify if any element is damaged for the given stresses. This approach can be used to predict the strength of a composite joint. However, the damage initiation mechanisms, particularly for complex structural elements, such as beam-to-column connections, do not necessary lead to a complete loss of structural integrity and load-carrying capacity may still increase due to stress redistribution. Therefore, several works have been conducted to simulate the progressive damage of GFRP. Nonetheless, most of the used damage progression models are complex and their success often depends on the structural problem to be solved.

Chapter 6 presented an experimental study of GFRP beam-to-column connections using stainless steel connections. This chapter presents predictions of their initial stiffness, *i.e.* until the end of proportionality (*cf.* Chapter 6), and strength by using analytical and numerical tools, focusing on the monotonic behaviour of the reinforced connections (the non-reinforced connections are not addressed, as their performance of was severely hindered by premature column web-flange junction). The main objective was to develop design-oriented analytical and numerical procedures to predict the behaviour of the GFRP beam-to-column connections.

7.2. OVERVIEW OF THE PROPOSED ANALYTICAL AND NUMERICAL DESIGN PROCEDURES

As mentioned, the study presented in the present chapter concerns the prediction of the stiffness and strength of the reinforced beam-to-column GFRP connections experimentally tested in Chapter 6. Four different reinforced connection series, illustrated in Figure 7.1, were considered: (i) series BC-3-F-R, using 3 mm thick cleats and one bolt row; (ii) series BC-8-F-R, using 8 mm thick cleats and one bolt row; (iii) series BC-6-F2-R, using 6 mm thick cleats and two bolt rows; and (iv) series BC-8-F2-R, using 8 mm thick cleats and two bolt rows. The beam-to-column connections were materialized by means of (i) one 900 mm long GFRP column, (ii) one 800 mm long GFRP beam (connected at mid-height of the column), (iii) two stainless steel cleats (Grade AISI 304), (iv) four or eight (depending on the connection series) stainless steel M8 rods (Grade A2-70), and (v) four or eight (depending on the connection series) stainless steel M8 bolts (Grade A2-70). Washers were used in-between the bolts and the GFRP and the 3 mm stainless steel plates. As mentioned, the analytical and numerical studies focused only on the reinforced series, as the other connection systems presented poor structural performance and, therefore, their use in real applications is not recommended (*cf.* Chapter 6).

Regarding the prediction of initial stiffness (*cf.* Section 7.3), two approaches were considered: (i) analytical, using an adapted "component method", which is often applied in the design of steel connections; and (ii) numerical, using FE models with geometric non-linearity. According to the "component method", the behaviour of a joint is determined by the contribution of its basic components [7.21]. In accordance to EN 1993-1-8 [7.21], a basic component is a constituent of a joint that affects its structural behaviour. Therefore, the stiffness of a joint is modelled through an assembly of rigid links and springs representing certain parts of the connection (components) that influence its stiffness. On the other hand, the numerical models were developed using ABAQUS FE software. The mechanical properties considered in the FE models were previously determined from material characterization tests, presented in Chapter 6. The predictions of initial stiffness provided by both methods were compared and validated against the stiffness measured in the experimental tests.

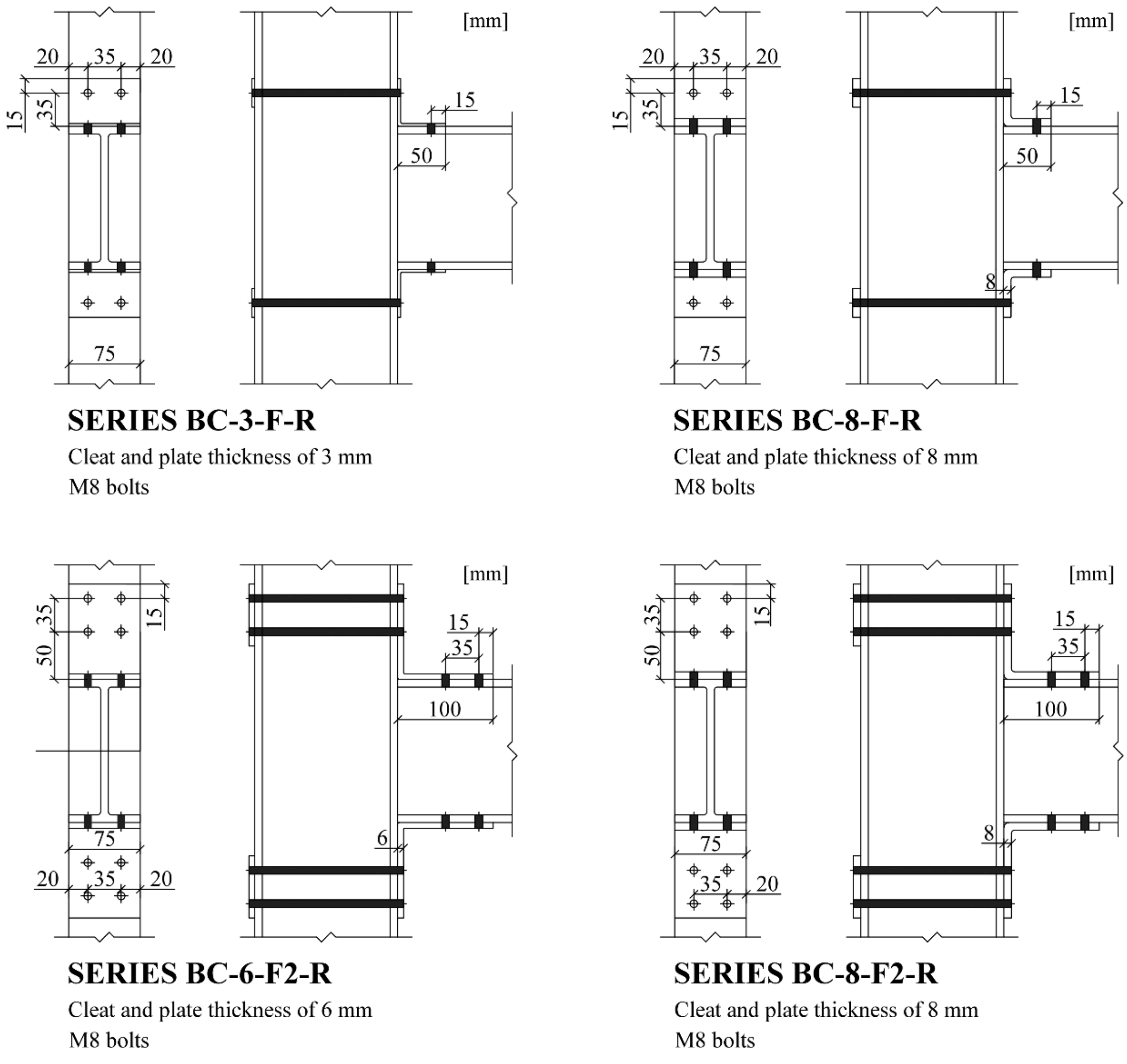

Figure 7.1 - Reinforced cleated beam-to-column connection series.

The strength of the reinforced connection series (*cf*. Section 7.4) was predicted by a combination of analytical and numerical procedures. Two main reasons explain this approach: (i) a pure analytical strength prediction would require estimating/assuming the connections' stress distribution, which would be impractical given the complex configuration of the connections studied and their highly non-linear response; (ii) the strength prediction resorting only to FE models would require the definition of proper damage initiation and propagation models – in this case, comprehensive experimental data would be needed (relying on relatively complex tests) and the computational costs would be high, most likely impractical for design purposes. Therefore, the local failure mechanisms considered in the design verifications were those provided by FRP structural design standards [7.1-7.3] and, consequently, their associated strength was predicted analytically with design equations. In parallel, the same FE models developed for the stiffness predictions were also used to define the load distribution per bolt, as well as the transverse compressive loads in the column web. The predicted failure modes and corresponding strengths were validated by comparison with experimental results.

7.3. STIFFNESS PREDICTION

7.3.1. Analytical estimation of connection stiffness

Most of the components considered in the "component models" of each connection were based in recommendations provided in EN 1993-1-8 [7.21], namely for flange-cleated beam-to-column connections between I-section steel profiles. Figure 7.2 shows the components used in the prediction of the connections' stiffness, namely: (i) column web panel in shear (stiffness parameter k_1); (ii) bottom column web in transverse compression (k_2); (iii) top column web in transverse compression (k_3); (iv) top rods in tension (k_4); (v) flange cleat in bending (k_5); and (vi) top beam bolts in shear (k_6). The contribution of each component to the overall stiffness (k_{an}) is then combined in series,

$$k_{an} = \frac{z^2}{\sum_{i=1}^{6} \frac{1}{k_i}} \tag{7.1}$$

where, k_i is the stiffness of component i and z is the moment lever arm as illustrated in Figure 7.3. The stiffness formulae corresponding to the stainless steel components were derived from EN 1993-1-8 [7.21]. On the other hand, the stiffness formulae applied for the GFRP components were based on simple physical models, accounting for the materials' orthotropic behaviour.

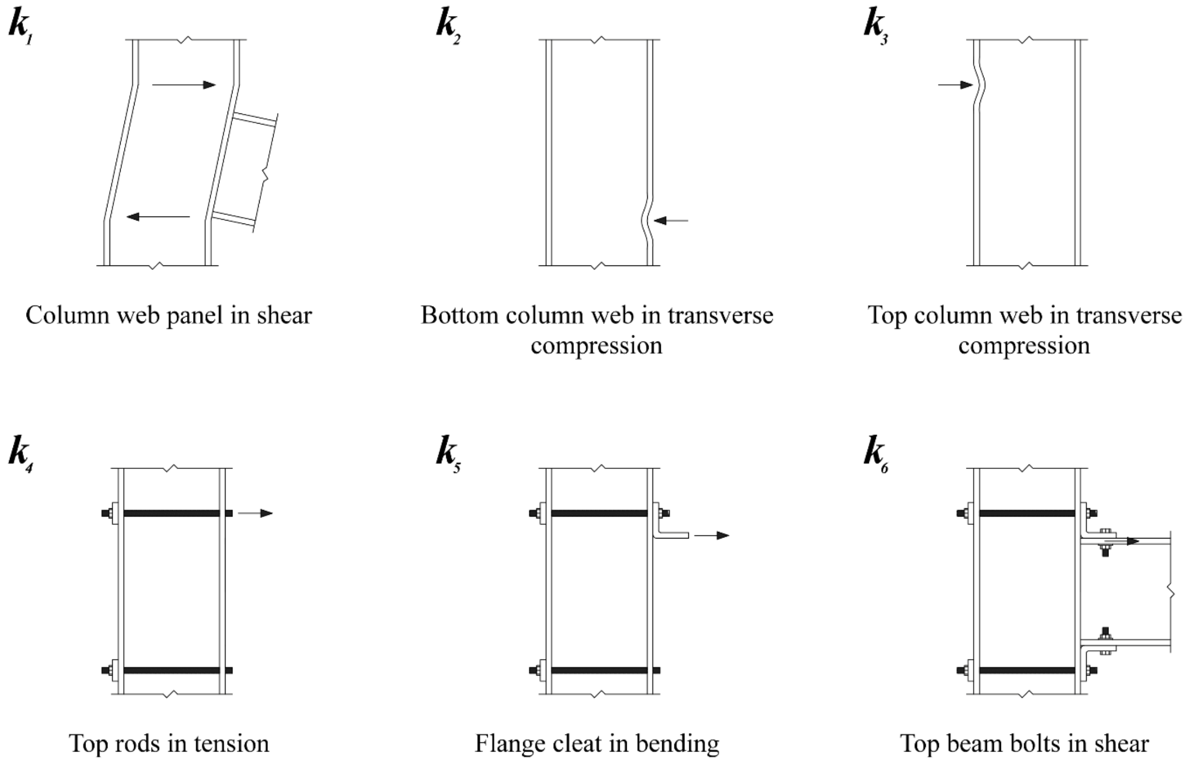

Figure 7.2 - Connection components considered in the stiffness predictions.

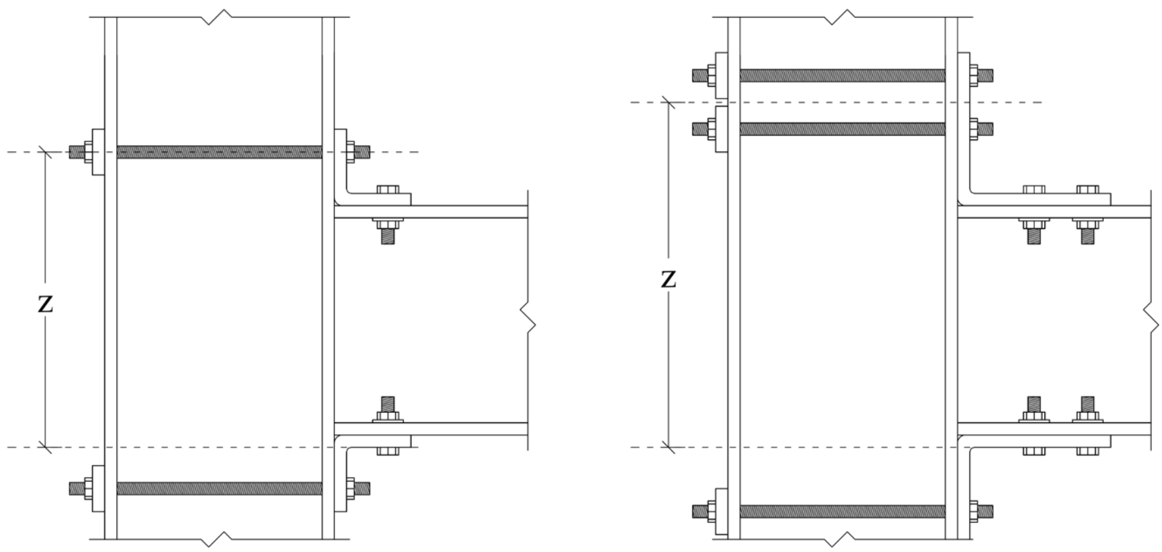

Figure 7.3 - Lever arm considered in the stiffness predictions.

The stiffness of the column web panel in shear (k_1) was taken as,

$$k_1 = \frac{A_{vc}\,G_{LT}}{z} \tag{7.2}$$

where, A_{vc} is the columns' shear area and G_{LT} is the corresponding shear modulus (*cf*. Chapter 6).

The stiffness of the bottom and top column web in transverse compression (k_2 and k_3) were estimated with Eqs. (7.3a) and (7.3b), respectively:

$$k_2 = \frac{b_{eff,c,bottom}\, t_{w,c}\, E_{c,T}}{h_{w,c}} \tag{7.3a}$$

$$k_3 = \frac{b_{eff,c,top}\, t_{w,c}\, E_{c,T}}{h_{w,c}} \tag{7.3b}$$

where, $b_{eff,c,bottom}$ and $b_{eff,c,top}$ are the columns' effective widths, $t_{w,c}$ is the columns' web thickness, $E_{c,T}$ is the transverse compressive elasticity modulus of the columns web (*cf.* Chapter 6) and $h_{w,c}$ is the column's web height.

The effective width was defined considering a 1:1 stress spreading angle for both stainless steel and GFRP components. While this hypothesis has been suggested for steel components by several authors [7.22], its validity for the GFRP components is demonstrated through FE modelling in Appendix C. Thereafter, the bottom effective width of the column web, near the bottom cleat, was estimated with Eq. (7.4), following the stress distribution schematized in Figure 7.4,

$$b_{eff,c,bottom} = t_a + 2(t_{fc} + r_c) \tag{7.4}$$

where, t_a is the thickness of the flange cleat, t_{fc} is the thickness of the column's flange and r_c is the column's web-flange junction radius. Regarding the top effective width of the column's web, near the back reinforcement spreading plate, the following expression is proposed,

$$b_{eff,c,top} = s_{nut} + 2\left(t_{wh} + t_p + t_{fc} + r_c\right) \tag{7.5}$$

where, s_{nut} is the nut minimum width (representing the applied load length), t_{wh} is the washer thickness (used for series BC-3-F-R only, *cf.* Chapter 6) and t_p is the auxiliary back plate thickness.

The stiffness of each row of top rods in tension (k_4) was estimated according to Eurocode 3 [7.21],

$$k_4 = \frac{1.6\, A_s\, E_s}{L_b} \tag{7.6}$$

where, A_s is the cross-section of the rods, L_b is the rod elongation length (free length in-between the centre of both nuts) and E_s is the stainless steel elasticity modulus.

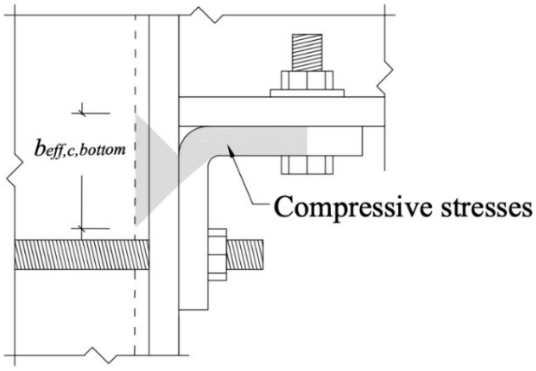

Figure 7.4 - Bottom effective width of the column's web.

The stiffness of the top flange cleat in bending (k_5) was estimated using Eq. (7.7) [7.22],

$$k_5 = \frac{0.9\, l_{eff}\, t_a^3\, E_s}{m^3} \tag{7.7}$$

where, l_{eff} is the effective length of the flange cleat, as defined in Figure 7.5a, t_a is the flange cleat thickness, E_s is the stainless steel elasticity modulus and m is the vertical distance between the rod and the top of the cleat minus $0.2r_a$, as shown in Figure 7.5b. It should be noted that EN 1993-1-8 [7.21] states that Eq. (7.7) is valid for flange cleats with only one bolt row, not providing information for cases where more than one bolt row exists. Nevertheless, in this study, Eq. (7.7) was also adopted for series with two bolt rows (BC-6-F2-R and BC-8-F2-R) as the stiffness of this element is more influenced by its bending lever arm (m) than by the number of bolt rows.

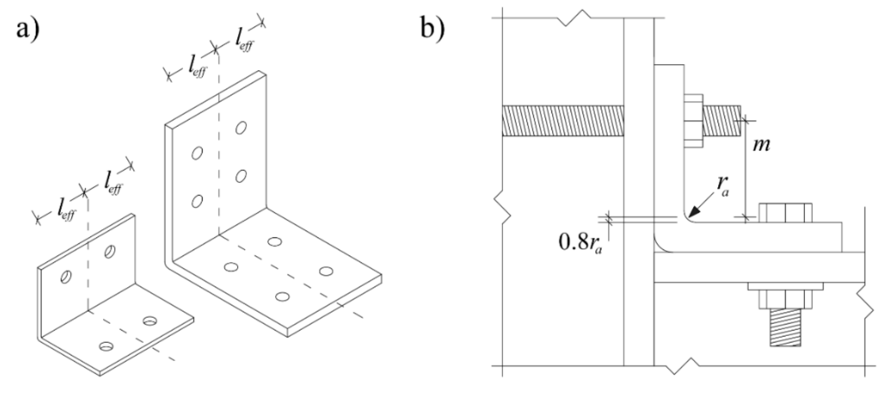

Figure 7.5 - Flange cleat geometric parameters: a) effective length (l_{eff}); b) parameter m.

Finally, the stiffness of the beam's top bolts in shear (k_6) was estimated using the results obtained in the double-lap tests, namely those of series DL-35 and DL-2B (*cf.* Chapter 6). It should be noted that the stiffness of these bolts is best represented by the double-lap test configuration, since the secondary bending effects which depend on the flexibility of the plates an inherent eccentricity of the single-lap shear test configuration [7.23] do not occur on the restrained bolt shear connections of the beam-to-column tests. In order to separate the contribution of the bolt-hole interaction, the k_6 stiffness was computed with Eq. (7.8),

$$k_6 = \frac{1}{\frac{1}{k_b} - \frac{1}{k_{plate}}} \tag{7.8}$$

where, k_b is the stiffness measured in the double-lap tests (*cf.* Chapter 6) and k_{plate} is the stiffness of the free GFRP plate (in-between the GFRP measuring section and the bolts), which was estimated from,

$$k_{plate} = \frac{E_{t,L}\, A_{plate}}{l} \tag{7.9}$$

where, $E_{t,L}$ is the longitudinal tensile elasticity modulus of the 40 mm plates (*cf.* Chapter 6), A_{plate} is the section area of the GFRP plate and l is the free length of the GFRP plate.

The predicted stiffness for each reinforced connection series (and relative difference with respect to the initial stiffness obtained in the tests) are presented in Table 7.1 and Figures 7.6 (including the experimental curves) and 7.7. Additionally, a design example for the analytical stiffness determination of one connection series is provided in Appendix D. The analytical predictions agree relatively well with the data from the monotonic tests with an average relative difference of -23%. All predictions are conservative, with series BC-6-F2-R, presenting a very low relative difference to the experimental mean stiffness of-8.3%, with the predictions for the remaining series presenting worse agreement with the experimental results. Nevertheless, it should be mentioned that the stiffness measured experimentally presented significant scatter with CoV up to ~40%.

Table 7.1 - Predicted initial stiffness and strength of the reinforced series (relative percentage difference to experimental monotonic tests results in brackets).

Series	Analytical stiffness (kN.m/rad)	Numerical stiffness (kN.m/rad)	Bolt row	Failure load predictions (kN)						Predicted failure
				SOF	BF	POF	IOF	CWTF	CWBF	
BC-3-F-R	99.7 (-28.5%)	118.9 (-14.3%)	1	7.5	9.1	12.0	4.6	6.4	7.6	IOF (-34.6%)
BC-8-F-R	195.7 (-16.6%)	236.2 (0.6%)	1	8.7	10.6	9.5	4.5	12.0	12.1	IOF (-20.1%)
BC-6-F2-R	200.5 (-8.3%)	203.2 (-7.1%)	1 2	30.6 15.2	26.0 18.5	16.2 32.4	10.0 10.4	10.4	11.4	IOF (-8.2%)
BC-8-F2-R	231.3 (-37.5%)	281.4 (-23.9%)	1 2	34.8 14.9	29.6 18.0	22.5 32.4	12.8 10.2	11.6	12.6	IOF (17.8%)

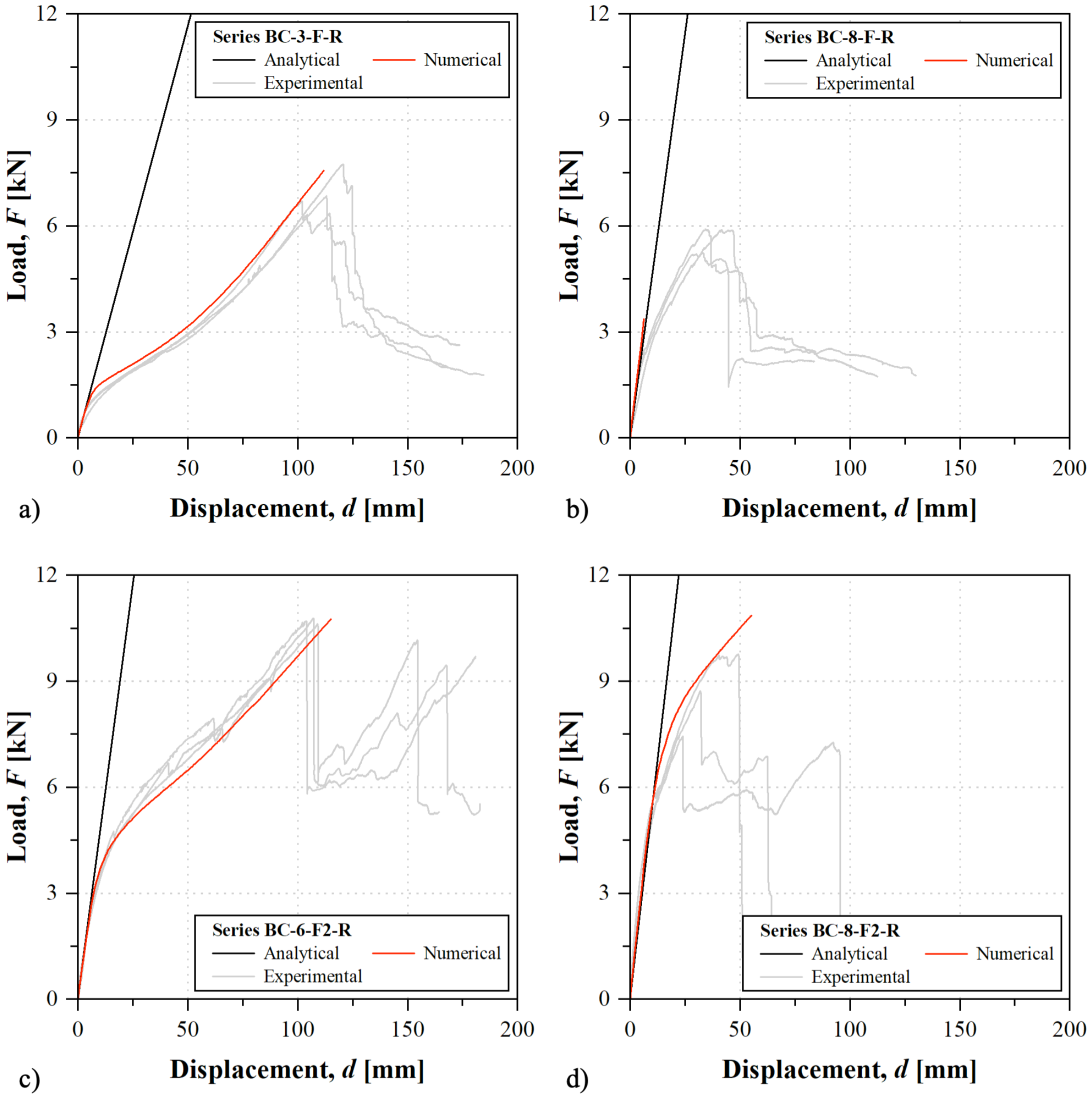

Figure 7.6 - Load *vs.* displacement curves of the reinforced connection series including the experimental, analytical and numerical curves: a) series BC-3-F-R; b) series BC-8-F-R; c) series BC-6-F2-R; d) series BC-8-F2-R.

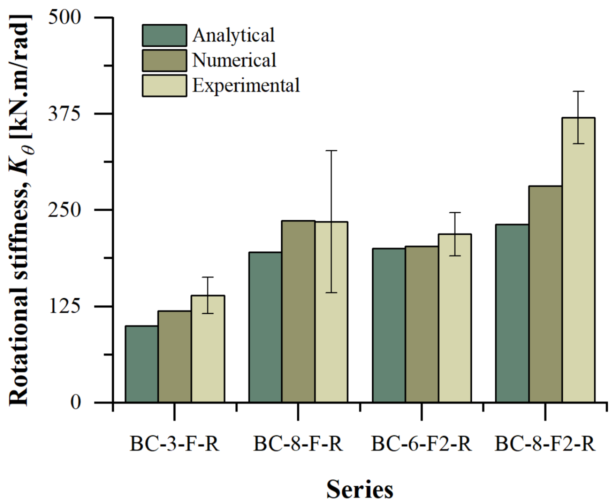

Figure 7.7 - Rotational stiffness: analytical and numerical predictions, and experimental results (*cf.* Chapter 6).

In order to better understand the relative contribution of each component to the overall stiffness, for each series, the difference (*$diff_i$*) between the predicted overall connection stiffness (k_{ov}) and that without one of the individual components ($k_{ov\text{-}i}$) was evaluated:

$$diff_i = k_{ov} - k_{ov-i} \tag{7.10}$$

$$\frac{1}{k_{ov-i}} = \frac{1}{k_{ov}} - \frac{1}{k_i} \tag{7.11}$$

where k_i is the estimated stiffness of the component *i* being assessed.

The relative influence of each component ($\Delta_{diff,i}$) was then computed with Eq. (7.12):

$$\Delta_{diff,i} = \frac{diff_i}{\sum_{j=1}^{6} diff_j} \tag{7.12}$$

where *n* is the total number of components.

Figure 7.8 shows the relative influence of each component in the predicted analytical stiffness for each connection series.

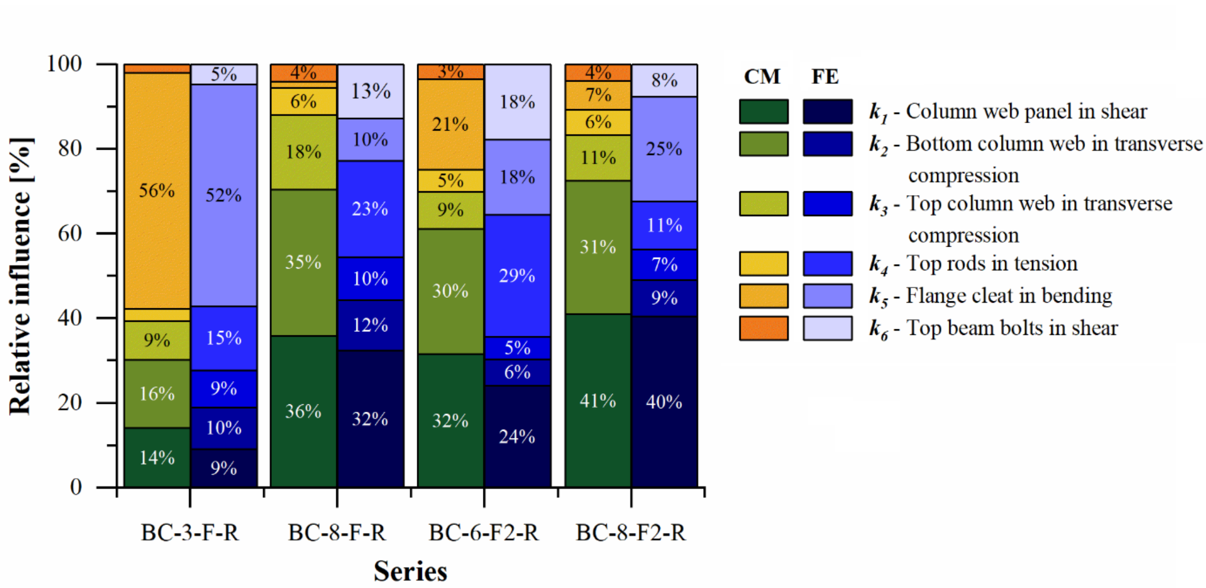

Figure 7.8 - Relative influence of the components to the stiffness of the reinforced series on the analytical (CM) and numerical (FE) analysis.

There are four major contributors to the overall initial stiffness: (i) the column web panel in shear (k_1); (ii) the bottom and (iii) top column web in transverse compression (k_2 and k_3); and (iv) the flange cleat in bending (k_5). As expected, the top flange cleat in bending has the highest influence for series BC-3-F-R and its influence decreases as the thickness of the cleat was increased. On the other hand, the column web panel in shear has a remarkable influence for all connection series, although more pronounced for the thicker cleats, with relative influence of ~36-40% for series BC-8-F-R and BC-8-F2-R. It is also important to notice that the components related to the GFRP (k_1 to k_3) material have a significant influence, particularly for the series with thicker cleats, with a combined relative influence of (i) 39% for BC-3-F-R series, (ii) 88% for BC-8-F-R series, (iii) 70% for series BC-6-F2-R, and (iv) 83% for series BC-8-F2-R.

7.3.2. Numerical estimation of connection stiffness

The stiffness of the different series was also assessed by means of finite element (FE) models developed using ABAQUS software. An overview of one (representative) FE model is presented in Figure 7.9. The different components were all modelled in accordance to the geometric properties described in Section 7.1 and illustrated in Figure 7.1. The bolts/rods, nuts and washers were modelled as one part in order to simulate the attachment between them, and no pre-tension was considered. Every component was meshed using linear solid elements with full integration (C3D8 for the beam and column elements, and C3D10 for the stainless steel elements), and the contact between surfaces of the connections' components was modelled using the HARDCONTACT formulation without the consideration of friction. In order to accurately simulate the load application system used in the experimental tests (*cf.* Chapter 6), the displacement was applied to a rigid frame element, simulating the load cell, which was hinged at both ends. This frame was then connected to a steel plate (E_s = 200 GPa, υ = 0.3), which was tied to the beams' top flange. By conducting an analysis that accounted for geometric non-linearity, it was possible to accurately simulate the rotation of the load cell, which increased with the rotation of the beam, remaining perpendicular to it.

The GFRP material was modelled as a homogeneous (through the thickness) linear elastic material using the (orthotropic) mechanical properties obtained from the mechanical characterization tests of coupons taken from the web and flanges (*cf.* Chapter 6). On the other hand, the stainless steel material was modelled considering the full true stress *vs*. true strain curves also obtained from coupon tensile tests (*cf.* Chapter 6). Regarding the mesh size, after a mesh sensitivity study, the elements were meshed with the following global seeding sizes: (i) beam – 2 mm; (ii) column – 8 mm; (iii) cleats – 1 mm; (iv) bolts – 0.5 mm; and (v) rods – 3 mm. It should be mentioned that a coarser mesh could have been used with identical results if the computational costs were an issue. The analysis were performed with an initial step of 1×10^{-5}, which was allowed to increase up to 0.01.

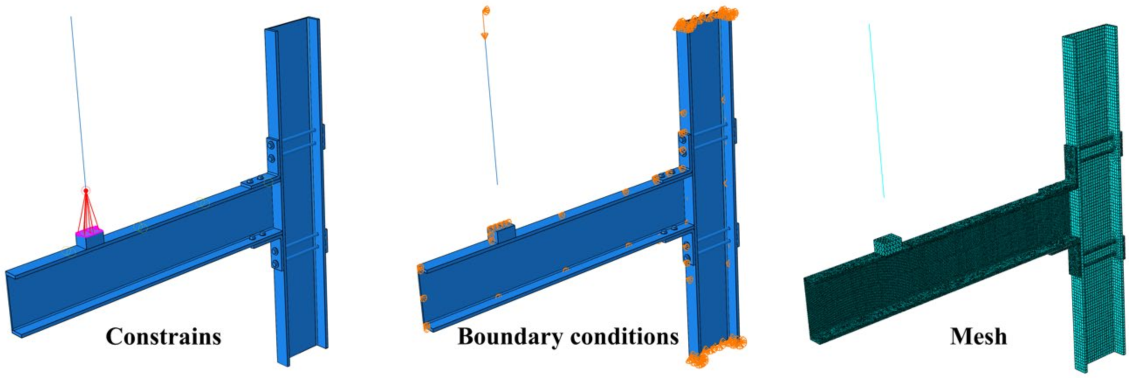

Figure 7.9 - Overview of the numerical models.

The following boundary conditions were considered in the models: (i) symmetry simplification along the longitudinal axis of the profiles; (ii) the column ends were fixed; and (iii) a vertical displacement of 120 mm was applied at the top of the load application system.

The load *vs*. displacement curves and stiffness obtained from the FE models are presented respectively in Figure 7.6 and Figure 7.7, together with the experimental results for comparison purposes. The initial stiffness values obtained from the FE models and the respective relative differences to the experimental results are presented in Table 7.1. The FE models were able to accurately predict the initial stiffness of the different reinforced connection series. The numerical curves present remarkably good agreement with their experimental counterparts up-to-failure, especially regarding the connection series with less stiff cleats (series BC-3-F-R, BC-6-F2-R and BC-8-F2-R) since the non-linear behaviour of these connections was associated with the deformation of the stainless steel cleats. On the other hand, the model of connection series BC-8-F-R was not able to predict the behaviour of the connection after the initial linear stage (displacement of ~5 mm), due to the fact that, unlike the other series, almost no plastic deformations were observed in the cleats while damage concentrated in the GFRP – which was not accounted for in the FE models, as mentioned earlier. As referred in Chapter 6, the cleats with higher thickness present considerably higher stiffness than that of the GFRP profiles, triggering the concentration of high contact stresses and the occurrence of localized damage in the profiles.

Finally, the influence of each component described in Section 7.2.1 to the overall connection stiffness was also assessed in the FE models. To that end, six different models per connection series were created and each one had a reference component modelled as rigid. For example, in order to evaluate the influence of component k_1, corresponding to the column web panel in shear, the shear modulus of the columns' web was set to a very high value. Following the same procedure described in Section 7.2.1, the stiffness of each model corresponding to each component was then compared with the stiffness of the "base" model following Eqs. (7.10) and (7.11), and the relative difference was estimated using Eq. (7.12). The numerical relative influence of each component to the connections' stiffness is presented in Figure 7.8. Similarly to the analytical predictions, the components that have greater influence on the stiffness of each series in the FE models are the top cleat in bending (component k_5) – especially for series BC-3-F-R - and those concerning the column's web (components k_1, k_2 and k_3) – especially for series BC-8-F-R and BC-8-F2-R. However, in the FE models, the tension of the top rods (k_4) seems to have significantly more influence in the stiffness of the connections than estimated in the analytical study. Such differences are likely related to the fact that the bending of these rods (captured by the FE models) was not considered in the analytical predictions, which may actually contribute to the lower overall stiffness of these elements in the numerical models.

7.4. STRENGTH PREDICTION

As mentioned earlier, the strength of each reinforced series was predicted using a combination of analytical and numerical methodologies. In the first part of this section, the formulas available in current design standards and corresponding to the several local failure modes are presented. After that, the load distribution on the connections' components obtained using FE models and the resulting strength predictions are shown and compared with test data.

7.4.1. Failure modes and corresponding strength

As mentioned, the available standards for FRP structures [7.1-7.3] present very limited guidance regarding the design of beam-to-column connections. However, such documents provide design equations to determine the strength associated to local failure modes that may occur in plates of beam-to-column connections, such as: (i) shear-out failure (*cf.* Figure 7.10a); (ii) bearing failure (*cf.* Figure 7.10b); (iii) pull-out failure (*cf.* Figure 7.10c); (iv) interaction between shear and pull forces in the bolts; and (v) web-crippling failure. These formulae, namely those proposed in CEN's Prospect [7.3], were used to predict the strength associated to each of these failure mechanisms. The shear-out failure strength (V_{sh}) was determined in accordance to Eq. (7.13) [7.3],

$$V_{sh} = \tau_{TL}\,(2e - d)t \tag{7.13}$$

where, τ_{LT} is the in-plane shear strength along the longitudinal direction, *e* is the bolt edge distance or the distance between two bolts from different rows, *d* is the bolt diameter and *t* is the thickness of the profile's plate. This equation proved to be able to predict the strength associated to this failure mode in the double-lap tests (*cf.* Chapter 6).

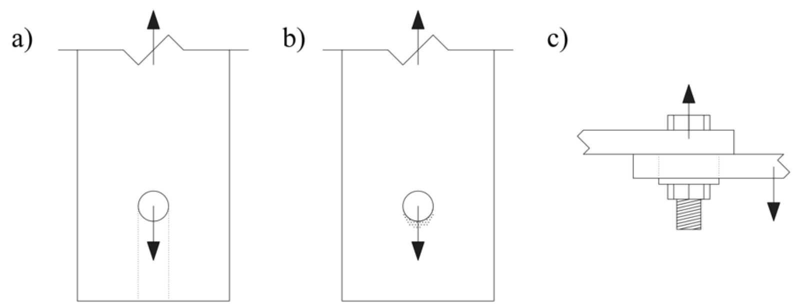

Figure 7.10 - Bolted GFRP plate failure modes considered in the strength predictions: a) shear-out failure; b) bearing failure; c) pull-out failure.

The bearing failure strength (V_{br}) was determined using Eq. (7.14) [7.3],

$$V_{br} = \frac{1}{k_{cc}}\,\sigma_{br,L}\,d\,t \tag{14}$$

where, $\sigma_{br,L}$ is the longitudinal bearing strength determined in the double-lap tests (*cf.* Chapter 6) and k_{cc} is a stress concentration factor due to hole clearance, equal to $(d_0/d)^2$, where d_0 is the hole diameter; this factor was considered equal to 1 as no clearance was provided in the connections tested.

The pull-out failure strength (N_{pull}) was determined with Eq. (7.15) [7.3],

$$N_{pull} = \tau_{th}\, \pi\, d_w\, t \tag{7.15}$$

where, τ_{th} is the shear strength in the through-thickness direction, which, in the absence of specific test data, was taken as the inter-laminar shear strength in the transverse direction ($\tau_{is,T}$, *cf.* Chapter 6), and d_w is the diameter of the washer.

For the in- and out-of-plane interaction between shear and axial forces, the recommendations of CEN's Prospect [7.3] were also followed:

$$\frac{V_s}{V_R} + \frac{N_s}{N_R} \leq 1 \tag{7.16}$$

where, V_s is the acting shear load in the bolt, N_s is the acting tension load in the bolt, V_R is the shear strength (the lowest between the shear-out and the bearing failure strengths) and N_R is the pull-out failure strength.

Finally, regarding the web-crippling failure near the top stainless steel plate and near the bottom cleat, since the CEN's Prospect [7.3] does not provide any design formulae to predict the strength associated with these phenomena, the expression proposed in the ASCE Pre-Standard [7.2], which was derived from the work of Borowicz and Bank [7.24] for interior-one-flange load configuration, was used:

$$R_{Rd,wc} = 0.7 h_c t_{w,c} \tau_{is,L} \left(1 + \frac{2\left(t_{fc} + r_c\right) + 6t_{pl} + b_{pl}}{h_{w,c}}\right) \tag{7.17}$$

where, h_c is height of the column, $t_{w,c}$ is thickness of column's web, $\tau_{is,L}$ is the longitudinal interlaminar shear strength of the column's web (*cf.* Chapter 6), t_{fc} is the thickness of the column's flange, r_c is the column's web-flange junction radius, t_{pl} is the thickness of the bearing plate, b_{pl} is the contact length of the bearing parts (top back flange plate or the bottom cleat), and $h_{w,c}$ is the height of the column's web. The contact length of the back plate and of the bottom cleat was defined by considering a spreading stress rate of 1:1 for the stainless steel material (*cf.* Section 7.3.1 and Appendix C).

7.4.2. Load distribution per connection element

The load distribution per bolt as well as the transverse compressive loads in the column web were obtained by means of the 3-dimensional linear elastic FE models described in Section 7.3.2. The pull and shear contact forces in the beams' top bolts, as well as the compressive contact forces in the front and back flanges of the column, are presented in Table 7.2 as a function of the applied load in the experimental setup (*cf.* Chapter 6); *e.g.* the shear load ratio represents the bolt's shear load divided by the load applied to the beam. The shear and pull-out ratio values obtained in the models were constant after an initial adjustment stage in the FE analysis. These results show that, for connections with only one bolt row, series BC-3-F-R presents higher shear load ratio than series BC-8-F-R. On the other hand, series BC-8-F-R presents the highest pull-out load ratios. This analysis highlights the influence of the cleat thickness in the stress distribution, as the thicker (stiffer) cleats do not accommodate the beams' deformation, resulting in higher pull-out forces and lower shear forces. These results are in accordance with the analysis of the relative influence of each component in the overall stiffness (*cf.* Section 7.3 and Figure 7.8), which showed that the relative influence of the flange cleat bending was ~5 times higher for series BC-3-F-R than for series BC-8-F-R. The shear load ratios of both series with two bolt rows are similar. Furthermore, for these series, it should be noted that the sum of the shear load ratios of the two bolt rows are very similar to the shear load ratio of series BC-F-8-R (ratio sum of 1.54 and 1.48 for series BC-6-F2-R and BC-8-F2-R, respectively). The pull-out load ratios of the series with two bolt rows are also quite similar; however, in this case the connection with thicker cleats presents the lowest pull-out load ratios. This somewhat unexpected result agrees with the analysis of the relative influence of each component in the stiffness (*cf.* Section 7.3 and Figure 7.6), which showed that the relative influence of the flange cleat in bending was higher for series BC-8-F2-R than for series BC-6-F2-R, precisely in the inverse proportion registered for the pull-out load ratio (~39%). Finally, the compression load ratios of the column's web are similar for every connection series, with the greatest difference being registered for series BC-3-F-R concerning the compression caused by the contact top plate.

Table 7.2 - Load distribution ratios obtained in the numerical models

Series	Bolt row	Shear load	Pull-out load	Compression load of column web top	Compression load of column web bottom
BC-3-F-R	1	1.82	1.30	3.92	5.45
BC-8-F-R	1	1.57	1.66	3.41	3.06
BC-6-F2-R	1	0.64	0.97	4.09	3.04
	2	0.90	0.48		
BC-8-F2-R	1	0.56	0.70	3.98	2.93
	2	0.92	0.48		

7.4.3. Results

The ultimate loads for each connection series were obtained by considering the strength associated to each failure mode (*cf.* Section 7.4.1) and the corresponding load distribution ratios. Table 7.1 presents the loads associated to each failure mechanism, indicating the (predicted) governing failure mode and the relative difference between the predicted and experimental failure loads. The nomenclature used in this table regarding the failure modes is: (i) SOF, for the shear-out failure at the beam's top bolts; (ii) BF, bearing failure at the beam's top bolts; (iii) POF, pull-out failure at the beam's top bolts; (iv) IOF, in- and out-of-plane failure at the beam's top bolts; (v) CWTF, column's web-crippling failure near the top auxiliary stainless steel plate; (vi) CWBF, column's web-crippling failure near the bottom stainless steel cleat.

Regarding series BC-3-F-R, the predicted failure mode was in- and out-of-plane interaction with a relative difference between predicted and experimental failure load of -35%. In this case, however, it is worth noting that the stress distribution obtained in the FE models may significantly overestimate the out-of-plane forces to which the beam's top bolts are subjected to, namely after the advent of some damage in the GFRP beam. In fact, the experimental observations indicate that, due to the extensive deformation presented by the top cleat (*cf.* Chapter 6), the beam's top bolts are subjected mostly to shear stress. Additionally, during the experimental tests (*cf.* Chapter 6) it was observed that some damage develops in the web-flange junction of the GFRP beam, further reducing the transfer of pull-out loads to the beam's top bolts. It should be mentioned that if the contribution of the out-of-plane stresses in that interface is disregarded, the governing failure mode would be shear-out, which is precisely the failure mode observed in the experimental tests (*cf*. Chapter 6), with a relative difference of only +3% to the experimental results. However, this assumption could not be made *a priori*. Nevertheless, for design purposes, the conservative prediction of the failure load (-35%) is deemed reasonable. Additionally, the results also indicate that this connection series is prone to failure by compression of the column's web (this failure mode presented the second lowest ultimate load), a failure mode observed in the cyclic tests described in Chapter 6.

Concerning series BC-8-F-R, the predicted failure mode was also in- and out-of-plane interaction, with similar load estimates to those of series BC-3-F-R. In this case, however, owing to the cleats' higher stiffness, significant out-of-plane stresses developed at the beam's top bolts. In fact, the failure modes observed in the monotonic tests reflected a clear combination of in-plane and out-of-plane stresses (*cf*. Chapter 6). Overall, a satisfactory prediction of the failure mode and failure load was obtained, with a relative difference of -20% w.r.t. the experimental failure load.

For series BC-6-F2-R, three failure modes presented very similar strengths, namely: (i) in- and out-of-plane interaction failure; (ii) top column's web compression failure; and (iii) bottom column's web compression failure. These failure modes presented a relative difference of ~5 to 8% w.r.t. to the experimental results. In this regard, the failure mode observed in the monotonic experimental tests was transverse compression of the column's web, but in the cyclic tests one specimen registered shear-out and tearing failure of the beam's flange (*cf*. Chapter 6), indicating that, as predicted by the proposed method, these failure modes are triggered for very similar loads.

Finally, the predicted failure mode for series BC-8-F2-R was interaction between in- and out-of-plane loads, in agreement with the experimental results, with a relative difference between the predicted and experimental failure load of +18%.

Overall, the design formulae presented and the associated stress distribution model provided reasonably accurate strength predictions of the different reinforced connection series, with an average relative difference of ~20%. It should also be mentioned that in all connection series with exception of series BC-8-F2-R, the strength predictions were lower than the experimental failure loads, thus providing conservative strength predictions, in agreement with the overall principles of safety design.

7.5. CONCLUSIONS

This chapter presented analytical and numerical investigations of beam-to-column connections between pultruded GFRP profiles using stainless steel cleats, supported by test results presented in Chapter 6, in order to predict their initial stiffness and strength.

The initial stiffness was predicted using both the analytical "component method" and numerical FE models. The stiffness of most components considered in the analytical predictions was computed from formulae duly adapted from steel structural design standards. The stiffness of the different connection series predicted using the "component method" were similar to those registered experimentally, with an average absolute relative difference of -23%, thus validating the proposed analytical models, especially considering the experimental scatter (CoV up to ~40%). Concerning the numerical models, the initial stiffness obtained for all connections was also in close agreement with the stiffness measured experimentally, with an average absolute relative difference of 11%. For both analytical and numerical models, it was possible to identify the components with more influence in the overall connections' stiffness: (i) the column web in shear; (ii) the bottom column web in transverse compression; (iii) the top column web in transverse compression; and (iii) the top flange cleat in bending.

The strength of the reinforced connection series was predicted using a combination of analytical and numerical procedures. The local failure strengths corresponding to the connections' components were estimated by means of formulae available in FRP structural design standards. The load distribution of the relevant components of the connections was determined by means of FE models. The strength was underestimated for connection series BC-3-F-R due to the inherent limitations of the FE models, namely the non-consideration of GFRP damage in the numerical models. For series BC-8-F-R and BC-8-F2-R, the failure mode (in- and out-of-plane interaction failure) and the corresponding failure load were predicted with reasonable accuracy. Finally, regarding series BC-6-F2-R, three failure modes presented very similar ultimate loads: (i) in- and out-of-plane interaction failure; (ii) top column's web compression failure; and (iii) bottom column's web compression failure.

Overall, the proposed methods to predict the initial stiffness and strength of beam-to-column connections not only provided accurate predictions of the monotonic response of the connections, but also allowed to obtain a better understanding of the mechanisms that influence their behaviour, proving to be a valuable and straightforward design tool for engineering practice. Nevertheless, future research should pursue new simulation and design tools, including the introduction of GFRP damage progression models in FE modelling, which can be applied for any generic case.

7.6. REFERENCES

[7.1] CNR-DT 205/2007 – Guide for the Design and Construction of Fiber-Reinforced Concrete Structures.

[7.2] ASCE (2010). Pre-Standard for Load & Resistance Factor Design (LRFD) of Pultruded Fiber Reinforced Polymer (FRP) Structures.

[7.3] CEN/TC250/WG4 (2014). Fibre Reinforced Polymer Structures: scientific and technical report.

[7.4] Abd-El-Naby SFM, Hollaway L. (1993). The experimental behaviour of bolted joints in pultruded glass/polyester material. Part 1: Single-bolt joints. *Composites*, 24(7), 531-538.

[7.5] Abd-El-Naby SFM, Hollaway L. (1993). The experimental behaviour of bolted joints in pultruded glass/polyester material. Part 2: Two-bolt joints. *Composites*, 24(7), 539-546.

[7.6] Hassan NK, Mohamedien MA, Rizkalla SH. (1997). Multibolted joints for GFRP structural members. *Journal of Composites for Construction*, 1(1), 3-9.

[7.7] Erki MA. (1995). Bolted glass-fibre-reinforced plastic joints. *Canadian journal of civil engineering*, 22(4), 736-744.

[7.8] Rosner CN, Rizkalla SH. (1995). Bolted connections for fiber-reinforced composite structural members: experimental program. *Journal of materials in civil engineering*, 7(4), 223-231.

[7.9] Mosallam A. (2011). Design guide for FRP composite connections. *American Society of Civil Engineers*.

[7.10] Agarwal BL. (1980). Static strength prediction of bolted joint in composite material. *AIAA Journal*, 18(11), 1371-1375.

[7.11] Camanho PP, Matthews FL. (1999). A progressive damage model for mechanically fastened joints in composite laminates. *Journal of Composite Materials*, 33(24), 2248-2280.

[7.12] Dano ML, Gendron G, Picard A. (2000). Stress and failure analysis of mechanically fastened joints in composite laminates. *Composite Structures*, 50(3), 287-296.

[7.13] Dano ML, Kamal E, Gendron G. (2007). Analysis of bolted joints in composite laminates: Strains and bearing stiffness predictions. *Composite Structures*, 79(4), 562-570.

[7.14] Girard C, Dano ML, Picard A, Gendron G. (2003). Bearing behavior of mechanically fastened joints in composite laminates--Part I: strength and local strains. *Mechanics of Advanced Materials and Structures*, 10(1), 1-21.

[7.15] Hahn HT, Tsai SW. (1973). Nonlinear elastic behavior of unidirectional composite laminae. *Journal of Composite Materials*, 7(1), 102-118.

[7.16] Smith SJ, Parsons ID, Hjelmstad KD. (1999). Finite-element and simplified models of GFRP connections. *Journal of Structural Engineering*, 125(7), 749-756.

[7.17] Harte AM, Cann D. (2001). Finite element modelling of the semi-rigid behaviour of pultruded FRP connections. *Journal of Materials Processing Technology*, 119(1-3), 98-103.

[7.18] Zhang Z, Wu C, Nie X, Bai Y, Zhu L. (2016). Bonded sleeve connections for joining tubular GFRP beam to steel member: Numerical investigation with experimental validation. *Composite Structures*, 157, 51-61.

[7.19] Tsai SW. (1965). *Strength Characteristics of Composite Materials*. Philco Corp Newport Beach CA.

[7.20] Feroldi F, Russo S. (2016). Structural behavior of all-FRP beam-column plate-bolted joints. *Journal of Composites for Construction*, 20(4), 04016004.

[7.21] EN1993 (2005). Design of Steel Structures – Part 1–8: Design of Joints.

[7.22] Aribert JM, Lachal A, Moheissen M. (1992). Modelling and experimental investigation of plastic resistance and local buckling of H or I steel sections submitted to concentrated or partially distributed loading. In *Contact Loading and Local Effects in Thin-walled Plated and Shell Structures* (pp. 101-110). Springer, Berlin, Heidelberg.

[7.23] Zhao L, Xin A, Liu, F, Zhang J, Hu N. (2016). Secondary bending effects in progressively damaged single-lap, single-bolt composite joints. *Results in physics*, 6, 704-711.

[7.24] Borowicz DT, Bank LC. (2011). Behavior of pultruded fiber-reinforced polymer beams subjected to concentrated loads in the plane of the web. *Journal of Composites for Construction*, 15(2), 229-238.

[7.25] Faella C, Piluso V, Rizzano G. (1999). *Structural steel semirigid connections: theory, design, and software* (Vol. 21). CRC press

Chapter 8

Monotonic and cyclic behaviour of a cuff connection system for I-section profiles

8.1. INTRODUCTION

Departing from the promising results reported in Chapter 5 (concerning the behaviour of a cuff connection system for pultruded tubular profiles), this chapter presents an experimental study focused on the assessment of the monotonic and cyclic performance of a similar stainless steel cuff connection system, now developed to join beams and columns comprising I-section pultruded GFRP profiles, which are more often used in civil engineering structural applications. The main objective of this study is to investigate if the main advantages provided by cuff tubular parts also apply to open section profiles. To that end, the monotonic behaviour (initial stiffness, strength and failure modes) of four different connection series with two different cuff plate thicknesses and lengths was assessed. Subsequently, the series with the best performance in the monotonic tests was subjected to cyclic tests to evaluate its hysteretic response and, specifically, its energy dissipation capacity. Finally, the cuff connection series were benchmarked against a beam-to-column connection system using stainless steel flange cleats that was recently proposed and tested by the author (*cf.* Chapter 6).

8.2. EXPERIMENTAL PROGRAMME

Monotonic and cyclic tests were performed in full-scale beam-to-column connection specimens. These consisted of two pultruded I-section GFRP profiles, corresponding to the beam and column, one stainless steel cuff part (with varying geometry) and M8 stainless steel rods, washers and nuts. This section presents the materials characterization, the geometry of the beam-to-column connection specimens and the test setup.

8.2.1. Material characterization tests

The pultruded GFRP profiles used in the connection specimens had a I-shaped cross-section with dimensions 150×75×8 mm. These profiles were manufactured by *ALTO, Perfis Pultrudidos, Lda.*, using E-glass fibres and isophthalic polyester resin matrix. The following material properties of the profiles were characterized by means of coupon testing: (i) compressive strength in both longitudinal ($\sigma_{cu,L}$) and transverse ($\sigma_{cu,T}$) directions and corresponding elastic moduli ($E_{c,L}$ and $E_{c,T}$); (ii) longitudinal tensile strength ($\sigma_{tu,L}$), modulus of elasticity ($E_{t,L}$) and Poisson ratio (ν_{LT}); (iii) longitudinal interlaminar shear strength ($\tau_{is,L}$); and (iv) in-plane shear strengths (τ_{LT} and τ_{TL}) and shear moduli (G_{LT} and G_{TL}). The aforementioned properties are summarized in Table 8.1, together with the test standards adopted. The mass fibre ratio of the GFRP profile was also determined in accordance with ISO 1172 [8.6] (calcination tests up to 800ºC), being of 60% and 55% for the web and flange laminates, respectively.

The AISI 304 stainless steel sheets used in the cuff connection parts were previously characterized in Chapter 6. The 0.2% tensile proof stress ($f_{0.2\%}$), the tensile strength (f_u) and corresponding strain (ε_u) and elastic modulus (E_s) of these stainless steel (before cold-forming) are presented in Table 8.2. The stainless steel rods, nuts and washers were of grade A2-70 with 450 MPa of nominal yield stress and 700 MPa of nominal ultimate stress, according to ISO 3506-1 [8.8].

Table 8.1 - Mechanical properties of the GFRP material (average ± standard deviation).

Test	Method	Property	Element	Average ± std. Dev.	Unit
Tension	EN ISO 527 [8.1]	$\sigma_{tu,L}$	Web	388.0 ± 25.0	[MPa]
			Flange	353.4 ± 32.7	
		$E_{t,L}$	Web	43.4 ± 1.0	[GPa]
			Flange	39.6 ± 1.2	
		υ_{LT}	Web	0.23 ± 0.02	[-]
			Flange	0.29 ± 0.02	
Compression	ASTM-D6641 [8.2]	$\sigma_{cu,L}$	Web	461.9 ± 31.0	[MPa]
			Flange	353.5 ± 32.7	
		$E_{c,L}$	Web	44.9 ± 1.7	[GPa]
			Flange	39.6 ± 1.2	
		$\sigma_{cu,T}$	Web	64.2 ± 2.12	[MPa]
		$E_{c,T}$	Web	8.1 ± 0.6	[GPa]
	ASTM-D695 [8.3]	$\sigma_{cu,T}$	Flange	41.0 ± 3.6	[MPa]
		$E_{c,T}$	Flange	2.8 ± 0.2	[GPa]
Interlaminar shear	ASTM-D2344 [8.4]	$\tau_{is,L}$	Web	27.0 ± 1.3	[MPa]
			Flange	31.2 ± 1.0	
In-plane shear	ASTM-D5379 [8.5]	τ_{LT}	Web	46.8 ± 3.1	[MPa]
			Flange	47.9 ± 2.6	
		G_{LT}	Web	3.0 ± 0.3	[GPa]
			Flange	3.7 ± 0.3	
		τ_{TL}	Web	31.2 ± 2.3	[MPa]
			Flange	27.3 ± 5.0	
		G_{TL}	Web	3.3 ± 0.5	[GPa]
			Flange	2.5 ± 0.2	

Table 8.2 - Mechanical properties of the stainless steel material (average ± standard deviation).

Property	Thickness	Average ± std. Dev.	Standard
$f_{0.2\%}$	1.0 mm	288.8 ± 5.1 MPa	EN 10002-1 [8.7]
	1.5 mm	440.5 ± 37.4 MPa	
f_u	1.0 mm	707.1 ± 0.6 MPa	
	1.5 mm	679.7 ± 5.4 MPa	
ε_u	1.0 mm	0.569 ± 0.012 m/m	
	1.5 mm	0.463 ± 0.024 m/m	
E_s	1.0 mm	198.9 ± 3.5 GPa	
	1.5 mm	157.0 ± 18.0 GPa	

8.2.2. Beam-to-column connection tests

8.2.2.1. Description of test series

Four different series were studied using I-section profiles. Two I-section GFRP profiles (150×75×8 mm) were used per specimen, one 800 mm long for the beam and another 900 mm long for the column. The influence of the cuff part geometry was assessed (*cf*. Figure 8.1) by considering two plate lengths (270 mm and 360 mm) and two plate thicknesses (1.0 and 1.5 mm). As illustrated in Figure 8.2, the cuff parts were manufactured by welding five stainless steel sheets (two of the sheets were previously cold-formed). The cuff parts were connected to the GFRP profiles with six M8 stainless steel rods, two connecting to the beam and four connecting to the column. The nomenclature adopted for the experimental series was "BC-IC-L×t", where *BC* denotes beam-to-column, *IC* denotes I-section cuff connection system, *L* refers to the cuff length (270 and 360 mm) and *t* refers to the cuff walls thickness (1.0 and 1.5 mm).

For the four series mentioned above, three replicate specimens were tested under monotonic loading. Then, from the analysis of the monotonic test results, series BC-IC-360×1.0 – the best performing one (*cf.* Sections 8.3 and 8.5.1) – was chosen to be tested under cyclic loading; three replicate specimens were also used in these cyclic tests.

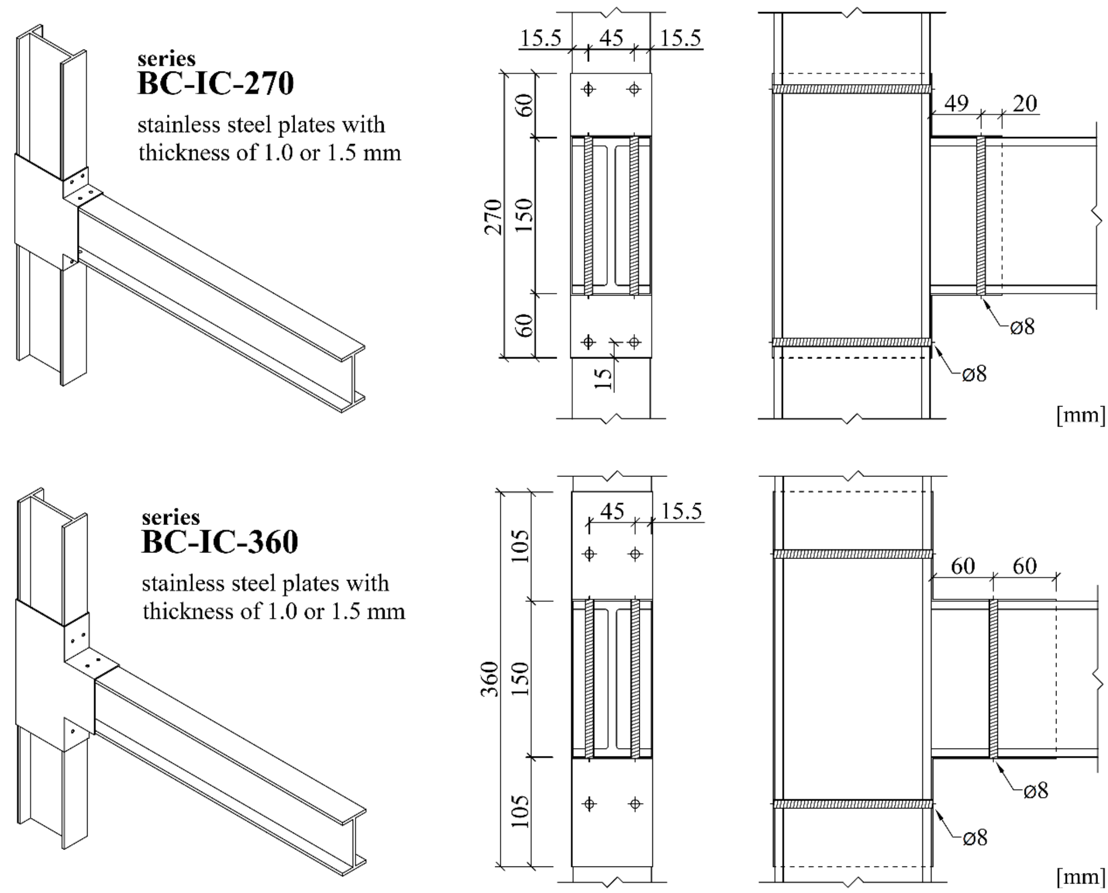

Figure 8.1 - Beam-to-column connection tests: test series.

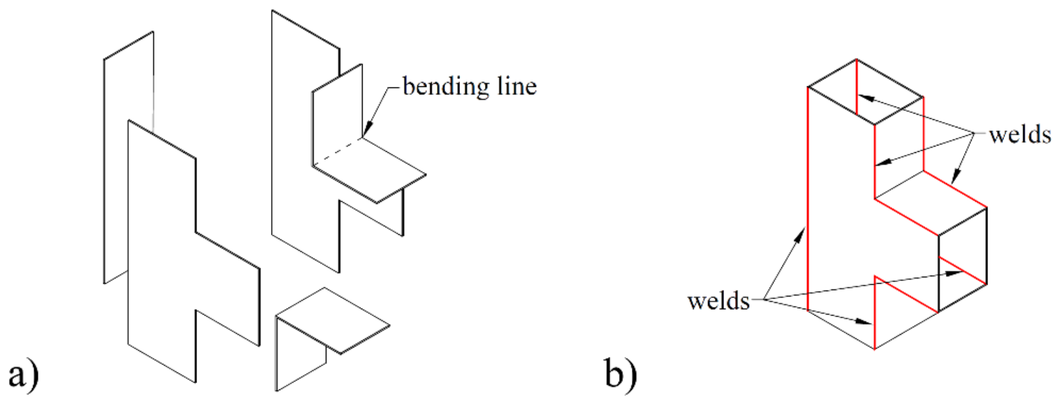

Figure 8.2 - Beam-to-column connection tests: cuff connection part – a) stainless steel sheets; b) weld location.

8.2.2.2. Test setup

All beam-to-column tests were performed in a closed steel loading frame fixed to the laboratory's strong floor. Figure 8.3 presents the test setup and the instrumentation used in the tests. The load was applied at a distance of 670 mm from the columns' longitudinal axis. The loading system comprised: (i) a *Dartec* hydraulic jack (*cf.* Figure 8.3, point A) with capacity of 250 kN and maximum stroke of 400 mm, (ii) a *TML* load cell (*cf.* Figure 8.3, point B) with capacity of 300 kN, and (iii) two metallic hinges (*cf.* Figure 8.3, points C) to assure the perpendicularity of the applied load relatively to the beam profile. Two aluminium bars were used to avoid lateral deflections of the beam free-end, while allowing free vertical displacements, (*cf.* Figure 8.3, point D); and two steel blocks with indentations matching the profile's cross-section were used to fix both column ends (*cf.* Figure 8.3, point E), restraining their displacements and rotations in all directions.

The rotations of the beam and column were measured with two *TML* inclinometers with ranges of ±10° and precision of 0.5%. However, only the beam's inclinometer was considered in the analysis, as the buckling of the cuffs' lateral walls hindered the accuracy of the columns' rotation measurements. However, results of previous investigations using the same test setup (Chapters 3, 4, 5 and 6) allow assuming negligible rotations on the columns. The vertical displacement of the hydraulic jack was measured by its built-in transducer. The loading histories for both the monotonic and cyclic tests were imposed by a *Dartec* control console. The data were collected at a rate of 5 Hz using a *HBM* data logger and stored in a computer.

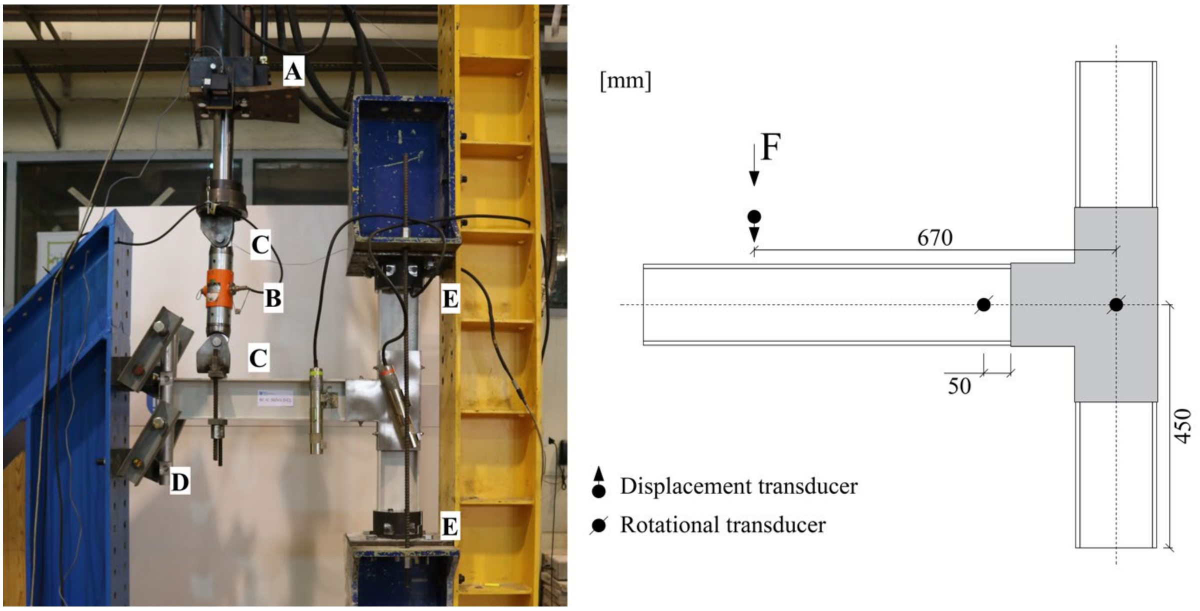

Figure 8.3 - Beam-to-column tests: test setup and instrumentation.

8.2.2.3. Test procedure

The monotonic tests were performed under displacement control at a rate of 0.25 mm/s. The tests ended when the maximum stroke of the hydraulic jack was attained or when the mechanical integrity of the specimen was considerably degraded due to extensive damage.

The cyclic tests were also conducted under displacement control, at a rate of 0.5 m/s [1], and followed a displacement history defined in accordance with the ECCS protocol [8.9]. This protocol, developed for steel structures, was adopted in the present work as the monotonic performance of the cuff connections was highly related to the plastic damage progression in the stainless steel cuff parts (*cf.* Section 8.3). Furthermore, to date, no comprehensive cyclic protocol for FRP structures has been proposed. The first four cycles corresponded to maximum absolute displacements of ¼, ½, ¾ and 1 times the end of proportionality (EP) displacement. After this point, groups of three cycles were applied with maximum

[1]The displacement rate of the cyclic tests was twice that of the monotonic test due to time constraints. Nonetheless, both rates prevented the occurrence of strain-rate phenomena, namely creep, and allowed monitoring the damage progression.

absolute displacement corresponding to *2n* of the EP displacement; where *n* is an integer which increases at every three cycles. The EP displacement of series BC-IC-360×1.0 was 17 mm, being defined as the point where the initial linearity was lost in the monotonic tests (*cf.* Section 8.3.1); this is one of the definitions suggested by the ECCS protocol [8.9], already used in previous works (*cf.* Chapters 4, 5 and 6). The displacement history of the cyclic tests for this connection is presented in Figure 8.4. The criteria used to define the end of the cyclic tests were similar to those used for the monotonic tests: either reaching the end of the hydraulic jack's stroke or the loss of structural integrity of the specimens.

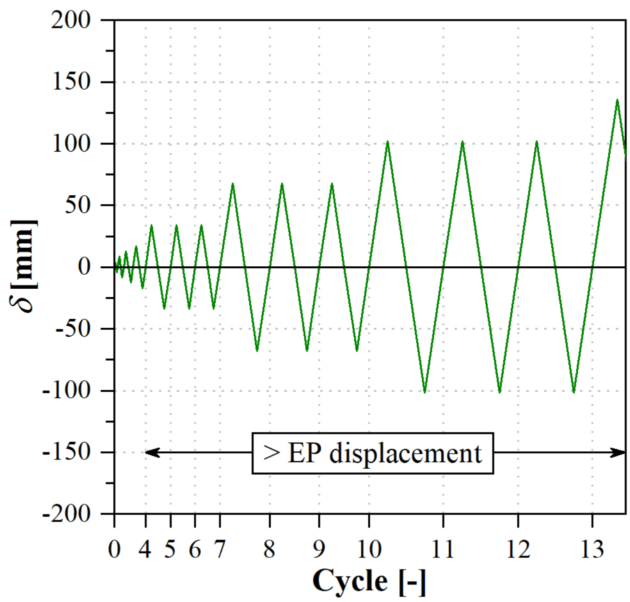

Figure 8.4 - Cyclic tests: load history.

8.3. MONOTONIC TESTS

This section presents the main results obtained in the monotonic tests, being divided in two subsections: (i) load *vs*. displacement and bending moment *vs*. rotation performance; and (ii) failure modes. Table 8.3 presents the summary of the results of the monotonic tests, namely the maximum load (F_u), the displacement corresponding to the maximum load (d_{Fu}), the ultimate moment (M_u), the initial rotation stiffness (K_θ), the ultimate failure mode and the ductility index (μ_d).

Table 8.3 - Beam-to-column monotonic tests: summary of experimental results (average ± standard deviation)

Series	F_u (kN)	d_{Fu} (mm)	M_u (kN.m)	K_θ (kN.m/rad)	Ultimate failure mode	μ_δ(-)
BC-IC-270×1.0	6.27 ± 0.4	91.29 ± 11.0	4.20 ± 0.3	79.38 ± 15.9	Cuff's plate tearing failure	0.86 ± 0.07
BC-IC-270×1.5	7.41 ± 1.1	51.05 ± 4.7	4.97 ± 0.7	104.99 ± 2.4	Beam's shear-out failure	0.67 ± 0.05
BC-IC-360×1.0	7.87 ± 0.7	80.17 ± 6.3	5.28 ± 0.4	96.33 ± 20.8	Beam's shear-out failure and bottom flange delamination	0.85 ± 0.04
BC-IC-360×1.5	9.10 ± 0.6	49.69 ± 6.5	6.10 ± 0.4	121.87 ± 9.0	Beam's shear-out failure and bottom flange delamination	0.61 ± 0.03

8.3.1. Load *vs*. displacement and moment *vs*. rotation behaviour

Figure 8.5 presents the monotonic load *vs*. displacement curves of all specimens of each series, while a corresponding representative moment *vs*. rotation curve for each series is presented in Figure 8.6; this figure also contains a representative curve of a cleated connection (series BC-6-F2-R, tested in Chapter 6), which is compared with the cuff connections in Section 8.5.2. It should be mentioned that the load *vs*. vertical displacement curves are necessary to assess the displacement at the end of proportionality, a parameter used in the definition of the cyclic loading history (*cf*. Section 8.4.1), while the moment *vs*. rotation curves, more commonly used to characterize the behaviour of connections, allow the assessment of the rotational stiffness and ultimate moment.

The specimens of series BC-IC-270×1.0 presented almost linear behaviour up to ~2.5 kN. This linear stage ended shortly after the start of the test, being consistent with the damage visible at 15 mm of vertical displacement, as described in Section 8.3.2. After that, a progressive loss of stiffness was registered, with some minute load losses, until the ultimate load was attained. For specimens M1 and M2, this peak occurred for a displacement of ~90 mm, while for specimen M3 it was observed at 107 mm. Following the maximum load, the load decreased rapidly for all specimens.

In series BC-IC-270×1.5, the initial response was linear until approximately ~5 kN, close to the instant when the first damage was observed (*cf*. Section 8.3.2). After that, a slight decrease of stiffness was registered followed by a succession of load drops and recoveries up to the ultimate load, reached for displacements between 40 to 60 mm. Then, an abrupt load loss was observed followed by a gradual load decrease until the end of the tests.

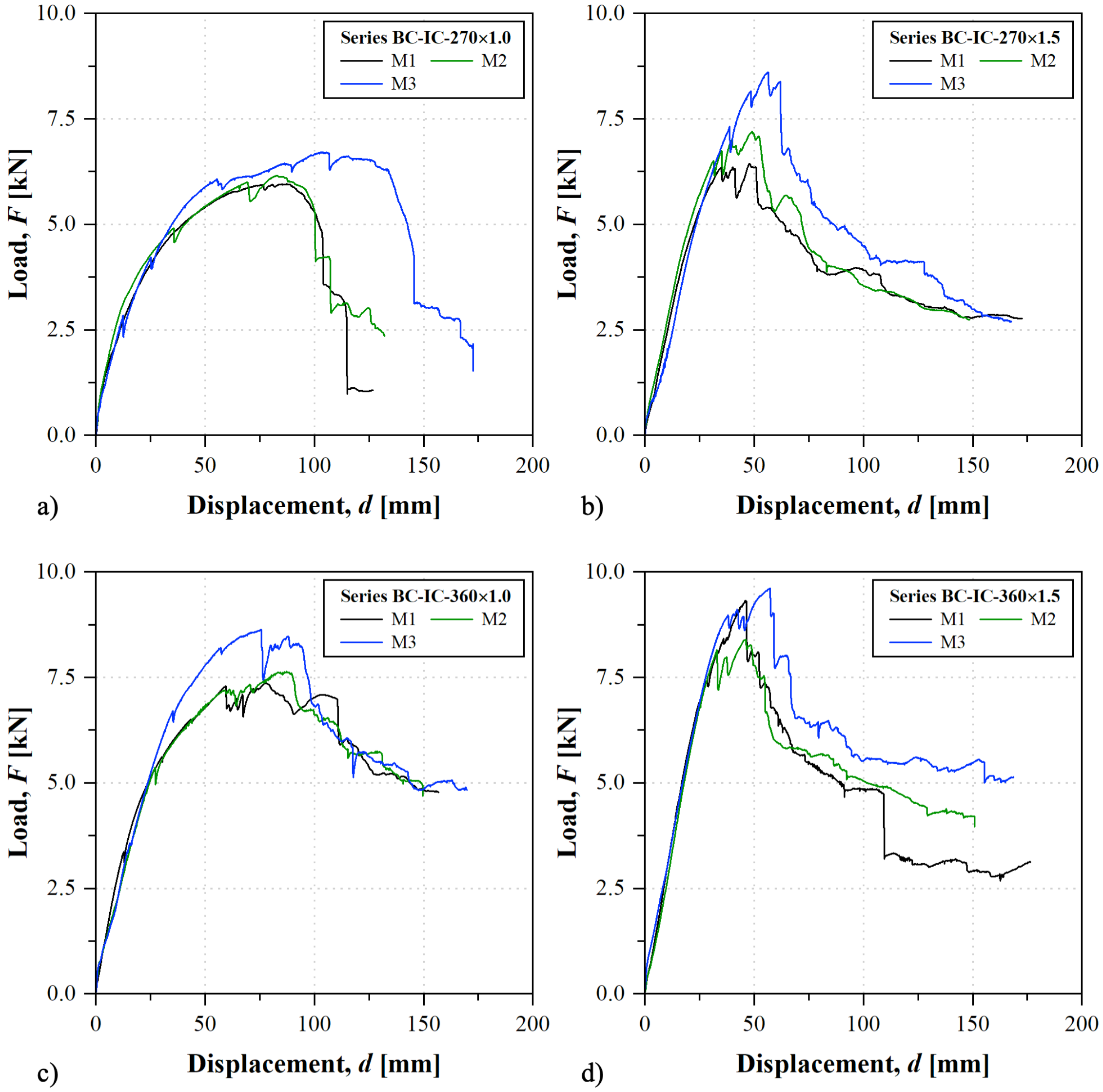

Figure 8.5 - Monotonic tests: load *vs.* displacement curves of a) series BC-IC-270×1.0; b) series BC-IC-270×1.5; c) series BC-IC-360×1.0; d) series BC-IC-360×1.5.

The specimens of series BC-IC-360×1.0 presented a similar qualitative behavior to that described for series BC-IC-270×1.5: (i) an initial linear stage up to ~4 kN, when first damage was observed in the cuff parts, as described in Section 8.3.2; (ii) a second stage characterized by stiffness loss, with minute load drops, owing to progressive damage on the GFRP material (*cf.* Section 8.3.2), until attaining a maximum load of ~8 kN; and (iii) a final stage with progressive load reductions.

Finally, the specimens of series BC-IC-360×1.5 presented a linear elastic response up to ~6 kN, when GFRP cracking noises were heard (*cf.* Section 8.3.2). After that point, the stiffness presented several reductions together with slight load decreases and recoveries until the ultimate load was reached; this was followed by a sudden load drop. After this point, the load reduced gradually until the end of the test.

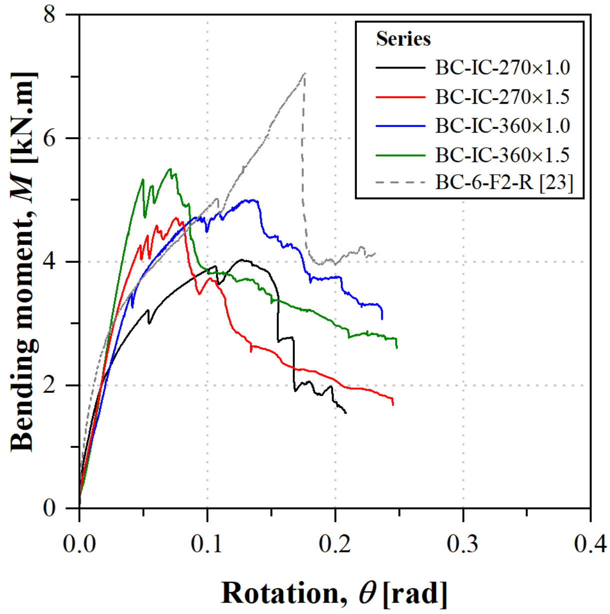

Figure 8.6 - Monotonic tests: representative moment *vs*. rotation curves for each series (representative specimen of series BC-6-F2-R included).

Increasing the thickness and the length of the cuff parts led to an increase of initial stiffness and strength of the connections (*cf*. Figures 8.7a and 8.7b, respectively), although these increases were higher when varying the cuff thickness than its length. In terms of initial stiffness: (i) by increasing the thickness of the cuff part, series BC-IC-270×1.0 *vs*. BC-IC-270×1.5 and series BC-IC-360×1.0 *vs*. BC-IC-360×1.5, the initial stiffness increased by 32% and 26%, respectively, while (ii) by increasing the length of the cuff parts, series BC-IC-270×1.0 *vs*. BC-IC-360×1.0 and series BC-IC-270×1.5 *vs*. BC-IC-360×1.5, increases of 21% and 16%, respectively, were registered. Regarding the strength of the connections, the thickness of the cuff part had the highest influence: (i) series BC-IC-270×1.5 achieved a moment 24% higher than that of series BC-IC-270×1.0; and (ii) the ultimate moment of series BC-IC-360×1.5 was 38% higher than that of series BC-IC-360x1.0. On the other hand, when evaluating the influence of the cuffs' length, the ultimate moment of series BC-IC-360×1.0 and BC-IC-360×1.5 were +14% and +26% higher than those of series BC-IC-270×1.0 and BC-IC-270×1.5, respectively.

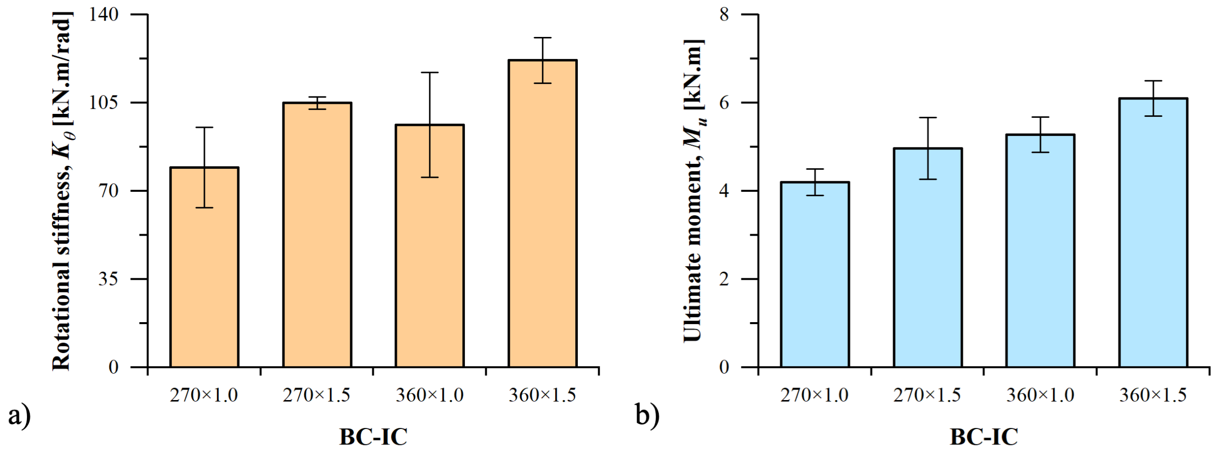

Figure 8.7 - Monotonic tests: a) initial stiffness; b) ultimate moment.

8.3.2. Failure behaviour

This section presents the damage modes observed in the monotonic tests. Since the cuffs hinder the visibility of the GFRP portions they encompass, during the tests it was not always possible to identify the exact point where damage in those segments developed. The damage of these areas was fully disclosed and assessed after the tests upon disassembly of the specimens.

Regarding series BC-IC-270×1.0, cracking noises, buckling of the cuffs' lateral walls and bearing in the stainless steel cuffs near the beam rods (*cf.* Figures 8.8a and 8.8b) started soon after the beginning of the tests, at a vertical displacement of ~15 mm, preceding a slight stiffness decrease (*cf.* Figure 8.5a). Bearing failure of GFRP was visible in the beam top holes at ~80 mm; for this displacement, in specimen M1 the welds also failed at the intersection of the beam and column members (*cf.* Figure 8.8c). After that, at a displacement of ~100 mm, tearing failure at the cuff plate in contact with the beam rods was observed in specimens M1 and M2 (*cf.* Figure 8.9d), which was followed by considerable load drops (*cf.* Figure 8.5a). Regarding specimen M3, the ultimate failure, at ~120 mm, involved a combination of bearing in the GFRP in one beam top hole and tearing in one hole of the cuff connection part.

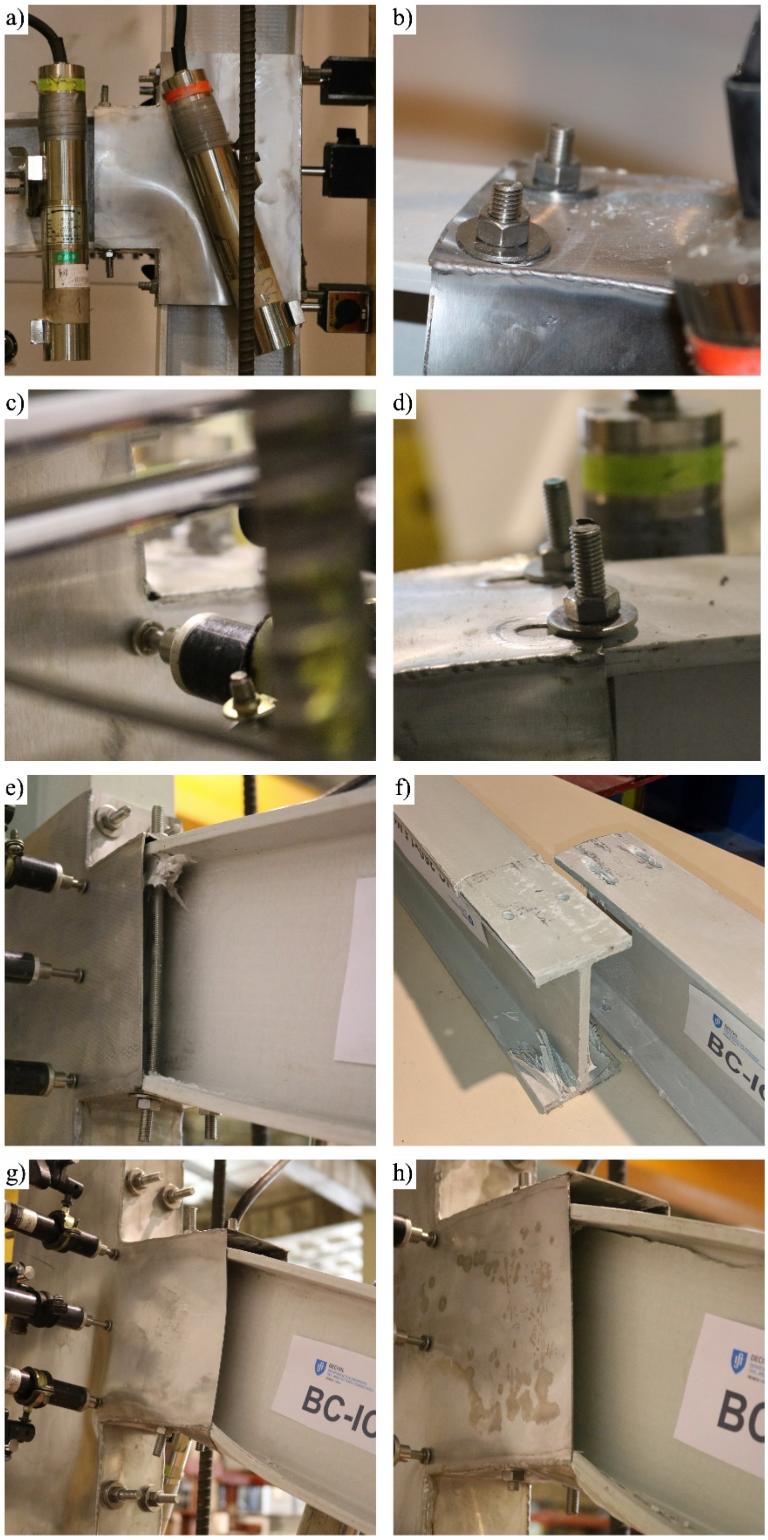

Figure 8.8 - Monotonic tests: failure modes - a) buckling of the cuffs' lateral walls (series BC-IC-270×1.0); b) bearing in the stainless steel cuffs near the beam rods (series BC-IC-270×1.0); c) cuff weld failure at the intersection of the beam and column members (series BC-IC-270×1.0); d) tearing failure at the cuff plate in contact with the beam rods (series BC-IC-270×1.0); e) GFRP bearing in the beam top holes and delamination of the beams' bottom flange and bending of the cuffs' walls (series BC-IC-270×1.5); f) GFRP bearing in the beam top holes (series BC-IC-360×1.0); g) delamination of the beams' bottom flanges (series BC-IC-360×1.0); h) delamination of the beams' bottom flanges and beam web-crippling (series BC-IC-360×1.5).

Every specimen of series BC-IC-270×1.5 presented the same damage progression until ultimate failure: (i) bearing at the stainless steel cuff near the beam rods (similar to Figure 8.8b) at ~30 mm of displacement; and (ii) bearing in the GFRP beam near the rods at 40-60 mm, which later developed into shear-out failure at the maximum load (*cf.* Figure 8.8e). For specimens M1 and M2, delamination of the beams' bottom flange was also observed, accompanied by plastic deformations on the cuff walls in contact with that area (*cf.* Figure 8.8e).

In series BC-IC-360×1.0, the lateral walls started to buckle at a displacement of ~20 mm and GFRP cracking was audible from ~40 mm, possibly due to bearing in the beam (confirmed after disassembly at the end of the tests, *cf.* Figure 8.8f). The ultimate failure modes observed were: (i) delamination of the beams' bottom flanges in all specimens (*cf.* Figure 8.8g), between 80 to 100 mm of vertical displacement; (ii) and flexural failure of the columns' back flange in specimens M1 and M2 for the same displacement.

Finally, regarding series BC-IC-360×1.5, all specimens presented bearing in the beams' top holes (confirmed after disassembling the specimens at the end of the tests), which probably started when GFRP cracking noises were audible (at ~30 mm of displacement) and, after that point, delamination of the beams' bottom flanges (*cf.* Figure 8.8h) was observed. The buckling of the lateral walls and plastic deformations on the bottom walls of the cuffs were also visible. In specimen M1, web-crippling of the beam was also observed at ~110 mm (*cf.* Figure 8.8h).

8.4. CYCLIC TESTS

This section presents the results of the full-scale beam-to-column cyclic tests of series BC-IC-360×1.0, namely its overall cyclic behaviour (subsection 8.4.1) and the assessment of its hysteretic parameters (subsection 8.4.2).

8.4.1. Overall cyclic behaviour

A representative moment *vs.* rotation curve of the cyclic tests of series BC-IC-360×1.0 is presented in Figure 8.9 which also includes a representative monotonic curve of this series. The hysteretic response of the connections was considerably symmetric, as expected, given the geometric symmetry of the connection system analyzed, and presented considerable pinching (the moment-rotation curves were mostly concentrated in Quadrants I and III, *cf.* Figure 8.9). Additionally, the negative stage of the cyclic loops was almost perfectly enclosed within the monotonic curve, while the maximum moments exceeded the monotonic values in the positive stages. For each group of cycles with the same maximum absolute rotations (*e.g.* cycles 8, 9 and 10), the moment *vs.* rotation curve of the first cycle was considerably wider and presented higher absolute moments than those of the remaining two cycles (*cf.* detail of cycle 8 *vs.* cycles 9 and 10 in Figure 8.9). This trend was also measured in the different hysteretic parameters analyzed (*cf.* Section 8.4.3) and is attributed to the occurrence of unrecoverable damage (both in the GFRP profiles and stainless steel cuffs) in the first cycle of these groups.

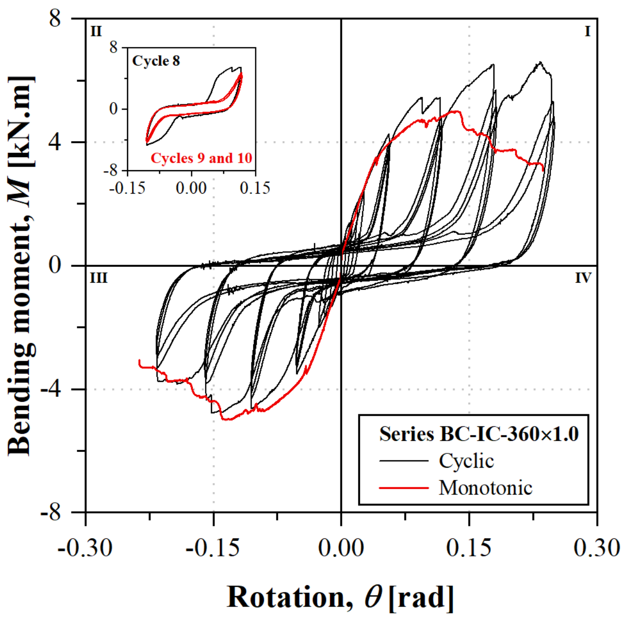

Figure 8.9 - Cyclic tests: representative moment *vs.* rotation curves for series BC-IC-360×1.0 (representative monotonic curve included).

In these tests, cracking noises were audible from the first cycle and the registered damage modes were very similar between specimens, occurring also for similar displacements: (i) the first noticeable damage in the specimens was the buckling of the cuff lateral walls (similarly as in Figure 8.8a) at the cycle with the maximum absolute displacement of 12.8 mm (3rd cycle); (ii) at the first cycle with absolute displacement of 68 mm (4×EP displacement, cycle 8), the flexural failure of the columns' back flange was observed; and (iii) at cycle 11, with maximum absolute displacement of 102 mm (6×EP displacement), the delamination of the beam flange (similar to Figure 8.8g) and the welding failure of the cuff in the corner where the beam and column meet (similar to Figure 8.8c) were observed. The described damage modes progressed until the end of the tests.

8.4.2. Hysteretic parameters

Three different hysteretic parameters were evaluated in accordance to the ECCS protocol [8.9]: (i) the stiffness ratio (ξ), corresponding to the ratio between the slope of the moment *vs*. rotation curve at the intersections with the horizontal axis (α_i^+ or α_i^-, *cf.* Figure 8.10) and the monotonic initial stiffness (K_θ, *cf.* Table 8.3); (ii) the strength, corresponding to the moment at the points of maximum and minimum displacement of the cycle (M_i^+ or M_i^-, *cf.* Figure 8.10); and (iii) the dissipated energy ratio (η), estimated using Eq. (8.1):

$$\eta_i = \frac{W_i}{\Delta M_{EP}(\Delta\theta_i - \Delta\theta_y)} \tag{8.1}$$

where W_i is the energy dissipated in cycle i (area enclosed by the cycle curve, W_i of Figure 8.10), ΔM_{EP} is the range between positive and negative EP moments, $\Delta\theta_i$ is the range of imposed rotations in cycle i, and $\Delta\theta_{EP}$ is the range of rotation between positive and negative EP rotations.

Figure 8.11a presents the progression of the stiffness ratio (ξ) per cycle for every specimen of series BC-IC-360×1.0, as well as a representative curve of the previously tested cleated connection series BC-6-F2-R (*cf.* Chapter 6), to be compared ahead in Section 8.5.2. This parameter presented a steep reduction between cycles 4 and 5, with an average decrease of -38%, corresponding to the transition between the elastic stage to a non-linear stage, with pinching being registered from that point onwards. Following cycle 6, this parameter continued to decrease, although with a less pronounced trend than observed initially, attaining a final average absolute value of 0.14. The variation of this parameter was very similar in all specimens and considerable symmetry was registered in its positive and negative incursions.

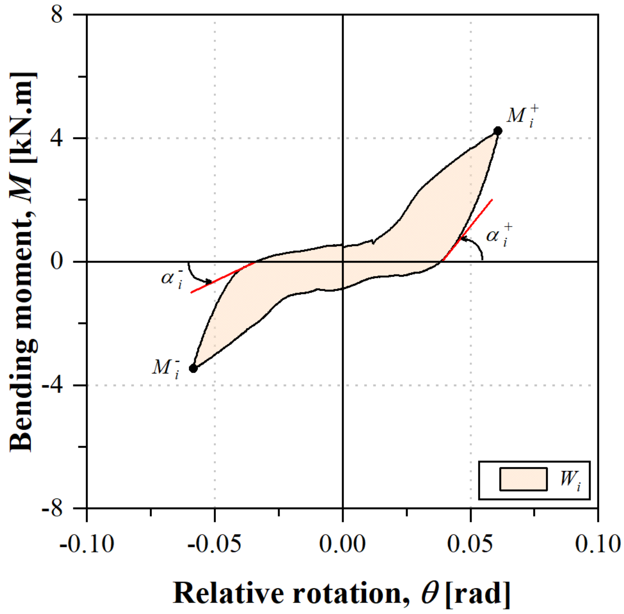

Figure 8.10 - Cyclic tests: ECCS [8.39] parameters.

Figure 8.11b depicts the moment variation per cycle for series BC-IC-360×1.0; the monotonic EP moment (M_{EP}) (corresponding to the EP rotation) was also added to this plot, as well as a representative curve of cleated series BC-6-F2-R (*cf.* Chapter 6), also to be compared in Section 8.5.2. This parameter presented a similar progression for all specimens. At cycle 4, the moment in the positive plots was close to the M_{EP}, as expected, since the maximum absolute rotation attained in this cycle corresponded to the EP rotation. On the other hand, for negative moments, the M_{EP} was not achieved in this cycle. Similarly, the strength at the ascending branch of the plot, corresponding to the first stage of each cycle, was considerably higher than the one at the descending branch (*e.g.* 5.5 kNm *vs*. -4.3 kNm at cycle 8). This may be explained by the fact that damage occurred/progressed during the ascending branch of each cycle reducing the stiffness and, therefore, the moment in the descending branch of the same cycle. Additionally, the maximum positive and minimum negative moments were attained in cycle 11, corresponding to an average of 110% and 76% of the ultimate moment registered in the monotonic tests, respectively.

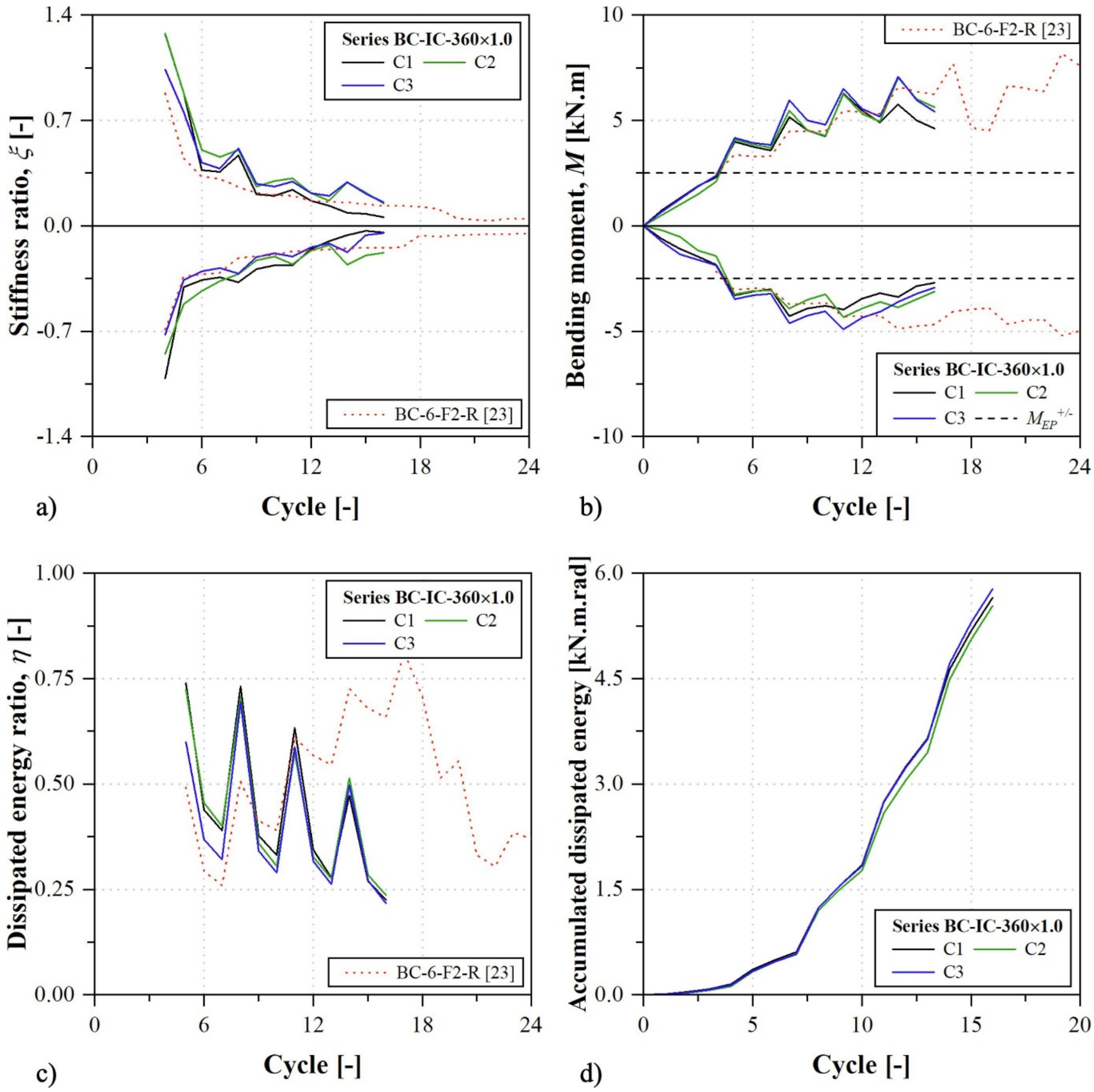

Figure 8.11 - Main results of cyclic tests of series BC-IC-360×1.0: evolution of the a) stiffness ratio (ξ), b) strength and c) dissipated energy ratio (η); and d) accumulated dissipated energy. Note: a), b) and c) include a representative specimen of series BC-6-F2-R.

As a consequence of the damage that occurred in the first cycle of each group (of three cycles) with the same maximum absolute deflection, the stiffness ratios and moments were lower in the 2nd and 3rd cycles when compared to the 1st cycle of the same rotation; *e.g.* cycle 5 *vs*. cycles 6 and 7. As the dissipated energy is correlated to the stiffness and strength at each ratio, this behaviour was reflected in the evolution of the energy dissipation ratio (η), presented in Figure 8.11c for every specimen. This parameter presented peak values on cycles 5, 8, 11 and 14, corresponding to the first cycles of each group with the same maximum absolute rotation, and on the 2nd and 3rd cycles of each group the energy dissipation ratio decreased. This parameter presented a decreasing trend, with the energy dissipation ratio of cycle 16 being -67% than that of cycle 5.

Finally, the accumulated dissipated energy was also quantified and is presented in Figure 8.11d, showing a very similar increasing trend for all specimens (with more pronounced increases after cycle 4, corresponding to the EP cycle). This parameter presented more substantial increases when transitioning to cycles with higher maximum absolute rotations, *e.g.* from cycle 4 to 5 and from cycle 7 to 8.

8.5. DISCUSSION

8.5.1. Influence of the cuff geometry

The behaviour of the various series presented remarkable differences, highlighting the influence of the length and thickness of the cuff part. As mentioned, thicker and longer cuff parts led to higher initial stiffness (+29% and +19%, as described in Section 8.3.1), due to the thicker walls and to the increased contact length provided by longer cuffs. The stiffness of all series fall within the “semi-rigid” classification range (from 51 kNm/rad to 2529 kNm/rad) defined in Eurocode 3 – Part 8 [8.10] for steel structures analysis – assuming the same limits for GFRP structures analysis would allow to consider these connections’ stiffness in the design, which is deemed relevant to reduce deflections of members, which is often a governing design criterion.

Regarding the strength of the connections, the influence of the thickness and geometry of the cuff must be assessed on par with the observed failure modes. With exception of series BC-IC-270×1.0, all series presented extensive GFRP damage. The series with smaller cuff parts (270 mm) - series BC-IC-270×1.0 and BC-IC-270×1.5 – failed near the beams rods due to the reduced hole edge distance. However, the series using stainless steel sheets with lower thickness (1.0 mm) failed by tearing in the cuff part, while the series using cuff parts with thicker steel sheets (1.5 mm) failed by shear-out in the GFRP material, for higher loads (+20%). Regarding series using longer cuff parts (360 mm) - series BC-IC-360×1.0 and BC-IC-360×1.5 - both exhibited similar damage patterns and, therefore, the higher strength attained in the latter series (+38%) can be attributed to the fact that the thicker cuff resulted in higher plate buckling and stainless steel yielding loads.

As mentioned, both series with 1.0 mm thick cuff parts registered considerable non-linear behaviour before reaching the maximum moment, unlike the series with thicker cuff parts. In fact, bearing and tearing near the beam rods and plate buckling in the cuff part started earlier in the tests, for lower loads, owing to the lower cuff thickness in series BC-IC-270×1.0 and BC-IC-360×1.0. As a consequence of early cuff buckling and plastic deformations in stainless steel, the damage on the GFRP profiles was delayed and the specimens presented improved ductility.

In the absence of a specific ductility index for GFRP structures, the ductility of the different series was quantified using the ductility index (μ_d) proposed by Jorissen and Fragiacomo [8.11] for timber structures, given by:

$$\mu_d = \frac{d_u - d_{EP}}{d_u} \tag{8.2}$$

where, d_{EP} is the EP displacement and d_u is the ultimate displacement, considered at the point where the load is 80% of the maximum load in a decreasing branch of the load-displacement curve. Table 8.3 presents the ductility index (μ_d) obtained for each series, showing that thinner cuffs have higher ductility than their thicker counterparts; in particular, μ_d was 28% higher for series BC-IC-270×1.0 than for series BC-IC-270×1.5 and 39% higher for series BC-IC-360×1.0 than for series BC-IC-360×1.5.

It was in light of these results that series BC-IC-360×1.0 was chosen to be tested under cyclic loading. In fact, this series did not present the highest maximum load and initial stiffness; however, it presented considerably higher ductility than series BC-IC-360×1.5 (+40%), and only slightly lower (–16%) strength. As one of the main objectives of this study was to develop a connection with considerable ductility and ability to dissipate energy, most useful in seismic areas, the author considered that this series presented a more balanced behaviour and was more promising in terms of hysteretic response.

8.5.2. Comparison with cleated connection system

The monotonic and cyclic performances of the cuffed connection series tested herein were compared to those of stainless steel flange cleated connections, which were investigated in previous chapters.

Figure 8.7 includes the monotonic moment *vs*. rotation curve of a representative specimen of the cleated series BC-6-F2-R (illustrated in Figure 8.12, the best performing one in Chapter 6). When compared to this cleated connection, the cuff connections registered considerably lower initial stiffness (-67%) and strength (-19%), but presented similar ductility (-7%).

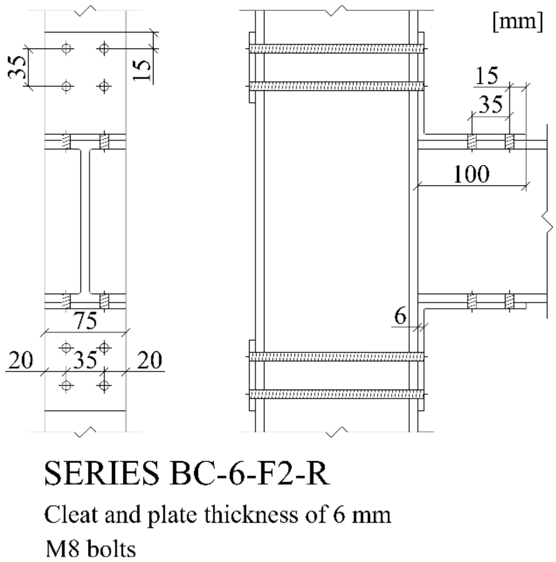

Figure 8.12 - Overall view of the cleated beam-to-column connection series BC-6-F2-R (*cf.* Chapter 6)

Figure 8.13 includes a representative hysteretic moment *vs*. rotation curve of the cleated connection system BC-6-F2-R. It can be seen that the cyclic performance of the cuff series BC-IC-360×1.0 was worse than that of the cleated system, the latter providing higher overall absolute moments and less pinching (*cf.* Figure 8.10).When comparing these connection systems in terms of the ECCS protocol [8.9] parameters, illustrated in Figures 8.11a to 8.11c, both exhibit similar stiffness trends (*cf.* Figure 8.11a), but the cleated connection system presented higher moments than series BC-IC-360×1.0[2] (*cf.* Figure 11b). In terms of energy dissipation ratio, series BC-IC-360×1.0 presented higher

[2] It should be noted the EP displacement of series BC-6-F2-R was 9 mm, and therefore the comparison regarding the absolute moment should be made for cycles with similar maximum absolute displacement: (i) cycles 5 to 7 of series BC-IC-360×1.0 *vs*. cycles 8 to 10 of series BC-6-F2-R; and (ii) cycles 11 to 13 of series BC-IC-360×1.0 *vs*. cycles 20 to 22 of series BC-6-F2-R.

values in the initial cycles and lower values from the middle of the test until the end (*cf.* Figure 8.11c). However, by analysing the moment *vs*. displacement curves for cycles with similar maximum absolute rotation (0.57 rad *vs*. 0.61 rad for series BC-IC-360×1.0 and BC-6-F2-R, respectively), as shown in Figure 8.14, it is clear that the cuff connection presented worse hysteretic behaviour than the cleated connection: series BC-6-F2-R presented considerably wider curves, with less pinching, resulting in a higher ability to dissipate energy (+50% for the cycles presented in Figure 8.14).

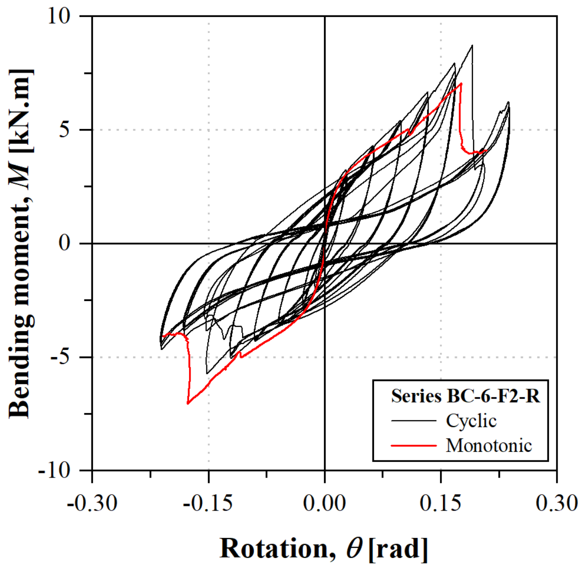

Figure 8.13 - Representative cyclic moment *vs.* rotation curves for series BC-6-F2-R (representative monotonic curve included) (*cf.* Chapter 6).

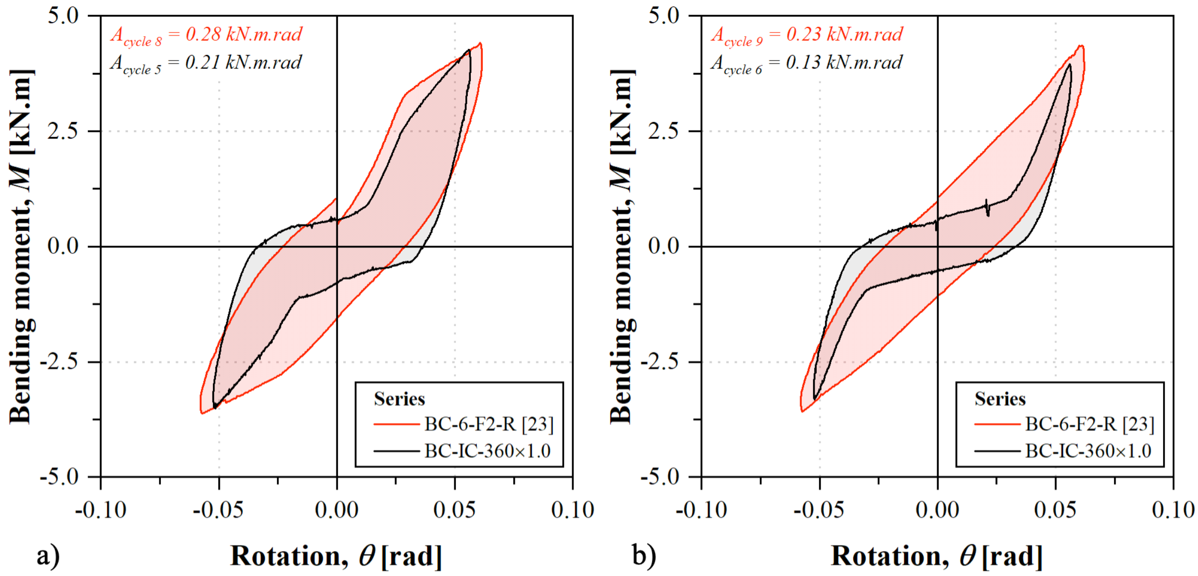

Figure 8.14 - Representative cyclic moment *vs.* rotation curves for series BC-6-F2-R (representative monotonic curve included) (*cf.* Chapter 6).

Overall, the mechanical advantages of the cuff connection system when used to join tubular profiles, shown in a previous study by the author (*cf.* Chapter 5), were not verified for I-section profiles. Two main reasons explain this difference in performance: (i) the cuff walls are more prone to buckle in connections between I-section profiles than when joining tubular profiles, as the latter restrain the out-of-plane displacements of the cuff plates in one of the directions; and (ii) the I-section profile is more prone to present flexural failure of the flanges, because they are less restrained than those of a tubular section.

8.6. CONCLUDING REMARKS

Previous investigations showed the potential of using stainless steel cuff parts to join pultruded GFRP tubular profiles. The main objective of the experimental study presented in this chapter was to assess if the same potential exists when joining I-section profiles. For that purpose, four different beam-to-column connection series, differing in the cuff's plate thickness and length, were studied by means of monotonic and cyclic tests. The results showed that the geometry of the cuff connection parts has significant influence on the connections behaviour. The following main conclusions can be drawn from this study:

- Cuff parts with higher thickness and length provided the connections with higher initial stiffness and strength; conversely, connections with thicker cuffs presented lower ductility;
- Plastic deformations were observed in all cuffs, but extensive GFRP damage was also registered in all series, with exception of that with thinner and shorter cuff part;
- The series with thinner and longer cuff part exhibited limited energy dissipation capacity under cyclic loading, depicting pronounced pinching;
- The cuff connection system presented herein was outperformed by a previously tested flange cleated connection system (*cf.* Chapter 6), presenting lower initial stiffness, strength, ductility and ability to dissipate energy.

Overall, these results indicate that the cuff connection system presented in this work is not as suited to join I-section GFRP profiles as it is to join tubular GFRP profiles – in other words, for structures comprising I-section GFRP profiles, stainless steel cleated connections seem to present an overall better performance. Nevertheless, future research should develop and investigate the performance of I-shaped cuff parts, tailored for a close fit to I-shaped pultruded GFRP profiles, as such solution could considerably reduce the pinching effect observed in the cyclic tests.

8.7. REFERENCES

[8.1] EN ISO 527-1 (1997) Plastics – Determination of Tensile Properties – Part 1: General Principles. Brussels.

[8.2] ASTM D 6641/D 6641M-16e1 (2016) Standard Test Method for Compressive Properties of Polymer Matrix Composite Materials Using a Combined Loading Compression (CLC) Test Fixture. West Conshohocken.

[8.3] ASTM D 695-02 (2006) – Standard Test Method for Compressive Properties of Rigid Plastics. West Conshohocken.

[8.4] ASTM D 2344/D 2344M-00 (2006) – Standard Test Method for Short-Beam Strength of Polymer Matrix Composite Materials and Their Laminates. West Conshohocken.

[8.5] ASTM D 5379/D 5379M (2005) – Standard Test Method for Shear Properties of Composite Materials by the V-Notched Beam Method. West Conshohocken.

[8.6] ISO 1172 (1996) Textile-glass-reinforced plastics. Prepregs, moulding compounds and laminates. Determination of the textile-glass and mineral-filler content. Calcination methods.

[8.7] ISO/TC 164/SC 1 (2019). ISO 6892-1:2019. Metallic Materials - Tensile Testing - Part 1: Method of Testing at Room Temperature. British Standards Institution.

[8.8] CEN ISO 3506-1 (2001) Fasteners — Mechanical Properties of Corrosion-Resistant Stainless Steel Fasteners – Part 1: Bolts, Screws and Studs with Specified Grades and Property Classes.

[8.9] ECCS/TC1. (1986). Recommended testing procedure for assessing the behaviour of structural steel elements under cyclic loads.

[8.10] EN1993 (2005). Design of Steel Structures – Part 1–8: Design of Joints.

[8.11] Jorissen A, Fragiacomo M. (2011). General notes on ductility in timber structures. *Engineering Structures*, 33(11), 2987-2997.

PART IV

2-dimensional frames made of pultruded GFRP profiles

Chapter 9

Monotonic and cyclic sway behaviour of 2-dimensional frames made of pultruded tubular profiles

9.1. INTRODUCTION

The guidance available for the design of pultruded GFRP frames is very limited, especially in what concerns their response under monotonic and cyclic horizontal loads [9.1,9.2]. Such guidance is very much needed to enable a wider acceptance of GFRP construction, especially in seismic areas. This lack of design guidelines seems to be explained by the very limited number of experimental and numerical investigations about the structural behaviour of pultruded GFRP frames. Those investigations are briefly reviewed next.

The earliest research reported on pultruded GFRP frames focused on their behaviour under vertical loading. Bank and Mosallam [9.3,9.4] tested full-scale GFRP open frames, comprising I-shaped profiles and all-FRP bolted connections, under vertical loads applied to the beam (4-point bending). By performing short-term quasi-static and creep tests, they concluded that the stiffness of the joints was a key parameter for the structural behaviour of the frames. Additionally, failure of the frames was governed by the (reduced) strength of the connection system used. Recently, Seçer and Kural [9.5] also performed creep tests on GFRP open frames, comprising tubular pultruded profiles and top-and-seat cleat connections with GFRP angles, which confirmed the relevance of viscoelasticity in the response of these structures.

To the author's best knowledge, only two studies on the experimental behaviour of GFRP frames under horizontal loads has been reported. In particular, Na [9.6] performed monotonic sway tests on braced full-scale GFRP frames comprising tubular profiles to investigate the influence of the connection system (all-GFRP and steel flange cleats) and the bracing scheme on the frame behaviour. He showed that these two parameters are fundamental for the structural behaviour of the GFRP frames. Very recently, Cavaleri *et al*. [9.7] reported an experimental test on a portal frame designed for an emergency housing system. The authors loaded the frame vertically and then tested it under horizontal sustained and monotonic loading. The authors showed that the frame's performance complied with service and ultimate limit state requirements set in Italian codes [9.1,9.8]. Although the authors have applied the horizontal load in both directions (reversal) they did not performed cyclic tests.

Additionally, modal identification tests have been reported on a large GFRP tri-dimensional frame structure comprising C-shaped profiles [9.9] and on plane frames also using C-shaped profiles [9.10]. The latter research highlighted the influence of the bolt torque used in the connections; higher bolt torques contributed to an improved structural interaction between the elements, leading to increased vibration frequencies and damping ratios.

Regarding the numerical analysis of lateral sway behaviour of GFRP frames, Na [9.6] compared his experimental results with numerical models, using frame elements and linear rotational spring joints. He concluded that, in general, the stiffness of the beam-to-column connections is semi-rigid, and such stiffness was calibrated to match the linear stage of the experimental results. More recently, Xiao *et al*. [9.11] presented a numerical study on the sway cyclic behaviour of GFRP frames with bonded sleeve joints, comparing their energy dissipation capacity with that of equivalent steel frames. The hysteretic behaviour of those joints was determined based on the hysteresis model proposed by Chui and Chan [9.12] for steel frames with flexible joints and the experimental results of monotonic beam-to-column tests. Based on that numerical study, the authors concluded that GFRP frames presented adequate levels of energy dissipation, comparable to those of equivalent steel frames. Nevertheless, it should be highlighted that these results were not validated by experimental data at the frame level; moreover, the hypothesis of using Chui and Chan [9.12] hysteresis model (which presents low levels of pinching) in the modelling of GFRP joints was also not validated.

In what concerns the experimental studies reviewed above, only two of them [9.6,9.7] focused on the lateral sway behaviour of GFRP frames, although this is a fundamental aspect of their behaviour, particularly regarding seismic performance. Moreover, none of the studies addressed the effects of cyclic loading or the influence of in-fill walls in the behaviour of the frames. Additionally, to the author's best knowledge, a numerical study on the cyclic sway behaviour of GFRP frames (validated by experimental results) has not yet been reported.

This work, developed in the frame of the ClickHouse project (*cf*. Chapter 3), presents experimental and numerical investigations about the sway behaviour of GFRP plane frame structures, comprising tubular profiles and bolted steel sleeve joints. The present chapter reports the results of monotonic and cyclic sway tests on full-scale GFRP plane frames, including the assessment of the effects of infill walls, materialized by sandwich panels made of two GFRP face skins and a polyurethane foam core. The cyclic behaviour of the GFRP frames without infill walls was also object of a numerical investigation, using the knowledge gathered from (i) the monotonic and cyclic tests on the beam-to-column connection system (*cf*. Chapters 3 and 4), and (ii) the numerical modelling of that connection system (*cf*. Chapter 4). The main goal of the numerical simulation was to assess the feasibility of modelling the cyclic behaviour of GFRP frames using relatively simple and design-oriented finite element (FE) models, with frame elements and link joints. In particular, the possibility of using the properties of the joints determined from experimental beam-to-column connection tests (avoiding the need to perform full-scale frame experimental tests) was investigated.

9.2. EXPERIMENTAL PROGRAMME

9.2.1. Test series and frame components

Figure 9.1 illustrates the GFRP closed frame specimens used in the sway tests. They comprise four pultruded GFRP tubular profiles (120×120×10 mm^2) – two beams and two columns - whose mechanical properties were presented in Chapter 3. The connection system, depicted in Figure 9.2, comprises two steel sleeve auxiliary parts. The beam part is bolted to (i) the beam's flanges with 2 M8 bolts per flange, and to (ii) the column part with 4 M10 bolts. The column part is also bolted to the column with 4 M10 bolts per face (for more details, please refer to Chapter 3). Among the different series of the connection system developed by the author, the joints of the GFRP frames were materialized by series F2S, as it presented the best performance in beam-to-column monotonic (*cf*. Chapter 3) and cyclic (*cf*. Chapter 4) tests.

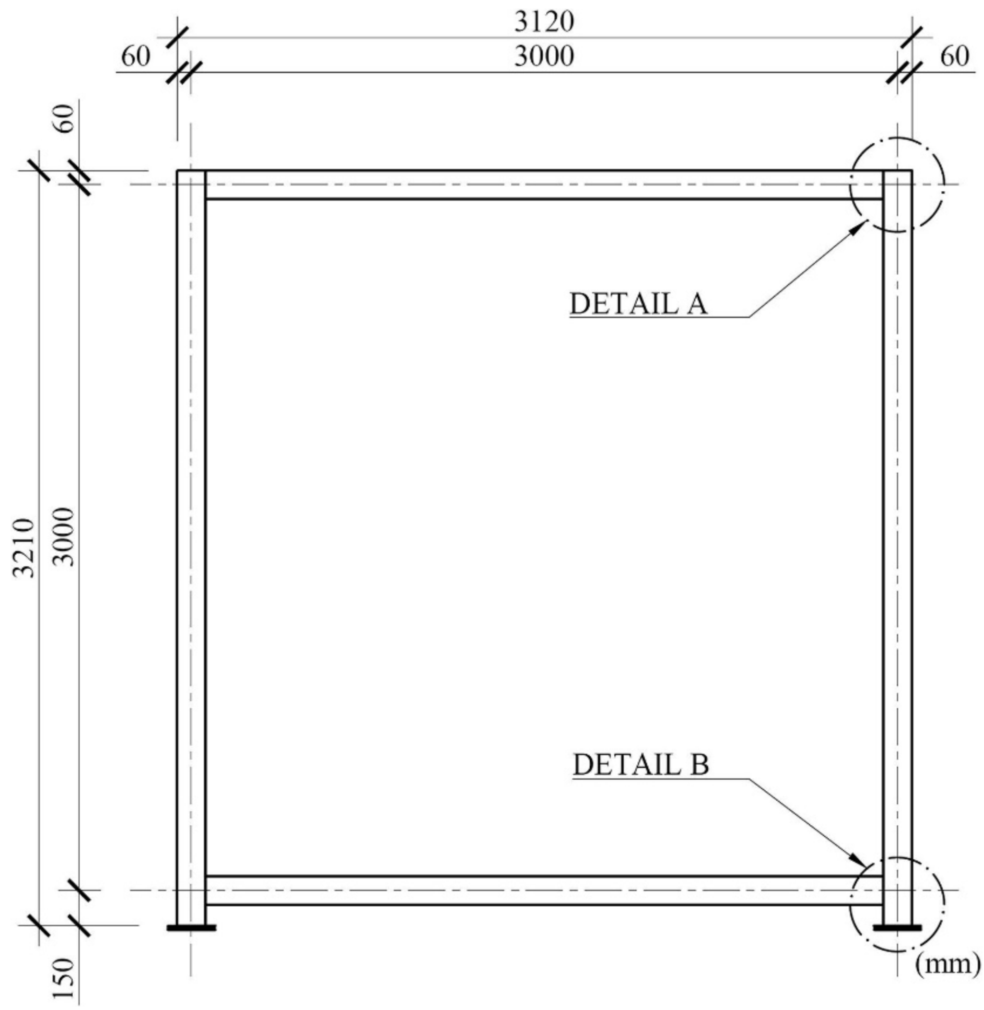

Figure 9.1 - Side view of the structure of the full-scale frame sway test specimens.

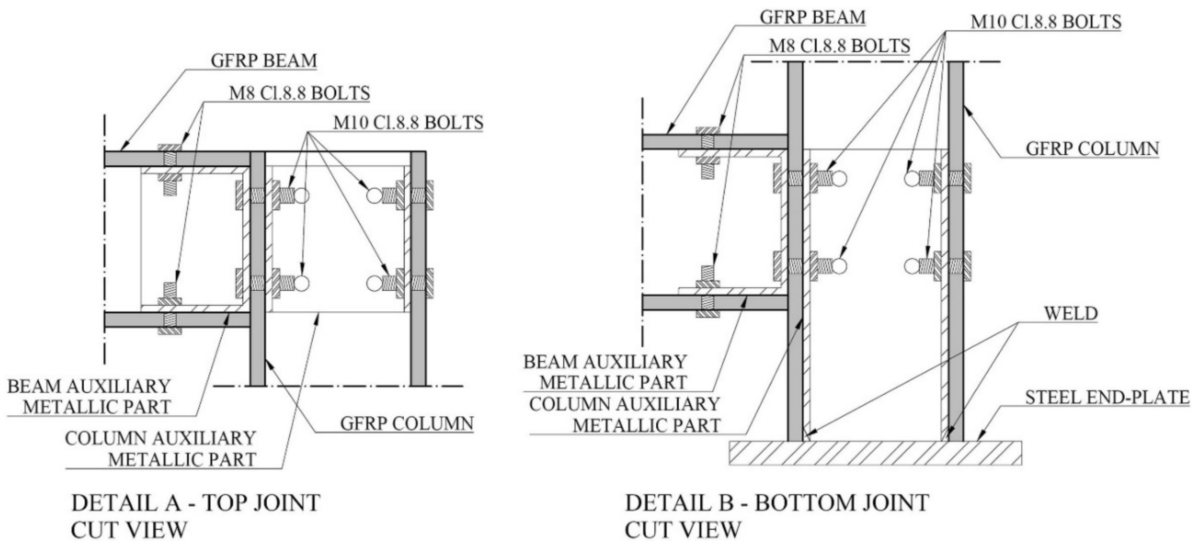

Figure 9.2 - Details of the top and bottom beam-to-column connections.

Five frame specimens were tested, namely (i) three frames without infill walls (2 under monotonic loading – series UF-M; and 1 under cyclic loading – series UF-C), and (ii) two with infill walls (1 under monotonic loading – series FF-M; and 1 under cyclic loading – series FF-C). For series UF-M, two specimens were tested (UF-M1 and UF-M2), because the first one presented premature failure on the weld fillets of the base fixing system, as discussed in Section 9.3.

The walls of the filled frames (FF-M and FF-C) were materialized by composite sandwich panels with polyurethane (PUR) foam core (density of 40 kg/m^3) enclosed between two 2 mm thick GFRP skins, presenting total thickness of 70 mm. The main properties of the GFRP skins and the PUR foam core are presented in Table 8.1, namely the tensile strength in both longitudinal ($\sigma_{tu,L}$) and transverse ($\sigma_{tu,T}$) directions, and the respective elasticity moduli ($E_{t,L}$ and $E_{t,T}$) of the GFRP skins; and the compressive, tensile and shear strengths (σ_{cu}, σ_{tu} and τ_u, respectively), as well as the elastic and shear moduli (E_c and G) of the PUR foam. Each frame was filled with three wall panels, each with plane dimensions of 0.96×2.88 m^2. The wall panels were connected (to the GFRP frame and between themselves) with an interlock connection system; this system, depicted in Figure 9.3, includes pultruded GFRP U-shaped profiles (60×45×5 mm^2) positioned in the contour of the panels and auxiliary pultruded GFRP tubular square profiles (50×50×5 mm^2) adhesively bonded to the main (structural) GFRP profiles. The base connections, shown in Figure 9.2, Figure 9.4, were materialized by extending the columns' connection auxiliary parts until the bottom edge of the column profile, where they were welded to a base steel plate

(200×200×16 mm^3). The steel auxiliary parts were made with S235 grade steel and the steel bolts used were 8.8 class.

Table 9.1 - Main mechanical properties of the sandwich wall panels [9.13].

Material	Test	Property	Average ± Std. deviation	Standard
GFRP skins	Tension	$\sigma_{tu,L}$	117.0 ± 12.2 MPa	ASTM D3039 [9.14]
		$\sigma_{tu,T}$	116.9 ± 28.9 MPa	
		$E_{t,L}$	9.6 ± 0.7 GPa	
		$E_{t,T}$	10.3 ± 0.8 GPa	
PUR core	Compression	σ_{cu}	0.30 ± 0.03 MPa	ASTM C365-03 [9.15]
		E_c	6.30 ± 0.57 MPa	
	Tension	σ_{tu}	0.49 ± 0.04 MPa	ASTM C297-04 [9.16]
	Shear	τ_u	0.15 ± 0.02 MPa	ASTM C273-0 [9.17]
		G	3.15 ± 0.38 MPa	

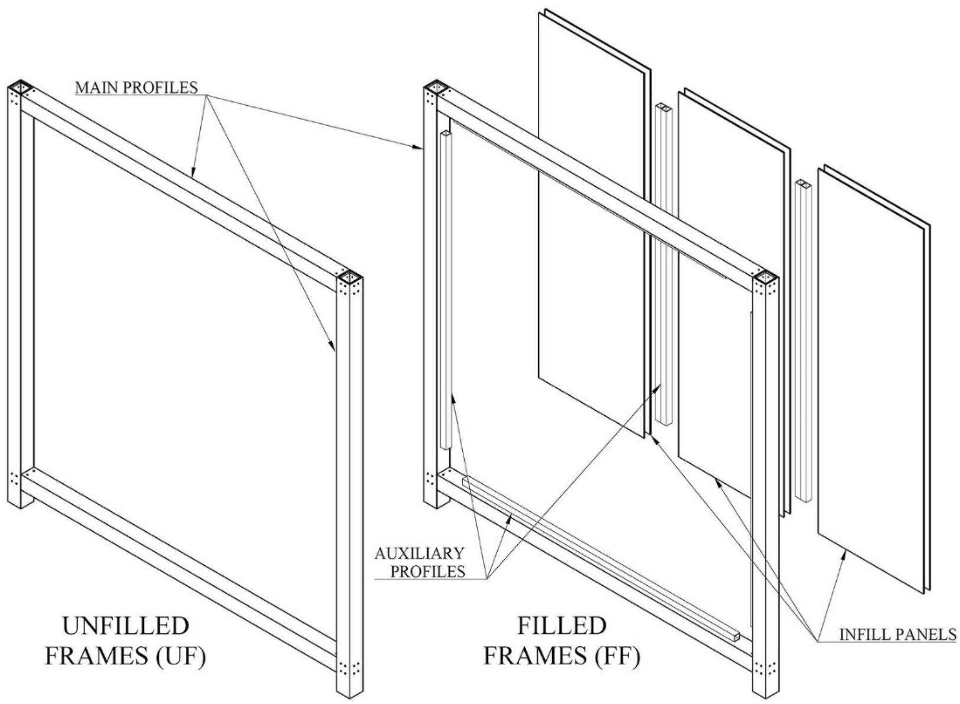

Figure 9.3 - Overview of the unfilled (UF) and filled (FF) frame specimens.

9.2.2. Test setup and instrumentation

Figure 9.4 illustrates the setup used in the frame sway tests. The displacements were imposed at the top beam of the frames by a mechanical actuator, with capacity of 1000 kN and stroke of 400 mm, mounted in a reaction wall. In the cyclic tests, two *dywidag* bars were used together with the mechanical actuator in order to transfer the load to the opposite side of the frame, in case of reverse (cyclic) loading. The steel bases of the frames (*cf*. Figure 9.2, Figure 9.4) were welded to steel plates that were bolted to a rigid beam anchored to laboratory's strong floor. The out-of-plane displacements of the frames were prevented by a lateral bracing system applied to the top beam (*cf*. Figure 9.4).

Figure 9.4 - Overview of the test system and detail of the bottom connections.

Figure 9.5 shows the position of the instrumentation used, where: (i) F represents the load cell (*Novatech*, capacity of 300 kN) used to measure the applied load; (ii) Δ_i represents the string pot displacement transducers (*TML*, stroke of 500 mm); (iii) θ_{1B} and θ_{1C} represent the rotation transducers, which measured the rotations at a top connection, in the beam and in the column, respectively; (iv) δ_i represents the general displacement transducers (*TML*, strokes ranging from 10 mm to 100 mm), to measure the columns' midspan displacement ($\delta_{1\text{-}2}$) and to estimate the rotation at a bottom connection, in the beam ($\delta_{3\text{-}4} \equiv \theta_{2B}$) and in the column ($\delta_{5\text{-}6} \equiv \theta_{2C}$); and (v) ε_i represents the electrical strain gauges used in the profiles ($i_{=1\text{-}24}$). Additionally, the vertical displacements of the base plates were measured during the tests, registering negligible displacements, thus showing that there was no uplift of the frames. Data acquisition was carried out at a rate of 5–10 Hz using *HBM* dataloggers.

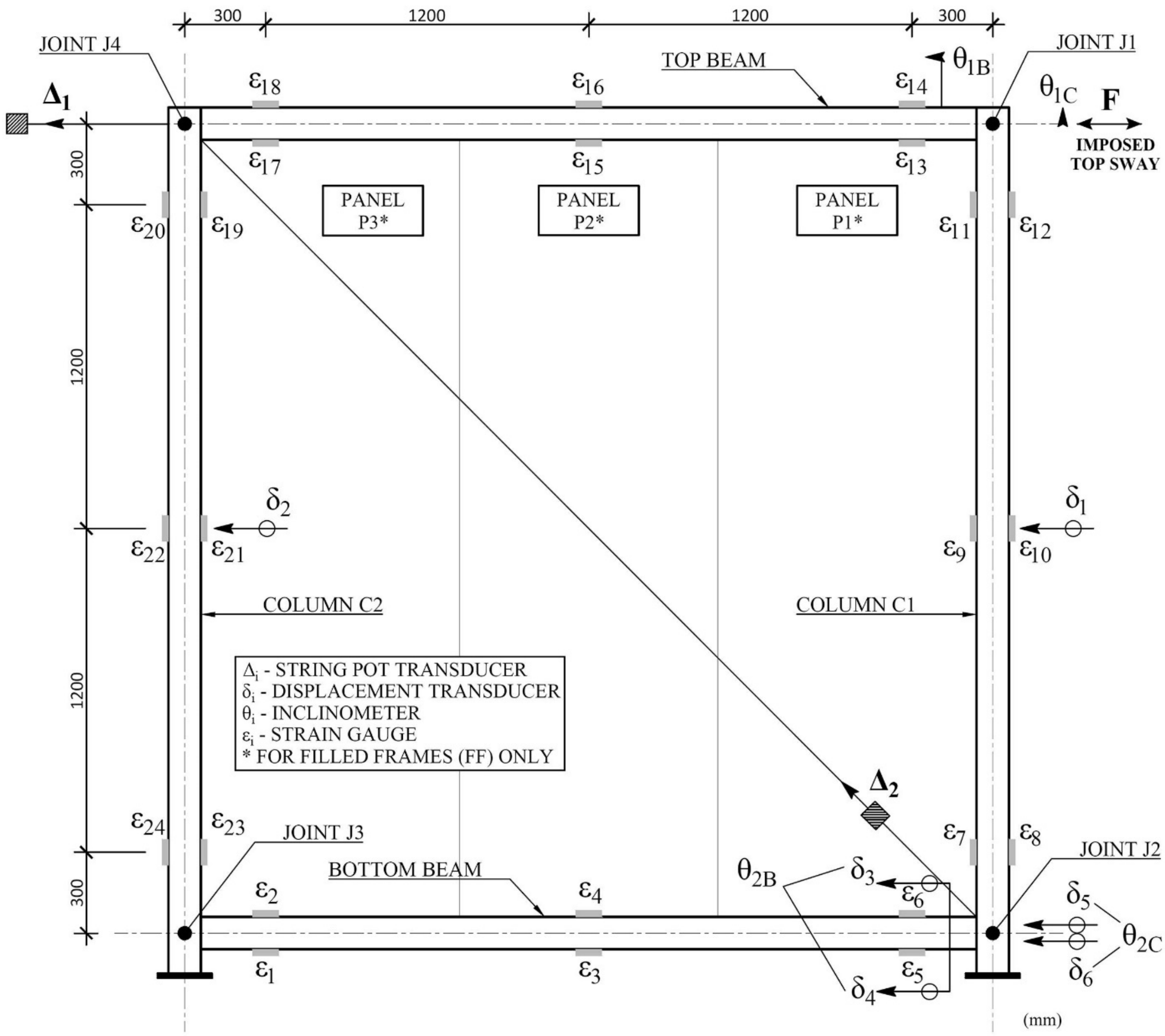

Figure 9.5 - Instrumentation of the test specimens.

9.2.3. Load protocols

Monotonic tests were performed under displacement control (controlling displacement Δ_1), imposed by the actuator, at a rate of 15 mm/min, until either its maximum stroke was reached or the safe continuation of the test was compromised by evident damage/buckling of the frame specimen.

In the cyclic tests, the displacemente history followed the recommendations of the ECCS [9.18]. For that, the cycles were defined based on the "yield" displacements (δ_y) estimated from the monotonic tests, which were defined by the end of the elastic range, corresponding to top-sway displacements (Δ_1) of: (i) 50 mm for the unfilled-frame (UF-C); and (ii) 101 mm for the filled frame (FF-C) (*cf.* Section 9.3). The loading history of each frame is presented in Figure 9.6. Four cycles were performed until the "yield" displacement was reached – at ¼, ½, ¾ and 1 times the "yield" displacement – followed by cycles of multiples of the δ_y: (i) for the unfilled frame, two cycles at $2\times\delta_y$, followed by two cycles at $4\times\delta_y$ were considered; while (ii) for the filled frame, only four cycles of $2\times\delta_y$ were performed.

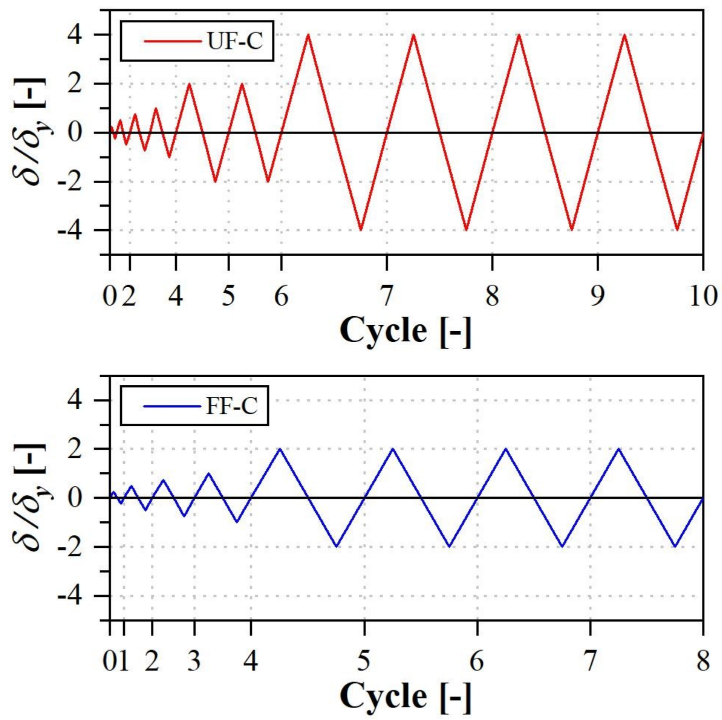

Figure 9.6 - Displacement history of the frame sway cyclic tests.

9.3. MONOTONIC TESTS – RESULTS AND DISCUSSION

This section presents and discusses the experimental results of the monotonic tests in the GFRP frames, namely regarding (i) the load *vs*. displacement and (ii) the moment *vs*. rotation responses; (iii) the failure modes; and (iv) the internal forces and overall frame deformations. Table 9.2 summarizes the main results obtained in these tests that support the following discussion.

9.3.1. Load *vs*. displacements responses

The load *vs*. top displacement (Δ_1) curves of the specimens subjected to monotonic loading are presented in Figure 9.7. It is worth mentioning that the test of the filled frame (FF-M) was stopped before collapse, due to safety reasons, namely when the top displacement was around half of the maximum stroke of the actuator, due to evident damage on the frame elements and buckling of the panels' skins (*cf*. Section 9.3.3.2). Figure 9.8 presents a general view of the unfilled and filled frames near the end of the tests.

Table 9.2 - Experimental results obtained in the monotonic GFRP frame tests.

Parameter		ID	Unfilled frame [UF-M2]		Filled frame [FF-M]	
			First damage	Maximum load	First damage	Maximum load
Load		F	5.6 kN	13.6 kN	26.9 kN	38.6 kN
Top drift		SW	3.3%	12.4%	3.4%	6.8%
Displacemen	top-sway	Δ_1	100 mm	372 mm	101 mm	204 mm
	diagonal	Δ_2	67 mm	252 mm	65 mm	132 mm
	mid-height column	δ_1 (column C1)	45 mm	–	45 mm	–
		δ_2 (column C2)	47 mm	–	50 mm	–
Rotation	top connection (joint J1)	θ_{1B} (beam)	+0.14º	–0.01º	–1.09º	–2.12º
		θ_{1C} (column)	+1.82º	+7.80º	+1.78º	+4.51º
		$\Delta_{\theta 1}$	(+1.68º)	(+7.81º)	(+2.87º)	(+6.63º)
	bottom connection (joint J2)	θ_{2B} (beam)	–0.06º	–0.19º	+0.82º	+0.70º
		θ_{2C} (column)	+0.59º	+2.72º	+0.61º	+1.17º
		$\Delta_{\theta 2}$	(–0.65º)	(–2.91º)	(+0.21º)	(–0.47º)
Stiffness		K_Δ	55 kN/m	–	264 kN/m	–

NOTES:
Frame UF-M: maximum load above final load for which the actuator's maximum stroke was reached (*ca*. 400 mm).
Frame FF-M: maximum load attained at the end of the test (stopped voluntarily).

The unfilled frames (series UF-M) exhibited an approximately linear behaviour (constant stiffness, K_Δ) up to a top displacement of ~50 mm, when the load-displacement proportionality was lost. The first visible damage of frame UF-M1 was due to the premature failure of the base plates' weld; thereafter, the analysis of frame UF-M1 was no longer pursued. In the repetition of this test, after the elastic limit (Δ_1=50 mm, F_y=2.9 kN) frame UF-M2 presented gradual loss of stiffness until the maximum load was attained (13.6 kN), with several damage modes being visible at the connections (*cf*. Section 3.3.1). The filled frame (FF-M) initially presented a very stiff adjustment stage, up to around 4 kN, with the wall panels and the frame resisting together like a rigid body. After that stage the internal static friction between the panels and the frames was overcome, with the frame FF-M presenting an approximately linear behaviour until the occurrence of the first local damage (Δ_1=50 mm, F_y=26.9 kN). Afterwards, the frame FF-M also presented gradual and successive losses of stiffness, consequence of several local failures, until the maximum load (38.6 kN) was reached, *cf.* Section 3.3.2. The above-mentioned peak loads correspond to the following top-sway deformations (Δ_1) and drifts (*SW*), respectively: (a) 372 mm and 12.4% for the unfilled frame UF-M2; and (b) 204 mm and 6.8% for the filled frame FF-M.

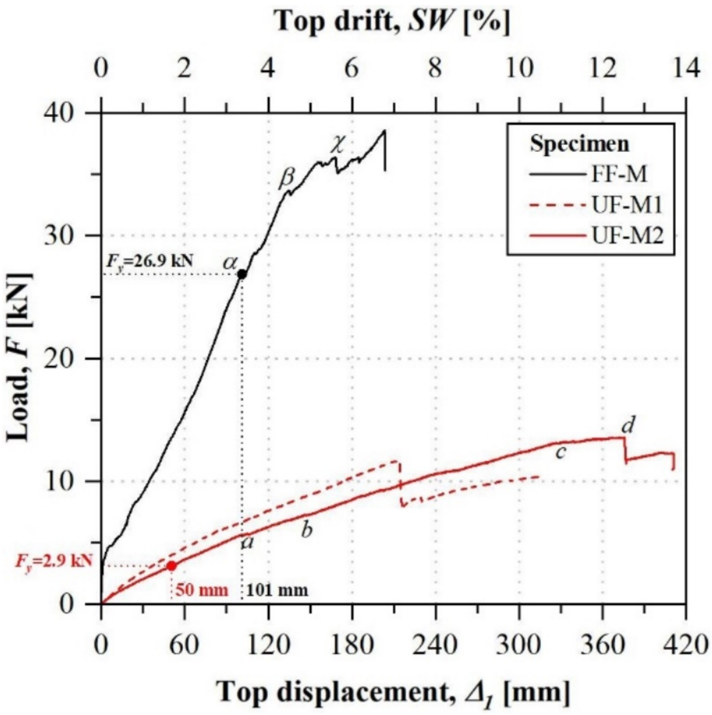

Figure 9.7 - Monotonic tests: load *vs*. top displacement curves.

Figure 9.8 - Deformed shapes of the monotonic tests: a) UF-M2; b) FF-M.

The filled frame FF-M presented considerably higher stiffness (+380%, disregarding the first adjustment stage) and strength (+184%) than the unfilled frame UF-M2. The better performance of the frame FF-M is naturally associated with the load transmission through the infill panels, which acted as bracing members and reduced the frame's horizontal deformability. Conversely, the frame UF-M2 was able to sustain a higher top-drift than its filled counterpart (+82%).

Figure 9.9 presents the load *vs*. diagonal displacement (Δ_2) and load *vs*. columns mid-height displacement (δ_1-δ_2) curves of frames UF-M2 and FF-M. For the unfilled frame UF-M2, the diagonal displacements throughout the test were ~70% of the top displacement ($\Delta_2 \approx \Delta_1 \times sin\ 45°$) and the mid-height displacements of both columns were similar, around 50% of the top displacement. The filled frame FF-M presented a diagonal displacement (Δ_2) around ~65% of the top displacement (Δ_1), while the mid-height displacements of the columns presented some differences, being approximately 50% and 45% of the top displacement, with respect to δ_1 and δ_2. These slight differences should be attributed to the influence of the wall panels in the overall deformability of the filled frame, particularly regarding the symmetry of the overall shape of its deformation.

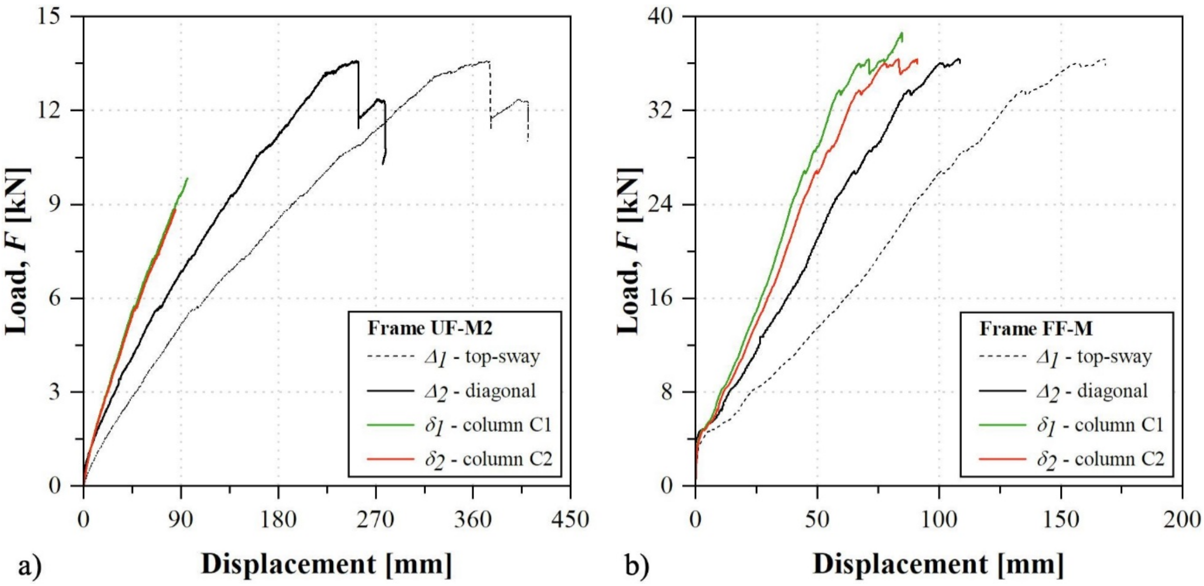

Figure 9.9 - Load *vs*. displacement curves of the monotonic tests: a) UF-M2; b) FF-M.

9.3.2. Moment *vs*. rotations responses

Figure 9.10 presents the rotations measured at the top (θ_{1B} and θ_{1C}, at the beam and column, respectively) and at the bottom (θ_{2B} and θ_{2C}, at the beam and column, respectively) joints of the column next to the actuator

(Column C1, *cf.* Figure 9.5) against the top-sway displacement (Δ_1). Additionally, the relative rotations at each joint ($\Delta\theta_1$ and $\Delta\theta_2$) are also presented.

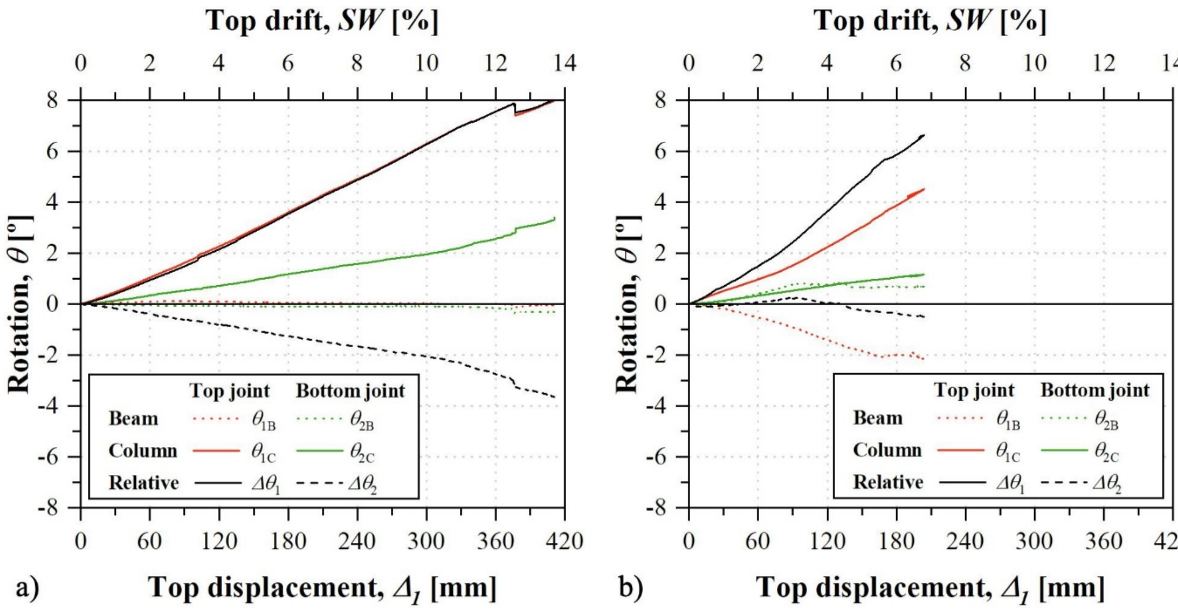

Figure 9.10 - Rotations measured at Joints J1 and J2 during the monotonic tests: a) UF-M2; b) FF-M (positive/negative relative rotations indicate the opening/closing of the internal right angles).

For the unfilled frame UF-M2, the rotations measured at the column were much higher than those measured at the beams; the latter were negligible, owing to the relatively high flexural/shear deformation exhibited by the columns together with the flexibility of the beam-to-column connections, quite clear in Figure 9.8. As expected, the absolute relative rotations at the top joint ($\Delta\theta_1$) were higher than those obtained at the bottom joint ($\Delta\theta_2$). In opposition, for the filled frame FF-M, the beams' rotations at each joint were of the same magnitude as those of the column(s). The relative rotations at the bottom joint ($\Delta\theta_2$) were approximately null throughout the test, while the relative rotations at the top joint ($\Delta\theta_1$) were higher (for the same top-sway displacement) than those of the unfilled frame UF-M2. These differences are justified by the significant flexural deformation of the top beam of the FF-M frame, which was imposed due to the contact stresses induced by the in-fill panels (this mechanism is further discussed in Section 9.3.3.2).

Figure 9.11 presents the bending moment[1] *vs*. relative rotation ($\Delta\theta_I$) curves of the top joint of Column C1 (J1, *cf*. Figure 9.5). This analysis was performed for the UF-M frame only, since the bending moments were estimated from the strain measurements, assuming a constant curvature of the beams' cross-section and a linear bending moment distribution. Note that this last assumption is not valid for the FF-M frame since the in-fill walls induced concentrated contact loads in the frame elements. The relative rotation was obtained from the differential of rotations θ_{IB} (beam) and θ_{IC} (column).

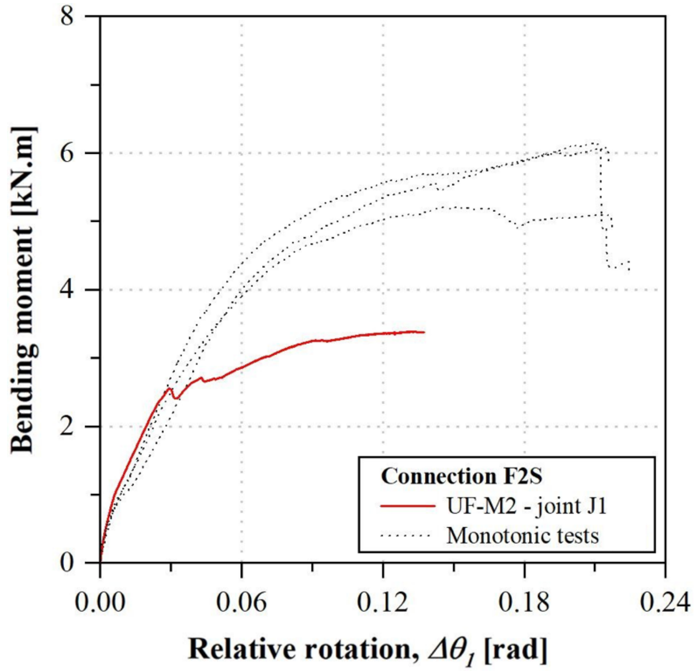

Figure 9.11 - Moment *vs*. rotation curves of Joint J1 of frame UF-M2 measured in the monotonic tests.

After an initially (stiffer) adjustment stage, the top joint (J1) of the unfilled frame UF-M2 presented linear behaviour up to a minute load capacity drop (M = 2.6 kN.m; $\Delta\theta_I$ = 0.03 rad), presenting rotational stiffness (K_θ) of 73 kN.m/rad, quite similar to that registered in the full-scale connection tests (71 kN.m/rad, in Chapter 3). Subsequently, the response was almost linear until the end of the test, yet with reduced stiffness, when the maximum bending moment was registered (M_{max}=3.4 kN.m; $\Delta\theta_I$=0.13 rad). It should be mentioned that the end of the linear branch of the moment *vs*. rotation curve of Joint J1 was coincident with the occurrence of the first damage in the frame (*cf*. point *a* in Figure 9.7), as discussed ahead in Section 9.3.3.1. In spite of presenting an initial linear stage similar to that observed

[1] The bending moment was estimated as the average of those measured at the beam and column sections nearest to Joint J1.

in the full-scale connection tests, the behaviour of the frame connection diverged from the former for $M > 2.6$ kN.m. In this regard, it should be mentioned that the full-scale connection tests simulated an intermediate storey connection, with the column fixed above and below the beam level (*cf*. Chapters 3 and 4), whereas Joint J1 presents and upper free-end edge, which justifies this difference. Nevertheless, the results clearly indicate a relatively ductile behaviour of the joint in the frame (qualitatively similar to that observed in the connection tests), owing to the plastic deformations underwent by the steel auxiliary connection parts.

9.3.3. Failure modes

9.3.3.1. Unfilled frame UF-M2

The damages registered on the unfilled frame UF-M2 were concentrated essentially in its connections. As depicted in Figure 9.12a, the first damage observed was the development of compressive cracks in the web-to-flange junctions of both GFRP columns bases. This damage corresponded to point *a* in Figure 9.7, and progressed throughout the duration of the test (during which the length and width of those cracks increased). From the analysis of Figures 9.11, it should be mentioned that this damage was coincident with the loss of rotational stiffness at joint J1, although no visible damage was still detected on that joint at that instant. However, the crushing of the top beam against the column was visible immediately afterwards (point *b* in Figure 9.7), as shown in Figure 9.12b.

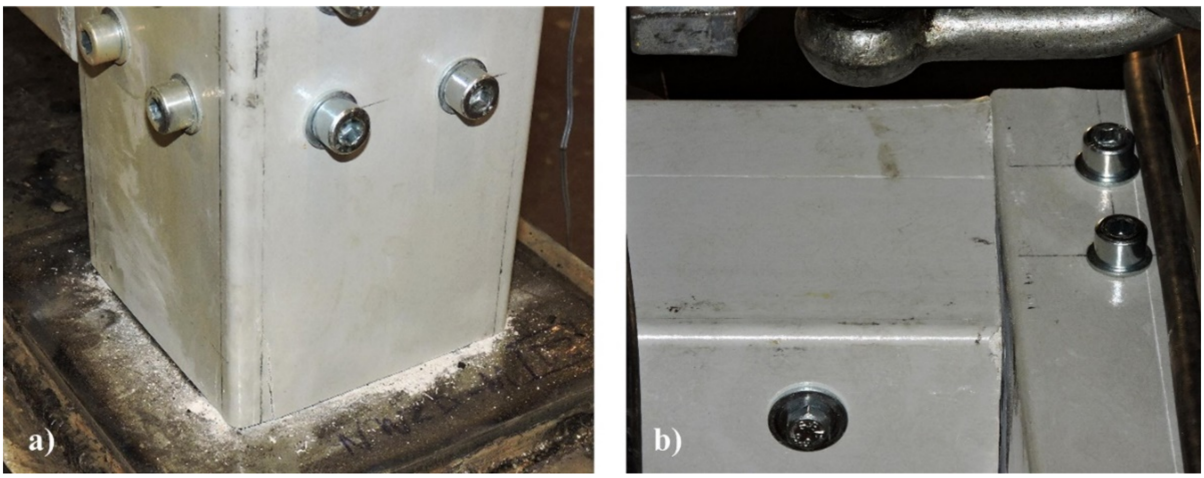

Figure 9.12 - Monotonic tests, local damage modes of frame UF-M2: a) cracking of the GFRP column at the base connection; and b) crushing of the top beam at joint J1.

Near the end of the test (point *c* in Figure 9.7), severe damage occurred at both top joints, with failure concentrating mainly at the columns, as shown in Figure 9.13. The damage on the top joint (J4) of column C2, depicted Figure 9.13a, included: (i) the crushing of the web-flange junction due to the compressive stresses induced by the beams' bottom flange; and (ii) the tensile rupture of the web-flange junction, beginning at the top of the column, caused by the prying force induced by the tension of the bolts. Regarding the top connection (J1) of column C1, the damage occurred in the form of web-crippling, as shown in Figure 9.13b, due to the compressive stresses induced by the top flange of the beam.

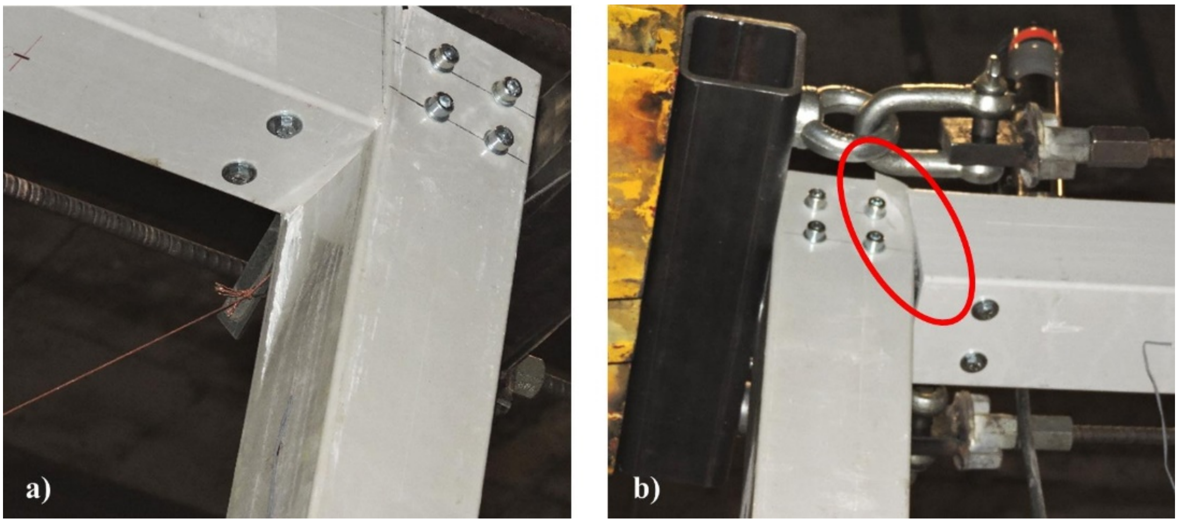

Figure 9.13 - Monotonic tests, local damage modes of frame UF-M2 at the top joints: a) joint J4; and b) joint J1.

The final failure of the unfilled frame occurred due to a combination of local failure modes on the bottom joint (J2) of column C1 (point *d* in Figure 9.7), which occurred for a top-sway displacement of 380 mm (12.7% drift). It should be stressed that such high levels of top-drift are not expected in real applications. Figure 9.14 presents this combination of local failure modes, all concentrated in the column, namely: (i) web-crippling, due to compression stresses at the contact point with the top flange of the beam; (ii) web-flange junction tensile rupture propagating from the bottom of the column; and (iii) transverse flexural failure of the column's flange.

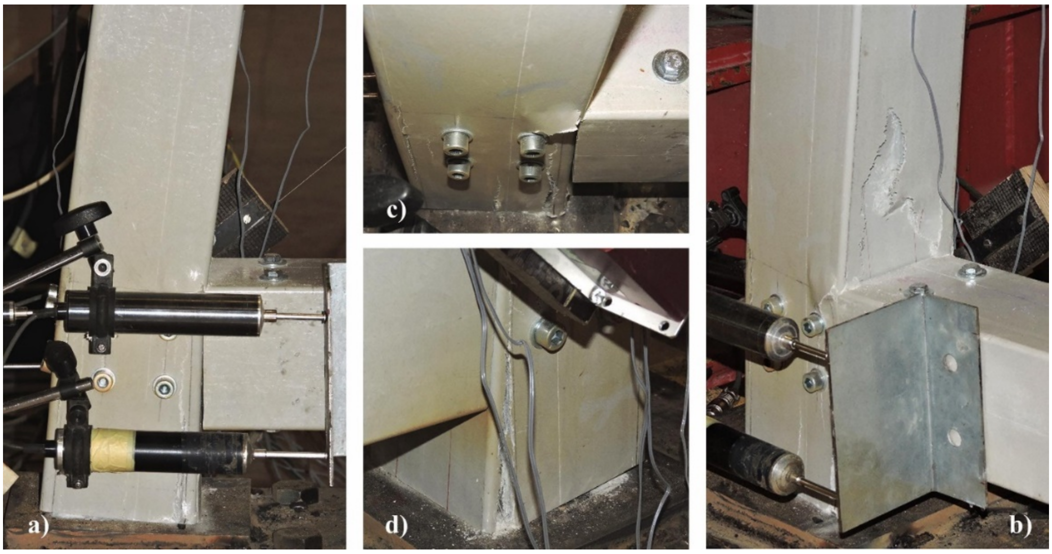

Figure 9.14 - Monotonic tests, local damage modes of frame UF-M2 at joint J2: a) web-flange junction tensile rupture; b) transverse flexural failure of the column's flange; c) web-crippling of the column; d) web-flange junction tensile rupture (opposite side).

9.3.3.2. Filled frame FF-M

The first local failure observed in the filled frame FF-M (point α in Figure 9.7) was caused by the penetration of wall panel P1 (*cf.* Figure 9.5) into the bottom beam, as depicted in Figure 9.15a, causing the rupture of the beams' top flange, together with the crushing, local buckling (wrinkling) and debonding of the skins of wall panel P3, near the bottom joint (J3) of column C2 (Figure 9.15b). Afterwards, the penetration of wall panels P2 and P3 into the top beam was also observed (*cf.* Figure 9.16a), corresponding to points β and χ in Figure 9.7.

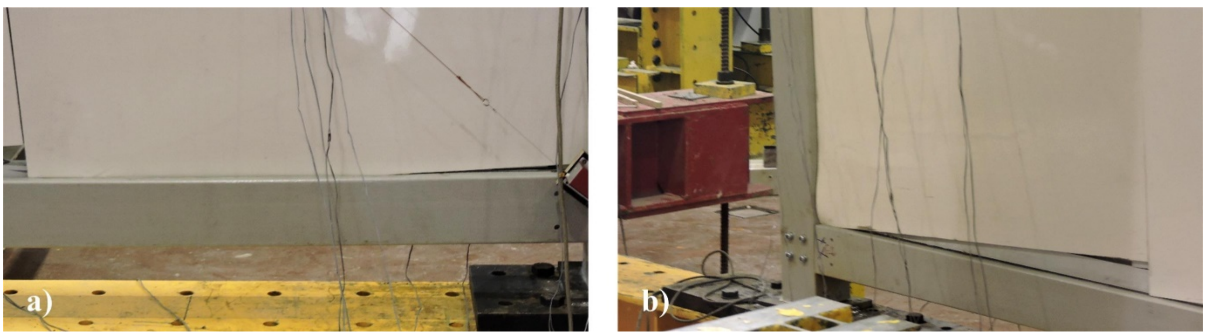

Figure 9.15 - Monotonic tests, local damage modes of frame FF-M: a) rupture of the top flange of the bottom beam; b) wrinkling of panel P3's skin.

After this stage, several local failures occurred, depicted in Figures 9.16b and 9.17, without being possible to clearly identify their initiation point and order, namely: (i) damage on the panels' interlock system, in particular the debonding and delamination of the small auxiliary tubular profiles adhesively connected to the inner flange of the beams and columns (*cf.* Figure 9.16b); (ii) compressive damage with delamination in the top connection (J1) of column C1 (in the webs and web-flange junctions, *cf.* Figure 9.17a); and (iii) web-crippling and web-flange junction tensile rupture at the columns' bases (*cf.* Figure 9.17b).

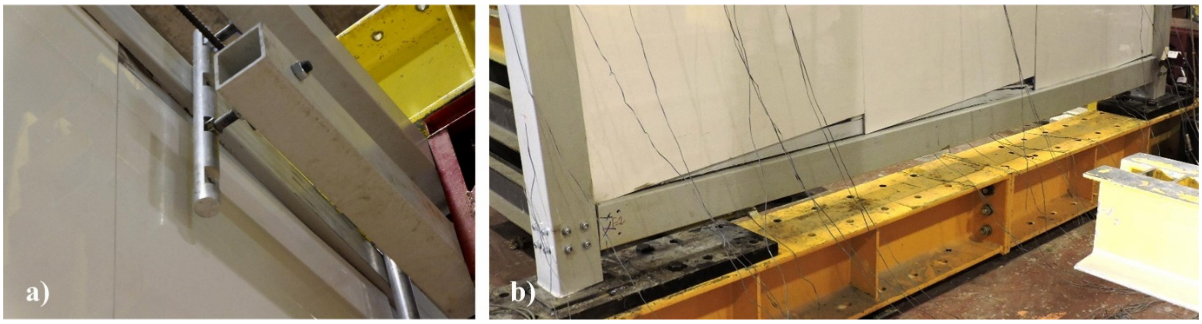

Figure 9.16 - Monotonic tests, local damage modes of frame FF-M: a) rupture of the bottom flange of the top beam; b) debonding and damage of the interlock system.

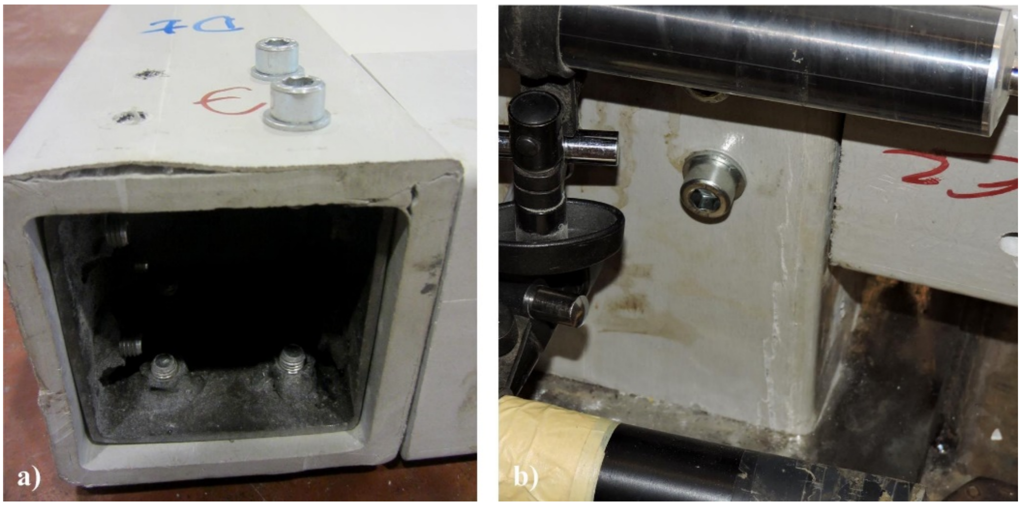

Figure 9.17 - Monotonic tests, local damage modes of frame FF-M: a) compressive damage with delamination in the top connection; b) web-flange junction tensile rupture at the columns' bases.

9.3.4. Internal forces and overall frame deformations

Figure 9.18 shows the bending moment distribution in the members of frames UF-M2 and FFM, for two load levels: (i) the first local failure load (5.6 kN and 26.9 kN for the frames UF-M2 and FF-M, respectively) and (ii) the maximum load (13.6 kN and 38.6 kN for the frames UFM2 and FF-M, respectively). As mentioned, the bending moments were derived from the strain measurements, near the extremities and at mid-span of all profiles (*cf.* Figure 9.5), considering material's linear behaviour.

For the frame UF-M2, a linear distribution of bending moments was assumed in-between those points, represented by solid lines in Figure 9.18a. As mentioned earlier, such assumption is not valid for the frame FF-M, owing to the effect of the infill panels in the internal force distribution; therefore, in Figure 9.18b only local bending moment values at the strain measurement points are shown.

As expected, the bending moment distribution of the unfilled frame UF-M2 is consistent with an almost perfect linear distribution, with higher bending moments in the base of the columns, where they are connected to the supports with a high rotational restraint degree. Moreover, while the beams presented an approximately null bending moment at mid-span throughout the test, in the columns the point with null bending moment progressed from the vicinity of mid-height to the top of the column, as the applied load increased. This indicates that with the damage progression in the top joints they were not able to support increased bending moments (*cf.* Figure 9.11) and therefore the additional load was directly supported by the base connections, similarly to a frame with pinned (internal) joints.

For the filled frame FF-M, it is worth noting that the (measured) maximum bending moments of the beams occurred at the mid-span sections, while in the columns they were attained at their bases, similarly to the unfilled frame UF-M2. In the case of the FF-M frame, however, the bending moments in the columns are far from linear along their height, unlike in the UF-M2 frame. Moreover, unlike what was observed in the unfilled frame, in the filled frame the magnitude of the maximum bending moments in the beams and in the columns was similar. These observations confirm the significant influence of the in-fill panels in the internal stress distribution of the frame.

Lastly, regarding the overall deformations of the frames under monotonic loading, Figure 9.19 presents the deformed shapes of frames UF-M2 and FF-M (half-specimen, column C1 and both beams), which were estimated from the experimental measurements of rotations and deflections (*cf.* Figure 9.5) and from the bending moment distribution (*cf.* Figure 9.18), for the same level of top-drift (Δ_l = 50 mm, the proportionality limit for frame UF-M2) Since the bending moment distribution of the filled frame FF-M could not be established, Figure 19b presents the rotations and deflections measured, connected by dashed lines.

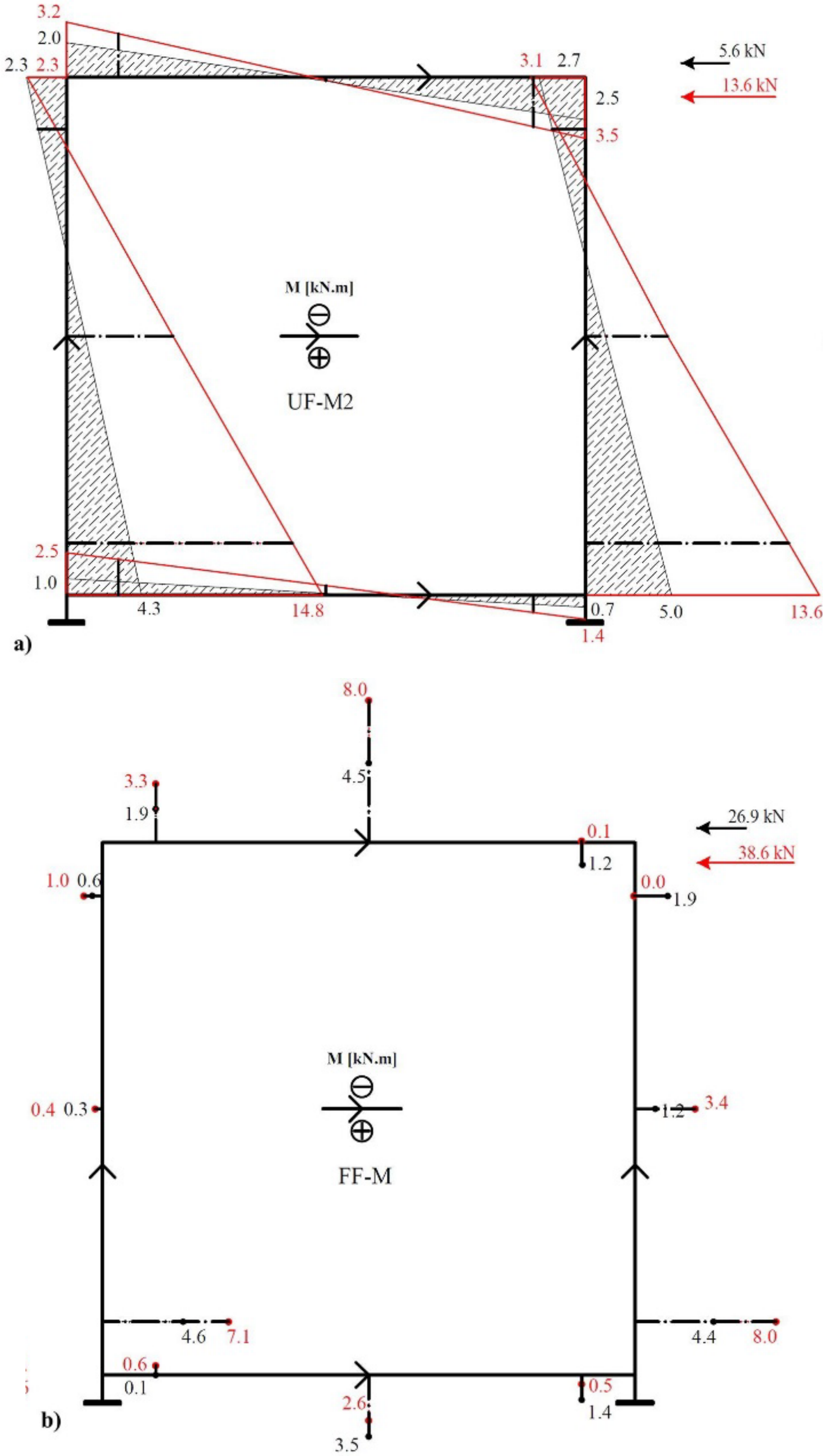

Figure 9.18 - Bending moment distributions in the monotonic tests, at first damage and at failure: a) UF-M2 frame; and b) FF-M frame.

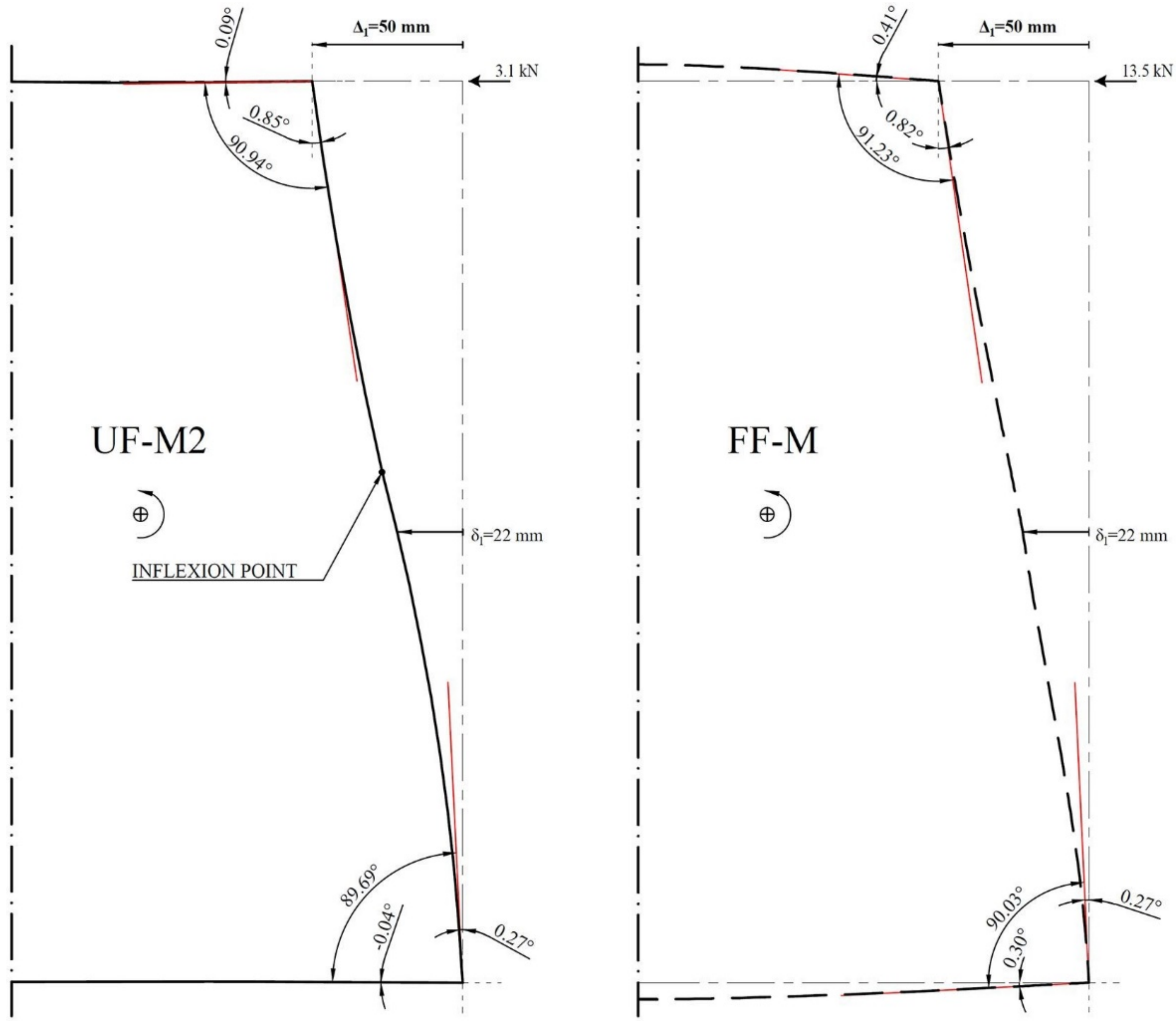

Figure 9.19 - Deformed shapes observed in the monotonic tests: a) frame UF-M2; and b) FF-M frame.

For the unfilled frame UF-M2, Figure 19a shows that the top beam presented negligible rotations, with the connection system presenting the necessary stiffness to induce an inflexion point in column C1, in the vicinity of its mid-height; overall, this frame presented a behaviour similar to that of a frame with semi-rigid connections, with the columns behaving like double-clamped members. Conversely, the filled frame FF-M presented significant rotations on the beams, owing to the contact stresses induced by the infill wall panels (*cf*. Section 9.3.3.2).

9.4. CYCLIC TESTS – RESULTS AND DISCUSSION

This section presents and discusses the experimental results of the cyclic frame tests, including (i) the load *vs*. displacement and (ii) the moment *vs*. rotation behaviours; (iii) the cyclic performance, and (iv) the failure modes.

9.4.1. Load *vs*. displacement responses

The load *vs*. top displacement (Δ_1) curves of the cyclic tests are presented in Figure 9.20, which also includes the curves obtained in the monotonic tests as reference. Both unfilled (UF-C) and filled (FF-C) specimens presented symmetric hysteric behaviour with evidence of marked pinching phenomenon. As expected, the frame filled with sandwich panels presented considerably higher loads at the end of each cycle due to the additional stiffness afforded by the in-fill walls.

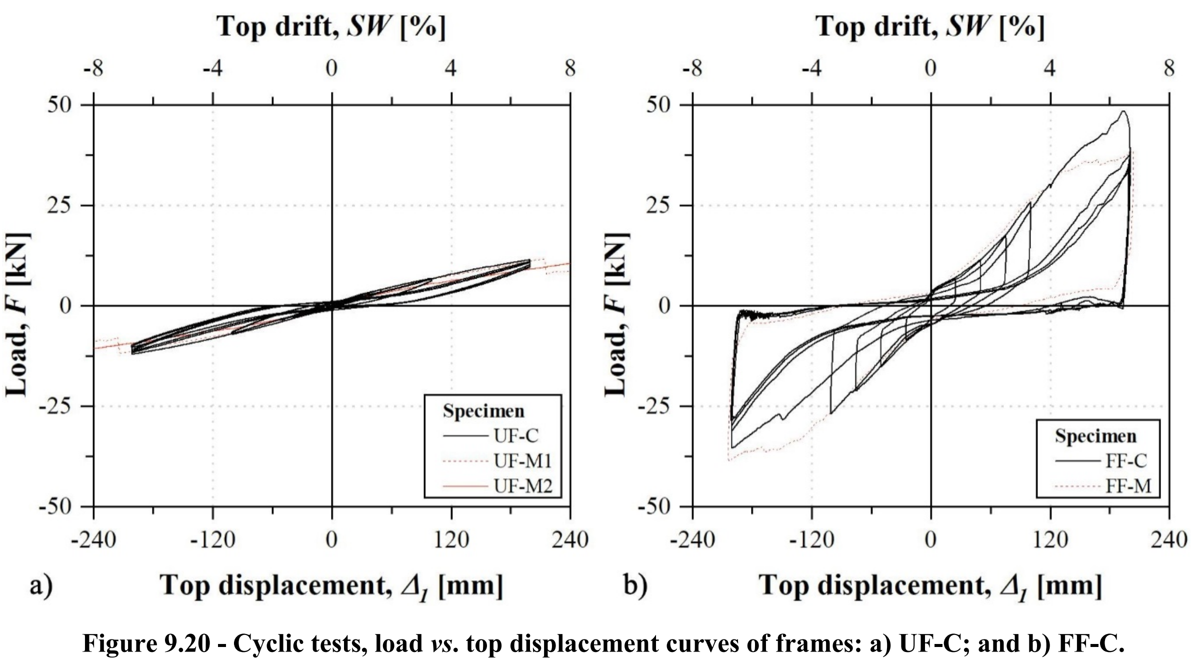

Figure 9.20 - Cyclic tests, load *vs*. top displacement curves of frames: a) UF-C; and b) FF-C.

The hysteresis diagram of the unfilled frame UF-C indicates that the specimen sustained the loads in a quasi-elastic behaviour up to the “yield” displacement (δ_y=50 mm), with almost negligible load and stiffness degradation. However, after that point, pinching was noticeable for the repeating load cycles. When comparing the curves obtained from the monotonic and cyclic tests, it is clear that they are similar in terms of stiffness and elastic limit forces, namely considering the response of the first monotonic test (UF-M1).

The hysteresis diagram of the filled frame FF-C is characterized by an initial stage with high initial stiffness (due to the initial adjustment of the panels), which was followed by a subsequent stage with lower stiffness, similarly to what was observed in the monotonic test. Pinching effect was registered before the elastic limit deformation was reached (at the 3rd cycle, Δ_I < 75 mm). Finally, the maximum load of the last three cycles was considerably lower than the maximum registered on the first cycle of the same magnitude (200 mm), showing damage accumulation.

9.4.2. Moment *vs*. rotation responses

Figure 9.21 presents the bending moment *vs*. relative rotation ($\Delta\theta_I$) curves at the top joint (J1, *cf*. Figure 9.5) of column C1 of frame UF-C; this figure also includes the bending moment *vs*. relative rotation ($\Delta\theta_I$) curves obtained from the monotonic tests of the frames and connections (*cf*. Section 9.3.2 and Chapter 3, respectively). This analysis was not performed for the filled frame as the bending moment does not follow a linear distribution (*cf*. Section 9.3.2). Connection J1 of the unfilled frame presented relatively asymmetric behaviour, which is explained by the fact that the connection system is also asymmetric – the column ends right above the beam-to-column intersection. Pinching effect was observed on this connection, from the beginning of the tests but being more noticeable in the last cycles. Overall, the monotonic tests seem to frame quite well the cyclic results, especially, for positive rotations, providing an approximate envelope curve.

9.4.3. Cyclic performance

The stiffness, strength and dissipated energy evolution per cycle of the frames were also assessed in the cyclic tests. As for the connections (*cf*. Chapter 4), the stiffness was estimated from the slope of the horizontal load *vs*. displacement curves at the intersection with the horizontal axis in both loading and unloading paths. The strength was defined as the horizontal load at the absolute maximum (positive and negative) displacement of each cycle. Regarding energy dissipation, both the dissipated energy ratio (η, *cf*. Eq. (4.1) of Chapter 4) and the accumulated absorbed energy per cycle were estimated.

Figure 9.22 presents the stiffness ratio evolution per cycle, from the 4th cycle, for the two frames tested. The stiffness ratio of frame UF-C decreased gradually until the end of the test, with reductions of 66% and 51% compared to the 4th cycle, for the negative and positive displacement branches, respectively. Regarding the frame FF-C, the stiffness ratio was always considerably lower than 1.0, indicating that the stiffness of the filled frame is very limited when unloading, contributing to a marked pinching effect, which increased as the test progressed. This shows that the relatively high stiffness measured in the monotonic tests relies greatly on contact and friction between the wall panels, the interlock connection auxiliary profiles and the frame (*cf*. Figure 9.3), which do not occur in the unloading path until the gaps created by the different damage modes are closed.

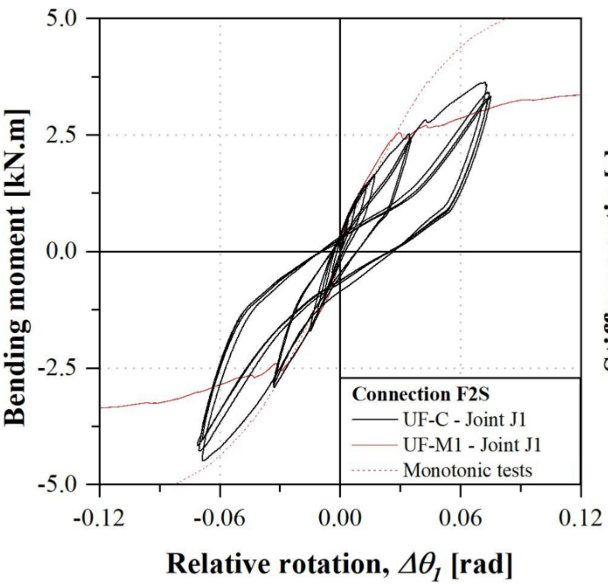

Figure 9.21 - Moment *vs*. rotation curves of Joint J1 measured in the cyclic tests of frame UF-C.

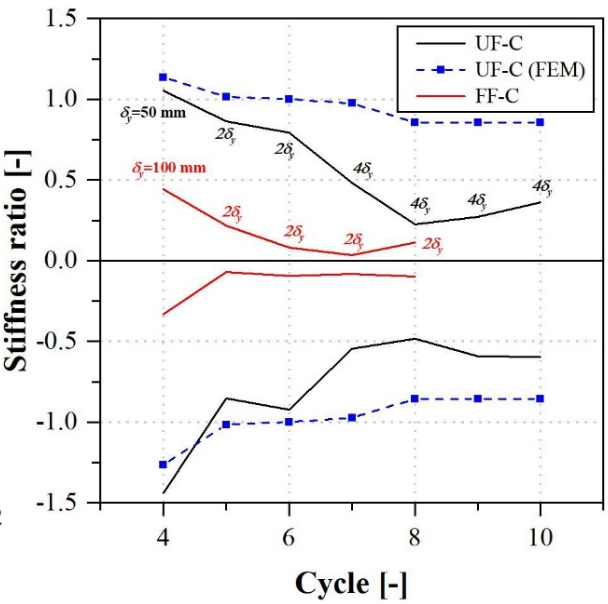

Figure 9.22 - Stiffness ratio evolution of the cyclic frame tests: UF-C (and FE model); and FF-C.

Figure 9.23 presents the strength evolution per cycle, including the “yield” horizontal loads (F_y) for both types of frames (numerical results obtained for the unfilled frame, discussed ahead, are also plotted). The load of the unfilled frame UF-C at the 4th cycle was similar to F_y, and increased for the cycles with higher maximum displacement. Yet, there is no relevant variation of strength between cycles of the same displacement range, showing that the frame did not underwent severe damage throughout the test. On the other hand, the load of the filled frame FF-C was slightly lower than F_y on the 4th cycle, although that strength was exceeded on the subsequent cycles of higher amplitude. Unlike the unfilled frame, in the filled frame a strength reduction for cycles of the same displacement magnitude (5th to 8th) was observed, showing that the frame suffered permanent damage at this stage.

Figures 9.24 and 9.25 present the relative dissipated energy ratio (η) from the 5th cycle, and the accumulated dissipated energy, respectively, for both types of frames (for the unfilled frame, numerical results, discussed ahead, are also shown). From the analysis of these curves, it can be concluded that the energy dissipation capacity decreased for repetitions of cycles with the same amplitude. This is in line with what was observed at the connection level (*cf.* Chapter 4) and can be attributed to the increase of the pinching effect due to damage developed in previous cycles. Finally, it is worth noting that the accumulated dissipated energy was considerably higher in the filled frame FF-C than in the unfilled frame UF-C. This expected result is justified by the much higher stiffness (+380%) and strength (+184%) of the former frame.

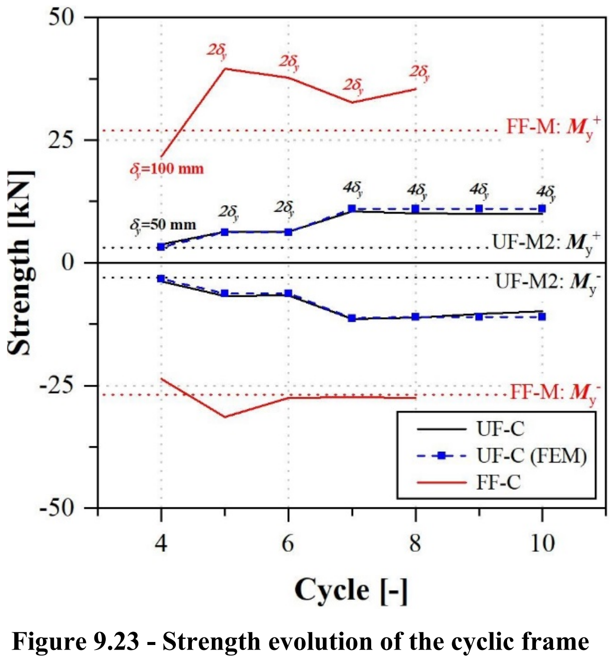

Figure 9.23 - Strength evolution of the cyclic frame tests: UF-C (and FE model); and FF-C.

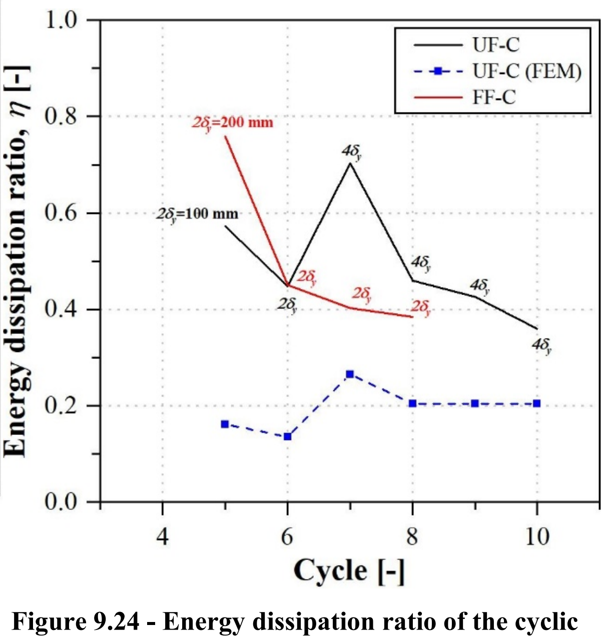

Figure 9.24 - Energy dissipation ratio of the cyclic frame tests: UF-C (and FE model); and FF-C.

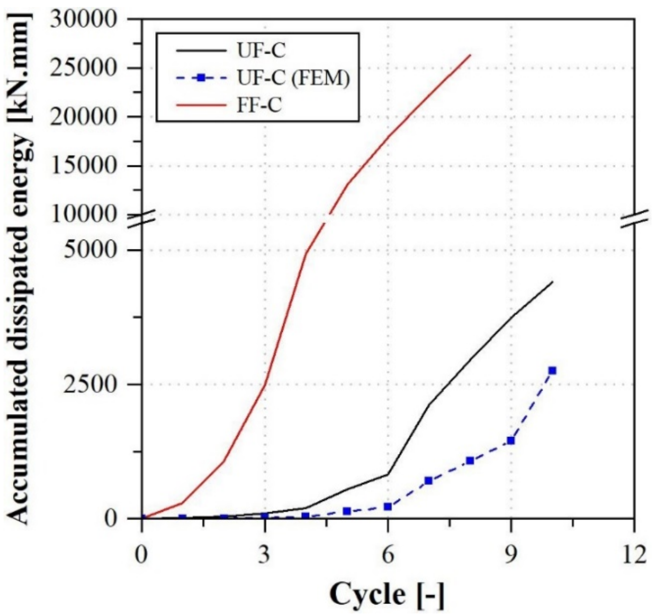

Figure 9.25 - Accumulated dissipated energy of the cyclic frame tests: UF-C (and FE model); and FF-C.

9.4.4. Failure modes

For both frames, the damage modes observed during the cyclic tests were identical to those observed in the monotonic tests (*cf.* Section 9.3.3). In the unfilled frame UF-C, the first signs of damage occurred at the 5th cycle, with cracking being visible on the web-flange junctions of the column at the base joints, which progressed in the last three cycles (*cf.* Figure 9.26a). Afterwards, web-crippling was observed at the top joint (J1) of column C1 (*cf.* Figure 9.26b), during the positive branch of the first cycle at 200 mm of drift. The combination of these effects is likely to be responsible for the pinching phenomenon registered in the final cycles. Regarding the filled frame FF-C, the following damage modes were observed: (i) crushing of the panels' corners against the beams (*cf.* Figure 9.26c) – visible after the 1st cycle; (ii) cracking at the columns' bases – during the 3rd cycle, possibly inducing some initial pinching; (iii) penetration of the panels inside the bottom beam (*cf.* Figure 9.26d) and web-flange junction failure on the top connection of column C2 (*cf.* Figure 9.26e) – which occurred in the vicinity of the maximum top drift, at the 4th cycle ($\Delta_1 \approx$ -98 mm); and finally, (iv) wrinkling of the panels' skins, crushing of the top beam against the columns, debonding and flexural failure of the auxiliary tubular profiles (*cf.* Figure 9.26f), separation of the web-flange junctions of the bottom beam, near column C2 (*cf.* Figure 9.26f), and penetration of the panels on the top beam – all occurring at the first 200 mm cycle.

Figure 9.26 - Local damage modes observed in the cyclic tests: a) web-flange junction rupture (UF-C); b) web-crippling at column C1's top (UF-C); c) crushing of the infill panels' skins (FF-C); d) penetration of the infill panels in the bottom beam (FF-C); e) web-junction rupture at column C2's top (FF-C); and f) debonding of the auxiliary tubular profiles and rupture of the bottom beams' top flange (FF-C).

9.5. DESIGN-ORIENTED NUMERICAL ANALYSIS OF THE UNFILLED FRAME

9.5.1. Objectives and model description

The main objective of the numerical study was to evaluate the feasibility of analysing the cyclic behaviour of pultruded GFRP frame structures with relatively simple numerical models, possible to be used by civil engineering practitioners when seismic design is required. This goal was set due to the concerns about the applicability of more complex models, namely regarding the damage initiation and progression in pultruded GFRP elements and their connections, which may need the definition of several material parameters not readily available (*e.g.*, fracture energies, cohesive laws), and that may present a wide range of values depending on the fibre architecture and matrix of the GFRP. Moreover, the high computational cost of those models renders them unusable for full-scale structures.

Thereafter, the author developed a design-oriented finite element (FE) model of the unfilled frame subjected to cyclic loading (UF-C), illustrated in Figure 9.27, using SAP2000 commercial package [9.19]. The GFRP was modelled as an orthotropic material, using the mechanical properties derived from experimental coupon testing (*cf.* Chapter 3). The frame elements were modelled with their real lengths, namely 2880 mm and 3210 mm for the beams and columns, respectively. The (beam-to-column) connections between the GFRP elements were modelled as non-linear 2-joint links (*MultiLinear Plastic*), with all directions fixed with the exception of the rotations around the out-of-plane orthogonal axis (R3), which were modelled with the Pivot hysteresis model [9.20]. The parameters considered for this model were the ones determined previously from the numerical analysis of the cyclic tests on beam-to-column connections: $\alpha_1 = \alpha_2 = 100$ and $\beta_1 = \beta_2 = 0.25$ (*cf.* Chapter 3). In the present case, however, the frame connections present an asymmetric behaviour (*cf.* Sections 9.3.2 and 9.4.3), owing to the different length of the column above and below the connection. Although symmetric Pivot hysteresis model parameters were used, this asymmetry was considered in the input monotonic moment *vs*. rotation curves, as illustrated in Figure 9.28. Thereafter, for the top-connections (J1 and J4) the input was derived from the monotonic tests on the beam-to-column connection (*cf.* Chapter 4) for negative rotations, while for positive rotations it was derived from the frame monotonic tests (Joint J1, *cf.* Section 9.3.2).

The base connections were modelled as semi-rigid with a linear joint spring for the rotations around the out-of-plane orthogonal axis (R3). The stiffness of such spring was calibrated so that the initial overall stiffness of the FE model matched the one measured experimentally; accordingly, a rotational spring stiffness of 500 kNm/rad was adopted.

In-plane geometrically linear time-history analysis was performed, in which the experimental deflection protocol (*cf.* Figure 9.6) was applied to a node of the top beam, simulating the experimental tests (*cf.* Section 9.2.2). In order to avoid dynamic effects, no mass was attributed to the models.

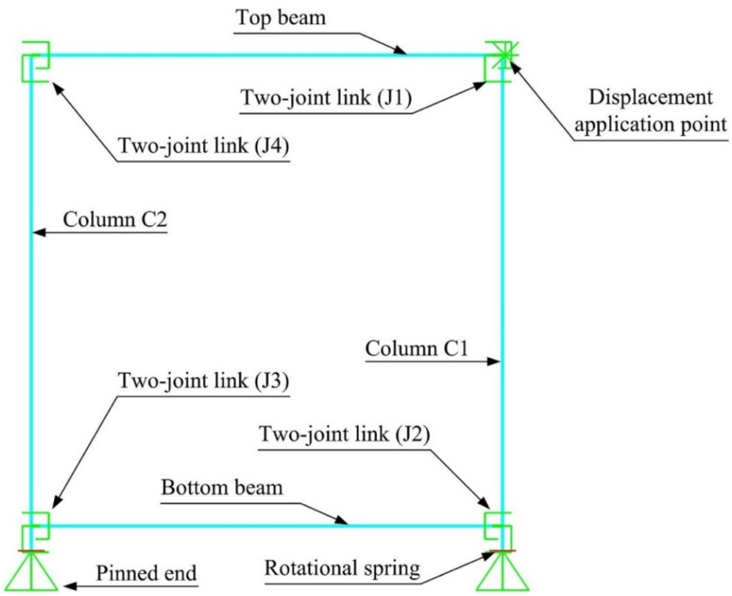

Figure 9.27 - FE model, including the identification of all elements, boundary conditions and displacement application point.

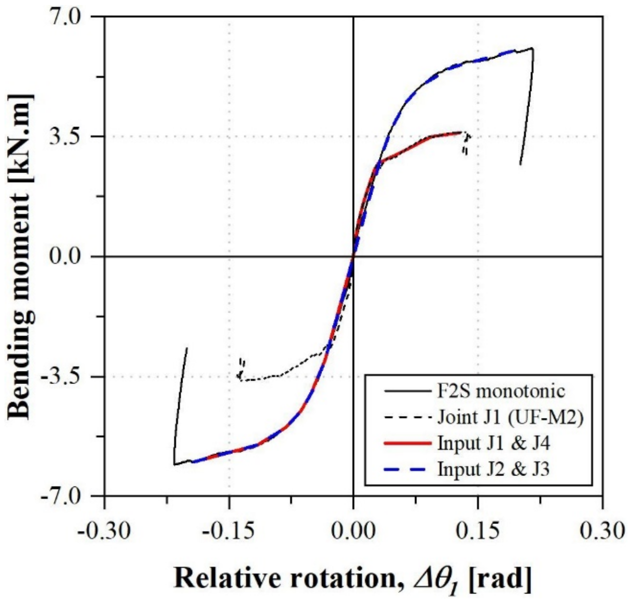

Figure 9.28 - Monotonic moment *vs.* rotation input curves used in the FE model and their experimental counterparts.

9.5.2. Numerical results and discussion

Figures 9.29a and 9.29b compare the hysteretic curves obtained with the simplified FE model to those obtained in the experimental tests, namely regarding the load-top sway behaviour and the moment-rotation of Joint J1. Although a reasonable overall agreement was achieved for the load-top sway curves (*cf*. Figure 9.29a), it can be observed that for the last cycles, the hysteretic loops obtained in the experimental tests are larger than their FE model counterparts, especially regarding the unloading paths. These results are justified by (i) the larger loops observed at the connection level (*cf*. Figure 9.29b) for negative rotations and, more importantly, (ii) the fact that the damage of the base connections (more extensive for these last cycles) is not accounted for in the FE model.

Figure 9.22 compares the evolution of the stiffness ratio measured experimentally with that computed from the FE model. It can be seen that the model underestimates the steeper stiffness degradation observed after the 6th cycle, which is likely caused by the afore-mentioned damage at the base connections, disregarded in the FE model. On the other hand, Figure 9.23 shows that the FE model predicts with quite good accuracy the strength progression, showing that the damage of the base connections affected mainly the unloading loops (which became larger in the experiments), and not the strength of the frame. Finally, Figures 9.24 and 9.25 compare the experimental and numerical results in terms of absorbed energy ratio and accumulated energy, respectively. This comparison shows that although the FE model underestimated the absorbed energy (by -37% after 10 cycles) due to aforementioned reasons, the main trends of numerical and experimental results are similar.

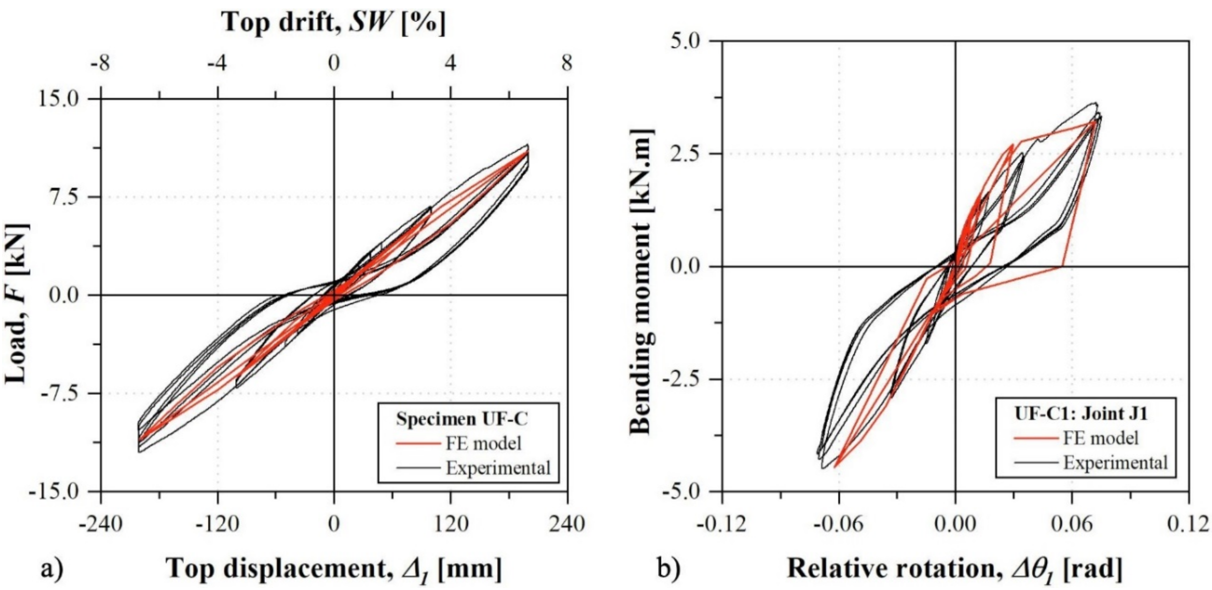

Figure 9.29 - Experimental *vs*. numerical hysteretic curves: a) load *vs*. top displacement; and b) moment *vs*. rotation of joint J1.

Overall, the results presented above point out the feasibility of using the Pivot hysteresis model to analyse the cyclic behaviour of GFRP pultruded frame structures with relatively simple FE models; in fact, these design-oriented models provided a reasonable agreement with the experimental data.

9.6. CONCLUSIONS

This chapter presented an experimental and numerical study on the lateral sway behaviour of pultruded GFRP plane frames. The beam-to-column connection system adopted in the frames was previously investigated by the author, regarding its monotonic (*cf.* Chapter 3) and cyclic behaviour (*cf.* Chapter 4).

In the monotonic tests, the GFRP frames initially exhibited linear elastic behaviour, which was followed by a gradual decrease of global stiffness until attaining very significant maximum top-drift of ~14% (unfilled frame) and ~7% (filled). The infill walls had a great influence on the structural performance of the frames, in particular, the initial stiffness and maximum load of the filled frame were about 4 and 3 times higher, respectively, than those of the unfilled frame. Regarding the failure behaviour, in the unfilled frame local failure modes were observed, which were concentrated at the connection level, leading to a smooth stiffness degradation until the maximum load was attained. Conversely, the filled frame presented extensive damage at the member level (beams), resulting in the loss of its structural integrity; ultimately, this test had to be stopped to avoid a sudden collapse of the frame.

In the cyclic tests, the unfilled frame presented an almost linear-elastic behaviour throughout the entire test (for a maximum drift as high as 6.7%), with very slender hysteretic loops. The filled frame presented larger hysteretic loops, indicative of the occurrence of a higher level of damage during the imposed cyclic deformations. On the other hand, both frames presented marked pinching effect, with almost no load in the pair quadrants of the hysteretic curves. The higher strength and stiffness of the filled frames, already observed in the monotonic tests, along with the larger hysteretic loops observed in the cyclic tests, resulted in a much higher energy dissipation capacity, when compared to the unfilled frame (+789%, after 8 cycles). Overall, albeit the filled frame showed better energy dissipation capacity, this was achieved at the expense of more damaging failure modes, which could have led to a brittle collapse of the frame structure. This needs to be duly accounted for when designing frame structures with high-stiffness and high-load carrying capacity infill walls.

Finally, a relatively simple FE model was developed to simulate the cyclic behaviour of the unfilled frame; the Pivot Hysteresis model [9.20] was used to simulate the hysteretic behaviour of the connections, with the parameters calibrated from the cyclic tests on beam-to-column connections (*cf.* Chapter 4). Although linear-elastic material behaviour was considered in this FE model and, therefore, it was not able to capture the damage at the base connections, the model was still able to reproduce the cyclic response observed in the test with fairly good accuracy, providing reasonably accurate (and conservative) estimates of the accumulated dissipated energy. This evidence points out the feasibility of using this type of simple models in the seismic design of GFRP frame structures.

9.7. REFERENCES

[9.1] CNR-DT 205/2007 – Guide for the Design and Construction of Fiber-Reinforced Concrete Structures.

[9.2] ASCE (2010). Pre-Standard for Load & Resistance Factor Design (LRFD) of Pultruded Fiber Reinforced Polymer (FRP) Structures.

[9.3] Bank LC, AS Mosallam AS. (1992). Creep and failure of a full-size fiber-reinforced plastic pultruded frame. *Composites Engineering*, 2(3), 213–15,217–227.

[9.4] Mosallam AS, Bank LC. (1992). Short-term behaviour of pultruded fiber-reinforced plastic frame. *Journal of Structural Engineering*, 118, 1937–54.

[9.5] Seçer M, Kural ME. (2017). Creep behaviour of plane frame structures made of GFRP profiles. *Mechanika*, 23(3), 341–6.

[9.6] Na G. (2008). *Load-displacement behaviour of frame structures composed of FRP composite materials*. PhD thesis in Civil Engineering, Georgia Institute of Technology.

[9.7] Cavaleri L, Di Paola M, Ferroto MF, Valenza A. (2019). Structural performances of pultruded GFRP emergency structures – Part 2: Full-scale experimental testing. *Composite Structures*, 214, 304-15.

[9.8] TC (2008). Nuove Norme Tecniche per le Costruzioni. Italian Building Code.

[9.9] Russo, S. (2012). Experimental and finite element analysis of a very large pultruded FRP structure subjected to free vibration. *Composite Structures*, 94(3), 1097–05.

[9.10] Boscato G, Russo S. (2013). Free vibrations of a pultruded GFRP frame with different rotational stiffnesses of bolted joints. *Mechanics of Composite Materials*, 48(6), 655-668.

[9.11] Xiao X, Zhang Z, Bai Y. (2017). Comparative study of energy dissipation capacity of steel and glass fibre-reinforced polymer frames with bonded sleeve connections. *Journal of Reinforced Plastics and Composites*, 36(22), 1665-1679.

[9.12] Chui PPT, Chang SL. (1996). Transient response of moment-resistant steel frames with flexible and hysteretic joints. *Journal of Constructional Steel Research*, 39(3), 221-243.

[9.13] Abdolpour H, Escusa G, Roca J, Sena-Cruz J, Valente IB, Barros J. (2015). Evaluation on the structural behaviour of wall GFRP sandwich panels. *Task: 4.4: report 4.4.4 – ClickHouse project,* Minho University.

[9.14] ASTM D3039 (2007) – Standard Test Method for Tensile Properties of Polymer Matrix Composite Materials". West Conshohocken.

[9.15] ASTM C365-03 (2004) – Standard Test Method for Flatwise Compressive Properties of Sandwich Cores. West Conshohocken.

[9.16] ASTM C297-04 (2004) – Standard Test Method for Flatwise Compressive Strength of Sandwich Constructions. West Conshohocken, PA.

[9.17] ASTM C273-0 (2000) – Standard Test Method for Shear Properties of Sandwich Core Materials. West Conshohocken.

[9.18] ECCS/TC1. (1986). Recommended testing procedure for assessing the behaviour of structural steel elements under cyclic loads.

[9.19] CSI (2016). SAP 2000 - Version 18, Integrated Software for Structural Analysis and Design, Analysis Reference Manual. *Computer & Structures Inc*., Berkeley.

[9.20] Dowell OK, Seible F, Wilson EL. (1998). Pivot hysteresis model for reinforced concrete members. *ACI structural journal*, 95, 607-617.

Chapter 10

Monotonic and cyclic sway behaviour of 2-dimensional pultruded frames made of I-section profiles

10.1. INTRODUCTION

This chapter presents an experimental and numerical study concerning the sway behaviour of 2-dimensional full-scale frames composed by pultruded GFRP I-section profiles and non-corrodible stainless steel auxiliary parts. In the experimental campaign, five frame series were tested under monotonic and cyclic loading. Two of the frames' typologies differed on the connection systems used to in the beam-to-column joints, namely one cleated connection and one cuff connection, previously characterized in Chapters 6 and 7 and Chapter 8, respectively. Additionally, the effects of using a bracing system, comprising stainless steel cables, or a non-structural infill wall were also investigated. In the numerical investigation, FE models of the unbraced and unfilled frame with the best monotonic performance were developed using frame elements and link joints. To evaluate the feasibility of using these models in the design of GFRP frames, the FE models were developed using a commercial software widely used by civil engineers in structural design. Finally, the validated FE model was used to evaluate the hysteretic response of the referred frame when including a GFRP bracing system encompassing a steel plate damper element.

10.2. EXPERIMENTAL STUDY

10.2.1. Experimental programme

10.2.1.1. Test series

All frame specimens comprised two 3000 mm long column profiles and two 2500 mm long beam profiles, illustrated in Figure 10.1, joined using beam-to-column connection systems previously characterized, detailed in Figure 10.2. Four 2-dimensional frame series were studied in this work: (i) series F-R, with BC-6-F2-R beam-to-column connections (cleated connection with column reinforcement, *cf.* Chapters 6 and 7); (ii) series F-IC, with BC-IC-360×1.0 beam-to-column connections (cuff connection, *cf.* Chapter 8); (iii) series BF-R, with BC-6-F2-R beam-to-column connections (*cf.* Chapters 6 and 7) and a cable bracing system; and (iv) series WF-R, with BC-6-F2-R beam-to-column connections (*cf.* Chapters 6 and 7) and a plasterboard infill wall. No clearance was considered between the bolts/rods and the respective holes, and a torque of 10 N.m was applied to all bolts/rods using a torque wrench.

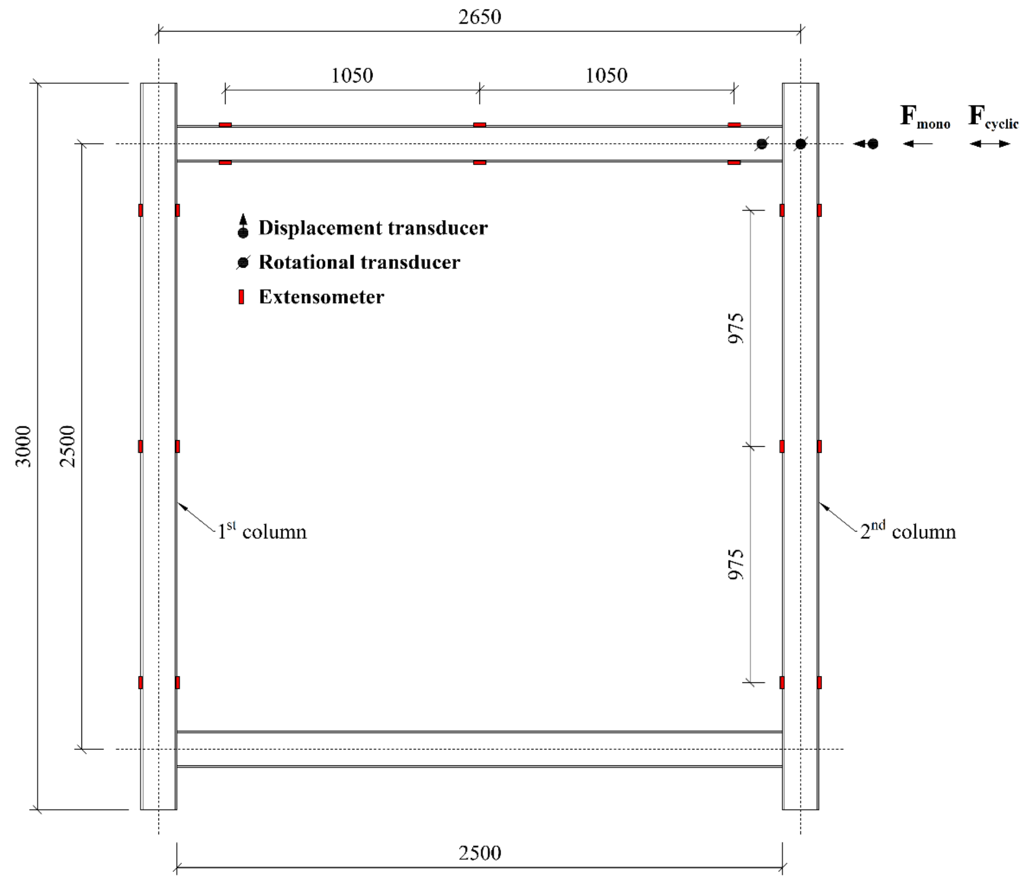

Figure 10.1 - Frame tests: geometry (dimensions in mm) and instrumentation.

To prevent the premature occurrence of web-crippling in the columns of series F-R due to the transverse compressive loads transmitted by the beams, two 150 mm long segments of a stainless steel channel section (with wall thickness of 4 mm), made to fit the inner space between the column flanges, were attached to the web of the columns at the intersection with the beams (one in each side of the web, *cf.* Figure 10.2). The selection of this reinforcing system was supported by means of web-crippling tests and its influence on the overall beam-to-column connection behaviour was also assessed by testing. Appendixes E and F present the studies of the web crippling resistance of the GFRP profile (column) and the effects of the web reinforcing parts on the behaviour of the beam-to-column connection, respectively.

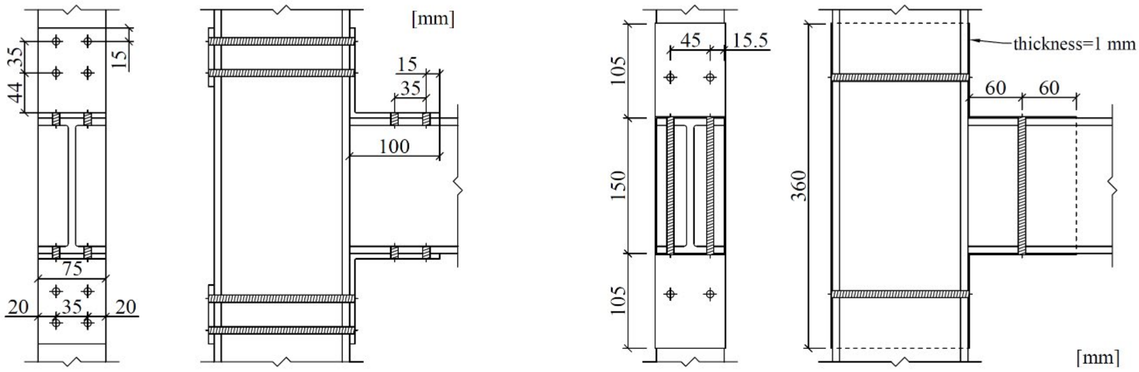

Connection
BC-6-F2-R

Connection
BC-IC-360×1.0

Figure 10.2 - Frame tests: geometry (dimensions in mm) of beam-to-column connections.

The bracing system adopted in series BF-R comprised two stainless steel cables (one per diagonal, *cf.* Figure 10.3a) with 6 mm of diameter (with 7×19 construction). The cables were secured to the eyebolts and to the turnbuckles using two clamps on each extremity and were stretched by hand, ensuring that they were in tension before the beginning of the tests. The eyebolts were welded to 6 mm thick stainless steel plates (same material of the cleat parts of series BC-6-F2 and BC-6-F2-R), which were bolted to one cleat (of the beam-to-column connections) per corner (*cf.* Figure 3b).

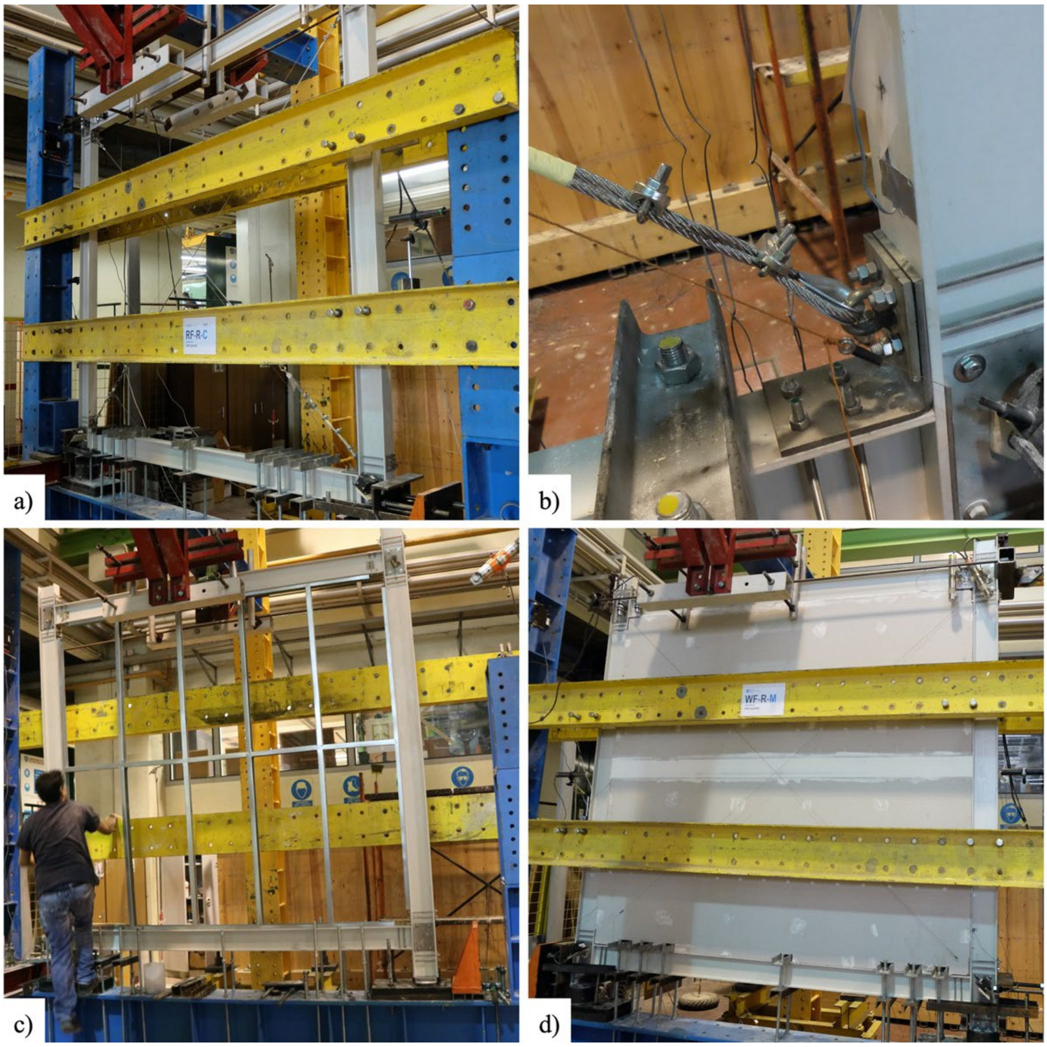

Figure 10.3 - Frame tests: a) frame with bracing system (BF-R); b) detail of bracing fixation (BF-R); c) interior frame to support plasterboards (WF-R); d) frame with walls (WF-R).

For the series WF-R, with an infill wall, an interior supporting frame comprising galvanized steel channel profiles and studs was built (*cf.* Figure 3c) to fix four plasterboards, two on each side of the frame. The interior frame comprised four vertical profiles spaced by 500 mm and horizontal profiles placed at mid-span of the vertical ones, both with C-section of 48×37×0.55 mm, fixed to a boundary interior frame made of different C-section profiles (48×30×0.55 mm). The plasterboards used were 2500 mm long, 1200 mm wide and 13 mm thick; they were trimmed before being fixed to the auxiliary metallic frame to achieve a perfect fit with the GFRP frame. Figure 3d shows the final appearance of the WF-R frame, after the application of a non-structural finishing coating over the plasterboards surface.

10.2.1.2. Materials

The 2-dimensional frames studied in this work were composed by pultruded GFRP I-section profiles (150×75×8 mm) and stainless steel connection parts (detailed in Section 10.2.1.1). The GFRP profiles were produced by *ALTO, Perfis Pultrudidos, Lda.*, using isophthalic polyester resin matrix and E-glass fibres. Stainless steel sheets, grade AISI 304, with thicknesses of 1.0, 4.0, 6.0 mm were cold-formed to produce the auxiliary connection parts and column reinforcements. The mechanical properties of the GFRP profiles, summarized in Table 10.1, were previously determined by means of coupon tests. According to ASTM A240 [10.6], the main properties of the stainless steel sheets are: (i) 0.2% tensile proof stress ($f_{0.2\%}$) of 205 MPa; and (ii) ultimate tensile stress (f_u) in tension of 515 MPa.

Rods, bolts, nuts and washers of grade A2-70 were used to join the profiles and the stainless steel parts. According to the manufacturer and based on ISO 3506-1 [10.7], the nominal mechanical properties of the bolts and rods are as follows: (i) 0.2% tensile proof stress ($f_{0.2\%}$) of 450 MPa; and (ii) ultimate tensile stress (f_u) in tension of 700 MPa.

As mentioned, a frame with cable bracings was also tested (*cf.* Section 10.2.2). The cables, turnbuckles, clamps, thimbles and eyebolts used in the bracings were made of stainless steel grade A4-70. For this material, the nominal 0.2% tensile proof stress ($f_{0.2\%}$) and ultimate tensile stress (f_u) in tension are of 450 and 700 MPa, respectively, according to ISO 3506-1 [10.7].

One of the frame series also included plasterboard infill walls (*cf.* Section 10.2.2). According to the manufacturer, *Fibroplac*, the flexural failure load of each board was 711 N and 282 N for the longitudinal and transverse directions, respectively, meeting the requirements of EN-520 standard [10.8] for gypsum plasterboards. The plasterboards were joined to the frames using galvanized steel channel profiles and studs.

Table 10.1 - Frame tests: mechanical properties of the GFRP profiles.

Test	Method	Specimen size	Property	Element	Average ± std. Dev.	Unit
Tension	EN ISO 527 [10.1]	15×8×300 mm^3	$\sigma_{tu,L}$	I150-W	388.0 ± 25.0	[MPa]
				I150-F	353.4 ± 32.7	
			$E_{t,L}$	I150-W	43.4 ± 1.0	[GPa]
				I150-F	39.6 ± 1.2	
			υ_{LT}	I150-W	0.23 ± .02	[-]
				I150-F	0.29 ± .02	
Compression	ASTM-D6641 [10.2]	12×8×156 mm^3	$\sigma_{cu,L}$	I150-W	461.9 ± 31.0	[MPa]
				I150-F	353.5 ± 32.7	
			$E_{c,L}$	I150-W	44.9 ± 1.7	[GPa]
				I150-F	39.6 ± 1.2	
		12×8×123 mm^3	$\sigma_{cu,T}$	I150-W	64.2 ± 2.12	[MPa]
			$E_{c,T}$	I150-W	8.1 ± 0.6	[GPa]
	ASTM-D695 [10.3]	20×8×35 mm^3	$\sigma_{cu,T}$	I150-F	41.0 ± 3.6	[MPa]
			$E_{c,T}$	I150-F	2.8 ± 0.2	[GPa]
Interlaminar shear	ASTM-D2344 [10.4]	18×8×48 mm^3	$\tau_{is,L}$	I150-W	27.0 ± 1.3	[MPa]
				I150-F	31.2 ± 1.0	
In-plane shear	ASTM-D5379 [10.5]	20×8×76 mm^3 (Notched specimens)	τ_{LT}	I150-W	46.8 ± 3.1	[MPa]
				I150-F	47.9 ± 2.6	
			G_{LT}	I150-W	3.0 ± 0.3	[GPa]
				I150-F	3.7 ± 0.3	
			τ_{TL}	I150-W	31.2 ± 2.3	[MPa]
				I150-F	27.3 ± 5.0	
			G_{TL}	I150-W	3.3 ± 0.5	[GPa]
				I150-F	2.5 ± 0.2	

Note: I150-F refers to the profile flange and I150-W refers to the profile web.

10.2.1.3. Test setup and procedure

The monotonic and cyclic tests of series F-R were performed in a reaction wall (*cf*. Figure 10.4a), while the remaining series were tested using an equivalent steel reaction frame (*cf*. Figure 10.4b). The top displacements were imposed at the frames' top beam by either a mechanical jack with capacity of 1000 kN and stroke of ± 200 mm (tests in the reaction wall), or by a hydraulic jack with capacity of 250 kN and stroke of ± 200 mm (tests in the steel reaction frame) - both identified in Figure 10.4, point A. Two mechanical hinges were used between the frame and the jack to guarantee the orthogonality of the applied load to the column face. In the cyclic tests, two *dywidag* bars were used together with the hydraulic jack to allow reversing the loading direction in the setup plan (Figure 10.4, point B).

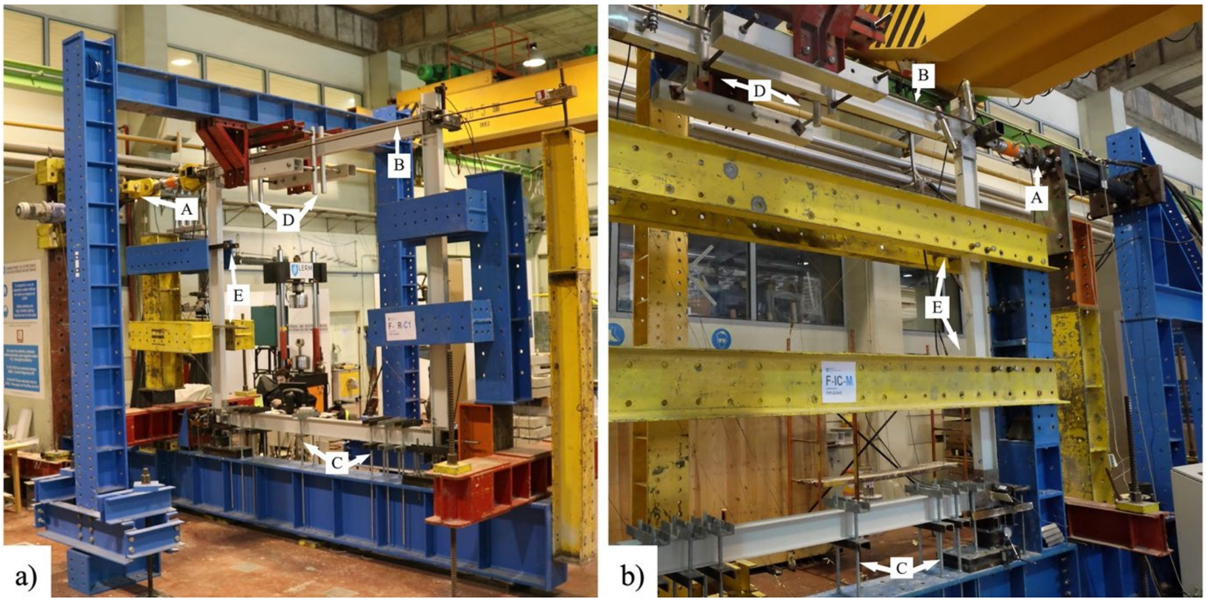

Figure 10.4 - Frame test setup: a) series F-R; b) series F-IC, BF-R and WF-R.

The following fixations/constraints were used in the frame tests: (i) the vertical displacements of the bottom beam were restricted using 7 vertical restraining fixtures (Figure 10.4, point C), each comprising one pair of UPN100 steel profiles and two stainless steel bars fixed to a rigid beam anchored to laboratory's strong floor; (ii) the out-of-plane displacements of the top beam were prevented by two pairs of aluminium bars fixed to a steel frame, transverse to the specimens' plane, anchored to the laboratory's strong floor (Figure 10.4, point D); (iii) the out-of-plane displacements of each column were prevented by two pairs of aluminium bars attached to steel profiles at vertical distances of ~0.8 m and ~1.6 m from the top flange of the bottom beam (Figure 10.4, point E); (iv) the column bases were clamped to a cylindrical steel part (with 4.5 cm deep grooves) bolted to a thick steel plate (Figure 10.5, point F), the latter being bolted to the rigid beam; (v) the uplift displacements at the frames' bases were also prevented by two stainless steel cleats placed on each face of the columns' webs and bolted to both the pultruded profiles and the cylindrical steel part (Figure 10.5, point G) and by an all-steel restraining system comprising 4 UPN100 profiles, 4 threaded rods and 4 bars (Figure 10.5, point H); and (vi) the horizontal displacements of the bottom beam were prevented by 1 (or 2 in case of cyclic tests) steel angle profile(s) centred with the beam's longitudinal axis (Figure 10.5, point I).

In the tests of series F-R, the top displacement was measured using a string pot transducer from *Celesco* with stroke of 400 mm, identified in Figure 10.1. In the remaining tests, the same top displacement was measured by the hydraulic jack built-in displacement transducer. The applied load was measured using a load cell from *TML* with capacity of 300 kN. In the monotonic tests of the frames without bracings and infill walls (series F-R and F-IC), pairs of electric strain gauges were attached at three points of the top beam and of both columns, allowing to measure the strains in selected locations of the structure (the position of the strain gauges is illustrated in Figure 10.1) and to estimate curvatures and corresponding bending moments (*cf.* Section 10.2.2). Additionally, in these tests, a pair of inclinometers from *TML* was positioned near one top beam-to-column connection (*cf.* Figure 10.1); with these inclinometers, one positioned on the top beam and the other on the column, it was possible to assess the relative rotation at this node.

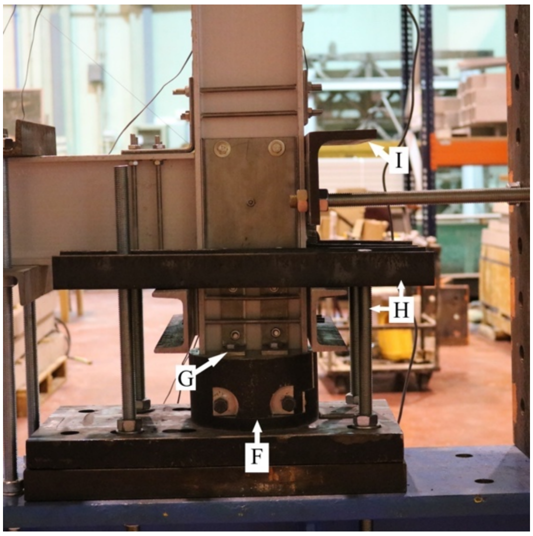

Figure 10.5 - Frame tests: detail of column fixations.

The monotonic and cyclic displacement rates were chosen to avoid dynamic and strain-rate effects. The monotonic tests were performed under displacement control, at a rate of 0.5 mm/min, and were stopped when either the maximum stroke of the hydraulic jack was attained or the frames' structural integrity was highly compromised.

The cyclic tests were performed under displacement control, at a rate of 1.0 mm/min. The top displacement history (illustrated in Figure 10.6a, as a function of the end of proportionality displacement – δ_{EP}) was defined according to the recommendations of the ECCS protocol [10.9], as follows: (i) four initial cycles corresponding to maximum absolute top displacements of ¼, ½, ¾ and 1 times the top displacement δ_{EP} were first performed; (ii) next, groups of three cycles with maximum absolute top displacements of $2n \times \delta_{EP}$ were carried out, n being an integer that increases after each three cycles. The δ_{EP} of each series was defined using the monotonic load *vs*. top displacement curves, following a procedure recommended by the ECCS protocol [10.9], duly explained in Section 10.2.2. This protocol was also adopted in previous chapters, concerning the behaviour of GFRP beam-to-column connections (*cf.* Chapters 4, 5, 6 and 8) and GFRP frames[1] (*cf.* Chapter 9). The cyclic tests ended when either the maximum stroke of the hydraulic jack was reached or extensive damage (compromising the frames' integrity) was observed.

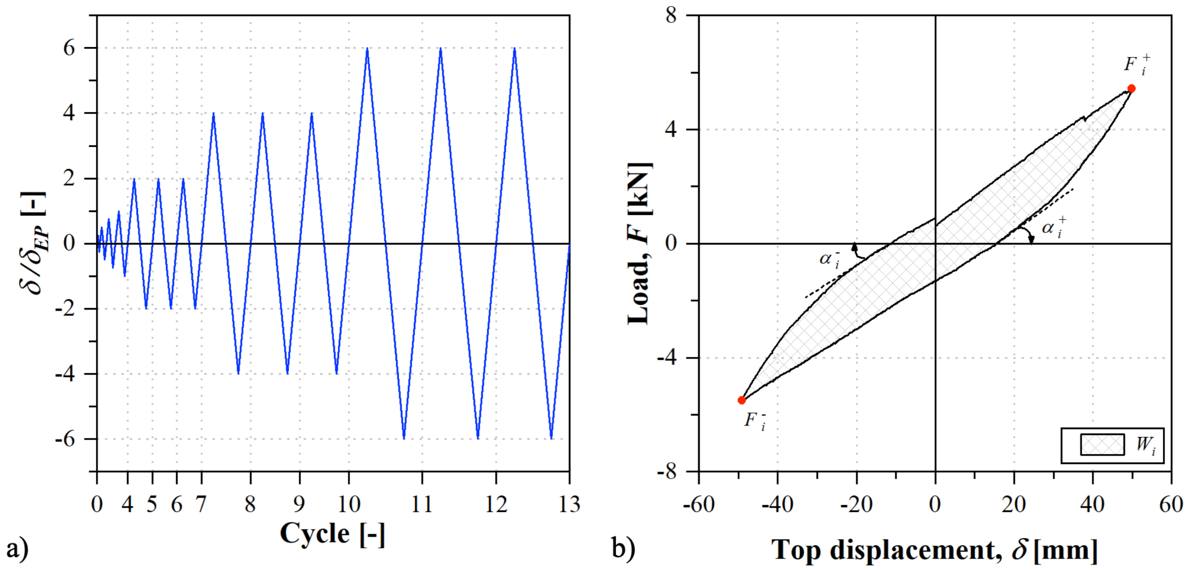

Figure 10.6 - Frame tests: a) cyclic top displacement history; b) ECCS [10.9] hysteretic parameters.

The ECCS protocol [10.9] proposes the evaluation of several parameters to assess the cyclic response of the structure, namely: (i) the stiffness ratio (ξ), which corresponds to the ratio between the slope of the load *vs*. top displacement hysteretic curves when crossing the horizontal axis (α_i^+ or α_i^-, as depicted in Figure 10.6b) and the initial monotonic stiffness (K, *cf.* Table 10.2); (ii) the strength ratio (ε), which is estimated by dividing the load when the maximum and minimum top displacement of each cycle are attained (F_i^+ or F_i^-, depicted in Figure 10.6b) by the load corresponding to δ_{EP} (F_{EP}, *cf.* Table 10.2); and (iii) the dissipated energy ratio (η) per cycle, estimated by:

[1] Although this protocol was defined for steel structures, it was firstly used in the beam-to-column connection tests as their behaviour was highly influenced by the plastic deformation occurring in the steel elements. For the sake of coherence, the same protocol was employed in the frame tests.

$$\eta_i = \frac{W_i}{\Delta F_{EP}(\Delta\delta_i - \Delta\delta_{EP})} \tag{10.1}$$

where W_i is the energy dissipated in cycle i (area delimited by the hysteric cyclic curve, as depicted in Figure 10.6b), ΔF_{EP} is the difference between the positive and negative EP loads, $\Delta\delta_i$ is the difference between the positive and negative imposed top displacement in cycle i, and $\Delta\delta_{EP}$ is the difference between the positive and negative EP top displacement (δ_{EP}, *cf.* Table 10.2).

10.2.2. Monotonic tests

Figure 10.7 presents the monotonic load *vs.* top displacement curves of all series. The main results of these tests are summarized in Table 10.2, namely regarding the initial stiffness (K), the δ_{EP}, the F_{EP} and the maximum load (F_u).

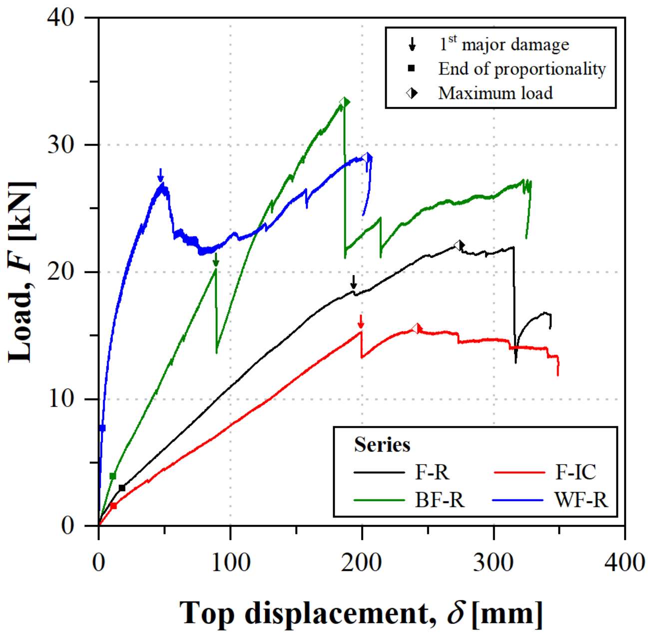

Figure 10.7 - Frame tests: monotonic load *vs.* top displacement curves.

Series F-R presented an initial bi-linear behaviour, with the second linear branch occurring after crossing δ_{EP} (17 mm) and presenting 30% lower stiffness compared to the initial branch (Figure 10.7). The first slight load drop occurred at a top displacement of 194 mm (18.4 kN) – coinciding with the occurrence of shear-out failure in the 2nd column (member identified in Figure 10.1) base bolts. This was followed by a gradual load increase until the maximum load was reached, for a top displacement of 274 mm (22.4 kN), when failure of the web-flange junction of the top beam occurred (*cf.* Figure 10.8a). Afterwards, the load maintained an almost constant plateau, up to a top displacement of 315 mm (21.9 kN), after which the frame lost its structural integrity due to the transverse compressive failure of the 1st column (member identified in Figure 10.1), at the vicinity of the test setup's horizontal restraint (*cf.* Figure 10.8b). It should be noted that the stainless cleats presented substantial plastic deformations during this test (as can be observed in Figure 10.8a).

Table 10.2 - Frame tests: summary of monotonic test results.

Series	K (kN/m)	δ_{EP} (mm)	F_{EP} (kN)	F_u (kN)
F-R	158.5	16.9	2.9	22.4
F-IC	128.7	11.9	1.8	15.6
BF-R	365.5	10.9	3.8	33.4
WF-R	3060.6	2.6	7.4	29.1

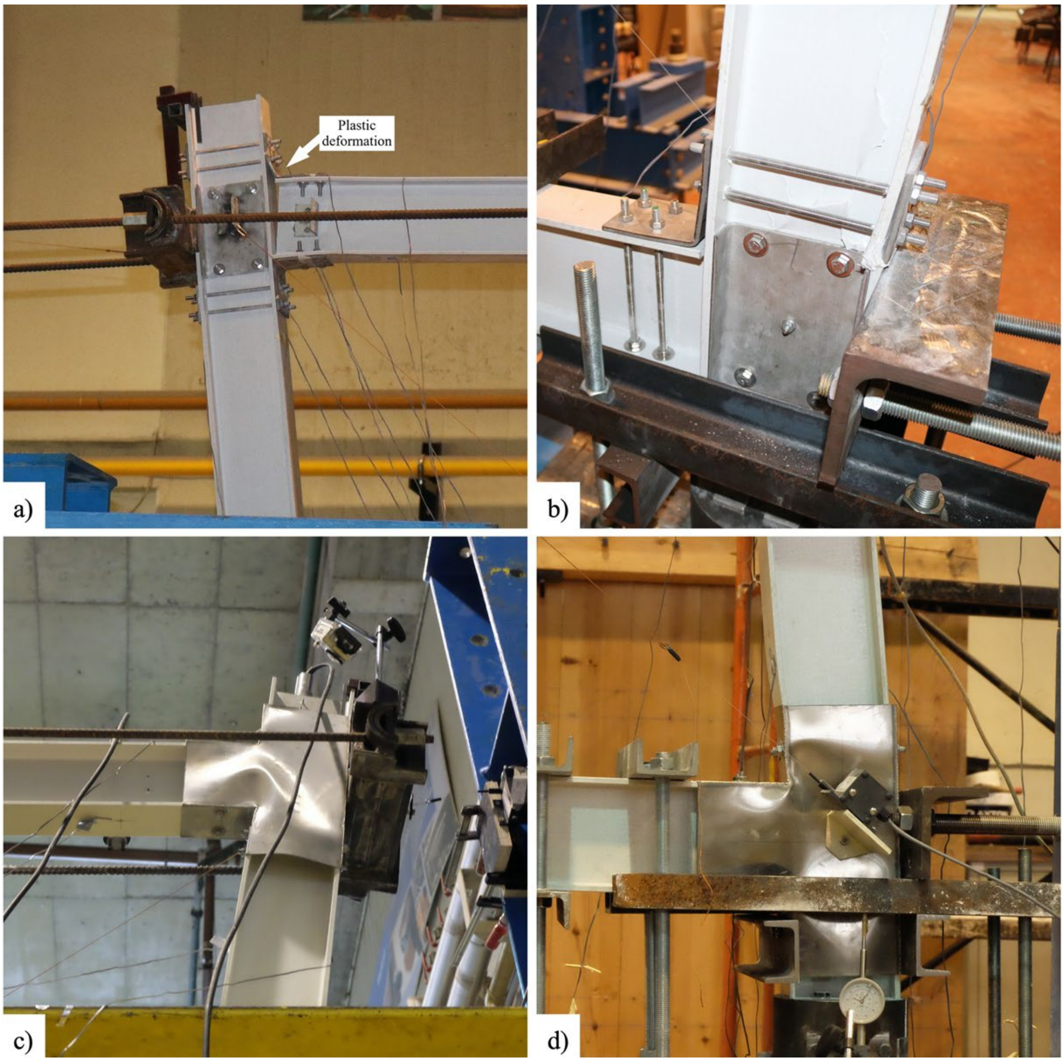

Figure 10.8 - Frame tests: failure modes in monotonic tests - a) tensile failure of top beam's web-flange junction (F-R); b) compressive failure of 1st column's web (F-R); c) cuff walls' bucking (F-IC); d) compressive failure of 2nd column's web (F-IC).

Series F-IC presented an initial linear behaviour (until δ_{EP}, 12 mm), followed by a gradual stiffness loss until reaching a stage with constant stiffness, 54% lower than the initial one (Figure 10.7). The cuff connection part presented buckling of the lateral walls, starting at a top displacement of 35 mm (3.5 kN; *cf*. Figure 10.8c). The first load drop occurred for a top displacement of 198 mm (15.3 kN) due to the compressive failure of the 2nd column's web, visible at the cuff's edge, owing to the bearing load transmitted to the bottom beam (*cf*. Figure 10.8d). The specimen was able to recover from this load reduction – the load remained at a relatively constant level until the jack stroke was attained, albeit registering a similar failure mode at the opposite column (*cf*. Figure 10.9a). It should be mentioned that GFRP cracking noises were heard throughout the test, most likely caused by the bearing contacts between the beam and the column profiles; after disassembly, no damage was visible at the connections.

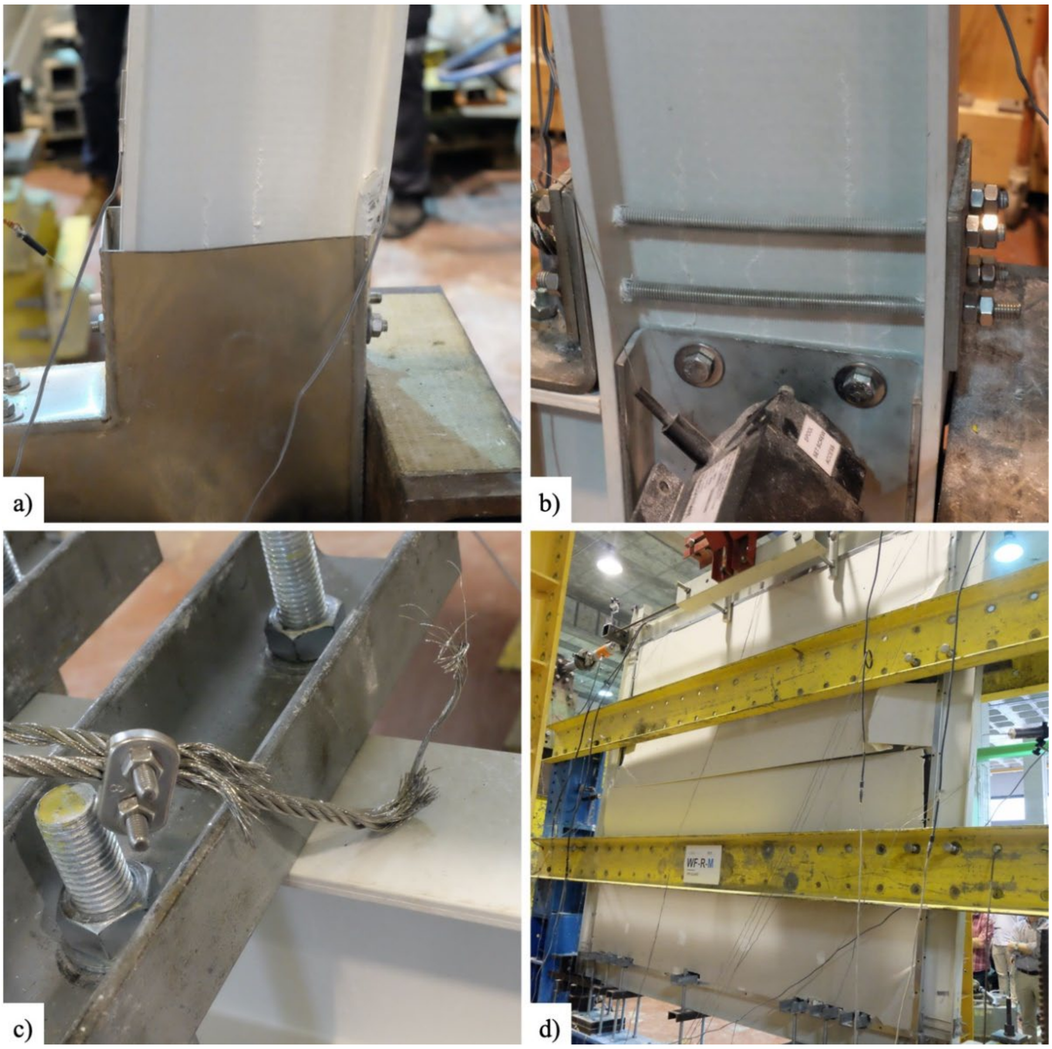

Figure 10.9 - Frame tests: failure modes in monotonic tests - a) compressive failure of 1st column's web (F-IC); b) compressive failure of 2st column's web (BF-R); c) failure of tensioned stainless steel cable (BF-R); d) failure of wall-to-frame joints (WF-R).

Regarding the braced frame, series BF-R, it also presented an initial bi-linear behaviour: (i) a first linear stage until a top displacement of 11 mm (3.5 kN); (ii) a transitional stage with gradual stiffness reduction; and (iii) a second linear stage with 55% of the initial stiffness. Two major load drops were observed in the test of series BC-R. The first load drop occurred for a top displacement of 90 mm (20.2 kN), associated with the occurrence of transverse compressive failure at the 2nd column, due to the load transmitted by the bottom beam (*cf.* Figure 10.9b). Afterwards, the specimen was able to fully recover the load, yet presenting slightly lower stiffness. The second load drop occurred after the maximum load was attained (33.4 kN, for a top displacement of 187 mm), due to failure of the tensioned stainless steel cable, near the clamps (*cf.* Figure 10.9c). Afterwards, the specimen was still able to retain a significant load capacity, slightly higher than that of series F-R – and exhibited qualitatively similar behaviour to that series (Figure 10.7).

Finally, series WF-R presented an initial linear stage (until δ_{EP}, 3 mm), which was followed by a gradual stiffness reduction associated with damage development in the wall and in the wall-to-frame joints. The out-of-plane displacements of the plasterboards were evident from a top displacement of 40 mm (25.2 kN); one side of the wall began to detach from the frame for a top displacement of 50 mm, being fully disconnected at 80 mm (21.4 kN; *cf.* Figure 10.9d). After that point, the load slowly increased until the end of the test, but the specimen presented much lower stiffness. At a top displacement of 160 mm (26.3 kN), transverse compressive failure of the 2nd column was observed, due to the load transmitted by the bottom beam; the test was ended at a top displacement of 204 mm (28.7 kN), when large portions of plasterboard began to fall (to prevent damaging the instrumentation).

Figure 10.10 present the bending moment *vs*. relative rotation curves of the 2nd column's top beam-to-column connection (*cf.* Figure 10.1) for series F-R and F-IC. These figures also include the curves obtained in previous monotonic beam-to-column connection tests using the same connection systems (*cf.* Chapters 6 and 8). Qualitatively, connections BC-6-F2-R and BC-IC-360×1.0 presented similar overall behaviour in the frame tests and in the isolated beam-to-column tests, although exhibiting lower stiffness in the frame tests. The lower connection stiffness registered in the frame tests can be attributed to the (very different) test setups and load conditions, namely the fact that: (i) in the isolated beam-to-column tests, the column was fixed on both ends, while in the frame tests the top edge of the column was free; on the other hand, (ii) in the frame tests, the considerable axial compressive load of the top beam was transmitted by (and to) the columns - this load was not present in the isolated beam-to-column tests.

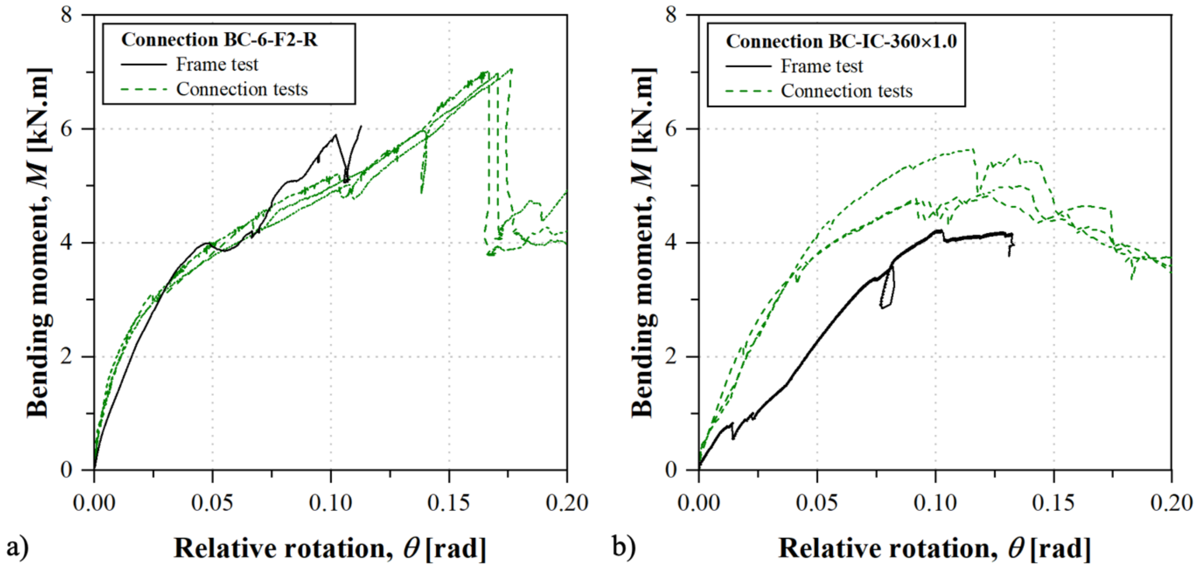

Figure 10.10 - Frame tests: beam-to-column bending moment *vs.* relative rotation curve obtained in monotonic test of a) series F-R and b) series F-IC.

10.2.3. Cyclic tests

Figure 10.11 present the cyclic load *vs*. top displacement curves of each series, together with the corresponding monotonic curves. All series presented a quasi-symmetric cyclic behaviour, with an envelope very close to the monotonic curves, and pronounced pinching (curves mostly concentrated in Quadrants I and III). The main damage modes observed in the cyclic tests were: (i) for series F-R, web-crippling failure at both columns and tensile rupture of the web-flange junction at the top beam near the top connections (*cf*. Figure 10.12a), with both failure modes occurring during the cycles with maximum absolute top displacement of 102 mm; (ii) for series F-IC, buckling of the cuff walls (similar to Figure 10.8c), during the cycles with maximum absolute top displacement of 50 mm; (iii) for series BF-R, failure of both stainless steel cables during the cycles with maximum absolute top displacement of 170 mm (similar to Figure 10.9c); and, finally, (iv) for series WF-R, damage of the plasterboards corners in contact with the frame connections (*cf.* Figure 10.12b) during the cycles with maximum absolute top displacements of 50 mm, which then progressed throughout the test.

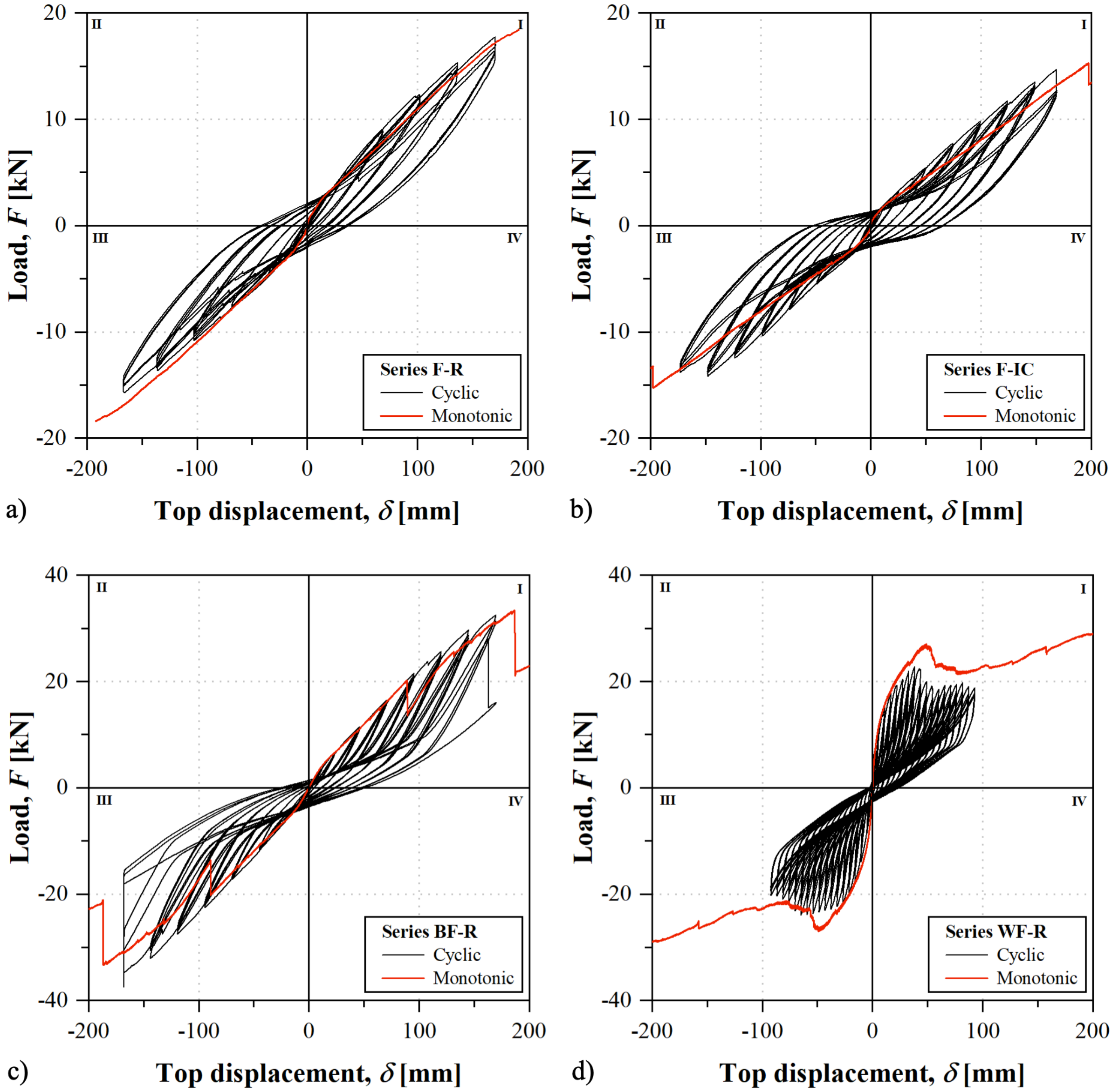

Figure 10.11 - Frame tests: cyclic load *vs.* top displacement curves of a) series F-R, b) series F-IC, c) series BF-R and d) series WF-R.

Figure 10.13 present the evolution of the ECCS [10.9] parameters (*cf.* Section 10.2.1.3) for all series, namely the stiffness, strength and dissipated energy ratios. In all cases, all parameters presented a similar trend within each group of cycles with the same maximum absolute top displacements (*i.e.* cycles 5, 6 and 7): as a consequence of the damage that occurred in the 1st cycle of a given group, the stiffness, strength and dissipated energy ratios decreased in the 2nd and 3rd cycles of the same group. Regarding the evolution of the stiffness ratio (ξ, *cf.* Figure 10.13a), series F-IC presented higher values of stiffness ratio than its counterparts, justified by the slightly higher stiffness registered in the cyclic test in comparison to that of the monotonic test, while series WF-R presented the worst performance, explained by the degradation of the wall panels and their connections during the cyclic test. Series F-R and BF-R presented similar evolutions of the stiffness ratio, especially in the positive branch of the curves. The strength ratio (ε, *cf.* Figure 10.13b) of all frames presented a very similar evolution, except for series WF-R, which registered much lower values than the other series; again, since the infill walls were responsible for a large part of its higher strength, their contribution was very limited after the occurrence of panel and panel-to-frame connection damage. Finally, regarding the dissipated energy ratio (η, *cf.* Figure 10.13c), as expected, series F-IC and WF-R presented the best and the worst performances, respectively. This is due to the fact that the dissipated energy ratio is correlated to the stiffness and strength at each cycle.

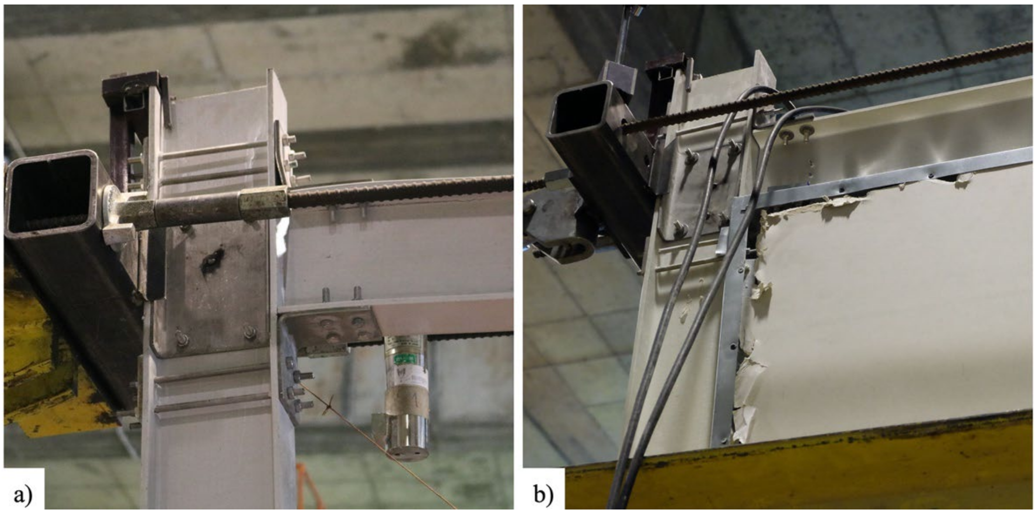

Figure 10.12 - Frame tests: failure modes observed in cyclic tests - a) web-crippling and web-flange junction damage near top connections (F-R); b) damage of plasterboards near edges (WF-R).

10.2.4. Discussion

The type of beam-to-column connections had considerable influence in the monotonic response of the frames (*cf.* Section 10.2.2), namely in the stiffness and overall shape of the load *vs*. top displacement curves (*cf.* Figure 10.7). The initial stiffness of the series with reinforced cleated connections (series F-R) was 23% higher compared to series F-IC, difference that increased to 64% after both crossed the EP top displacement. These results are in line with the relative mechanical properties of these connection systems, assessed in the beam-to-column connection tests (*cf.* Chapters 6 and 8), as the cuffed connection BC-IC-360×1.0 registered lower stiffness than the cleated connection BC-6-F2-R. Finally, owing to the high flexibility of the columns, the frames were able to withstand considerable drift before the connections attained their full capacity, presenting limited damage (particularly in the monotonic frame tests of series F-IC). Therefore, it was not possible to fully evaluate the influence of the connection system on the load capacity of the frames. Nevertheless, it is worth noting that the stainless steel parts of connection systems BC-6-F2-R and BC-IC-360×1.0 still presented considerable plastic deformations during the frame tests.

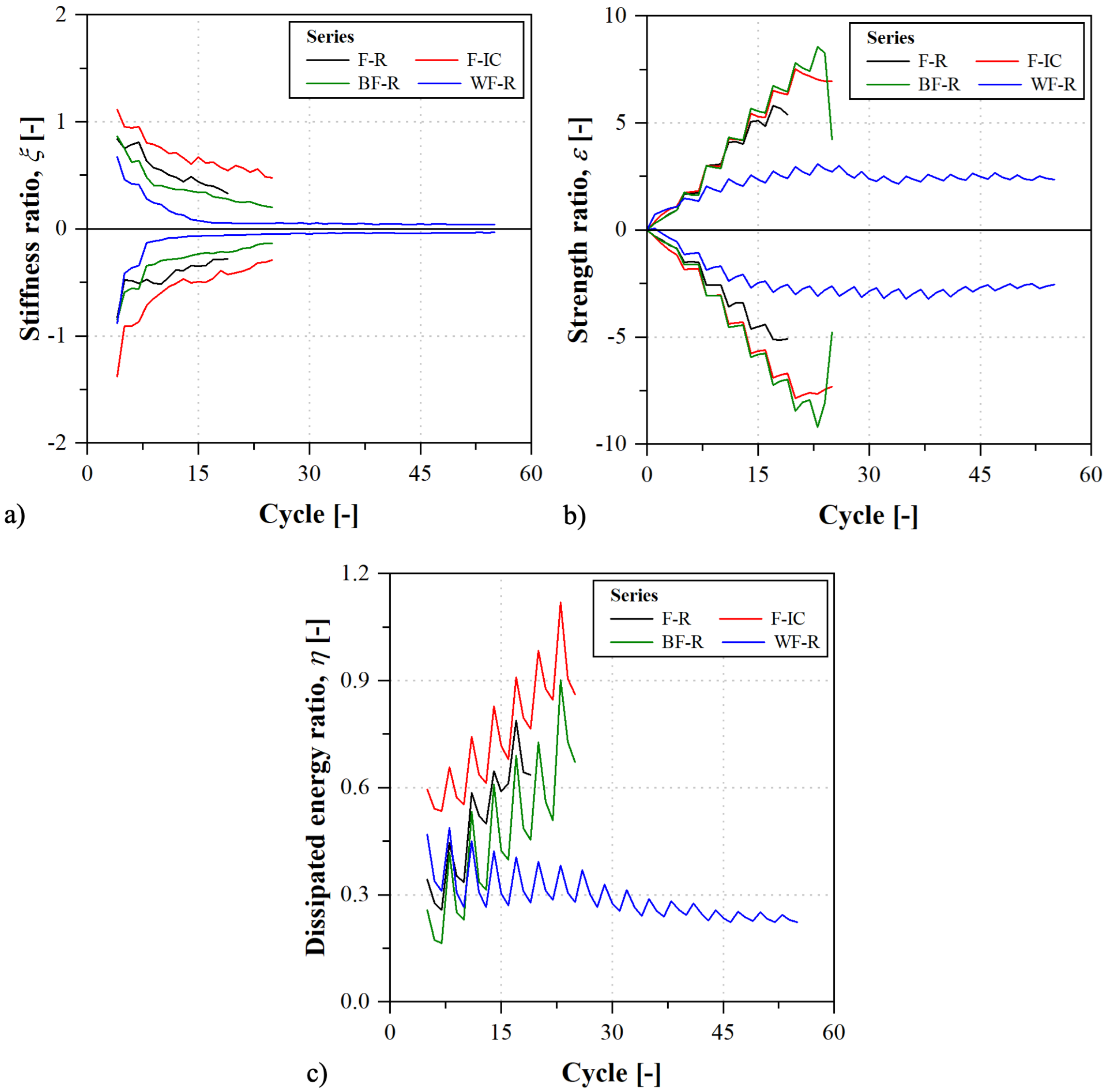

Figure 10.13 - Frame tests: hysteretic parameters - a) stiffness ratio (ξ); b) strength ratio (ε); c) dissipated energy ratio (η).

The hysteretic response of the frames was not significantly influenced by the type of connections used to join the profiles, as described in Section 10.2.3. Series F-R and F-IC presented similar amounts of dissipated energy owing to the pronounced pinching that was registered. In fact, due to the high flexibility of the GFRP profiles, in particular of the columns, the hysteretic behaviour of these frames was mostly elastic regardless of the beam-to-column connections used. These results show that while it is important to guarantee that the joints present high rotational capacity and ability to dissipate energy – which needs to be provided by a ductile behaviour in these connections – in order to increase the frames' capacity to dissipate energy, it is necessary to use complementary systems, such as material adapted bracings and dampers – this is further analysed in Section 10.3.3.

Finally, the bracing system and the plasterboard drywall used in series BF-R and WF-R, respectively, had considerable influence in the overall response of the frames. In the monotonic tests, the frame with higher stiffness was the one with infill walls (WF-R, 1831% compared to series F-R), while the series that registered higher strength was the braced one (BF-R, 49% compared to series F-R). Regarding the hysteretic behaviour, series WF-R presented the highest capacity to dissipate energy up to ~70 mm of top displacements. However, this result stemmed mostly from its higher stiffness and strength, as the frame presented considerable pinching, which was reflected in the poor performance regarding the dissipated energy ratio (*cf.* Figure 10.13c), and in the ensuing stiffness and strength ratios (Figures 10.13a and 10.13b). Therefore, this particular plasterboard wall system should not be accounted for in the design of the GFRP frames, especially regarding cyclic loading conditions, such as seismic actions, as it is prone to lose its connection to the frame.

Conversely, while series BF-R was able to dissipate considerably more energy than its unbraced counterparts, this was also due to its higher initial stiffness and strength, as it presented a lower performance regarding the dissipated energy ratio. In fact, these results show that the bracing system tested in this series may present a good monotonic performance, but is not particularly well suited for cyclic loads. In fact, as the top displacement increases, a large part of the deformations of the bracing system (in the eyebolts, the turnbuckles, clamps and the cables themselves) become permanent; thereafter, in the next cycles, the bracings are not active until those permanent deformations are exceeded. An example of an alternative bracing system with better hysteretic performance is presented in the following numerical study.

10.3. NUMERICAL STUDY

The main objective of the numerical study was to develop FE models that can simulate the non-linear behaviour of GFRP frames under lateral loads. The models were developed using commercial software currently used by civil engineering practitioners (*SAP2000* [10.10]) and they are intended to be simple enough to be easily replicated in the design of pultruded GFRP frame structures, namely for seismic loading conditions. Additionally, the validated numerical models were used to evaluate the hysteretic response of the same frame comprising a bracing system composed by GFRP profiles and a steel hysteretic damper.

The numerical simulations presented herein focus on series F-R due to the following reasons: (i) as discussed in Section 10.2.4, the behaviour of the infill walls should not be considered in the structural design, and the experimental results showed that the bracing system used is not particularly well-suited for seismic loading; (ii) series F-R presented the best monotonic and cyclic performance among the unbraced series without infill walls; (iii) similarly, the connection system used in series F-R also presented the best performance in the isolated beam-to-column tests (*cf*. Chapters 6 and 8).

In this context, this section presents (i) the calibration of the hysteretic parameters of connection BC-6-F2-R, followed by (ii) the model of the F-R frame (as tested and with pinned and rigid connections), and by (iii) the model of the F-R frame with the inclusion of GFRP bracings and the referred steel damper.

10.3.1. Finite element model of BC-6-F2-R beam-to-column connection

Figure 10.14 presents an overview of the FE model of the BC-6-F2-R beam-to-column connection. In this model, the beam (with length of 875 mm) and the column (with length of 900 mm) were modelled using one-dimensional frame elements, based on Bathe and Wilson formulation [10.10], and were joined by a *link* element. The GFRP material of the profiles was defined as an orthotropic linear-elastic material - the properties were previously obtained by coupon testing and are summarized in Table 10.1.

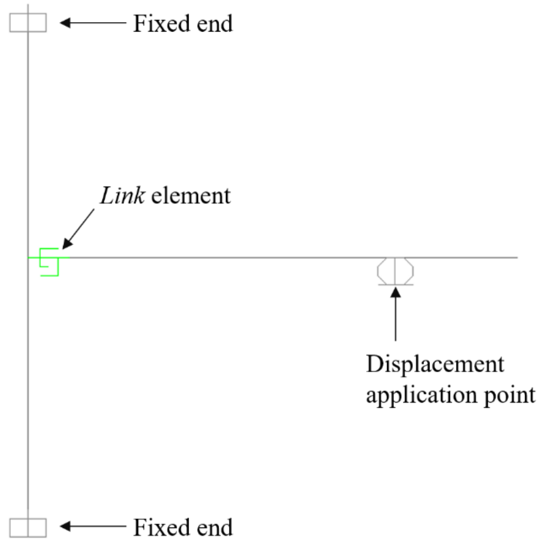

Figure 10.14 - Numerical models: FE model of BC-6-F2-R beam-to-column connection.

The beam was joined at mid-span of the column using a non-linear 2-joint *link* element (*MultiLinear Plastic*). In this element, all deformations were defined as fixed with exception of the rotation around the out-of-plane axis, for which the hysteretic response of the joint was simulated using the Pivot hysteresis model, developed by Dowel *et al*. [10.11] for reinforced-concrete members. This type of element was already used in previous chapters of the present thesis, presenting satisfactory results in the simulation of sleeve beam-to-column connections (*cf*. Chapter 5) and GFRP frames with sleeve beam-to-column connections (*cf*. Chapter 9). The definition of the *link* element using the Pivot hysteresis multilinear model requires the input of the experimental monotonic curve of the beam-to-column connection obtained in Chapter 6 and of parameters α_1, α_2, β_1 and β_2. These parameters are used to characterize the slopes of the hysteretic curves after the load reversal; more information regarding the parameters used in the Pivot hysteresis model can be found in [10.11]. After calibration, the parameters α_1 and α_2 were set as 100 and the parameters β_1 and β_2 were defined as 0.7.

The column was fixed at both ends and the displacement was applied to the beam at a distance of 655 mm from the column mid-axis. The displacement applied in the FE model replicated the experimental displacement history described in Chapter 6, which was defined in accordance to the

ECCS protocol [10.9]. To avoid any dynamic effects, the mass of the elements was not considered in the model. An in-plane geometrically linear direct integration time-history analysis was performed.

Figure 10.15a presents the resulting numerical hysteretic load *vs*. displacement curve, as well as the corresponding experimental curve for comparison. The numerical model was able to replicate the hysteretic behaviour of the BC-6-F2-R connection system with very good accuracy. Although a simplified multilinear hysteresis model was used in the numerical analysis, the FE model hysteresis curves presented very similar trends to those measured experimentally, in particular regarding the response after each load reversal or after the advent of major damage (for absolute rotations above 0.1 rad). The accumulated dissipated energy measured in the numerical analysis was also evaluated and compared to the values obtained in the tests (*cf*. Figure 10.15b) - the accumulated dissipated energy predicted by the FE model agrees very well with that estimated from the experiments; although predictions slightly overestimate test results, both present a very similar trend.

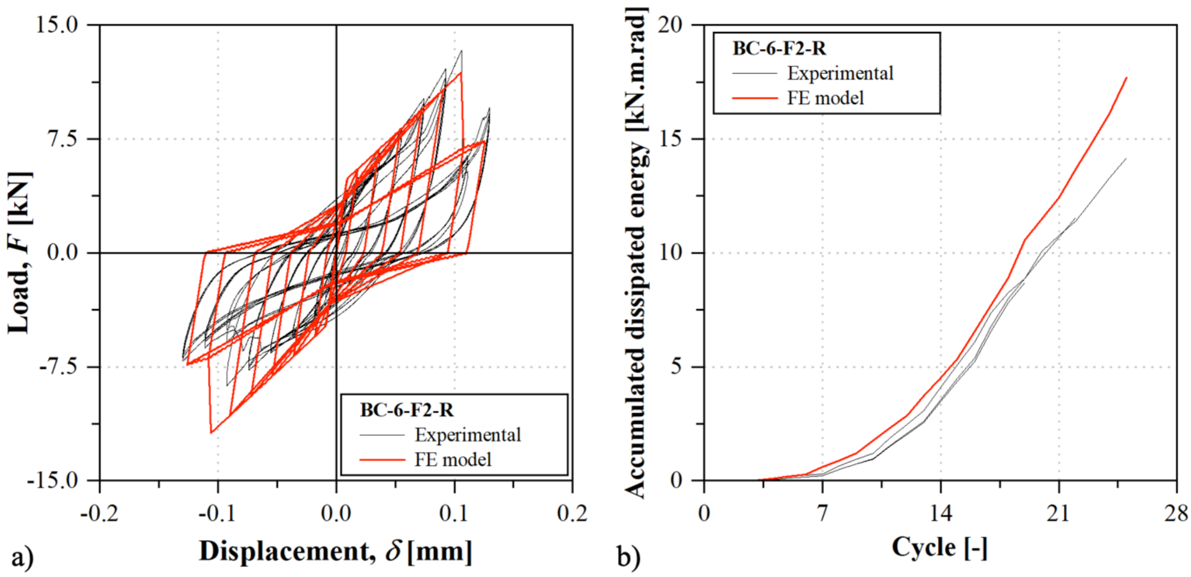

Figure 10.15 - Numerical models: FE model of BC-6-F2-R beam-to-column connection.

10.3.2. Finite element model of series F-R

The FE model of series F-R is depicted in Figure 10.16. The profiles and their joints were modelled using the same frame elements and 2-joint *links* used in the beam-to-column connection model. To simulate the experimental boundaries, the vertical displacements of the bottom beam were restricted in seven points. The horizontal displacement of the column was restrained at the intersection with the bottom beam (with a compression only support, simulating a bearing support). At the columns' base, both the horizontal and vertical displacements were restrained, and a linear joint spring for the rotations around the out-of-plane orthogonal axis (R3) was assigned at these points. The stiffness of these linear joint springs was calibrated to obtain the same initial stiffness registered in the experimental tests, resulting in a value of 100 kN.m/rad. The monotonic and cyclic top displacement history was imposed at the 2nd column, at the intersection with the top beam, and followed the experimental displacement history (*cf.* Section 10.2). In-plane geometrically linear time-history analyses were performed, and no mass was considered in the model elements to avoid dynamic effects.

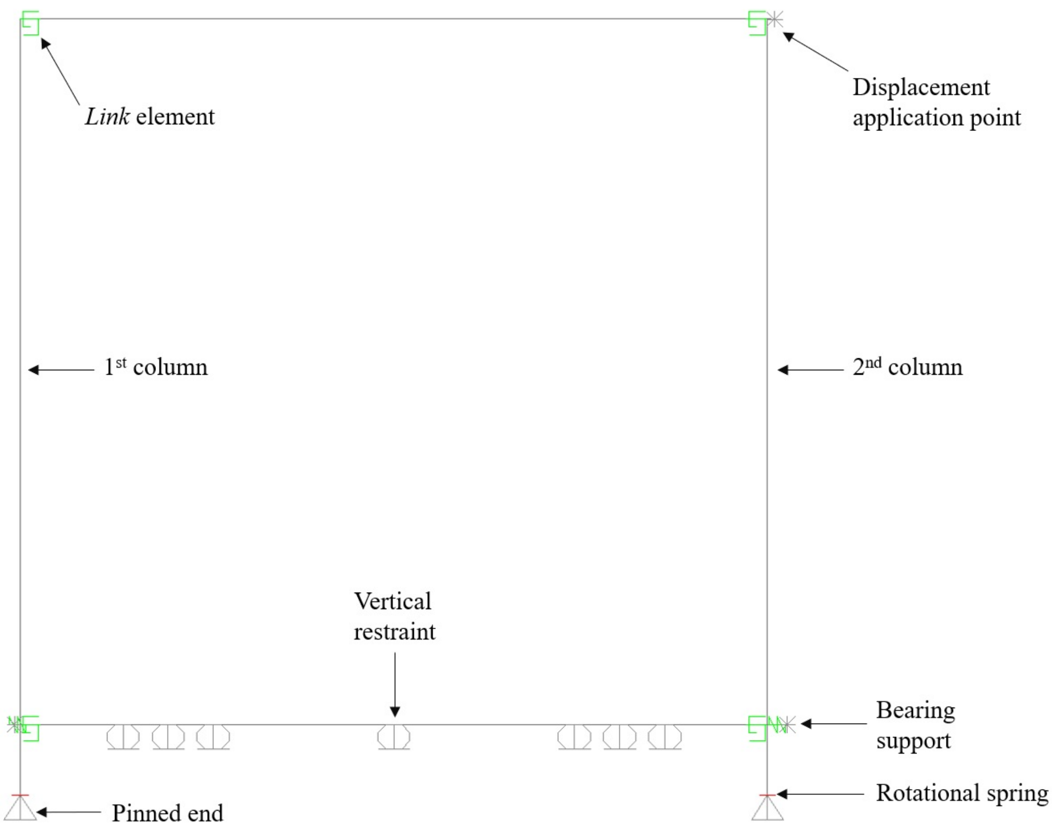

Figure 10.16 - Numerical models: FE model of F-R frame.

For comparison purposes, two frames using pinned and rigid beam-to-column connections were also analysed under monotonic loading conditions.

The numerical load *vs*. top displacement curves for the monotonic and cyclic analyses are presented in Figures 10.17a and 10.17b, respectively, which also include the experimental curves. Figure 10.17a also presents the curves corresponding to the numerical frames using pinned (F-pinned) and rigid (F-rigid) beam-to-column connections, as references. The FE model was able to predict the experimental behaviour of series F-R with good accuracy, up to a top displacement of ~190 mm. In particular, the model presented very similar initial stiffness compared to the experimental frame (-11%) and exhibited a similar bilinear behaviour. However, as the FE model did not account for the damage in the GFRP profiles, it was not able to simulate the occurrence of damage outside the beam-to-column connection. In this regard, as a consequence, the FE model did not capture the stiffness and load reductions observed in the monotonic tests after a top displacement of 194 mm, where GFRP failure develops at the column, which corresponds to a drift of 8%. However, it should be mentioned that this value of drift is above what is often considered in the design of structures. For example, the Eurocode 8 [10.12] provides limits to the interstorey drift for a seismic action with larger probability of occurrence than the seismic action (under the "damage limitation requirement") of 0.5-1.0% (12.5-25 mm, on this frame). Additionally, the same standard presents the interstorey drift sensitivity coefficient (θ, on Eq. 4.28 of [10.12]), used to quantify the second-order effects: (i) if $\theta \leq 0.1$, second-order effects need not to be accounted in the design, and (ii) θ should not exceed 0.3. The first limit of θ is often applied by civil engineering practitioners in the seismic design of structures; it corresponds to a maximum top displacement of 160 mm (drift of 6.4%) for the present frame when considering a Type 2 earthquake occurring in Lisbon and a type C ground[2].

On the other hand, in the cyclic analysis, the FE model presented narrower hysteretic curves that led to conservative predictions of energy dissipation, as displayed in Figure 10.17c, which compares numerical and experimental accumulated dissipated energy. These relative differences should also be attributed to the fact that the FE model does not account for the damage underwent by the GFRP material that is not covered by the constitutive relationship of the beam-to-column connection.

[2] For this frame, Lisbon, type II earthquake and type C ground: a_g=1.7 m/s^2; S=1.5; q=1; $S_{d,max} = a_g . S . \frac{2.5}{q}$.

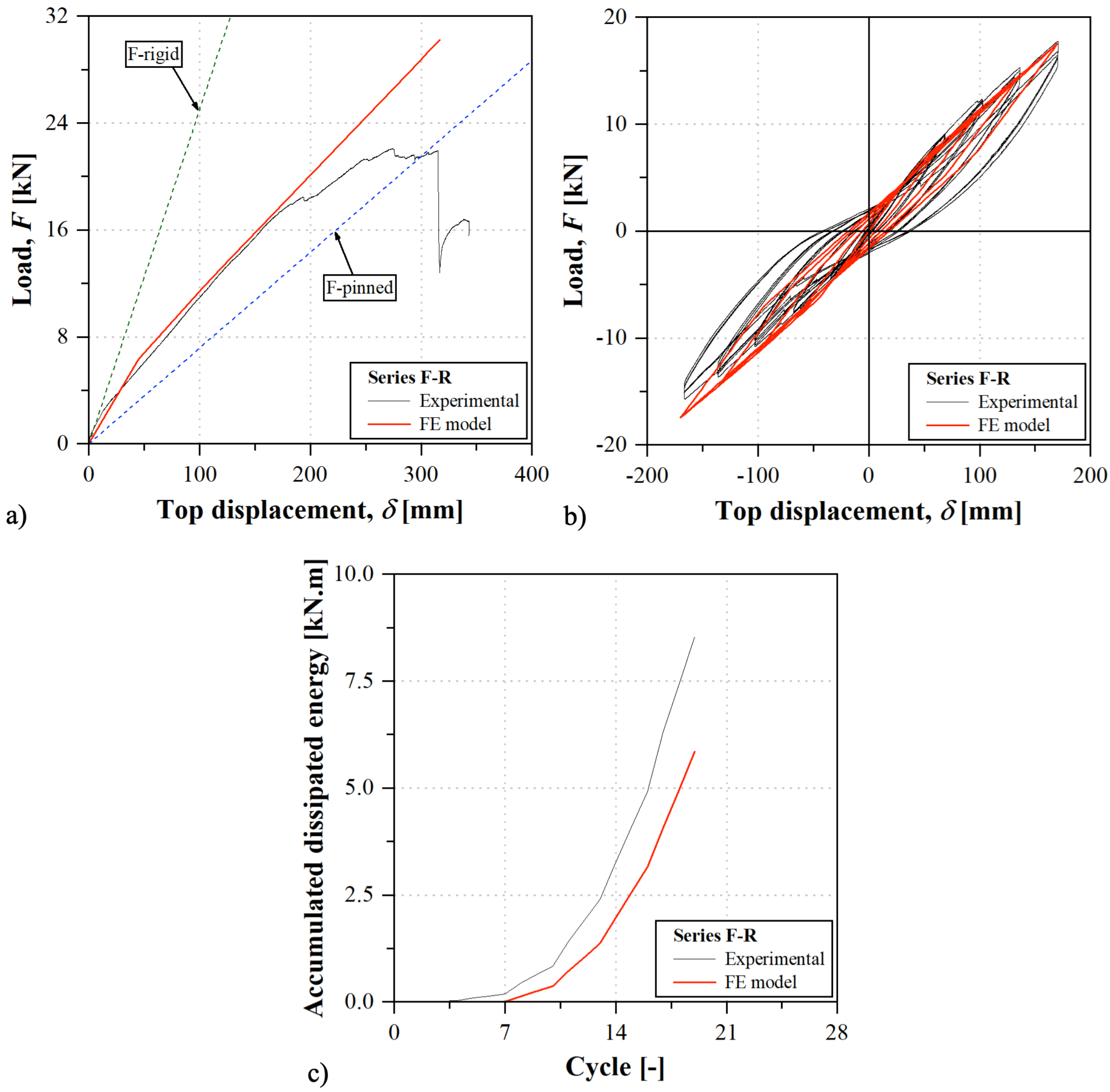

Figure 10.17 - Numerical models: a) monotonic load *vs.* top displacement curve of F-R frame - FE model *vs.* experimental results; b) cyclic load *vs.* top displacement curve of F-R frame - FE model *vs.* experimental results; c) accumulated dissipated energy of F-R frame - FE model *vs.* experimental results.

Finally, the monotonic response of the F-R numerical frame was compared to the response of a similar frame with pinned and rigid connections. Series F-R presented 96% higher initial stiffness compared to the F-pinned frame, confirming the benefits of considering the semi-rigid behaviour of the connections in the design of GFRP structures subjected to lateral loads. On the other hand, with rigid beam-to-column connections, the monotonic stiffness increased 44% compared to the tested frame. These relative differences highlight the importance of correctly considering the semi-rigid characteristics of the beam-to-column connections to properly simulate the behaviour of GFRP frames.

Overall, the numerical models showed reasonable agreement with the experimental results, confirming that they can be a useful tool in the design of GFRP frame structures, provided that their limits of validity are known - in this case, ~8% of inter-storey drift.

10.3.3. Finite element model of series F-R with bracing system and damper element

This section presents a study concerning the influence of including a bracing system comprising a damper element to the F-R frame. This device, named ADAS (Added Damping And Stiffness), is an assemblage of steel plates with the geometry detailed in Figure 10.18. The ADAS device was object of various studies [10.13,10.14], presenting several benefits: (i) constraining the dissipation of energy to locations designed for that purpose; (ii) increasing the energy dissipation capacity during earthquakes; (iii) reducing the energy dissipation demands on other structural members, and (iv) being easily replaceable after moderate or severe earthquakes.

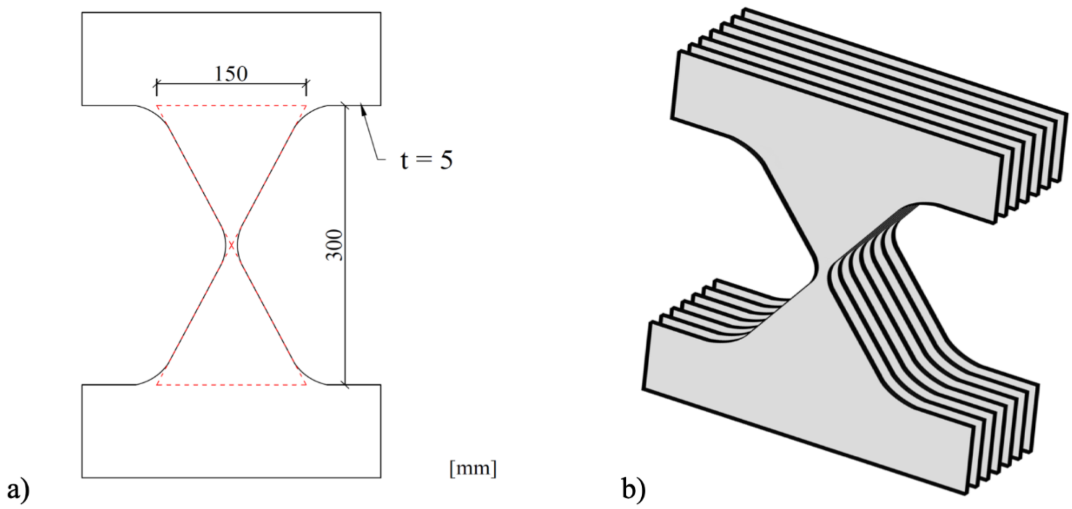

Figure 10.18 - Numerical models: a) geometry of the ADAS plate; b) assembly of 7 ADAS plates.

In this study, two pultruded GFRP bracing members, modelled using frame elements, and a new link element, used to model the ADAS device (comprising seven plates of grade S275 steel), were added to the previously developed and validated FE model of series F-R (as illustrated in Figure 18). The profiles used for the bracings had tubular square cross section of 50×50×5 mm, as found in Fiberline catalogue [10.15]. These members were modelled with pinned connections at both ends and considering a longitudinal modulus of elasticity of 23 GPa, the minimum value specified by the profiles' producer [10.15]. The bracing profiles were chosen to meet the requirement of not failing for both tension and compressive loads lower than those present at the instant of yielding of the ADAS device; the design verifications for both maximum tension and compressive loads[3] of the bracing profiles were performed in accordance to Eq. 4.1 and 4.5 of the CNR Italian standard [10.16].

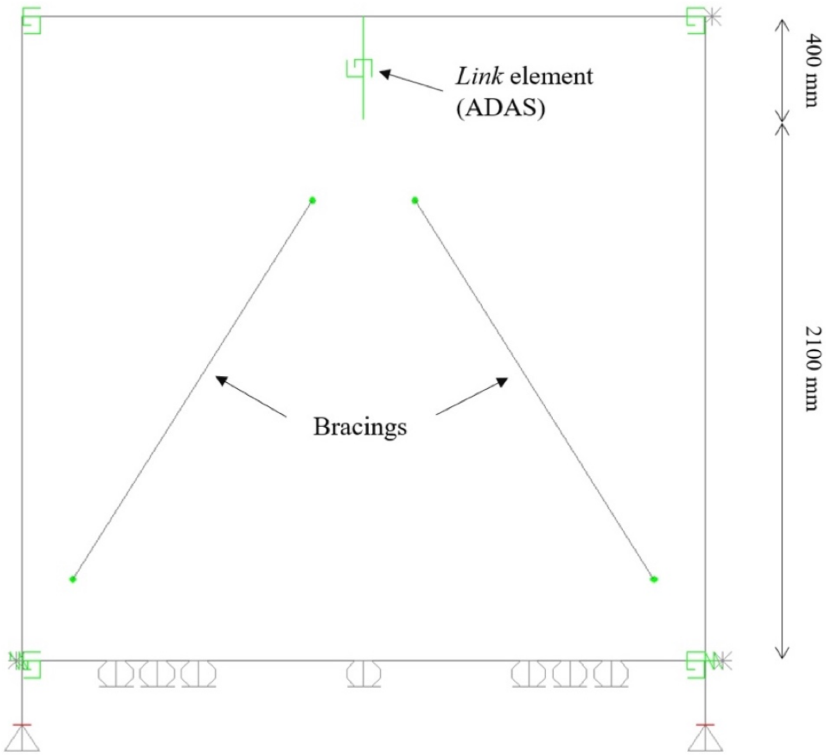

Figure 10.19 - Numerical models: FE model of F-R frame with bracings and ADAS element.

The ADAS device was modelled using a 2-joint link element with all deformations fixed with exception of the shear deformation along the frame's plane. In that direction, the hysteretic response of the device was defined using the kinematic hysteretic model [10.10], which requires the input of the envelop curve, presented in Figure 10.20a and defined in Appendix G. The top displacement history imposed in this FE model was the same as the one of the F-R model, allowing the comparison of the dissipated energy in cycles with the same displacement amplitude of those applied in the experimental test.

[3] Considering $\sigma_{tu,L} = \sigma_{cu,L}$=35 MPa.

Figure 10.20a presents the shear displacement *vs*. load curve of the ADAS device during the cyclic displacement history, which registered an overall shape similar to that reported in previous works concerning this device (albeit for different geometries [10.13]).

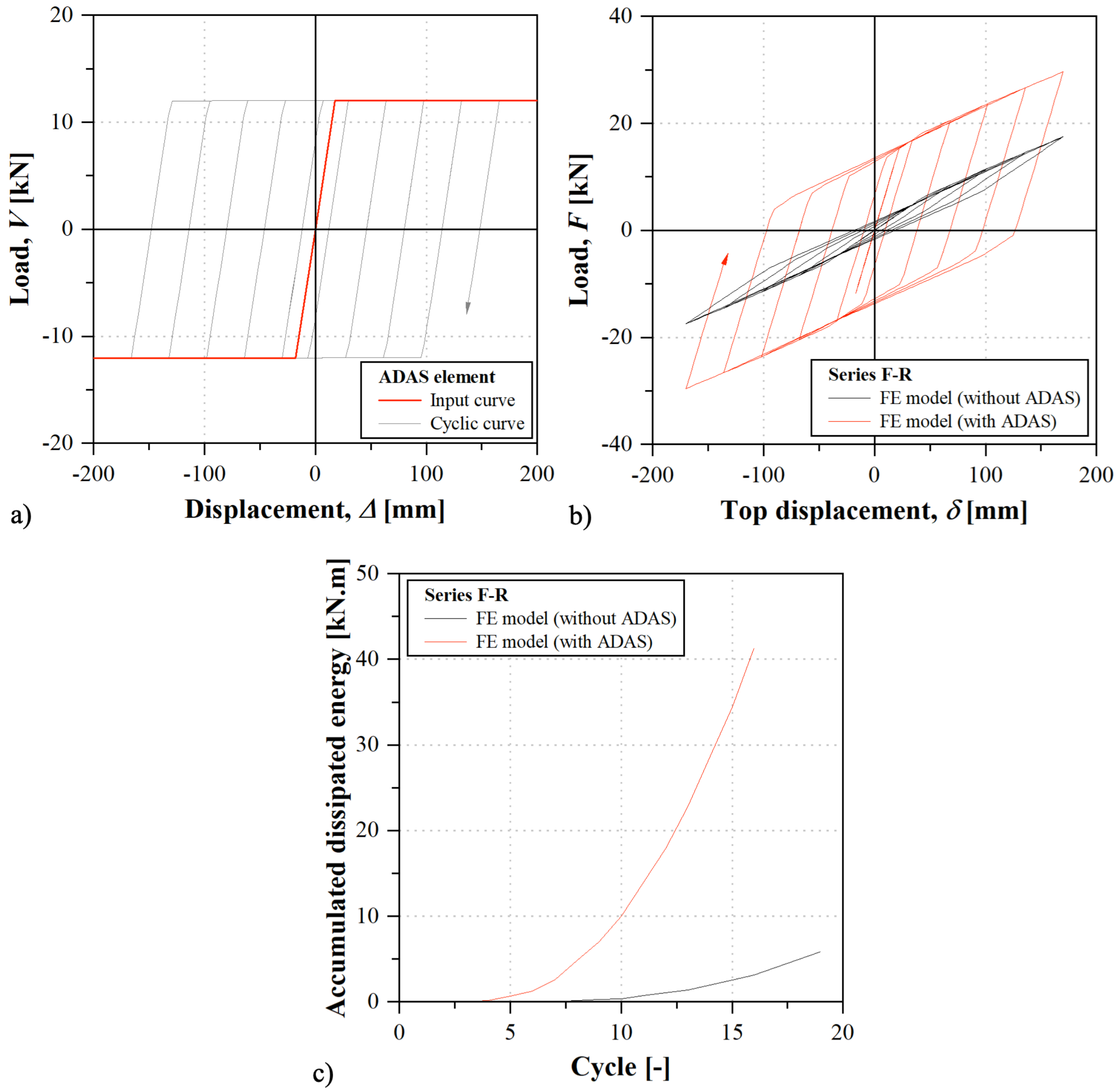

Figure 10.20 - Numerical models: FE model of F-R frame with bracings and ADAS element.

Figure 10.20b presents the numerical frame's top displacement *vs*. load; the numerical F-R curves were also added for comparison. The results show that the use of these GFRP bracings in combination with the ADAS device allows for significant increase of the frame's stiffness, strength and capacity to dissipate energy. By ensuring that the yield load of the ADAS device is (slightly) lower than the compressive resistance of the bracing profiles, it was possible to increase the overall stiffness of the frame, while controlling (and maintaining) its load carrying capacity through the yielding of the ADAS device. This resulted in the absence of pinching in the frame's hysteretic response (*cf*. Figure 10.20b), considerably increasing the dissipated energy (as shown in Figure 10.20c). These results show that this type of solution has potential to greatly improve the hysteretic behaviour of pultruded frames under seismic actions. Finally, it should be noted that, although not covered in the present work, it is essential to design appropriate connections for both the bracing members and the ADAS device in order to guarantee the efficiency of this system.

10.4. CONCLUSIONS

This chapter presented experimental and numerical investigations about the behaviour of 2-dimentional full-scale GFRP frames under lateral loading. Four different series were tested, two of them assessing different beam-to-column connection systems, and the remaining two investigating the influence of either a stainless steel cables bracing system or plasterboard infill walls. The monotonic and cyclic tests performed in all series allow drawing the following conclusions:

- Regarding the monotonic behaviour, series with infill walls and bracing system presented the highest stiffness and strength, respectively. For the remaining series, the connection type had significant influence on the frame response, with the series with cleated connections presenting the best behaviour.
- The cyclic tests showed that all series present significant pinching, hindering their ability to dissipate energy. The series without infill wall or bracings presented similar hysteretic behaviour, with the connection type having lower influence than in the monotonic tests, owing to the GFRP profiles flexibility.
- The frame with infill walls presented an apparent higher capacity to dissipate energy. However, this was due to the high stiffness of the plasterboard panels, which should not be considered in design, as these elements may be detached during a cyclic event, such as seismic actions, and would not further contribute to the frames' response.

- Regarding the frame with bracings, although it was able to dissipate considerably more energy than its unbraced counterparts, this was also due to its higher stiffness and strength. In fact, during the cyclic tests it was clear that the bracing system suffered large permanent deformations and, in the following cycles, it could not contribute to the frame's response until those permanent deformations were surpassed. Thereafter, this bracing system is not adequate for seismic areas.

In the numerical study, a relatively simple (and commercial) FE model was used to simulate the behaviour of the best performing frame series, the one with cleated connections. This FE model comprised frame elements, materializing the profiles, and link elements including the Pivot hysteresis model, to simulate the non-linear hysteretic behaviour of the beam-to-column connections. A good agreement was obtained between numerical predictions and experimental results, confirming that these models are a useful tool for the seismic design of GFRP frames. The validated FE model was then used to assess the hysteretic performance of the pultruded frame with the addition of a bracing system composed by GFRP profiles and a steel plate damper (ADAS device). The results show that this bracing system allowed for significant improvements of the cyclic response of the frame, reducing the pinching and, consequently, increasing the dissipated energy.

Overall, the results of this chapter show that the energy dissipation capacity of beam-to-column connections may not effectively translate directly into energy dissipation capacity at the structural level in GFRP frames, owing to the high flexibility of GFRP members, namely the columns. In this context, to improve the cyclic behaviour of GFRP structures under lateral loads, allowing their widespread use in seismic regions, future experimental and numerical research should focus on the development of material-adapted and tailored bracing systems able to dissipate energy, such as the solution presented in the numerical study included in the present work.

10.5. REFERENCES

[10.1] EN ISO 527-1. (1997). Determination of Tensile Properties – Part 1: General Principles. Brussels.

[10.2] ASTM D 6641/D 6641M-16e1. (2016). Standard Test Method for Compressive Properties of Polymer Matrix Composite Materials Using a Combined Loading Compression (CLC) Test Fixture. West Conshohocken.

[10.3] ASTM D 695-02. (2002). Standard Test Method for Compressive Properties of Rigid Plastics. West Conshohocken.

[10.4] ASTM D 2344/D 2344M-00. (2000). Standard Test Method for Short-Beam Strength of Polymer Matrix Composites Materials and their Laminates. West Conshohocken.

[10.5] ASTM D 5379/D 5379M. (2005). Standard Test Method for Shear Properties of Composites Materials by the V-Notched Beam Method. West Conshohocken.

[10.6] ASTM A240. (2020). Standard Specification for Heat-Resisting Chromium and Chromium-Nickel Stainless Steel Plate, Sheet, and Strip for Pressure Vessels. West Conshohocken.

[10.7] ISO 3506-1. (2020). Fasteners — Mechanical Properties of Corrosion-Resistant Stainless Steel Fasteners — Part 1: Bolts, Screws and Studs with Specified Grades and Property Classes. Geneve.

[10.8] EN 520 (2004). Gypsum Plasterboards – Definitions, Requirements and Test Methods. Brussels.

[10.9] ECCS (1996). Recommended Testing Procedures for Assessing the Behaviour of Structural Steel Elements under Cyclic Loads. Brussels.

[10.10] Computer and Structures, Inc. (2016). SAP2000 V18 – CSI Analysis Reference Manual. Berkeley.

[10.11] Dowell OK, Seible F, Wilson EL. (1998). *Pivot hysteresis model for reinforced concrete members*. ACI Structural Journal, 95, 607-617.

[10.12] EN1998-1 (2004). Design of Structures for Earthquake Resistance – Part 1: General Rules, Seismic Actions and Rules for Buildings. Brussels.

[10.13] Whittaker AS, Bertero VV, Thompson C. (1989). *Earthquake simulator testing of steel plate added damping and stiffness elements (Vol. 89, No. 2).* Earthquake Engineering Research Center, University of California, Berkeley.

[10.14] Xia C. (1990). *A Study of ADAS Element Parameters and their Influence on Earthquake Response of Building Structures*. PhD Thesis, University of Michigan, Michigan.

[10.15] Fiberline Composites web site: http://www.fiberline.com/, visited in March 2022.

[10.16] CNR-DT 205/2007 – Guide for the Design and Construction of Fiber-Reinforced Concrete Structures. Rome.

PART V

3-dimensional frames made of
pultruded GFRP profiles

Chapter 11

Seismic response of a 3-dimensional pultruded GFRP frame

11.1. INTRODUCTION

The number of studies conducted so far about the structural behaviour of pultruded GFRP frames, particularly of 3-dimensional structures, is very limited. The first experimental tests on 3-dimensional pultruded frames, performed by Mosallam [11.1], are referred in an ASCE manual [11.2]. In these tests, one and two storey reduced-scale frames were subject to ground motions aiming at assessing the effects of different connection systems on the dynamic response of the pultruded structures. However, it was not possible to obtain the original reference, presented in a conference.

Minghini *et al*. [11.3] developed a numerical study aiming at analysing how the stiffness of the beam-to-column connections and the profiles' shear deformations influenced the natural frequencies and mode shapes of a 3-dimensional frame. In this study, the authors showed that the consideration of pinned or rigid connections is not adequate to assess the modal properties of pultruded frames; the natural frequencies of the first three vibration modes of the frames with pinned and rigid connections were considerably lower and higher, respectively, than the frame with semi-rigid connections. Additionally, the authors compared the results of simulating the 3-dimensional frame with and without the consideration of shear deformations on the profile members and the results were fairly similar.

Boscato and Russo [11.4] performed numerical and experimental dynamic analysis of part of the temporary shelter structure to the church of S. Maria Paganica in L'Aquila; this structure was already presented in Chapter 2. In this work, the authors focused on two 3-dimensional frames that were interconnected. Firstly, the authors performed a numerical modal analysis considering the two frame structures coupled and with fixed connections between the pultruded profiles, which allowed to identify the first five natural frequencies and corresponding modal shapes. This was followed by experimental tests, in which the authors identified the natural frequencies and modal shapes for the two frames, but without considering them coupled. The authors verified that the two frames behaved independently, contrary to what was assumed in the preliminary numerical analysis. Finally, the authors developed a new finite element model that was calibrated to match the natural frequencies obtained experimentally; however, this calibration was performed by changing only the stiffness of the supports, while the connections between members was assumed to be rigid – this latter hypothesis was not supported by test data.

Nogueira [11.5] performed modal and seismic tests on a one-storey, one bay 3-dimensional frame composed by pultruded tubular profiles and sleeved connections, developed at IST in the scope of the ClickHouse project. The 3-dimensional frame comprised plane frames, similar to those analysed in Chapter 9 of this thesis. The author started by identifying the modal parameters of the frame with and without wall panels and vertical loads. Then, Nogueira [11.5] imposed a normative seismic action, defined in accordance with EN 1998 [11.6], through a uni-directional shaking table. It was concluded that the safety of the 3-dimensional frame was not governed by the considered earthquake. This work also included a numerical study, in which the finite element models developed retrieved similar modal parameters to the experimental ones. These models were then used in a parametric study to assess the influence of the rotational stiffness of the connections to the seismic response of the frame. It was verified that, for the limited range of rotational stiffnesses considered, the stiffness of the connections did not have considerable influence in the dynamic/seismic behaviour of that particular structure.

This chapter presents an experimental study concerning the dynamic and seismic behaviour of a full-scale 2-storey 3-dimensional frame comprising pultruded GFRP profiles. This study represents the final stage of this thesis, in which the main structural connections and members of the pultruded 3-dimensional frame, particularly the beam-to-column connections (*cf.* Chapters 6 and 7) and the individual plane frames (*cf.* Chapter 10), were already duly characterized. Firstly, the modal properties were experimentally assessed for different frame configurations: (i) without vertical loads and bracings; (ii) without vertical loads and with bracings; (iii) with vertical loads and without bracings; and (iv) with vertical loads and bracings. Then, the seismic response of the pultruded 3-dimensional frame with vertical loads and without bracings was investigated. For that purpose, a total of 18 displacement histories, simulating a design earthquake for mainland Portugal, was applied in the frame's base by means of a uni-directional shaking table – the structure was loaded in the major principal axis of the columns. These tests allowed to identify how the different seismic actions affected the structural behaviour of the frame and, specifically, to detect the ground acceleration value for which the structure lost its linear response.

11.2. 3-DIMENSIONAL PULTRUDED FRAME

11.2.1. Frame specimens

The 3-dimensional frame studied in the present work was built and fixed to a uni-directional shaking table (*cf.* Figure 11.1), comprising two stories and with the overall geometry illustrated in Figure 11.2. The pultruded frame was composed by pultruded GFRP I-section profiles (150×75×8 mm^2), presenting a total height of 4.7 m, with the storeys located at distances of 2.25 m and 5.0 m from the frame's base and the columns spaced by 2.5 m with respect to their mid axes. The beam members were joined to the column members by means of cleated connections: (i) in the longitudinal direction, parallel to the shaking table's operating direction (*cf.* Figure 11.2), the connections were materialized by a system characterized in previous chapters (*cf.* Chapters 6 and 7), composed by 6 mm thick stainless steel flange cleats and reinforcement back plates (*cf.* Figures 11.3a and 11.3b, connection series BC-6-F2-R described in Chapters 6 and 7); (ii) in the transverse direction, perpendicular to the shaking table's operating direction (*cf.* Figure 11.2), the connections were materialized by similar stainless steel cleats with the addition of filling GFRP plates to allow staggering the bolts in this direction with the rods on the perpendicular one (*cf*. Figure 11.3b). No gap was considered between the column and the beam members at the connection zones. The columns were fixed to the shaking table by means of bolted joints with steel cleats, which were then welded to steel plates, with the geometry depicted in Figure 11.3c. To prevent the columns' web-crippling damage in the joints with the beam members, the columns were reinforced by means two stainless steel channel profiles, with length of 150 mm and thickness of 4 mm, attached to the inner space between their flanges, as illustrated in Figure 11.3.

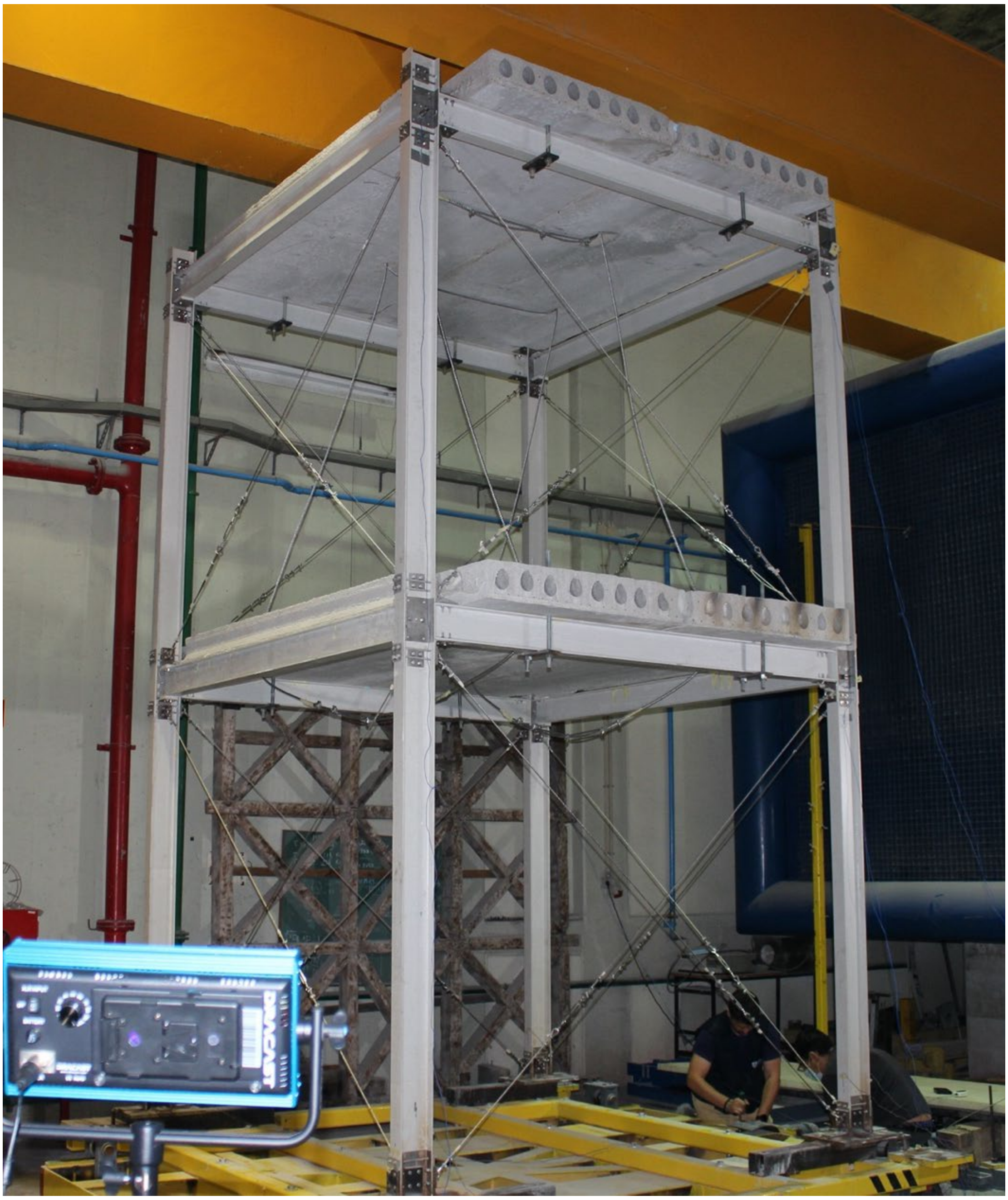

Figure 11.1 - Photograph of the 3-dimensional pultruded frame with slabs and bracings.

The vertical loads at the storey levels were simulated by fixing prefabricated reinforced concrete hollow slabs to the longitudinal beams. Two prefabricated slabs were used per storey, with 3000 mm of length, 1200 mm of width and 160 mm of thickness. These slabs had hollow cores and an average mass of ~990 kg, resulting in a uniformly distributed load of ~3.2 kN/m^2. This load corresponds approximately to the combination of actions for seismic design situations defined in EN 1990 [11.7] when considering (i) a floor made of composite sandwich panels with self-weight of 0.6 kN/m^2 (the weight of composite structural sandwich panels can vary significantly, for example from 35 kgf/m^2 [11.8] to 160 kgf/m^2 [11.9]), (ii) other permanent loads of 1.5 kN/m^2 (to account for floor claddings and non-structural walls), and (iii) live loads of 3 kN/m^2 (as recommended in EN 1991 [11.10] for office areas), with a combination factor ψ_2 = 0.3 (as recommended in EN 1990 [11.7] also for office areas). Each prefabricated slab was fixed to the longitudinal beams using steel rods and plates (two pairs in each beam, as depicted in Figure 11.1). The prefabricated slabs were chamfered in two of their corners to avoid contacts between the slabs and the beam-to-column connection parts. With respect to the vertical load level considered in the structure, it should be mentioned that preliminary numerical and analytical buckling analysis showed that the critical vertical load was ~3 to ~4 times higher than the applied load, indicating that the structural design should account for second-order effects but could do so with a simplified linear analysis, increasing the magnitude of the lateral loads [11.6].

This study included the assessment of the effects of using a bracing system on the modal response of the 3-dimensional frame. This bracing system, similar to that used in the 2D-frame tests (*cf.* Chapter 10) was composed by stainless steel cables with diameter of 6 mm (with 7×19 construction) and was applied in all frames and directions (filling the entire envelope of the structure). These cables were fixed (i) to eyebolts, attached to the frames in the vicinity of the beam-to-column connections, and (ii) to turnbuckles by means of two clamps per extremity. The eyebolts were welded to stainless steel plates with thickness of 6 mm, which were bolted to the cleats of the beam-to-column connections (*cf.* Figures 11.1 and 11.3). The cables were stretched by hand until it was guaranteed that they were in tension.

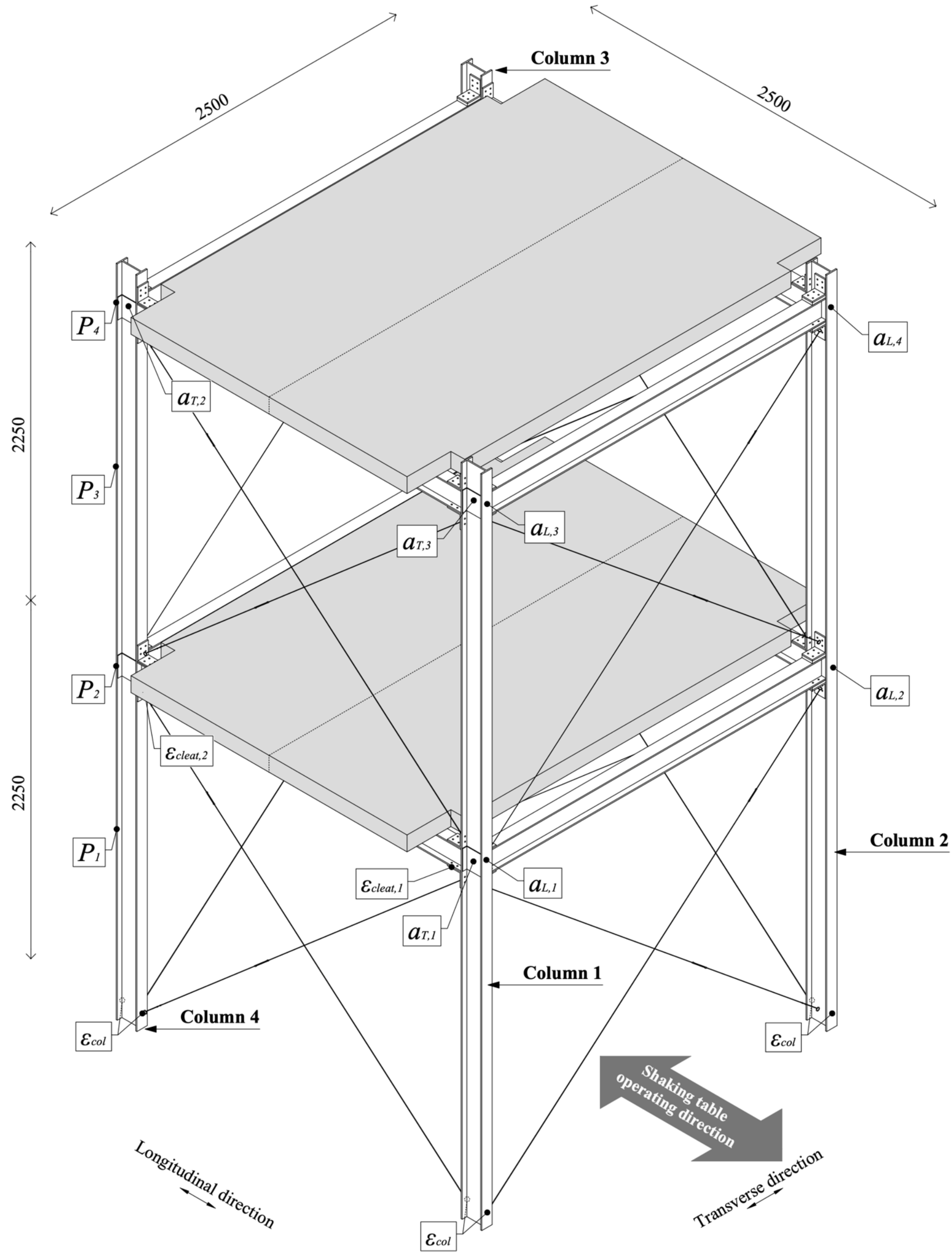

Figure 11.2 - Illustration of the 3-dimensional pultruded frame with slabs and bracings.

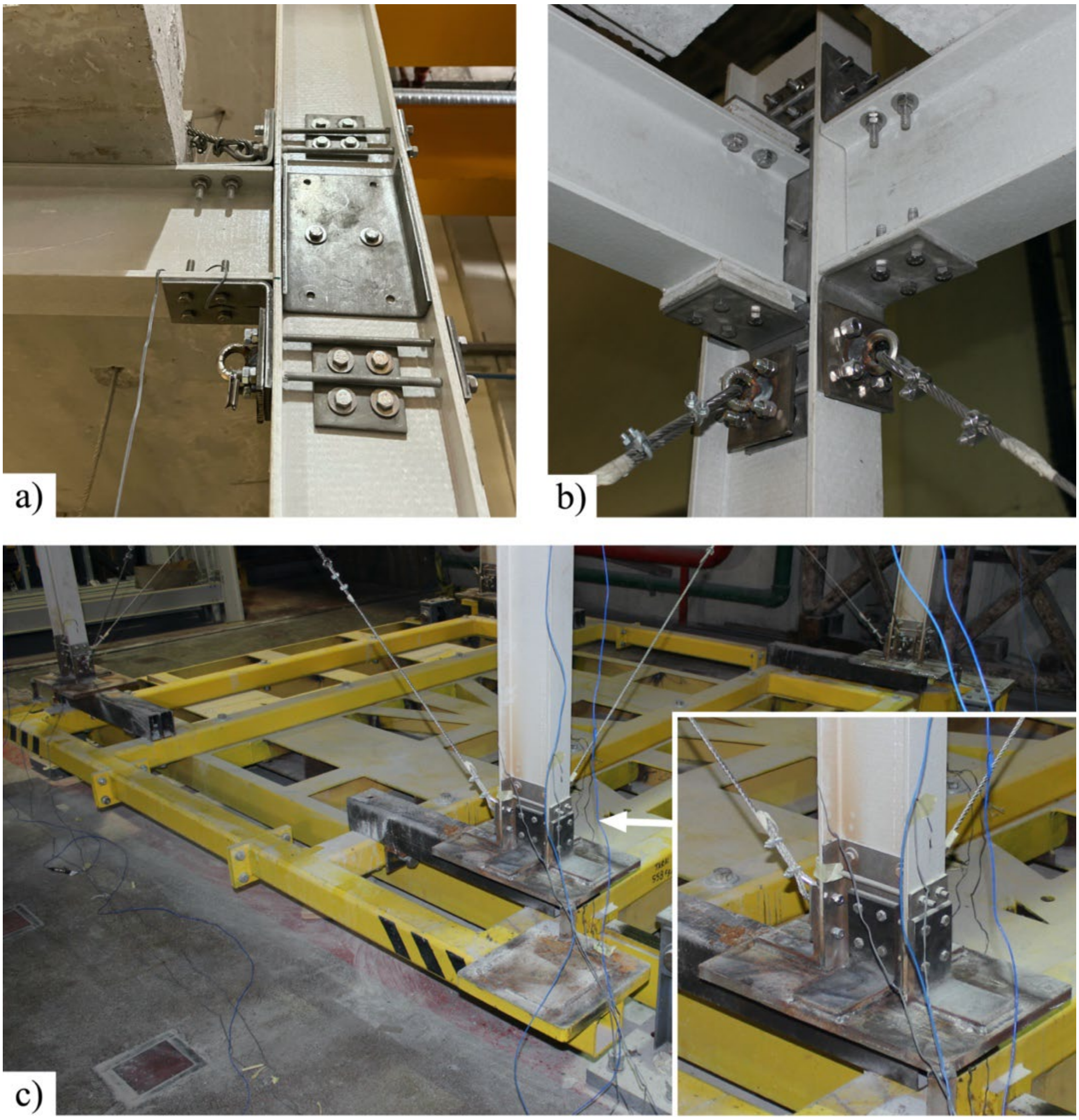

Figure 11.3 - Details of the 3-dimensional pultruded frame: a) longitudinal beam-to-column connection; b) longitudinal and transverse beam-to-column connection; c) base connections.

11.2.2. Materials

The pultruded GFRP profiles used in this study were constituted by isophthalic polyester resin matrix and E-glass fibres, and were produced by *ALTO, Perfis Pultrudidos, Lda*. These profiles were the same used in Chapters 6-8 and 10, which included the characterization of their mechanical properties, summarized in Table 11.1.

Table 11.1 - Mechanical properties of the pultruded GFRP profiles.

Test	Method	Property	Element	Average ± std. Dev.	Unit
Tension	EN ISO 527 [11.11]	$\sigma_{tu,L}$	Web	388.0 ± 25.0	[MPa]
			Flange	353.4 ± 32.7	
		$E_{t,L}$	Web	43.4 ± 1.0	[GPa]
			Flange	39.6 ± 1.2	
		υ_{LT}	Web	0.23 ± 0.02	[-]
			Flange	0.29 ± 0.02	
Compression	ASTM-D6641 [11.12]	$\sigma_{cu,L}$	Web	461.9 ± 31.0	[MPa]
			Flange	353.5 ± 32.7	
		$E_{c,L}$	Web	44.9 ± 1.7	[GPa]
			Flange	39.6 ± 1.2	
		$\sigma_{cu,T}$	Web	64.2 ± 2.12	[MPa]
		$E_{c,T}$	Web	8.1 ± 0.6	[GPa]
	ASTM-D695 [11.13]	$\sigma_{cu,T}$	Flange	41.0 ± 3.6	[MPa]
		$E_{c,T}$	Flange	2.8 ± 0.2	[GPa]
Interlaminar shear	ASTM-D2344 [11.14]	$\tau_{is,L}$	Web	27.0 ± 1.3	[MPa]
			Flange	31.2 ± 1.0	
In-plane shear	ASTM-D5379 [11.15]	τ_{LT}	Web	46.8 ± 3.1	[MPa]
			Flange	47.9 ± 2.6	
		G_{LT}	Web	3.0 ± 0.3	[GPa]
			Flange	3.7 ± 0.3	
		τ_{TL}	Web	31.2 ± 2.3	[MPa]
			Flange	27.3 ± 5.0	
		G_{TL}	Web	3.3 ± 0.5	[GPa]
			Flange	2.5 ± 0.2	

As referred in Section 11.1.1, the connections between the profiles and the web-crippling reinforcements were materialized by means of stainless steel plates with thickness of 6 mm and 4 mm, respectively. These plates were cold-formed to achieve their desired shape and were of grade AISI 304. As reported by ASTM A240 [11.16], the main properties of these stainless steel parts are: (i) 0.2% tensile proof stress ($f_{0.2\%}$) of 205 MPa; and (ii) ultimate tensile stress (f_u) in tension of 515 MPa. These connections and reinforcements parts were joined to the profiles using rods, bolts, nuts and washers of grade A2-70, which have the following properties, according to ISO 3506-1 [11.17]: (i) 0.2% tensile proof stress ($f_{0.2\%}$) of 450 MPa; and (ii) ultimate tensile stress (f_u) in tension of 700 MPa.

The prefabricated hollow core slabs were produced using concrete of grade C40/50, with characteristic compressive strength in cylinders ($f_{ck,cyl}$) of 40 MPa, and pre-stressed steel reinforcement bars, with nominal ultimate tensile strength (f_u) of 1770 MPa.

Finally, all elements used in the bracings, which included the cables, turnbuckles, clamps, thimbles and eyebolts, were made of grade A4-70 stainless steel grade. According to ISO 3506-1 [11.15], the main properties of this stainless steel grade are the following: (i) 0.2% tensile proof stress ($f_{0.2\%}$) of 450 MPa; and (ii) ultimate tensile stress (f_u) in tension of 700 MPa.

11.3. MODAL ANALYSIS

11.3.1. Test setup, procedure and instrumentation

The modal analysis tests were performed using input-output testing. In particular, the tests included the application of a localized excitation to the frame, by means of short impacts on several points of one column (points *P*; Figure 11.2), in both longitudinal and transverse directions, while measuring the resulting acceleration on seven points of the frame (points a_T and a_L for acceleration measurements in the transverse and longitudinal directions, respectively; Figure 11.2). The impacts were applied with a hammer, model *086D50* from *PCB*, equipped with a rubber tip and a load cell. Accelerations were measured with a set of three accelerometers, model *393B04* from *PCB*, with capacity of ± 5g. The output of the measuring equipment was conditioned with a signal conditioner, model *480C02* from *PCB*, and the data was gathered with a datalogger, model *QuantumX MX840B* from *HBM*, at a rate of 600 Hz, without filtering, and stored in a PC. For each input-output set, *i.e.* for each impact point (*P*) and direction and set of three direction dependent measurement points (a_T and a_L), five repetitions were made. This process was performed for all structural configurations: (i) without floor slabs and bracings (NF-NB); (ii) without floor slabs and with bracings (NF-WB); (iii) with floor slabs and without bracings (WF-NB); and (iv) with floor slabs and bracings (WF-WB).

11.3.2. Results and discussion

The modal analysis focused on the first 6 vibration modes of the structure. For each structural configuration, an initial analysis was performed to establish the range of the frequencies of interest. To this end, the first 6 frequencies were initially identified by applying the Fast Fourier Transform (FFT) algorithm to the half sum and half difference of the output acceleration signals; as an example, for the WF-NB frame, Figure 11.4 presents the FFT plots of the half sum (corresponding to the longitudinal translation modes) and of the half difference (corresponding to the torsional modes) for accelerations measured at points $a_{L,3}$ and $a_{L,4}$ after a stroke in the longitudinal direction at point P_1. The lowest frequency range of interest was limited to 6 Hz for the WF-NB frame, while highest range, for the NF-WB frame, went up to 28 Hz.

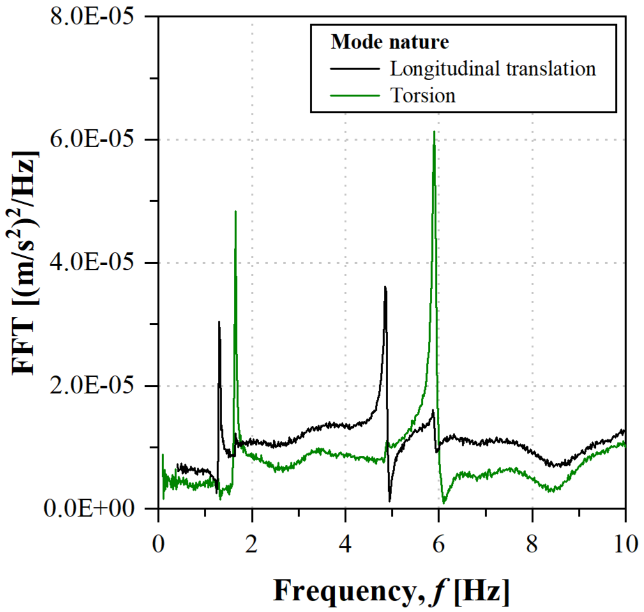

Figure 11.4 - Modal analysis: FFT curves for the half sum and half difference of accelerations at points $a_{L,3}$ and $a_{L,4}$ after a stroke in the longitudinal direction at point P_1 (frame WF-NB).

In a second stage, to retrieve the modal shapes of the structure, all acceleration signals were transformed in displacement signals. This operation was performed with the *Iomega MATLAB* script, namely by transforming the original acceleration signal into the frequency domain, with FFTs, integrating the result twice and, finally, converting the result into the time domain with inverse FFTs. The results obtained correspond to displacements in the time domain; however, the displacements "floated" around a non-zero displacement, with a polynomial low frequency trend (a zero displacement would be expected). In order to correct this non-null displacements, the polynomial trends were determined by means of curve fitting, using 50 degree polynomials, and then the signals were filtered through the resulting polynomial. Finally, to guarantee the robustness of the resulting displacement signals, these were transformed back to acceleration signals (by double derivation, again using the *Iomega MATLAB* script), and the back calculated acceleration signals were compared to the original acceleration signals, showing a good agreement and, thereby, validating the procedure.

Afterwards, each computed displacement signal was combined with the corresponding load signal in frequency-response functions (FRFs). The resulting FRF functions allowed confirming the modal frequencies identified in the preliminary analysis and, for each frequency, it was possible to determine the displacement modal amplitude, *i.e.* the dimensionless modal displacement, at each node. Table 11.2 and Figure 15.5 present the vibration frequencies associated to the first six vibration modes, and identifies also the nature of each mode, for each of the structural configurations, while Figures 11.5 and 11.6 depict the modal configurations graphically. The following nomenclature was adopted for the mode shapes: (i) transverse translation, TT; (ii) longitudinal translation, LT; and (iii) torsion, T.

Table 11.2 – Modal analysis: natural frequencies and modal configurations.

	NF-NB		NF-WB		WF-NB		WF-WB	
Mode	***f* (Hz)**	**Nature**	***f* (Hz)**	**Nature**	***f* (Hz)**	**Nature**	***f* (Hz)**	**Nature**
1	2.62	TT	7.71	TT	0.51	TT	1.85	TT
2	3.61	T	8.86	T	1.32	LT	2.30	LT
3	5.58	LT	9.86	LT	1.52	TT	3.60	T
4	6.72	T	19.03	TT	1.65	T	4.70	TT
5	7.55	TT	19.85	LT	4.87	LT	7.10	LT
6	8.69	T	26.24	T	5.91	T	9.75	T

The results of the modal analysis show that when the structure does not include floors or bracings (configuration NF-NB), the 2D frames that compose the 3D structure behave almost independently (*cf.* Figure 12.6). This is particularly evident for the torsional modes (modes 2, 4 and 6), which present deformations only in one of the directions (transverse for modes 2 and 6, and longitudinal for mode 4, *cf.* Figure 12.6), with the beams deflecting around their weak axis. When bracings are added to the structure (configuration NF-WB), for all modes of vibration the frequencies increase significantly, as expected. Although the mode shapes are similar to those obtained without bracings, their order was altered, showing that the bracings have some effect in the interaction between the lateral frames.

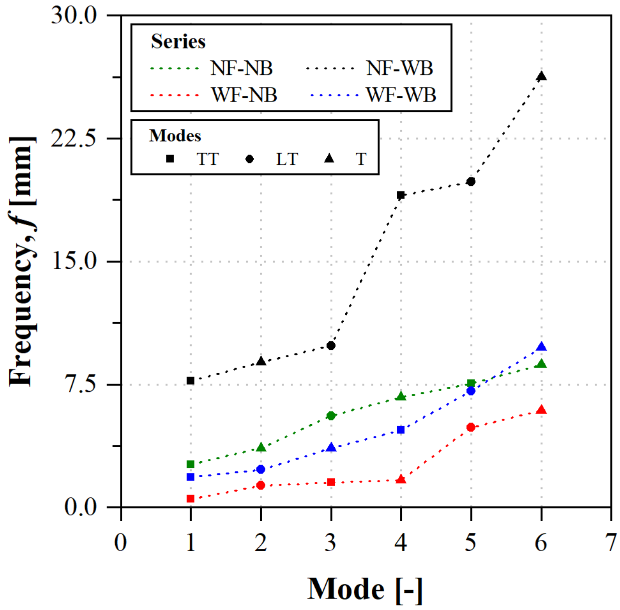

Figure 11.5 - Modal analysis: natural frequencies and modal configurations.

When the floor loads were introduced (configuration WF-NB), the vibration frequencies drop considerably, as expected - the mass increases significantly while only slight changes in stiffness may be expected (an increase in the beams and a decrease in the columns due to second order effects [11.18]), with the first vibration mode (transverse translation) registering a frequency of 0.51 Hz. The introduction of the floors had a visible effect on the structural behaviour: acting as a rigid diaphragm, it prevented the independent deformations of the lateral 2D frames. This resulted in torsional modes (modes 4 and 6) which involved the actual plane rotation of the floors (*cf.* Figure 12.7). At the same time, this resulted in very similar frequencies for modes 3 and 4 (second transverse translation and first torsional mode, respectively), namely 1.52 Hz and 1.65 Hz, which could potentially lead to mode coupling under seismic actions.

Finally, when both floors and bracings were combined (configuration WF-WB), the mode shapes were similar to those of the configuration with floors but without bracings (WF-NB), although with increased frequencies, reflecting the added stiffness provided by the bracings. The most noticeable difference was the change in the order of the 3rd and 4th modes, which for configuration WF-WB corresponded to the 1st torsion and 2nd transverse translation modes, respectively (*cf.* Figure 12.7). Moreover, the relative difference between the vibration frequencies associated to these modes further increased (3.60 Hz and 4.70 Hz, respectively).

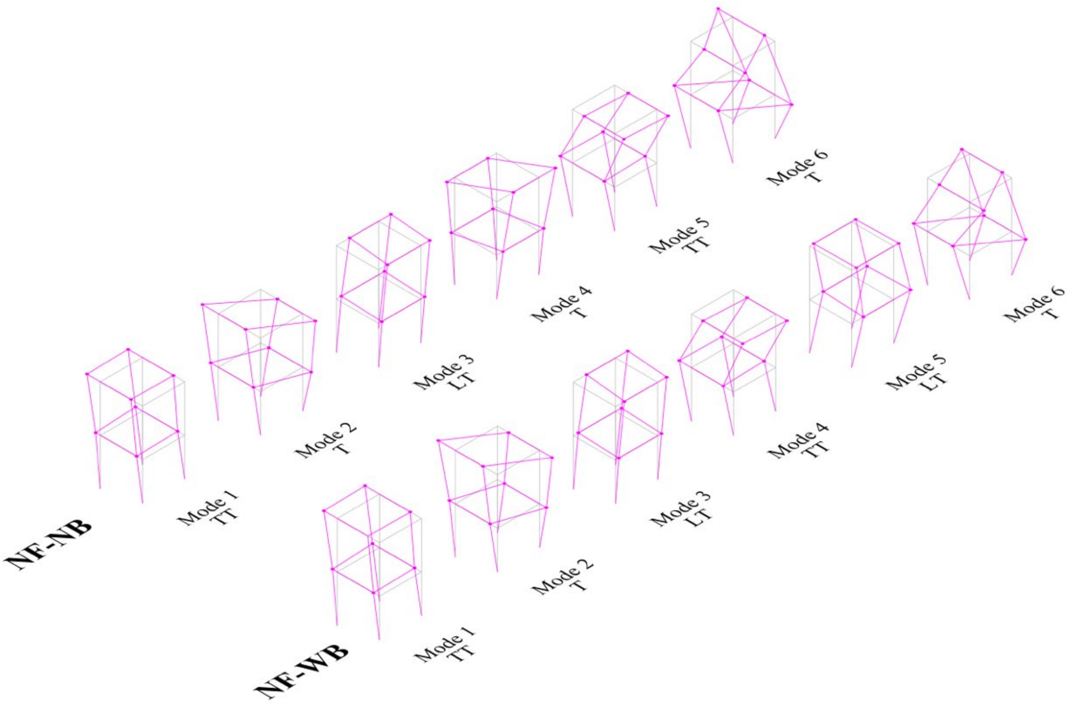

Figure 11.6 - Modal analysis: modal shapes for frames NF-NB and NF-WB.

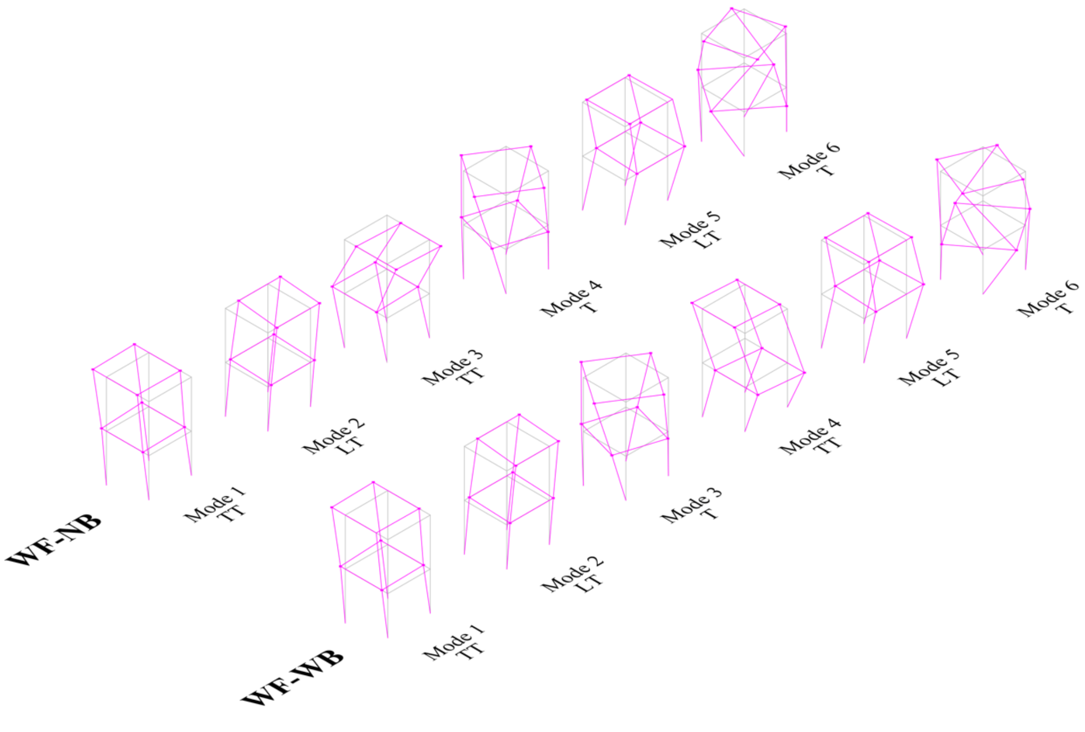

Figure 11.7 - Modal analysis: modal shapes for frames WF-NB and WF-WB.

11.4. SEISMIC TESTS

11.4.1. Test setup, procedure and instrumentation

The 3-dimensional frame seismic tests were performed in a shaking table of the Laboratory of Structures and Strength of Materials (*LERM*) of Instituto Superior Técnico. This shaking table is unidirectional and allows the testing of structures with a span area of up to 3.0×3.0 m^2 with maximum mass of 6 ton. The motion on the shaking table is imposed by a hydraulic actuator, from *Dartec*, with maximum capacity of 250 kN, maximum stroke of 400 mm, maximum possible acceleration of 1.3 g and maximum possible velocity of 16 cm/s. The hydraulic actuator is operated using a control unit, which allows the input of predefined displacement histories.

These tests were only performed in the 3-dimensional frame with loads and without bracings (WF-NB), as it was verified in preliminary tests that the cables of the bracing system tended to become lose when the frame was subjected to low energy induced white noise vibrations; this indicated that this bracing system cannot be used as an effective solution to improve the performance under seismic actions.

A total of 18 displacement histories were imposed to the base of the frame (*cf*. Figure 11.8). The displacement histories were defined based on an accelerogram generated in accordance with a response spectrum defined according to EN 1998 [11.6] for mainland Portugal (Type I earthquake, type A soil, considering a 5% damping). The seismic tests started by imposing the displacement history with lower absolute maximum displacements (red curve in Figure 11.8). Then, the remaining load displacements were imposed gradually, in an incremental manner: each new displacement history corresponded to a 10% increase of absolute displacements compared to the previous one. In the final displacement history, the difference between the maximum and minimum displacements was ~385 mm, corresponding to almost the maximum stroke of the shaking table. This way, the peak ground accelerations (*PGA*) ranged from 1.3 to 3.4 m/s^2 (or ~0.13g to ~0.35g), corresponding to the first and last displacement histories, respectively. It is also worth noting that the 10^{th} displacement history (+100% of absolute displacements with respect to the first history; blue curve in Figure 11.8) is associated to a *PGA* of 2.57 m/s^2, which corresponds approximately to the higher *PGA* included in EN 1998 [11.6] for mainland Portugal (2.5 m/s^2, for the city of Sagres). In between every displacement history up to 2.57 m/s^2 and at the end of all tests, a stroke was applied at point P_1 (*cf.* Figure 11.2) and the response of the frame was measured in what regards the longitudinal accelerations at points $a_{L,3}$ and $a_{L,4}$ aiming at identifying differences in the natural frequencies of the frame, caused by possible changes of its stiffness in the advent of considerable damage. The half-sum and the half-difference of these acceleration measurements were then introduced as input in an FFT algorithm, retrieving the natural frequencies corresponding to the longitudinal and torsional vibration modes; the configuration of the vibration modes of frame WF-NB are depicted in Figure 11.7, in particular longitudinal modes 2 and 5, and torsional modes 4 and 6.

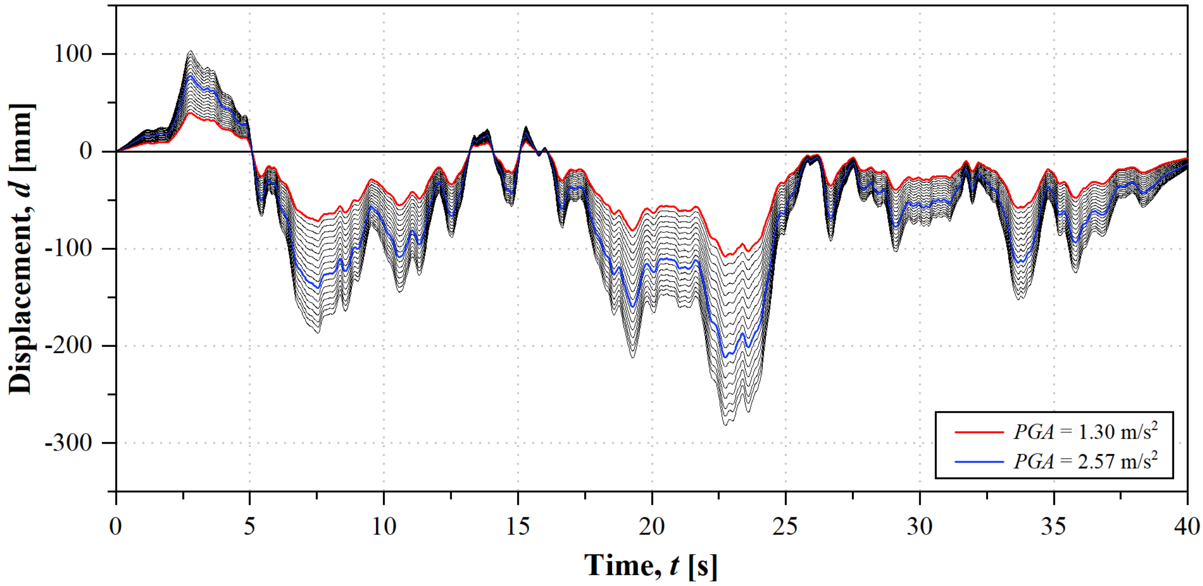

Figure 11.8 – Seismic tests: displacement histories.

The longitudinal accelerations were measured in the seismic tests until the *PGA* of 2.57 m/s^2 was achieved; the same accelerometers described in Section 11.2.1 were used at points a_L of Figure 11.2. After this point, the accelerometers were removed to prevent damaging the equipment in case of structural collapse. Additionally, the strains at the column bases were measured by means of pairs of electrical strain gauges (located at 175 mm from the column bases, at points ε_{col} indicated in Figure 11.2, also visible in Figure 11.3c), from *TML*, model *FLK-6-11-3L*. The measurement of these strains allowed estimating the curvatures and corresponding bending moments at those sections. Finally, the strains were also measured in two stainless steel cleats (located near the inside edge of the cleats, at points ε_{cleat} indicated in Figure 11.2, also visible in Figure 11.3a) using similar strain gauges; this aimed at assessing the evolution of strains on these components, in particular, at identifying the eventual occurrence of non-recoverable plastic deformations. The data was gathered with a datalogger, model *QuantumX MX840B*, from *HBM*, at a rate of 600 Hz, without any filtering, and stored in a PC.

11.4.2. Results and discussion

During the seismic tests, no visible damage was identified in the GFRP members. In fact, the only occurrence registered was the appearance of a gap between the beam members and the column members (*cf.* Figure 11.9), which increased as the tests progressed. This gap was due to the occurrence of non-recoverable plastic deformations on the stainless steel cleats, which was confirmed by the assessment of strains in these components.

Figure 11.9 - Seismic tests: gap between the beam and the column members.

As an example, Figure 11.10 presents the strain *vs*. time curves measured by ε_{cleat} strain gauges for the displacement history corresponding to a *PGA* of 2.57 m/s^2 (blue curve in Figure 11.8); as an example, this figure also identifies the strain parameters assessed at each test for strain gauge $\varepsilon_{cleat,1}$, namely the initial strains (ε_i), the final strains (ε_f), the maximum strains (ε_{max}) and the minimum strains (ε_{min}). It should be mentioned that, for this test, the initial strains of both strain gauges correspond to the final strains of the previous test (with lower displacements). For both strain gauges, but more noticeably for $\varepsilon_{cleat,1}$, the final strains are different than the initial ones, confirming the occurrence of plastic deformations in these components. The evolution of the strain parameters of both ε_{cleat} strain gauges *vs*.

the *PGA* of each displacement history is presented in Figure 11.11. This figure shows that strain gauge $\varepsilon_{cleat,1}$ presented overall higher maximum and minimum strains than strain gauge $\varepsilon_{cleat,2}$, even exceeding the capacity of the electrical strain gauge (which prevented the assessment of minimum and maximum strains for *PGA* above 2.57 m/s^2 and 3.09 m/s^2, respectively). Additionally, strain gauge $\varepsilon_{cleat,1}$ also presented considerably higher permanent strains that continued to increase until the end of the tests.

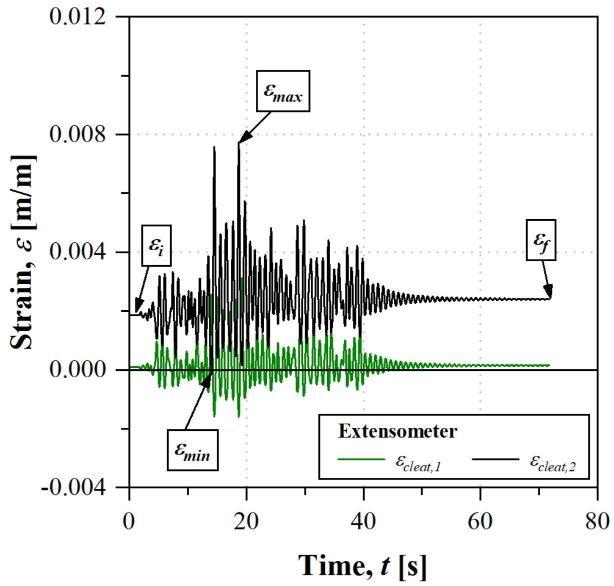

Figure 11.10 - Seismic tests: strain *vs.* time curve for displacement history with *PGA* of 2.57 m/s^2.

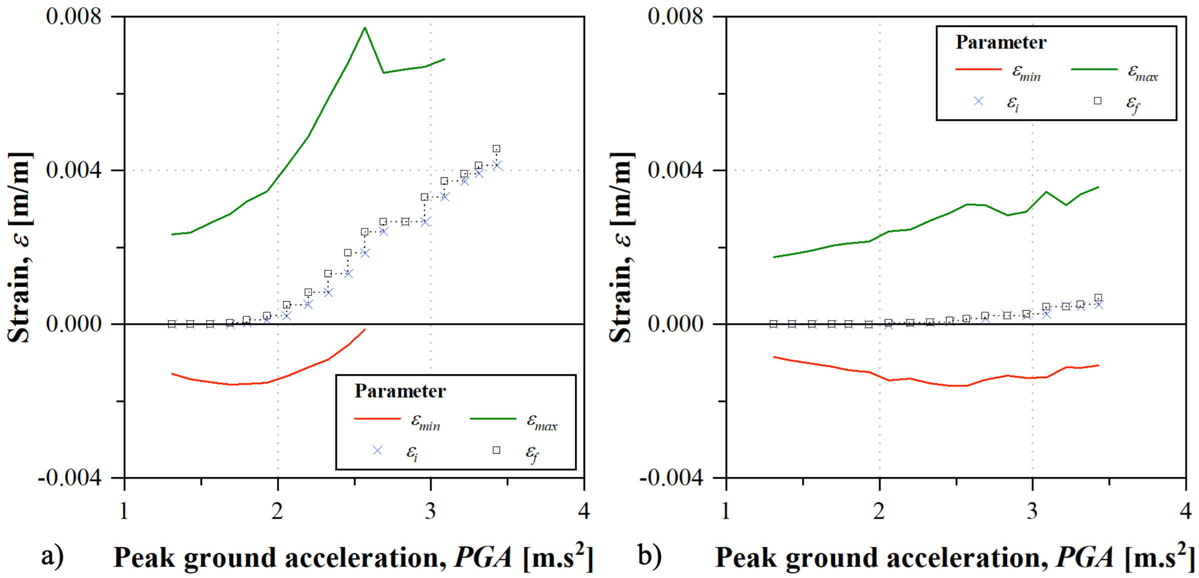

Figure 11.11 - Seismic tests: strain parameters *vs. PGA* of each displacement history for a) strain gauge $\varepsilon_{cleat,1}$ and b) strain gauge $\varepsilon_{cleat,2}$.

In order to identify the displacement history after which the structural response of the 3-dimensional frame lost its linearity and also to assess how it influenced the response of the frame on the subsequent displacement histories, the following analyses were performed: (i) the evolution of the frame's maximum top displacement *vs*. *PGA* at each displacement history; (ii) the evolution of the maximum and minimum bending moments at the column bases *vs*. *PGA* at each displacement history; and (iii) the variation of the frame's natural frequencies *vs*. *PGA* of the displacement history previously executed.

To assess the frames' top displacement, the longitudinal accelerations measured at the top level (points $a_{L,3}$ and $a_{L,4}$ of Figure 11.2) were converted into displacements using the Iomega algorithm developed using *MATLAB* commercial software (the procedure was explained in Section 11.3.2). As an example, Figure 11.12 presents the accelerations measured in point $a_{L,4}$ and the corresponding displacement for the base displacement history with *PGA* of 2.57 m/s^2. Figure 11.13 presents the maximum top displacement *vs*. *PGA* corresponding to the displacement histories until the point when the accelerometers were removed. For these histories, the behaviour of the frame was within its linear stage (R^2=0.99), which allowed concluding that the non-recoverable plastic deformation of the cleats did not influence the overall response of the frame until a *PGA* equal to 2.57 m/s^2. This way, it is worth noting that the 3-dimensional pultruded frame was able to maintain its structural integrity for the normative earthquake with maximum intensity in Portuguese territory.

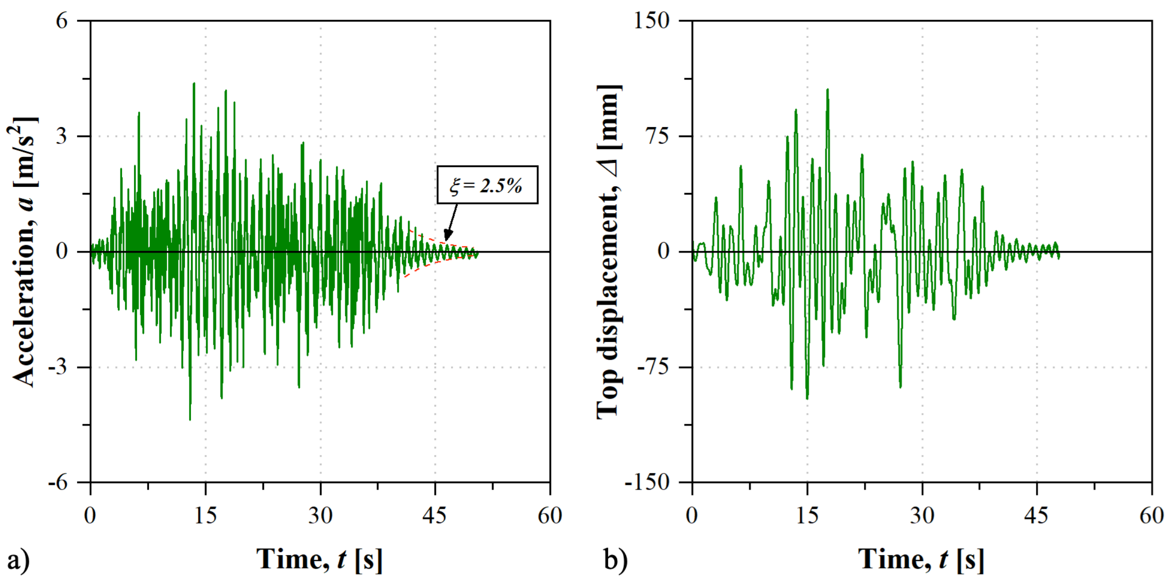

Figure 11.12 - Seismic tests: a) acceleration *vs.* time curve at point $a_{L,4}$ (the final part of the curve highlights the assessment of the damping, referred ahead); b) top displacement *vs.* time curve at point $a_{L,4}$.

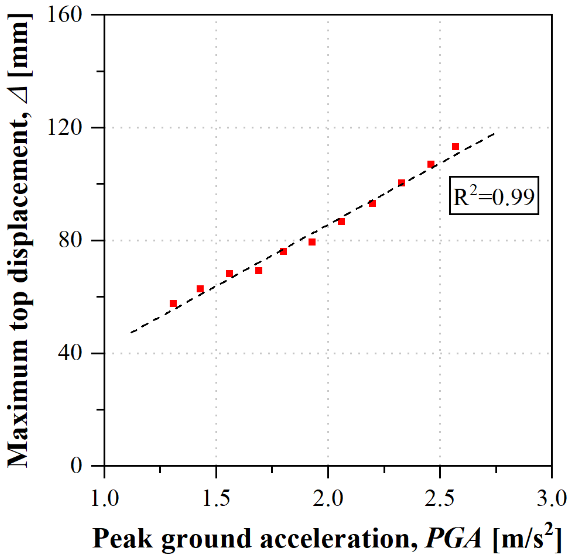

Figure 11.13 – Seismic tests: maximum top displacement *vs*. maximum base acceleration curve.

Figure 11.14 presents the evolution of the maximum and minimum bending moments[1] at the base of each column *vs*. the *PGA* attained in all displacement histories; the columns' numbering is identified in Figure 11.2. The variation of the maximum/minimum base bending moments was very similar in all columns, with exception of the maximum bending moment in column 1 and of the minimum bending moment in column 4, which in any case presented similar trends to the remaining ones. The bending moments presented a linear progression up to the displacement history with *PGA* of 2.57 m/s^2. After that point, the bending moments varied in a non-linear way, which indicated that the occurrence of unrecoverable damage started to influence the structural response of the 3-dimensional frame.

Figure 11.15 presents the FFT of the half-sum and of the half-difference of the longitudinal accelerations at points $a_{L,3}$ and $a_{L,4}$ obtained after conducting the seismic tests (procedure described in Section 11.3.1); as referred, the FFT of the half-sum gives the natural frequencies for the longitudinal modes and the FFT of the half-difference gives the frequencies for the torsional modes. There was no noticeable variation of the frequencies for the first two longitudinal and torsional modes, which indicates that despite the structural response of the frame reached the non-linear stage, its initial stiffness remained almost the same throughout all seismic tests.

[1] Estimated using the pairs of accelerometers located at the column members (points ε_{col} in Figure 11.2).

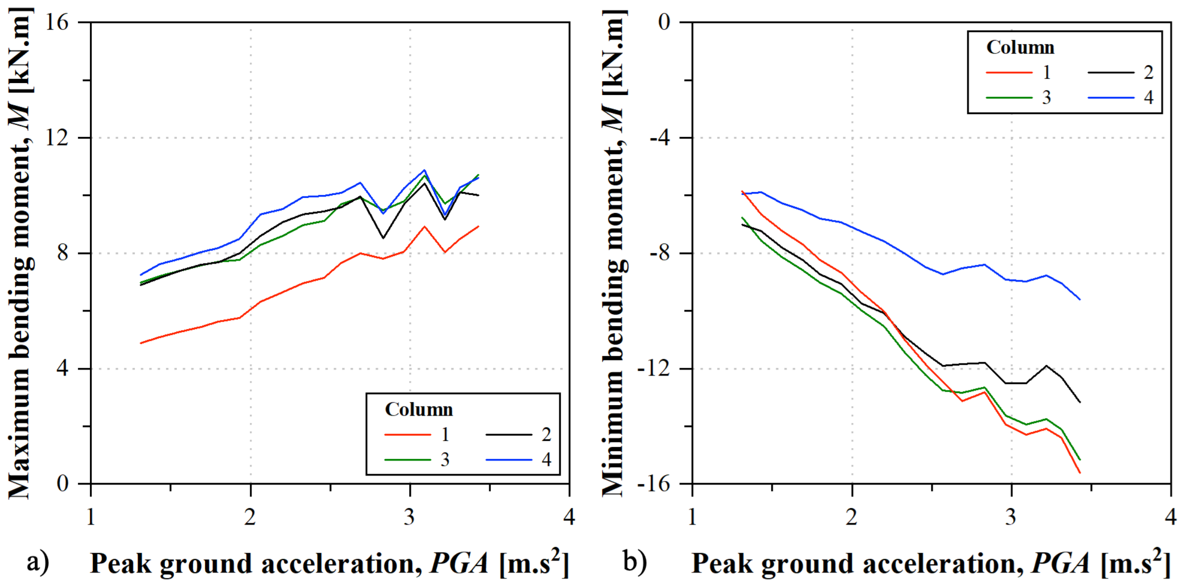

Figure 11.14 – Seismic tests: a) maximum column base moment *vs*. maximum base acceleration and b) minimum column base moment *vs*. maximum base acceleration curves.

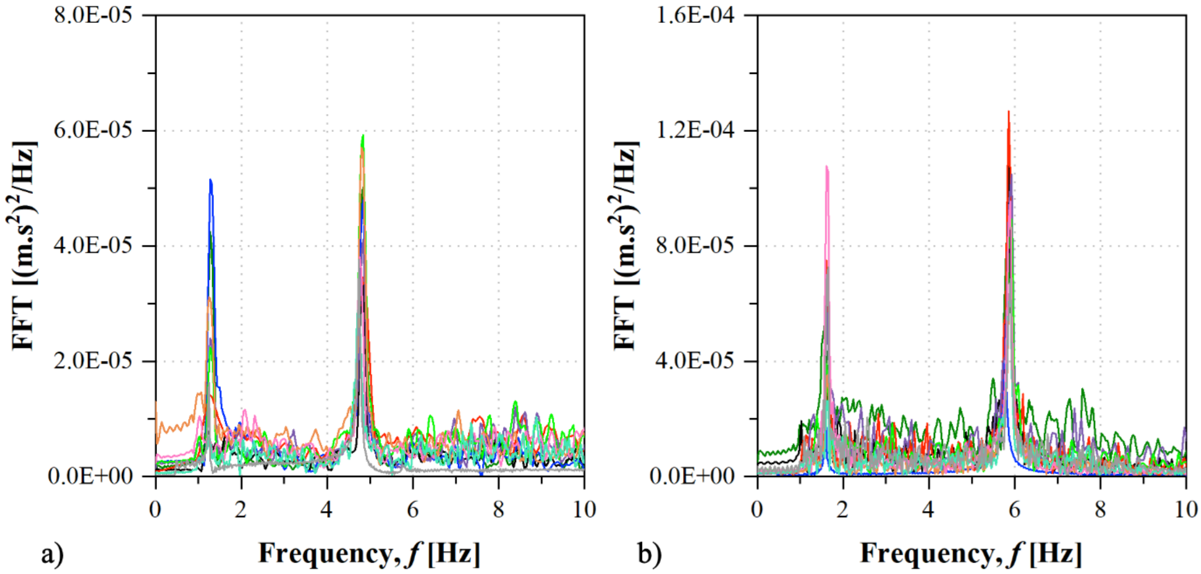

Figure 11.15 – Seismic tests: a) FFTs of the half-sum and b) FFTs of the half difference of accelerations measured at points $a_{L,3}$ and $a_{L,4}$ (each curve corresponds to a different PGA).

A final word to highlight that the seismic tests allowed also to estimate the damping coefficient (ξ) of the 3-dimensional pultruded frame. This coefficient was assessed at the end of each displacement history by estimating the logarithmic decrement of the frame's free vibrations, as exemplified in Figure 11.12a, and it was found to be 2.5% for all tests up to a *PGA* of 2.57 m/s^2. It should be mentioned that this damping value of the GFRP frame structure, which was obtained in the experiments, is half that considered in the definition of the response spectrum used to specify the base displacement histories

(5%). In practical terms, this means that the structure endured higher accelerations than those envisaged by the Eurocode 8 [11.6] elastic response spectra.

11.5. CONCLUSIONS

This chapter presented an experimental study of the dynamic and seismic behaviour of a full-scale, 2-storey, 3-dimensional frame structure comprising pultruded GFRP profiles and cleated connections. The beam-to-column cleated connections were selected based on results of previous research, namely the study of full-scale connection specimens and of full-scale 2-dimensional frames presented respectively in Chapter 6 and in Chapter 10.

The experimental modal analysis allowed determining the vibration frequencies and mode shapes for several structural configurations, namely with and without bracings and/or floor slabs. The introduction of the bracings leads to higher vibration frequencies, having minor effects on the mode shapes. Conversely, the addition of the floor slabs leads to a decrease of the frequencies and has a greater impact on the mode shapes, acting like rigid diaphragms.

On the seismic tests, the GFRP frame structure with floor slabs and without bracings was subjected to 18 base displacement histories, defined based on the Eurocode 8 [11.6] elastic response spectra, corresponding to *PGAs* ranging from 1.3 m/s^2 to 3.4 m/s^2, which were limited by the stroke of the shaking table. Although permanent plastic deformations were registered in the stainless steel connection cleats for *PGAs* above ~2 m/s^2, the structure presented linear behaviour up to a *PGA* of 2.57 m/s^2, which is slightly larger than the maximum design *PGA* for mainland Portugal. From that point on, the structure presented a non-linear behaviour, as attested by the evolution of the columns' base bending moments.

It should be mentioned that modal analysis carried our throughout the seismic tests showed that no variations of vibration frequencies occurred, indicating that the initial stiffness of the structure was not affected by the seismic actions imposed. This is corroborated by the non-occurrence of visible structural damage, besides the permanent deformations of the cleats. Overall, this study shows the feasibility of safely using GFRP structures in seismic areas.

11.6. REFERENCES

[11.1] Mosallam A. (2000). Fully reversed cyclic performance of pultruded frame structures. In *European Pultrusion Technology Association 5th Annual World Conference and Expo,* Berlin.

[11.2] Mosallam A. (2011). *Design guide for FRP composite connections*. American Society of Civil Engineers.

[11.3] Minghini F, Tullini N, Laudiero F. (2010). Vibration analysis of pultruded FRP frames with semi-rigid connections. *Engineering Structures*, 32(10), 3344-3354.

[11.4] Boscato G, Russo S. (2014). Dissipative capacity on FRP spatial pultruded structure. *Composite Structures*, 113, 339-353.

[11.5] Nogueira CM. (2017). *Comportamento dinâmico e sísmico de pórticos tridimensionais em perfis pultrudidos de GFRP*. MSc Thesis in Civil Engineering, Instituto Superior Técnico, Technical University of Lisbon, Lisbon.

[11.6] EN 1998-1 (2004). Design of Structures for Earthquake Resistance – Part 1: General rules, seismic actions and rules for buildings.

[11.7] EN 1990 (2002): Basis of Structural Design.

[11.8] Proença M, Garrido M, Correia JR, Gomes MG. (2021). Fire resistance behaviour of GFRP-polyurethane composite sandwich panels for building floors. *Composites Part B: Engineering*, 224, 109171.

[11.9] Keller T, Rothe J, De Castro J, Osei-Antwi M. (2014). GFRP-balsa sandwich bridge deck: Concept, design, and experimental validation. *Journal of Composites for Construction*, 18(2), 04013043.

[11.10] EN 1991-1-1 (2004): Actions on Structures – Part 1-1: General actions - Densities, self-weight, imposed loads for buildings.

[11.11] EN ISO 527-1 (1997). Determination of Tensile Properties – Part 1: General Principles. Brussels.

[11.12] ASTM D 6641/D 6641M-16e1. (2016). Standard Test Method for Compressive Properties of Polymer Matrix Composite Materials Using a Combined Loading Compression (CLC) Test Fixture. West Conshohocken.

[11.13] ASTM D 695-02. (2002). Standard Test Method for Compressive Properties of Rigid Plastics. West Conshohocken.

[11.14] ASTM D 2344/D 2344M-00. (2000). Standard Test Method for Short-Beam Strength of Polymer Matrix Composites Materials and their Laminates. West Conshohocken.

[11.15] ASTM D 5379/D 5379M. (2005). Standard Test Method for Shear Properties of Composites Materials by the V-Notched Beam Method. West Conshohocken.

[11.16] ASTM A240. (2020). Standard Specification for Heat-Resisting Chromium and Chromium-Nickel StainlessSteel Plate, Sheet, and Strip for Pressure Vessels. West Conshohocken.

[11.17] ISO 3506-1 (2020). Fasteners — Mechanical Properties of Corrosion-Resistant Stainless Steel Fasteners — Part 1: Bolts, Screws and Studs with Specified Grades and Property Classes. Geneve.
[11.18] Kucukler M, Gardner L, Macorini L. (2014). Stiffness reduction method for the design of steel columns and beam-columns. In *Proceedings of the SSRC Annual Stability Conference*, Toronto.

PART VI

Conclusions and future developments

Chapter 12

Conclusions and future developments

12.1. CONCLUSIONS

Pultruded glass fibre reinforced polymer (GFRP) profiles have high strength, low self-weight, high corrosion resistance and electromagnetic transparency. Due to these features, pultruded GFRP profiles are being increasingly used as structural members in civil engineering applications, especially when there are requirements of increased durability (e.g. in water treatment plants) and non-conductibility (e.g. in railways tracks) that cannot be easily fulfilled using traditional materials, such as reinforced concrete and steel. However, these profiles are not usually considered for non-industrial structural applications, mostly due to the lack of design methodologies and provisions that account for some of the material's limitations, like their lower stiffness (compared to traditional materials) and the brittle nature of their failure modes. To develop comprehensive design recommendations, research efforts should concentrate on critical topics regarding pultruded structures, such as their connections and their seismic behaviour.

As so, this PhD thesis presents a comprehensive experimental study, comprising three different scales of analysis, aiming at characterizing: (i) the quasi-static monotonic and cyclic behaviour of beam-to-column connections between pultruded GFRP profiles with tubular and I-sections; (ii) the quasi-static monotonic and cyclic sway behaviour of 2-dimensional frames made of pultruded GFRP profiles with tubular and I-sections; and (iii) the seismic behaviour of 3-dimensional frames made of pultruded GFRP I-section profiles.

Four beam-to-column connections systems were developed, comprising metallic auxiliary parts designed to improve the joints response by taking advantage of the material's ductility. Most proposed connection systems presented considerable initial stiffness, strength, ductility and capacity to dissipate energy, demonstrating their applicability for pultruded frame structures. The 2-dimensional frames that were tested included the aforementioned beam-to-column connection systems and it was shown that such systems had significant impact on the frames' sway behaviour. However, the 2-dimensional frames presented limited capacity to dissipate energy under cyclic loading, due to the high deformability of the column profiles. Additionally, the influence of walls or of a cable bracing system in the frames' response was also evaluated. As expected, the walled and braced frames presented higher stiffness and strength than the unfilled ones. Nonetheless, they also presented limited energy dissipation capacity. The 3-dimensional frame that was tested also included a beam-to-column connection system previously developed and characterized. The 3-dimensional frame was able to withstand seismic actions above the highest design earthquake for mainland Portugal, demonstrating the feasibility of using such structural systems in seismic prone zones.

Alongside the experimental campaign, the behaviour of most beam-to-column connections and 2-dimensional frames was simulated using numerical and/or analytical tools, which provided reasonable to good accuracy.

The following subsections present the detailed conclusions regarding the beam-to-column connections (*cf.* Sections 12.1.1. and 12.1.2. for connections between tubular and I-section profiles, respectively), the 2-dimensional frames (*cf.* Section 12.1.3.) and the 3-dimensional frames (*cf.* Section 12.1.4.)

12.1.1. Beam-to-column connections for tubular profiles

Two novel bolted connection systems were proposed for tubular profiles: (i) a sleeve connection system, comprising two internal steel parts; and (ii) a cuffed connection system, comprising an exterior stainless steel part.

Four different sleeve connection series were studied, differing in the bolt number and positioning. The number of bolts had influence mostly on the connections' stiffness, with more bolts leading to higher stiffness. On the other hand, it was demonstrated that the bolt edge distance had considerable impact on the connections' strength and capacity to dissipate energy, as it governs two different failure modes: (i) the brittle shear-out failure mode, occurring for short edge distances and lower bending moments, and (ii) the pseudo-ductile bearing failure mode, occurring for larger edge distances and higher bending moments. Additionally, when the shear-out failure was avoided/delayed, the sleeve connections presented marked non-linear behaviour, associated to the plastic deformation of the internal steel parts. As so, the sleeve connection series with better overall performance corresponded to the series with higher edge distance, which presented considerable initial stiffness, higher ultimate strength, higher ductility and higher dissipated energy. The stiffness of all sleeve connection series was predicted with reasonable accuracy using the analytical "component method". However, the strength could not be accurately estimated by using only analytical tools, due to the complexity of the internal forces/stresses distribution. Therefore, the strength of all sleeve connection series was predicted with reasonable accuracy using a combination of numerical (to obtain the pull and shear stresses on the bolts) and analytical (for the design verifications) methods.

Four cuff connection series were experimentally characterized, differing in the cuff's thickness and length. It was demonstrated that these parameters had considerable influence in the connections' initial stiffness and strength (thicker and longer cuff parts leading to higher initial stiffnesses and strengths). However, it should be noted that connections with thicker cuff parts also presented more extensive damage in the GFRP profiles. Nonetheless, all cuff connections presented considerable ductility, owing to the plastic deformations registered in the cuff parts. The hysteretic response of one cuffed connection series was also assessed, registering a significant amount of dissipated energy, even though it was limited by the occurrence of pinching.

When comparing these two connection systems for tubular profiles, the cuffed connections presented higher stiffness, higher strength, similar ductility and better cyclic performance (namely in what regards the ability to dissipate energy) than the sleeve connections. Therefore, they are better suited to join pultruded GFRP tubular profiles.

12.1.2. Beam-to-column connections for I-section profiles

This study comprised two connection systems for pultruded GFRP I-section profiles: (i) a cleated connection system, using stainless steel angle parts; and (ii) a cuffed connection system, comprising an exterior stainless steel part.

Regarding the cleated connections, nine different connection series were studied, differing in the thickness and positioning of the cleats, the number of bolts and the presence of column reinforcement (four series comprised reinforcements, the remaining one did not). It was concluded that the column reinforcement is essential to prevent the tensile rupture of the column's web-flange junction, which occurred for reduced rotations and considerably limited the strength attained by the non-reinforced connections. Additionally, it was demonstrated that a careful selection of the cleats' thickness is of great relevance, as higher thicknesses increase the connection stiffness but also lower its ductility, and eventually the strength (extensive damage may occur in the GFRP profiles due to the stainless steel-GFRP mechanical mismatch). As so, the connection series with intermediate cleat thickness presented the best overall performance regarding the aforementioned properties but also regarding the capacity to dissipate energy. The stiffness of the reinforced cleated series was predicted using the analytical "component model" and numerical finite element models. For the analytical predictions, the stiffness of most components was computed using formulae adapted from steel structural design standards, which when combined resulted in values of connection's stiffness considerably close to the ones registered experimentally, thus validating the methodology employed. The predictions obtained using three-dimensional finite element models were also very similar to the experimental stiffnesses. Additionally, these models allowed to identify the components with higher influence in the connections' overall stiffness; namely the column and cleat components. Finally, the strength of the reinforced connections was predicted with reasonable accuracy by a combination of analytical (for the components' design verifications) and numerical (to estimate the loads per component) procedures.

Four series were considered in the study regarding the cuff connections, which differed in the cuff thickness and length. The geometry of the cuff part had significant influence in the connection's response, with thicker and longer cuff parts providing higher stiffness and strength. On the other hand, the connections with thicker cuffs presented lower ductility than the remaining ones. Even though the cuff parts presented considerable plastic deformations, most series also presented extensive damage in the GFRP members, in some cases even preceding the steel plastic deformations. Additionally, one cuff series was evaluated in what regards its hysteretic behaviour and, although considerable pinching occurred, it could still dissipate a significant amount of energy.

Of these two systems, the cleated connections were found to be a better solution to join pultruded GFRP I-section profiles, as they presented higher initial stiffness, strength, ductility and capacity to dissipate energy.

12.1.3. 2-dimensional frames

Two types of 2-dimensional pultruded frames were considered in this study: (i) frames made of tubular profiles; and (ii) frames made of I-section profiles.

Regarding the frames composed by tubular profiles, two frame series were experimentally characterized, one unfilled and the other comprising a structural wall made of composite sandwich panels. The profiles of these frames were joined using the best performing sleeve connection series. The initial stiffness and strength of the walled frame were considerably higher than those of the unfilled frame. The unfilled frame presented a smother response, with the failure modes being located at the connections. On the other hand, the frame with walls presented extensive damage occurring in the beams, which led to a quicker loss of their structural integrity. Regarding the hysteretic behaviour, both unfilled and filled frames presented considerable pinching and limited capacity to dissipate energy. Nonetheless, the walled frame presented wider hysteretic curves and dissipated more energy in comparison to the unfilled frame; in the latter, the almost elastic hysteretic behaviour was associated to the high flexibility of the column profiles. However, the better cyclic behaviour of the walled frame was achieved at the expense of more extensive damage in the frames' members, which must be accounted for in the design of pultruded frames with high-stiffness and high-load carrying capacity walls.

Regarding the frames with I-section profiles, five series were studied, three differing in the beam-to-column connection systems and the remaining comprising a stainless steel cable bracing system or non-structural infill walls made of plasterboards. For the frames without bracings or walls, the connection system had considerable influence on the frames' response. The overall frame stiffness varied proportionally with the stiffness of the connections: as expected, higher connections' stiffness led to higher frame's stiffness. On the other hand, the frames with infill walls and with bracings presented the highest stiffness and strength, respectively. All frames presented substantial pinching and limited capacity of dissipating energy. In the case of the frames without bracings and walls, this was due to the high flexibility of the column profiles. For the braced and walled frames, the poor hysteretic performance was related to the occurrence of plastic deformations on the steel elements of the bracings or to the deterioration of the wall panels, which limited the mechanical contribution of these elements on subsequent cycles with similar displacements. Therefore, it was concluded that the bracing system used is not adequate for seismic areas and the plasterboard walls used in the tests should not be accounted for in the structural design of the frames.

In order to simulate the cyclic behaviour of unfilled frames with tubular and I-section profiles, numerical finite element models were developed using commercial software widely used by civil engineers in structural design. The profiles were modelled using frame elements and the connections were simulated using a multilinear hysteretic model (previously calibrated from the connections' cyclic tests). As these models were intended to be of relative simplicity, the GFRP material was modelled as having linear-elastic material behaviour and, therefore, the damage in the profiles was not accounted for. Despite that, the models were able to reproduce the hysteretic behaviour registered in the corresponding tests with reasonable accuracy, presenting an overall similar response and comparable (although conservative) estimates of dissipated energy, which demonstrated their applicability to the design of pultruded GFRP frame structures. An additional numerical model was developed for the frame with I-section profiles, which included a bracing system materialized by pultruded profiles and a steel plate damper. It was demonstrated that this bracing system improved the hysteretic response of the frame, particularly in what refers to its capacity to dissipate energy.

12.1.4. 3-dimensional frames

In this study, a full-scale, 2-storey, 3-dimensional frame was subjected to modal identification tests and to seismic tests. The structure included I-section pultruded GFRP profiles and cleated connections, similar to the ones previously characterized. In the modal analysis, the frame was tested (i) without floor slabs nor bracings, (ii) with floor slabs and without bracings, (iii) without floor slabs and with bracings and (iv) with floor slabs and with bracings. It was demonstrated that the inclusion of bracings increases the natural frequencies but does not affect considerably the mode shapes. On the other hand, adding floor slabs decreases the frame's natural frequencies and also affects the mode shapes, as the floors and the beams behave as rigid diaphragms.

Only the frame with floor slabs and without bracings was tested under seismic actions, which included 18 ground displacement histories. The load histories were defined in accordance to design codes for Portuguese territory and presented peak ground accelerations ranging from 1.3 m/s^2 to 3.4 m/s^2 (the maximum design peak ground acceleration for continental Portugal is of 2.5 m/s^2). In these tests, it was observed that the stainless steel connection cleats presented plastic deformations above peak ground accelerations of ~2 m/s^2. However, the 3-dimensional frame presented structural linear behaviour until reaching peak ground accelerations of 2.57 m/s^2, followed by a non-linear response for higher accelerations. Nonetheless, the initial stiffness of the structure equal throughout the seismic tests, as the frame's natural frequencies did not change. The seismic tests allowed to conclude that pultruded frame structures can be used in seismic areas, provided that the profiles and their connections are well designed and detailed.

12.2. FUTURE DEVELOPMENTS

The elaboration of the present work allowed to identify several research needs that should be addressed in future developments. Such developments are discussed in the following paragraphs.

In this PhD thesis, several connection systems were developed, which proved to be effective in joining pultruded profiles with specific cross sections and properties. However, further research should focus on defining the optimum geometry of the auxiliary metallic parts to take into account the different properties and cross-sections of other GFRP profiles, either by experimental tests or by numerical analysis. In addition, new connection configurations should be developed and assessed, so that more options are available when designing GFRP structures.

Future research should focus on topics regarding pultruded frame connections that were not covered in the present thesis, namely the (i) monotonic and cyclic behaviour of connections along the columns' minor axis (their weak direction), (ii) the creep behaviour of pultruded connections and (iii) their response for high temperatures (including fire actions).

In order to develop and study new connection systems for pultruded GFRP profiles, the numerical models are a very valuable tool. If these models are able to predict the complex behaviour of the GFRP material and their connection systems, they will allow for considerable time and cost savings in comparison to experimental testing. Therefore, it is of great relevance to develop more advanced numerical methodologies able to simulate more accurately the full response of such connections – this requires the inclusion of the damage progression in the GFRP material.

The lateral behaviour of GFRP structures is mostly linear-elastic, owing to the high deformability of pultruded columns. Under seismic loads, this feature has a key advantage – the recentring potential – however, it also limits the energy dissipation capacity of frames. Therefore, the development of material-adapted bracing systems is essential to enhance the hysteretic response of pultruded structures and to allow their widespread application in locations prone to seismic events.

In order to allow a broader use of pultruded GFRP profiles in structures, it is of the utmost relevance to develop proper design recommendations. The current design codes do not provide sufficient guidelines that allow for a proper detailing of the frame connections neither present the formulae needed to predict their behaviour – as mentioned available design provisions only cover very simple geometries and loading cases, typically in-plane. Additionally, the GFRP standards do not address the seismic behaviour of pultruded structures, which is essential for their adoption in seismic areas.

APPENDIX

Appendix A

Loading and unloading rules of the pivot hysteresis model

This appendix provides further details about the loading and unloading rules of the Pivot hysteresis model (described in Chapter 4), in each quadrant: (i) in quadrants Q_1 and Q_3, loading is limited by the monotonic envelope and by the pinching Pivot points while unloading moves along a line towards P_1 and P_3, respectively; (ii) in quadrants Q_2 and Q_4, loading moves along a line towards PP_2 and PP_4, respectively, while unloading moves along a line away from P_2 and P_4, respectively. It should be noted that, after yielding, the subsequent cycles are limited by new strength envelopes, defined by a line connecting the pivot pinching points and the maximum displacement point of the previous cycle over the initial envelope, S_1 or S_2, for the positive and negative branches, respectively.

In order to better illustrate the hysteretic behaviour defined by this model, consider Figure 4.12 (Chapter 4, page 85). Figure 4.12b presents an initial cycle (red line) from the origin to rotation θ_1 (maximum imposed positive rotation in the first cycle), reversing to rotation θ_2 (maximum imposed negative rotation in the first cycle) and then to zero rotation. This first cycle follows the (monotonic) strength envelope up to rotation θ_1, where, since the yielding rotation was surpassed, point S_1 is marked (otherwise, the unloading response would follow the elastic path). Then, the unloading follows a straight path from S_1 towards P_1 until it reaches the horizontal axis, from where the reverse loading path is directed at PP_2. After reaching PP_2, the hysteretic curve resumes the path of the monotonic envelope until rotation θ_2 is reached, where point S_2 is marked (since the negative yielding was exceeded). When the displacement is reversed, the loading is then directed at P_3 until it reaches the horizontal axis, from where it is redirected towards PP_4. The second cycle, depicted in Figure 4.12c, maintains that path until PP_4 is reached. Then, instead of resuming the initial envelope, the path is redirected to S_1 and, only then, it follows the initial strength envelope until rotation $\theta d'_1$ (maximum imposed positive rotation in the second cycle) is reached, where point S'_1 is marked. The rotation reversal is directed at P_1 until the horizontal axis is reached where the path shifts towards PP_2. There, again, the loading path is directed at S_2, instead of following the monotonic strength envelope; which is only followed between S_2 and θ'_2 (maximum imposed negative rotation in the second cycle), where point S'_2 is marked. Once again, the rotation reversal is directed at P_3 until the horizontal axis is reached. In quadrant Q_4, however, the load path is not directed at PP_4, but instead at PP_4', accounting for the strength reduction observed earlier in this cycle (*cf.* Eq. [4.2]). Finally, Figure 4.12d presents a third cycle in which the load paths are directed at the previous maximum displacement points S'_1 and S'_2 in quadrants Q_1 and Q_3, respectively, before resuming the monotonic strength envelope. As before, upon rotation reversal, the unloading paths are directed at P_1 and P_3, from quadrants Q_1 and Q_3, respectively. After the horizontal axis is reached, the load path is redirected at the new pivot points PP_2' and PP_4'' (*cf.* Eq. [4.2]), in quadrants Q_2 and Q_4, respectively.

Appendix B

Material characterization tests

PULTRUDED GFRP PROFILES AND PLATES

The main mechanical properties of the pultruded GFRP profiles (I-shaped cross section of 150×75(×8) mm^2) and plates (rectangular cross section of 40×8 mm^2) used in the present work were assessed by means of standardized coupon tests. Both pultruded materials were composed by E-glass fibres impregnated by an isophthalic polyester resin matrix, produced by *ALTO, Perfis Pultrudidos, Lda.*, and the section walls were designed to have the same fibre architecture. The coupons (laminates) used in the characterization tests were obtained from cutting the flanges (I150-F) and web (I150-W) section walls.

Prior to the coupon tests, burn-off tests were carried out, up to 800 ºC, in accordance with the ISO 1172 standard [6.1], to evaluate the fibre mass content of the profile. These tests disclosed also the fibre architecture of the profiles: uni-directional rovings (R), 0/90 woven (W) and chopped fibre mats (C), according to a C/W/R/C/R/W/C layup. The fibre mass content per direction of the GFRP laminates was found to be ~78% for 0° direction, ~4% for 90° direction and ~17% for the chopped fibre mats.

Table 6.1 (of Chapter 6) lists the tests performed on each laminate, the respective standard and specimen dimensions. For each test type and direction, 8 specimens were tested. The tensile [6.2], in-plane shear [6.6] and the combined load compressive (CLC) [6.3] tests were performed in an *Instron* universal test machine, model 1343, with 250 kN of load capacity and 100 mm of stroke, while the compressive [6.4] and interlaminar shear [6.5] tests were performed in a *Form+Test Seidner* press, with load capacity of 10 kN. The displacement rate used in each test followed the recommendations of the respective standard. Figures B.1 to B.5 present, as an example, representative strain/displacement *vs*. stress/load curves and illustrate the specimens after failure, for each test carried out in the longitudinal direction. The main results, which are summarized in Table 6.1, were determined according to the procedures recommended by the corresponding standards (*cf.* Table 6.1).

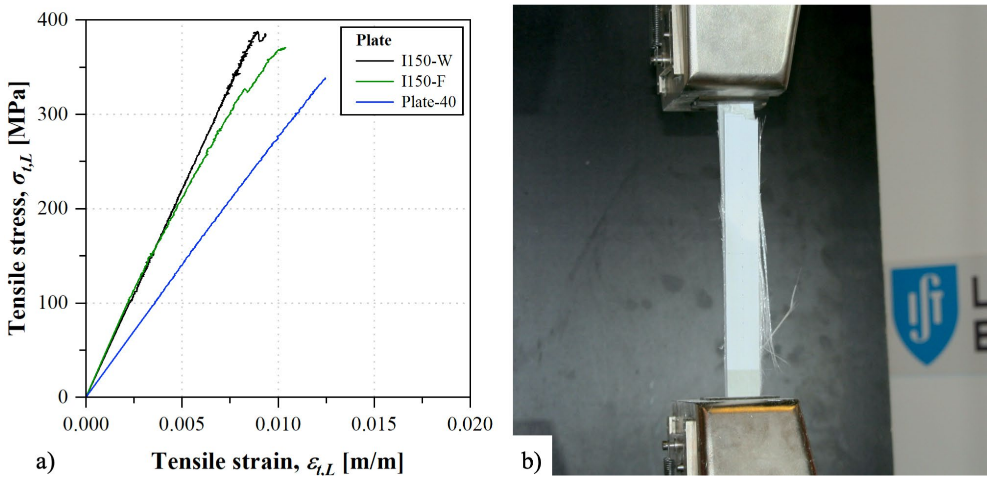

Figure B.1 - GFRP longitudinal tensile tests: a) representative stress *vs*. strain curves; b) specimen after failure.

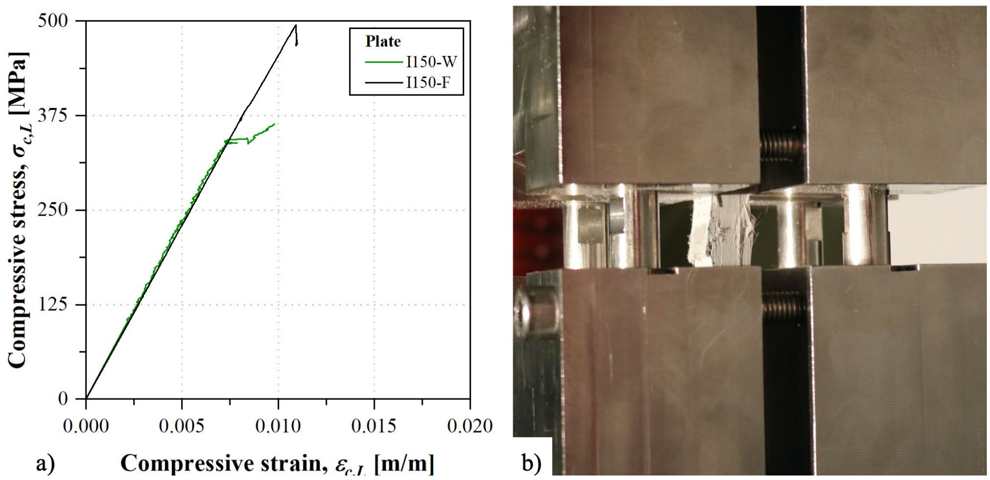

Figure B.2 - GFRP longitudinal CLC tests: a) representative stress *vs*. strain curves; b) specimen after failure.

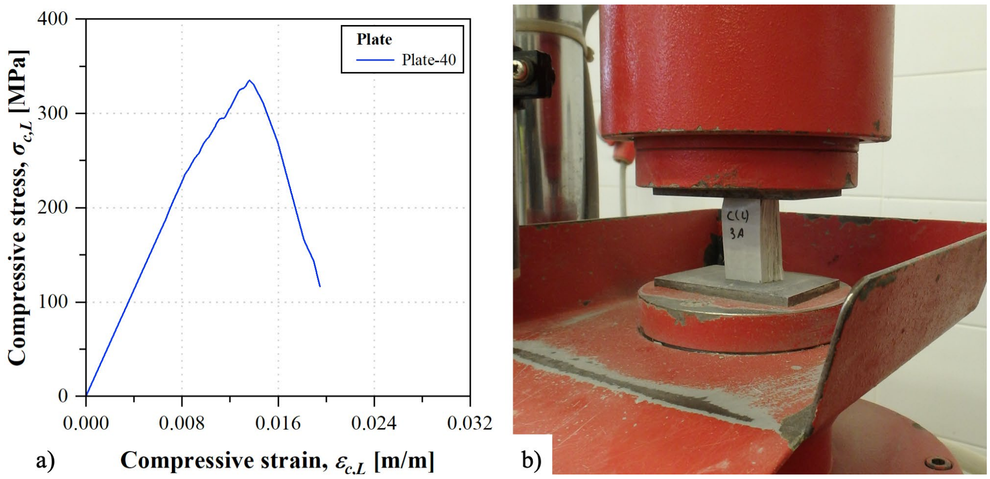

Figure B.3 - GFRP longitudinal compression tests: a) representative stress *vs*. strain curves; b) specimen after failure.

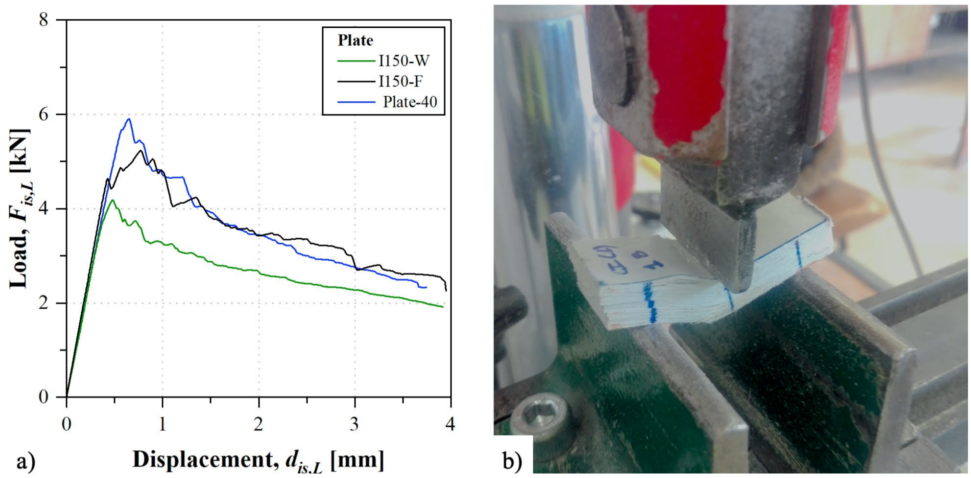

Figure B.4 - GFRP interlaminar shear tests: a) representative load *vs*. displacement curves; b) specimen after failure.

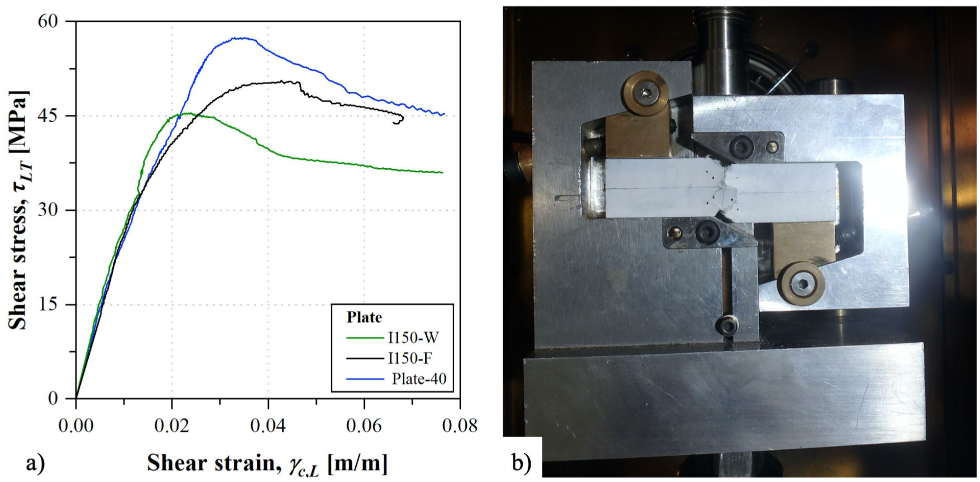

Figure B.5 - GFRP in-plane shear tests: a) representative stress *vs*. strain curves; b) specimen after failure.

STAINLESS STEEL PLATES

The stainless steel plates, grade AISI 304, with 3 and 8 mm of thickness were characterized (4 specimens of each plate were tested) regarding their mechanical properties in tension, following the recommendations of EN 10002-1 for metallic materials [6.7]. The tests were performed using the above-mentioned universal test machine. Figure B.6 illustrates the specimens' geometry and Figure A6b presents a representative stress *vs*. strain curve for both plates. The main results concerning the tensile properties of the stainless steel plates are summarized in Table 6.2 (of Chapter 6).

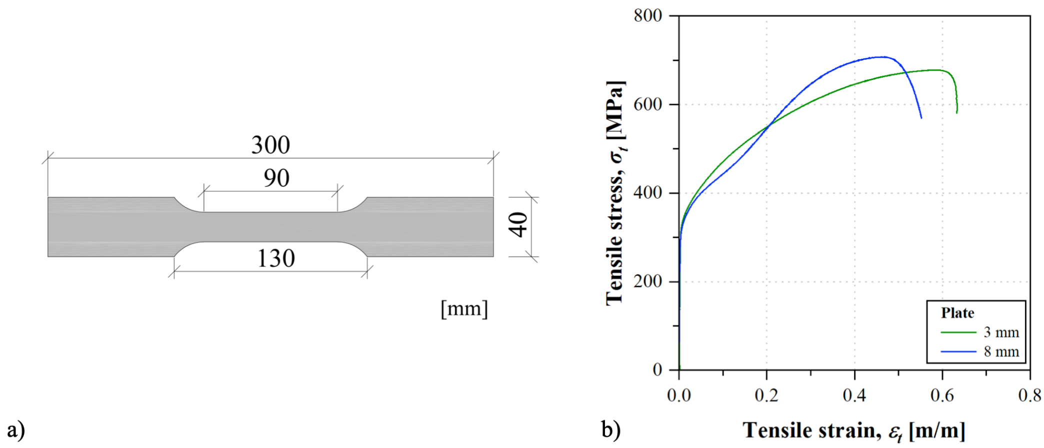

Figure B.6 - Stainless steel tensile tests: a) specimen geometry; b) representative true stress *vs*. true strain curves.

Appendix C

Numerical assessment of the stress spreading angle in GFRP members under concentrated loads

This appendix presents the procedure used to assess the spreading angle of transverse compressive stresses through the flange and web-flange junction of the pultruded GFRP profile used in the beam-to-column connections. In order to study this effect, Finite Element (FE) models were developed using ABAQUS commercial software.

The FE models (illustrated in Figure C.1) simulated a GFRP profile (taking advantage of symmetry boundary conditions), with I-shaped section (150×75×8 mm^2) and length of 900 mm, subjected to a concentrated load applied to its top flange. The load was applied by imposing a 1 mm displacement to a steel plate (E_s = 200 GPa), with 8 mm of width (the same size as the profile flange thickness), positioned at mid-span of the profile. Both ends of the profile were fully fixed, and the interaction between the steel plate and the profile was defined as HARDCONTACT without friction. In order to reduce the computational costs, symmetry boundary conditions were considered along the mid-plane of the profile. The GFRP material was modelled using the elastic and orthotropic mechanical properties obtained in the mechanical characterization tests (*cf*. Chapter 6). Hexahedron linear solid elements with full integration (C3D8) were used. Five different mesh sizes were considered in the mid portion (450 mm) of the GFRP profile, corresponding to: (i) 1 mm; (ii) 1.5 mm; (iii) 2 mm; (iv) 3 mm; and (v)

4 mm; the outer portions of the profile, not relevant for these particular analyses, were modelled with a fixed global size of 4 mm.

Figure C.2 presents the typical stress profiles obtained from the FE models immediately below the web-flange junction of the GFRP profile. The effective width (b_{eff}) of the GFRP material resisting the transverse compressive stresses was defined as,

$$b_{eff} = \frac{A_{stress}}{S_{max}} \tag{C.1}$$

where, A_{stress} is the area of the stress profile in the web and $S_{\max}$ is the maximum stress of such profile (*cf.* Figure C.2). More importantly, the transverse compressive stress spreading angle (α) (also illustrated in Figure C.2) is then given by,

$$\alpha = \tan^{-1}\left(\frac{b_{eff} - 0{,}5b}{k}\right) \tag{C.2}$$

where, b (8 mm) is the width of the loading plate and k (12 mm) is the depth in which the stresses spread. In this case, k corresponds to the flange thickness (8 mm) plus the web-flange junction fillet radius (4 mm).

Figure C.3 presents the stress spreading angle (α) obtained for different mesh sizes. All meshes presented very similar results, with the stress spreading angle tending to ~45º for finer meshes (*i.e.*, stress spreading at ~1:1). It should be noted that, even given the orthotropic nature of the GFRP material, this resulting spreading angle is similar to that proposed for steel [7.25].

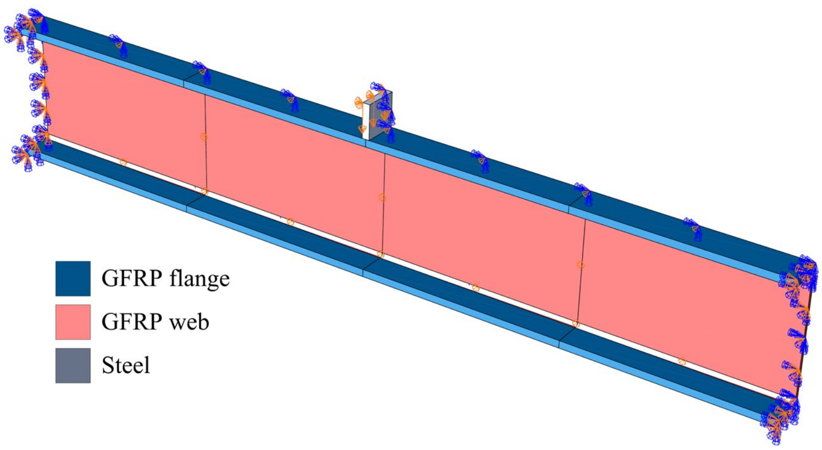

Figure C.1 - Overview of FE model to determine the stress spreading angle.

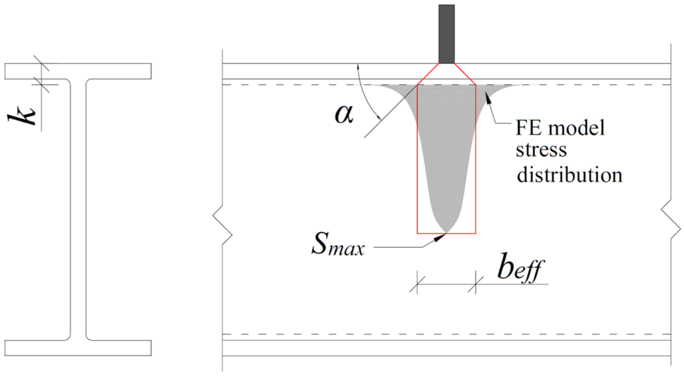

Figure C.2 - Stress distribution (qualitative) obtained from the FE model and definition of effective width (b_{eff}) and stress spreading angle (α).

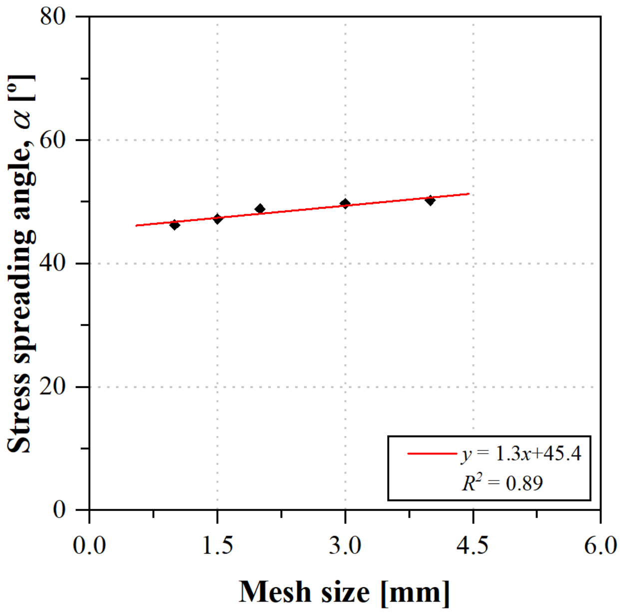

Figure C.3 - Stress spreading angle (α) for different mesh sizes.

Appendix D

Design example to determine the stiffness of connection BC-8-F-R using the component method

This appendix presents a design example of the component method described in Chapter 7 (Section 7.3). The determination of the rotational stiffness of connection series BC-8-F-R starts with the estimation of the stiffness of each component (*cf.* Figure 7.2 of Chapter 7) and is followed by their combination in series. The geometric properties of each component are summarized in Table D.1 according to Chapter 7 and the material properties are presented in Chapter 6.

Table D.1 - Parameters for the design example.

Parameters		
h_c	0.15	m
t_{fc}	0.008	m
r_c	0.004	m
$t_{w,c}$	0.008	m
G_{LT}	3	GPa
z	0.193	m
$E_{c,T}$	8.1	GPa
t_a	0.008	m
s_{nut}	0.013	m

Parameters		
t_p	0.008	m
A_s	36.6	mm^2
E_s	194	GPa
L_b	0.1725	m
l_{eff}	0.0325	M
m	0.0238	m
k_b	20080	kN/m
$E_{t,L}$	27.6	GPa
A_{plate}	320	mm^2
l	0.265	m

1. Stiffness of the column web panel in shear, k_1:

$$k_1 = \frac{A_{vc} \times G_{LT}}{z} \qquad \text{(Eq. 7.2)}$$

where,

$$A_{vc} = (h_c - 2(t_{fc} + r_c)) \times t_{w,c} = (0.150 - 2(0.008 + 0.004)) \times 0.008 = 1008 \times 10^{-6}\ m^2$$

$$G_{LT} = 3{,}000{,}000\ kN/m^2$$

$$z = 0.150 + 0.035 + 0.008 = 0.193\ m$$

resulting in,

$$k_1 = \frac{1008 \times 10^{-6} \times 3{,}000{,}000}{0.193} = 15{,}668.4\ kN/m$$

2. Stiffness of the bottom and top column web in transverse compression, k_2 and k_3:

$$k_2 = \frac{b_{eff,c,bottom} \times t_{w,c} \times E_{c,T}}{h_{w,c}} \qquad \text{(Eq. 7.3a)}$$

$$k_3 = \frac{b_{eff,c,top} \times t_{w,c} \times E_{c,T}}{h_{w,c}} \qquad \text{(Eq. 7.3b)}$$

where,

$$b_{eff,c,bottom} = t_a + 2\left(t_{fc} + r_c\right) = 0.008 + 2(0.008 + 0.004) = 0.032\ m$$

$$b_{eff,c,top} = s_{nut} + 2\ (t_p + t_{fc} + r_c) = 0.013 + 2\ (0.008 + 0.008 + 0.004) = 0.053\ m$$

$$t_{w,c} = 0.008\ m$$

$$E_{c,T} = 8{,}100{,}000\ kN/m^2$$

$$h_{w,c} = h_c - 2\left(t_{fc} + r_c\right) = 0.150 - 0.008 \times 2 - 0.004 \times 2 = 0.126\ m$$

resulting in,

$$k_2 = \frac{0.032 \times 0.008 \times 8{,}100{,}000}{0.126} = 16{,}457.1\ kN/m$$

$$k_3 = \frac{0.053 \times 0.008 \times 8{,}100{,}000}{0.126} = 27{,}257.1\ kN/m$$

3. Stiffness of each row of top rods in tension, k_4:

$$k_4 = \frac{1.6 \times A_s \times E_s}{L_b} \quad \text{(Eq. 7.6)}$$

where,

$$A_s = 36.6 \times 10^{-6}\ m^2$$

$$E_s = 194{,}000{,}000\ kN/m^2$$

$$L_b = 0.150 + 0.008 \times 2 + 0.0065 = 0.1725\ m$$

resulting in,

$$k_4 = \frac{1.6 \times 36.6 \times 10^{-6} \times 194{,}000{,}000}{0.1725} = 65{,}858.8\ kN/m$$

4. Stiffness of the top flange cleat in bending, k_5:

$$k_5 = \frac{0.9 \times l_{eff} \times t_a^{\,3} \times E_s}{m^3} \quad \text{(Eq. 7.7)}$$

where,

$$l_{eff} = {}^{0.075}/_{2} = 0.0325\ m$$

$$t_a = 0.008\ m$$

$$E_s = 194{,}000{,}000\ kN/m^2$$

$$m = 0.035 - 0.8 \times 0.004 - 0.008 = 0.0238\ m$$

resulting in,

$$k_5 = \frac{0.9 \times 0.0325 \times 0.008^3 \times 194{,}000{,}000}{0.0238^3} = 2{,}200{,}840\ kN/m$$

5. Stiffness of the beam's top bolts in shear, k_6:

$$k_6 = \frac{1}{\frac{1}{k_b} - \frac{1}{k_{plate}}} \quad \text{(Eq. 7.8)}$$

where,

$k_b = 20{,}080\ kN/m$ (*cf.* Chapter 6)

$$k_{plate} = \frac{E_{t,L} \times A_{plate}}{l} = \frac{27{,}600{,}000 \times 320 \times 10^{-6}}{0.265} = 33{,}328\ kN/m$$

$$E_{t,L} = 27{,}600{,}000\ kN/m^2$$

$$A_{plate} = 0.040 \times 0.008 = 320 \times 10^{-6} m^2$$

$$l = 0.265\ m$$

resulting in,

$$k_6 = \frac{1}{\frac{1}{20{,}080} - \frac{1}{33{,}328}} = 50{,}514.6\ kN/m$$

6. Rotational stiffness of series BC-8-F-R, k_{an}:

$$k_{an} = \frac{z^2}{\sum_{i=1}^{6} \frac{1}{k_i}} \qquad \text{(Eq. 7.1)}$$

resulting in,

$$k_{an} = \frac{0.193^2}{\frac{1}{15{,}668.4} + \frac{1}{16{,}457.1} + \frac{1}{27{,}257.1} + \frac{1}{65{,}858.8} + \frac{1}{2{,}200{,}840} + \frac{1}{50{,}514.6 \times 2}}$$
$$= 195.7\ kN.m/rad$$

Appendix E

Web-crippling tests

Prior to the frame tests presented in Chapter 10, web-crippling tests were performed to assess the resistance to transverse compression of the GFRP profiles (columns) and to evaluate the strength increase provided by a reinforcement system comprising cold-formed stainless steel (grade AISI 304) profiles. The reinforcement system, illustrated in Figure E.1, comprises two stainless steel channel section profiles acting as web jackets, designed to fit the inner faces of the profile's web and flanges, bolted to each web face with four M8 bolts. Web crippling tests were carried out in three series of specimens, namely: (i) non-reinforced specimens (ETF-NR); and specimens reinforced with (ii) 2 mm thick (ETF-R2) and (iii) 4 mm thick (ETF-R4) channel sections.

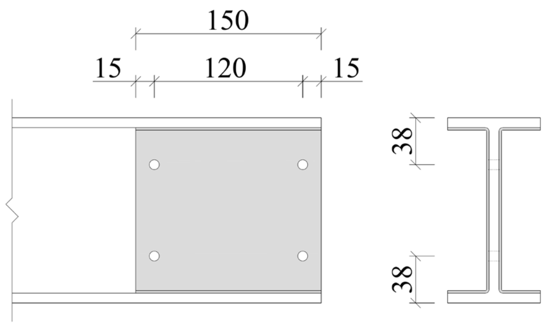

Figure E.1 - Web-crippling tests: overview of reinforcing system.

The web-crippling tests were performed in a universal testing machine from *Instron* with capacity of 250 kN, by applying a transverse compressive displacement at a rate of 0.01 mm/s, transmitted to the flanges of the GFRP profiles through two 20 mm thick steel plates with length of 15 mm. The specimens were tested according to the end two flange configuration (ETF, a common web-crippling test setup), as depicted in Figure E.2, and three specimens were tested per series.

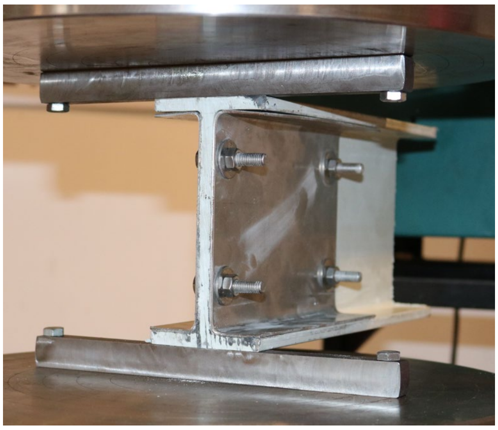

Figure E.2 - Web-crippling tests: test setup.

Figure E.3 presents representative load *vs*. displacement curves for all series and Table E.1 summarizes the main results of the web-crippling tests, namely in what concerns the stiffness (K), the (transverse) displacement at failure (δ_u) and the failure load (F_u). The specimens of series ETF-NR presented almost linear behaviour until the occurrence of web-crippling failure (due to compressive failure of the web near the web-flange junction), while reinforced specimens presented considerable non-linear behaviour, failing due to "failure mode". The stainless steel channel sections provided significant increases of web-crippling resistance, respectively ~ 2,5 and ~4,6 times for series ETF-R2 and ETF-R4.

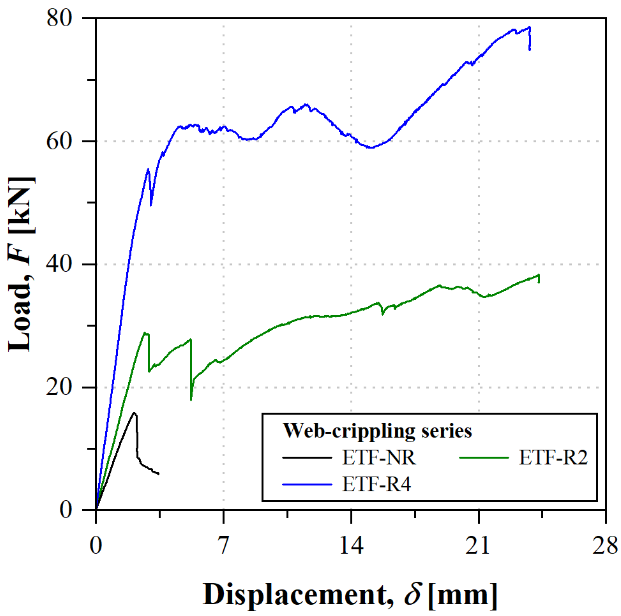

Figure E.3 - Web-crippling tests: load *vs*. displacement curves.

Based on these results, it was decided to apply the reinforcing system with 4 mm thick channel sections in the frame tests.

Table E.1 - Web-crippling tests: main results – stiffness (K), transverse deflection at failure (du) and failure load (Fu).

Series	***K* (kN/mm)**	**δ_u (mm)**	**F_u (kN)**
ETF-NR	8.0 ± 0.4	2.7 ± 0.1	15.7 ± 0.4
ETF-R2	10.6 ± 1.1	22.5 ± 3.2	39.3 ± 0.7
ETF-R4	18.6 ± 0.4	22.0 ± 6.2	72.4 ± 7.6

Appendix F

Beam-to-column test

Prior to the frame tests in Chapter 10, the behaviour of the BC-6-F2-R2 beam-to-column connection (corresponding to BC-6-F2-R connection but with column's web reinforcement to delay web-crippling failure) was assessed by means of a monotonic test. The results obtained in this test were compared to those regarding the same connection system without column's web reinforcement, which had been thoroughly characterized in Chapter 6.

The test was conducted in a steel closed loading frame anchored to the laboratory's strong floor (Figure F.1). The displacement was applied to the beam at 655 mm from the column's mid-axis by a hydraulic jack from *Dartec* with load capacity of 250 kN. Two mechanical hinges were used to guarantee the verticality between the applied load and the specimen's beam. The displacements and loads were measured, respectively, by the hydraulic jack's own transducer and by a load cell from *TML* with capacity of 300 kN. The displacement was applied at a rate of 0.25 mm/s. More information regarding the test setup and procedure can be found in Chapter 6.

The ultimate failure of the beam-to-column specimen occurred in the beam's web-flange junctions, as depicted in Figure F.2. The load *vs*. displacement curve obtained in this test is presented in Figure F.3; the curves corresponding to the monotonic tests of connection BC-6-F2-R are also included for comparison (*cf*. Chapter 6). It can be seen that the column's web reinforcement did not influence the overall response of the connection, with all specimens depicted in Figure F.3 presenting similar behaviour.

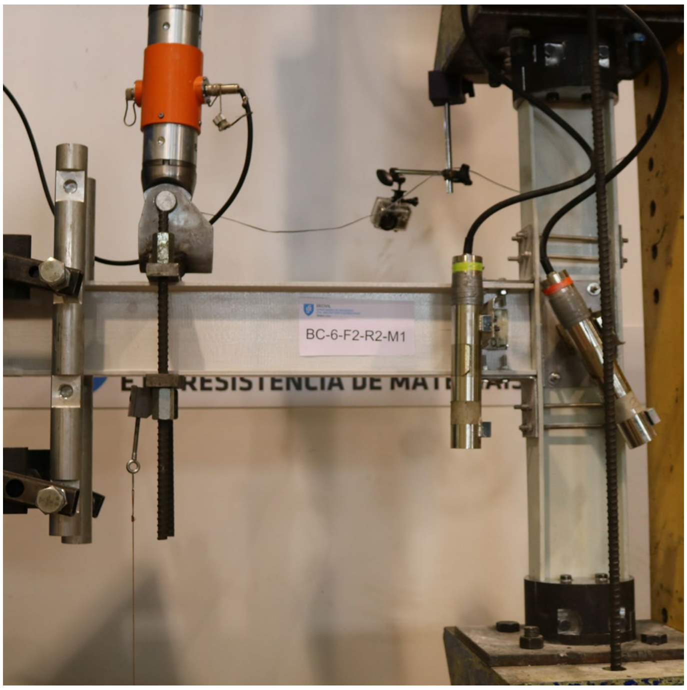

Figure F.1 - Beam-to-column test: test setup.

Figure F.2 - Beam-to-column test: tensile failure of the beam's web-flange junction.

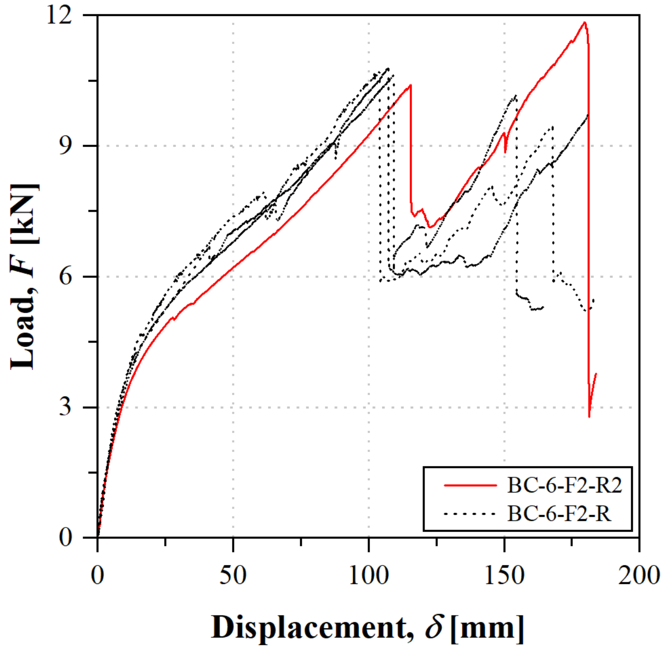

Figure F.3 - Beam-to-column test: load *vs*. displacement curves.

Appendix G

Properties of the ADAS element

The geometry of the ADAS plate used in the present work is detailed in Figure 10.18 of Chapter 10. The properties of this element were estimated for the idealized X-plate (red dashed line in Figure 10.18a) and for the ADAS element (composed of seven plates), using the procedure described in the EERC report [10.13] and considering S275 grade steel (f_y=275 MPa and ε_y=0.0013).

Firstly, the curvature of the steel at yield (χ_y^{PL}) was estimated using Eq. G1:

$$\chi_y^{PL} = \frac{\varepsilon_y}{t/2} = \frac{0.0013}{0.0025} = 0.524 \tag{G.1}$$

where t is the overall thickness of the plates.

By considering that both sides of the X-plate mid-height present constant curvature, the double integration of the curvature along the height of the steel plate results in a relative displacement between the top and the bottom of the plate of Δ_y^{PL}=0.01179 m.

The yield moment (M_y^{PL}) was then estimated as:

$$M_y^{PL} = f_y \frac{b \times t^2}{6} = 275000 \frac{0.15 \times 0.005^2}{6} = 0.172\ kN.m \tag{G.2}$$

The corresponding yield shear load (V_y^{PL}) is obtained from:

$$V_y^{PL} = \frac{2 \times M_y}{h} = \frac{2 \times 0.172}{0.3} = 1.146\ kN \tag{G.3}$$

The EERC report [10.13] then states that the yield displacement (Δ_y^{ADAS}) and strength (F_y^{ADAS}) of the ADAS element are approximately 150% of the yield displacement and strength of the X-plate element, respectively, to account for the slippage between plates in a ADAS element. Taking this into consideration and also multiplying the yield shear load by the number of plates, the resulting Δ_y^{ADAS} and F_y^{ADAS} for this ADAS element have values of 0.0177 m and 12.03 kN, respectively. The load *vs*. displacement curve of this device is presented in Figure 10.20a. It is worth noting that the maximum displacement attained by this ADAS element was not estimated. However, one ADAS element tested in the EERC report [10.13], with different geometry than the one used in this work, was able to withstand 13.6 times the yield displacement before collapsing.